To the Graduate Council:

I am submitting herewith a dissertation written by Omar A. Zeidan entitled "Spectroscopic Studies on High-Spin States in ^{128,129}Nd and ^{130}La." I have examined the final paper copy of this dissertation for form and content and recommend that it be accepted in partial fulfillment of the requirements for the degree of Doctor of Philosophy, with a major in Physics.

Leo L. Riedinger, Major Professor

We have read this dissertation
and recommend its acceptance:

Accepted for the Council:

Vice Provost and Dean of
Graduate Studies

Spectroscopic Studies on High-Spin States in ^{128,129}Nd and ^{130}La

A Dissertation
Presented for the
Doctor of Philosophy
Degree
The University of Tennessee, Knoxville

Omar A. Zeidan

May 2002

Thesis
2002b
.245

This dissertaion is dedicated
to my mother *Adla*
and
to my wife *Lara*

ACKNOWLEDGEMENTS

My special thanks goes to all the members of the nuclear structure group at the University of Tennessee whom I worked with in the past three and a half years. I felt lucky being part of this unique group as they provided a pleasant research atmosphere which allowed me to progress very rapidly in the field of high-spin physics.

I cannot find the words to describe my sincere gratitude to Dr. Lee Riedinger for being a wonderful advisor. I learned from him many things including the skill of how to look at the big picture and present the results professionally. Despite his heavy administrative responsibilities as a deputy director for science and technology at Oak Ridge National Lab, he always managed to find the time to discuss physics on a regular basis. My deepest gratitude goes to Dr. Daryl Hartley who had the great responsibility of advising all the graduate students in the group, teach introductory physics courses, and conduct his own research. He was always there for me when I got stuck on many research problems, and took the time to explain things clearly. My work would not have been accomplished without his tireless effort and great support. I also would like to thank Dr. Jing-ye Zhang for his willingness to answer my questions on the theoretical issues of this work.

Special thanks to all the physicists I have collaborated with on high-spin physics experiments. I have learned many things from the researchers at Oak Ridge National Lab, Argonne National Lab, and Yale University. Their collaboration made it easy for me to get the best experimental data from the best spectrometers available for research in the US. I would like to thank my committee members, Dr. Carrol Bingham, Witek Nazarewicz, and Dr. Larry Townsend for reviewing this manuscript. Thanks to Dr. Nazarewicz for giving me the first theoretical insights into the field of nuclear structure from his courses.

Last, but not least, my wife Lara deserve a special recognition for her essential role in my life during the past two years. I am grateful for her for standing by me at all times and making it always easy for me even in the hardest of times. I cannot imagine finishing this work without her love and understanding. I would like

to thank my family for their encouragement and support during my graduate school years. They live far away, but they are always close to my heart.

ABSTRACT

This dissertation reports the observation of high-spin states in the neutron-deficient ^{128,129}Nd and ^{130}La nuclei from three fusion evaporation experiments. In one experiment, high-spin states in ^{128,129}Nd were populated using the reaction ^{40}Ca + ^{92}Mo. The 170-MeV ^{40}Ca beam was supplied by the 25 MV tandem at Oak Ridge National Laboratory. The Recoil Mass Spectrometer provided mass identification, while γ-ray and charged-particle emissions were detected by the CLARION spectrometer in conjunction with the HyBall array. In a second experiment emphasizing the highest spin states possible, the same reaction was used at a beam energy of 184 MeV provided by the ATLAS accelerator at Argonne National Laboratory. Charged-particle and γ-ray emissions were detected by the Microball array operating in conjunction with the Gammasphere spectrometer. The third experiment was performed at the Wright Nuclear Structure Laboratory at Yale University where high-spin states of ^{130}La were populated using a ^{19}F beam of 100 MeV average energy delivered to a ^{116}Cd target, and the emitted γ rays were detected by the Yrast-Ball array.

For ^{128}Nd, the previously known ground-state band has been extended to $I^{\pi} = (34^{+})$ and four side bands were observed for the first time with a total of nearly 60 new transitions. A significant delay of the $\nu h_{11/2}$ crossing frequency was observed in the $A \sim 130$ region, with the largest values occurring consistently at $N = 70$. An attempt to understand the phenomenon was performed with calculations by the Cranked Shell Model (CSM) and the Projected Shell Model (PSM). The presence of octupole correlations in ^{128}Nd and nearby even-even nuclei was also investigated.

Nearly 150 new transitions were placed in a level scheme of ^{129}Nd that consists of four rotational structures, three of which have been observed for the first time. The bands were assigned configurations based on their $B(M1)/B(E2)$ ratios, aligned angular momentum, observed band crossings, and signature splitting. Evidence for the observation of the deformation-driving $\nu i_{13/2}[660]1/2$ orbital is presented. Signature splitting trends in the $\nu h_{11/2}$ bands of $A \sim 130$ nuclei were investigated within the framework of the CSM, and comparisons are made with observations in the $\pi h_{11/2}$

bands near $A \sim 160$.

For ^{130}La, the previously known level scheme was confirmed and new spin assignments for the $\pi h_{11/2}\nu h_{11/2}$ and $\pi h_{11/2}\nu g_{7/2}$ bands are proposed. In addition, new configuration and spin assignments were proposed for the previously observed oblate band. New (old) configurations in ^{130}La were proposed (confirmed) based on measured multipolarities of linking transitions, $B(M1)/B(E2)$ ratios, alignments, and energy level systematics of other odd-odd La nuclei. Based on our new spectroscopic information, the presence of the previously proposed chiral-twin band in the $\pi h_{11/2}\nu h_{11/2}$ configuration is questionable, and isomeric states below all the known structures have been established.

TABLE OF CONTENTS

CHAPTER PAGE

1 Introduction **1**

2 Theoretical Formalism **5**

2.1 Spherical Shell Model 5

2.1.1 Harmonic Oscillator Potential 5

2.1.2 Modified Harmonic Oscillator Potential 7

2.2 Deformed Shell Models 7

2.2.1 Nuclear Deformation Parameters 9

2.2.2 Collective Model 11

2.2.3 Nilsson Model 11

2.2.4 Woods-Saxon Model 18

2.3 Nuclear Rotation 19

2.3.1 Rotations of Axially Symmetric Deformed Nuclei 19

2.3.2 Cranked Shell Model 20

2.3.3 Symmetries in the Cranking Hamiltonian 21

2.3.4 Signature Splitting 23

2.3.5 The Pairing Interaction 24

2.3.6 Quasiparticle Diagrams, Band Crossings, and Alignment . . . 29

2.3.7 Transformation of Experimental Observables into the Rotating Frame 32

2.4 The Nuclear Electromagnetic Radiation 35

2.4.1 Multipole Radiations and Transition Probabilities 35

2.4.2 In-band Transition Rates 37

3 Experimental Techniques **39**
3.1 Population of High-Spin States 39
3.1.1 Heavy-Ion Fusion Evaporation Reactions 39
3.1.2 Decay of Compound Nuclei 41
3.1.3 Statistical Model Calculations for Reactions Cross Sections . . 44
3.2 Experimental Devices 46
3.2.1 Gamma-ray Detection and Properties of Germanium Detectors 46
3.2.2 Large Arrays of Escape Suppressed Spectrometers 52
3.2.3 Charged Particle Detection 58
3.2.4 Mass Spectroscopy with the Recoil Mass Spectrometer 66
3.3 Electronics and Data Acquisition Systems 68
3.3.1 Concept of Coincidence 68
3.3.2 Compton-Suppression Electronics 69
3.3.3 Data Acquisition and Sorting 72
3.4 Offline Data Analysis 73
3.4.1 Charged Particle Data Analysis 73
3.4.2 Ge γ-ray Data Analysis 75

4 Experimental Results of and Discussion of ^{128}Nd **84**
4.1 Overview 84
4.2 Experimental Details 84
4.3 The Level Scheme 91
4.4 Rotational Alignments and Configuration Assignments 94
4.4.1 Band 1 94
4.4.2 Band 2 96
4.4.3 Bands 3 and 4 97
4.4.4 Band 5 98
4.5 Octupole Correlations 99
4.6 Systematics of the $\nu h_{11/2}$ Crossing in $A \sim 130$ Nuclei 101

5 Experimental Results of and Discussion of ^{129}Nd 110
5.1 Overview 110
5.2 Experimental Details 111
5.3 Analysis of ^{129}Nd 112
5.3.1 The Level Scheme and Spin Assignment 112
5.4 Configuration Assignments 126
5.4.1 Alignments and band crossings 129
5.4.2 $B(M1)/B(E2)$ transition strength ratios 135
5.5 Discussion of Signature Splitting in $A \sim 130$ Nuclei 138
5.5.1 The Deformation-Driving Forces in the $h_{11/2}$ Subshells 139
5.5.2 Signature Splitting Systematics of the $\nu h_{11/2}$ Bands in Odd-$A \sim 130$ Nuclei 142
5.5.3 Signature Splitting in the $\nu h_{9/2}[541]1/2$ Band 147

6 Experimental Results of ^{130}La 151
6.1 Overview 151
6.2 Experimental Details 152
6.3 The Level Scheme 154
6.4 Configuration and Spin Assignments 159
6.4.1 Bands 1 and 2 : $\pi h_{11/2}\nu h_{11/2}$ and $\pi h_{11/2}\nu g_{7/2}$ 163
6.4.2 Band 3: Oblate Structure 167
6.5 Overview of Nuclear Chirality 172
6.6 Experimental Check for Chiral Bands in ^{130}La 175

7 Summary and Conclusions 181

BIBLIOGRAPHY 185

VITA 195

LIST OF FIGURES

FIGURE		PAGE
1.1	Calculated ground-state values $\|\epsilon_2\|$ for nuclei with N<40.	2
2.1	Single-particle energies for a simple harmonic oscillator	8
2.2	Nuclear shapes in relation to the parameters β_2 and γ.	10
2.3	Nilsson diagram for neutrons, $50 \leq N \leq 82$ ($\epsilon_4 = {\epsilon_2}^2/6$).	14
2.4	Nilsson diagram for protons, $50 \leq Z \leq 82$ ($\epsilon_4 = {\epsilon_2}^2/6$).	15
2.5	Diagram showing oblate, spherical, and prolate shapes.	16
2.6	Asymptotic quantum numbers of the deformed Nilsson model.	16
2.7	A schematic diagram of the energy spectrum under the influence of various nuclear potentials.	23
2.8	Depiction of partial occupancy due to pairing.	27
2.9	Illustration of the effect of pairing correlations and Coriolis interactions.	28
2.10	Quasiparticle Routhians calculated for both neutrons and protons in ^{128}Nd.	30
3.1	Schematic drawing of an incident nucleus impacting a target nucleus.	40
3.2	Angular momentum versus energy illustration of the decay of a compound nucleus.	43
3.3	Calculated cross sections for residual nuclei as a function of beam energy.	45
3.4	Schematics of an electrically-segmented detector.	50
3.5	A CLARION array clover and its BGO shield.	51
3.6	1/4 view of Gammasphere.	55
3.7	Calculated sensitivity for Gammasphere.	57
3.8	The effect of add-back and Compton suppression.	59

3.9 The YRAST Ball 60
3.10 Close-up photograph of the Micoball. 63
3.11 A schematic view of the ORNL Recoil Mass Spectrometer. 67
3.12 Schematic decay scheme illustrating correlated γ decays 69
3.13 A simple coincidence circuit for two non-suppressed Ge detectors. . . 70
3.14 The schematics of a sample Compton-suppression setup. 71
3.15 Energy versus particle identification ratio (PID) for a CsI detector. . 74
3.16 Calibration Spectra of ^{182}Ta and ^{152}Eu. 77
3.17 Efficiency calibration curve of Gammasphere detectors. 78
3.18 Gating on a cube in LEVIT8R. 81

4.1 The level scheme for ^{129}Nd. 86
4.2 Map of the observed and possibly populated nuclei. 87
4.3 Spectrum of the ground-state band (band 1) in ^{128}Nd. 92
4.4 Spectra of the side bands in ^{128}Nd. 93
4.5 The alignment plotted versus rotational frequency for bands 1-4 in ^{128}Nd. 95
4.6 Experimental neutron $h_{11/2}$ crossing frequencies. 104
4.7 Single-particle Cranked Shell Model calculations for quasineutrons in ^{130}Nd. 106
4.8 Three-dimensional plots of neutron crossing frequency ω_c for ^{128}Ce versus CSM parameters. 108

5.1 HIVAP theoretical predictions of reaction cross sections. 114
5.2 The level scheme for ^{129}Nd. 115
5.3 Transitions from $A = 129$ recoils in the ORNL experiment 116
5.4 Spectra of the negative-parity configurations in ^{129}Nd. 127
5.5 Spectra of the positive-parity configurations in ^{129}Nd. 128
5.6 Neutron single-particle levels as a function of quadrupole deformation. 129
5.7 The alignment plots for ^{129}Nd bands. 130
5.8 Cranked shell model calculation for quasineutrons in ^{129}Nd. 132

5.9 The $B(M1)/B(E2)$ ratios for ^{129}Nd bands. 137
5.10 The quasiparticle energies as a function of the γ deformation. 140
5.11 The quadrupole-driving force versus ϵ_2. 141
5.12 Signature splitting for the $\nu h_{11/2}$ bands in odd-A nuclei 144
5.13 Theoretical CSM calculations of signature splitting 145
5.14 Signature splitting of the $\nu h_{9/2}[541]1/2$ band. 149

6.1 The level scheme of ^{130}La. 153
6.2 Spectra of the bands in ^{130}La. 156
6.3 LEPS spectra of Ge-gated transitions. 157
6.4 The experimental (symbols) and theoretical (lines) $B(M1)/B(E2)$ ratios for the three bands in ^{130}La. 161
6.5 The alignment as a function of rotational frequency for bands 1-3 in ^{130}La. 162
6.6 Cranked Shell Model calculations for quasiprotons and quasineutrons in ^{130}La. 164
6.7 Energy level systematics of the $\pi h_{11/2}\nu h_{11/2}$ band signatures in $^{124-134}$La. 168
6.8 The dynamical moment of inertia $\mathcal{J}^{(2)}$ as a function of rotational frequency for bands 1-3 in ^{130}La. 169
6.9 Cranked Shell Model calculations for the oblate band in ^{130}La. 170
6.10 A 3-D triaxial nucleus with chiral symmetry 173
6.11 Gated spectra on bottom transitions of the $\pi h_{11/2}\nu h_{11/2}$ configuration in ^{130}La. 176
6.12 In-band gating on the proposed side-band transitions in Fig. 6.11. . . 178
6.13 The island of chirality in the $A \sim 130$ mass region. 180

LIST OF TABLES

TABLE		PAGE
2.1	Convention used for labeling quasiparticle configurations	31
2.2	Numerical values of Weisskopf estimates	37
3.1	Properties of Gammasphere	54
3.2	Properties of Microball	64
4.1	Data for levels and gamma rays in ^{128}Nd	88
4.2	Alphabetic quasiparticle labeling scheme for ^{128}Nd.	96
4.3	The experimental neutron $h_{11/2}$ crossing frequency for rotational bands in $^{128-134}$Nd, $^{127-133}$Pr, $^{126,128-132}$Ce.	103
5.1	HIVAP theoretical predictions of relative cross sections.	113
5.2	Data for levels and γ rays in ^{129}Nd	118
6.1	Quasiparticle labeling scheme for ^{130}La.	160

CHAPTER 1

Introduction

In a continuous effort to understand the structure of the atomic nucleus, nuclear physicists have developed techniques to study particle and radiation emissions following the excitation of nuclear matter. There are several methods to excite the nucleus, and the method of fusion evaporation reactions is of particular interest to high-spin spectroscopists. In these reactions, high nuclear angular momenta can be achieved by bombarding a given target nucleus with an accelerated nucleus that has enough energy to overcome the combined Coulomb interaction. Through the detection of the γ-ray emissions from the rapidly rotating product nuclei, spectroscopists can attain a great deal of information about these nuclei in the extreme of angular momentum. For well-deformed nuclei, the detected γ rays can be arranged in sequences called bands and are sorted based on their energy, intensity, and multipolarity. A given nucleus may have several of these bands at different excitation energies and they can be grouped in a level scheme. Level schemes are different for different nuclei and, therefore, they act as "fingerprints" that hold a wealth of information on the particular nucleus, including deformation and single-particle structure.

This dissertation work focuses on the study of high-spin states in some of the most proton-rich nuclei of the mass 130 region. The important nuclear mechanism that this work emphasizes is the competition between collective and single-particle behavior. The study included all possible combinations of core plus valence nucleons in this mass region: $^{128}_{60}$Nd (even-even), $^{129}_{60}$Nd (odd-A), and $^{130}_{57}$La (odd-odd). Fig. 1.1 shows the location of these nuclei on the nuclear chart. As seen from Fig. 1.1, the nuclei of interest fall in the middle of a deformation region defined by dark lines at the magic $Z = 50$ and $N = 82$ numbers. These lines define narrow regions where deformation-driving shell effects stabilize nuclei to spherical shapes. The influence of

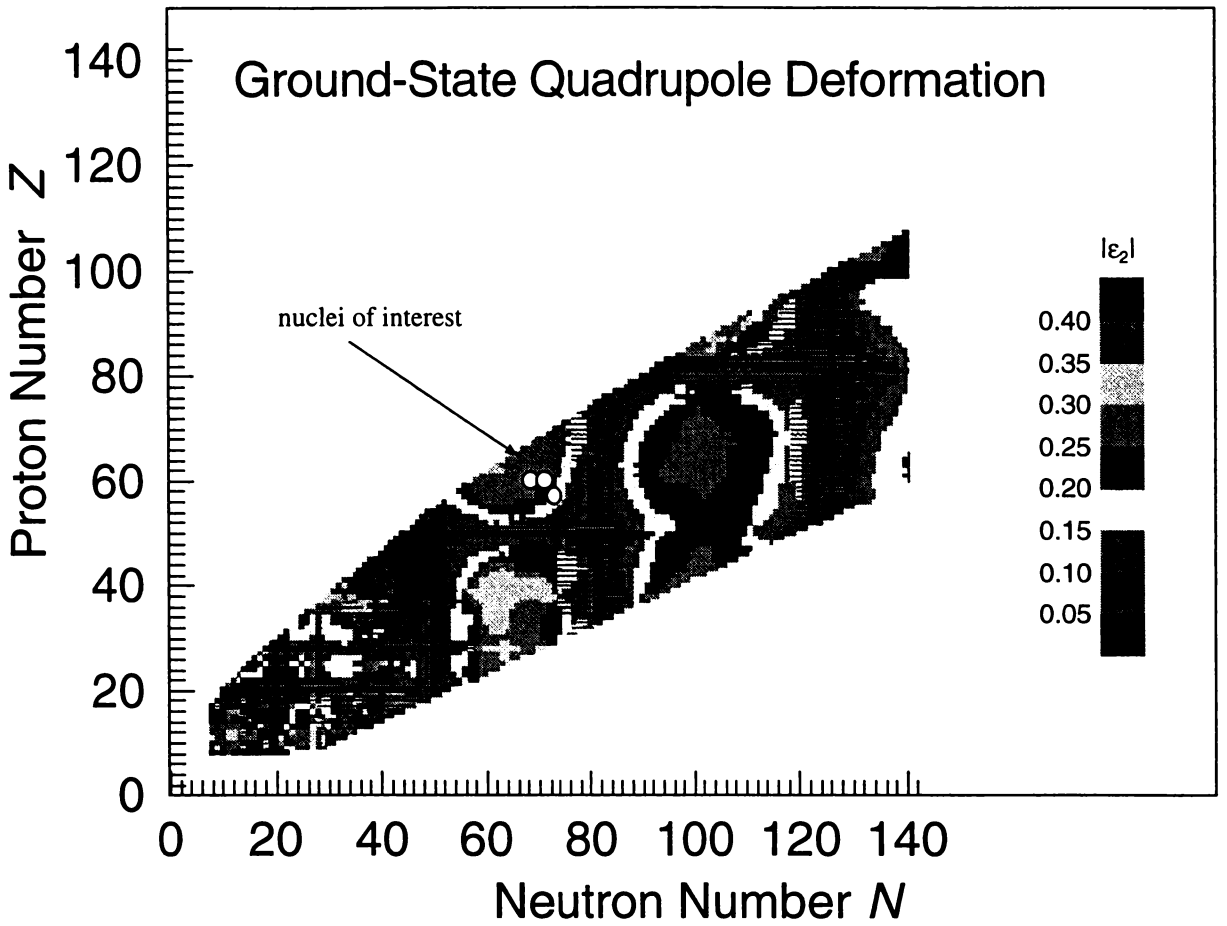


Figure 1.1: Calculated ground-state values $|\epsilon_2|$ for nuclei with $N<40$. Several deformed regions stand out, bordered or partially bordered by dark lines corresponding to magic nucleon numbers. The arrow points to the location of the nuclei (empty circles) ^{128,129}Nd and ^{130}La discussed in this dissertation. Reproduced from Ref. [1].

these shell effects on a given nucleus vary considerably depending on where the nucleus is located with respect to the Z and N magic numbers. The ^{128,129}Nd nuclei, for example, are located further away from the magic lines and closer to the proton drip line than ^{130}La, and hence, they are exposed least to shell effects leading to spherical shape. Therefore, one would expect them to have a larger ground-state deformation than ^{130}La. Indeed, the predicted ground-state quadrupole deformations [1] are β_2= 0.321, 0.322, and 0.218 for ^{128}Nd, ^{129}Nd, and ^{130}La, respectively. Although the total number of nucleons differs by one or two, the type of structures and level excitations observed are very different in each case, which makes the study of high-spin states in this mass region very interesting.

Atomic nuclei are complicated many-body objects, yet the excitation energies of rotational states of some nuclei can be approximated by a semi-classical rigid-rotor formula. However, a more complicated picture based on the quasiparticle formalism is used to interpret rotational sequences of nuclei in this dissertation. Chapter 2 discusses the theoretical aspects of the models used for explaining the experimental data with particular emphasis on the Deformed Shell Model, the Cranked Shell Model (CSM), and Total Routhian Surface (TRS) calculations. These models have been used extensively due to their great success in explaining the physics behind the experimental data in several regions. Yet, no model is perfect, and we point out some of the limitations and prediction accuracies of these models as we discuss the experimental results. In addition, the use of experimental observables such as alignment plots and transition strength ratios [$(B(M1)/B(E2)$] is described in detail to help in the configurational assignment of the bands.

Spectroscopic data for this dissertation work came from three different high-spin experiments performed at Argonne National Laboratory, Oak Ridge National Laboratory, and Yale University. Several detection systems were used, including Gammasphere and CLARION for γ-ray detection, Microball and Hyball for charged particle detection, and the Recoil Mass Spectrometer (RMS) for recoil-mass identification. These experimental equipment are described in detail in Chapter 3 with an introduction of the process of populating high-spin states and a brief account of the analysis techniques used to process the data from these detectors. Chapter 4 presents

new experimental results on high-spin states in ^{128}Nd with four bands observed for the first time. The systematics of the neutron $h_{11/2}$ crossing in $A \sim 130$ nuclei are also discussed and compared with CSM predictions. Evidence for the presence of octupole correlations in this lightest neodymium isotope is also presented. Chapter 5 discusses high-spin states in ^{129}Nd with three configurations observed for the first time. The systematics of signature splitting in lightest odd-A nuclei in the mass 130 region is discussed in terms of deformation trends in Z and N. Experimental signature splittings are then compared with CSM predictions and triaxial deformation trends in the lightest odd-A nuclei are established. Chapter 6 presents new results on the spin and configuration assignment of sequences in ^{130}La. A topic of present day interest is the possibility of chirality in nuclear systems. The nuclear conditions leading to the observation of chiral twin bands in $A \sim 130$ nuclei are presented in this chapter. Based on our analysis, the presence of these bands in ^{130}La is questionable. Finally, a summary of all experimental findings of this work is presented in Chapter 7. Future experimental and theoretical directions based on the experimental findings are presented with general remarks on future directions in the field of high-spin physics and nuclear physics in general.

CHAPTER 2

Theoretical Formalism

This chapter gives a brief account of the theory of nuclear rotation and the implementation of currently available theoretical models on various nuclear structure phenomena. We will particularly emphasize the use of semi-classical models like Nilsson and Cranked Shell Model in nuclear high-spin physics. These models proved to be successful in interpreting experimental spectroscopy data from rapidly rotating deformed nuclei due to their ability to model the interplay between single-particle and collective motion in atomic nuclei. While there is no unified model that describes the traits of all known nuclear phenomena, there are several models which describe particular nuclear structure effects more accurately than others. The predictive power and limitations of each model in interpreting experimental results are discussed in the following sections.

We start with the simplest and oldest nuclear semi-classical model based on the harmonic oscillator potential, and end with the more abstract quantum picture of the nuclear mean field. A brief summary of the theory of nuclear multipole radiation is also presented at the end of this chapter.

2.1 Spherical Shell Model

2.1.1 Harmonic Oscillator Potential

In the study of atomic nuclei, there is much evidence for nuclear shell structure. The peculiar stability of certain combinations of neutrons and protons was pointed out by Elasser [2] in 1934. Stability for light nuclei with N or Z values of 2 (^{4}He), 8 (^{16}O), and 20 (^{40}Ca) became well known, and strong evidence for additional "magic

numbers" at 50 and 82 for protons, and 50, 82, and 126 for neutrons was observed by Mayer [3] in 1948. The magic numbers were explained by Mayer and Jensen [4] in terms of a "shell model", where nucleons moved in a spherically symmetric potential well. The form of this potential is given by

$$V(r) = -V_0 \left[1 - (r/R)^2\right], \tag{2.1}$$

where $V(r)$ is the potential at distance r from the center of the nucleus and R is the nuclear radius. Solving the Schrödinger equation of the above spherical shell potential gives quantum states that can be characterized by n, the principal quantum number related to the number of radial nodes in the wave function, and by l, the orbital angular momentum of the particle. States with $l = 0, 1, 2, 3, \ldots$ are designated as s, p, d, f, ..., respectively, and the states are identified by as $1s$, $2f$, $3p$, ... etc. The level energies are given by

$$E_{nl} = \hbar\omega_0 \left[2n + l - \frac{1}{2}\right] + E_0, \tag{2.2}$$

where

$$\omega_0 = \left[\frac{2V_0}{MR^2}\right]^{1/2}, \tag{2.3}$$

M is the nucleon mass, and $E_0 = 3/2\ \hbar\omega_0$. The energy levels have two important properties that are evident from the expression for E_{nl}. First, the energy levels fall into degenerate multiplets defined by the (integer) values of $2n+1$. Secondly, a given multiplet generally contains more than one value of the principle quantum number n and of the orbital angular momentum l. It is this sequencing of energy levels as a function of n and l that provides the shell structure required of any central potential useful for real nuclei. Since each energy level has $2(2l + 1)$ degenerate m states by the Pauli principal, each shell has a specific number of particles. Hence, such a potential automatically gives a shell structure rather than, say, a uniform distribution of levels. Unfortunately, except for the lowest few, these shells do not correspond to the empirical magic numbers.

2.1.2 Modified Harmonic Oscillator Potential

Although the harmonic oscillator potential is a reasonable first order approximation to the effective nuclear potential, it must be modified to describe real nuclei. It was the monumental achievement of Mayer [5] and Haxel *et al.* [6] to concoct a simple modification to the harmonic oscillator potential that enabled it to reproduce the empirical magic numbers. They showed that an interaction between the intrinsic angular momentum (spin) of the particles and their orbital angular momentum l of the form $V_{ls} \propto l \cdot s$ would split the orbitals into two substates with $l \pm 1/2$ (*e.g.* $1p_{1/2}$ and $1p_{3/2}$). If the "spin-orbit" interaction is of the same order as the spacing between oscillator shells, and states with $j = l + 1/2$ are more stable than states with $j = l - 1/2$, then the magic numbers can be reproduced.

Another modification to the harmonic oscillator potential is to add an attractive term proportional to l^2 [7]. The effect of an l^2 term increases with the orbital angular momentum of the particle and, thus, high angular momentum particles feel a stronger attractive interaction that lowers their energies. Because of the centrifugal force, these particles spend a larger fraction of their time at larger radii. Therefore, the addition of the l^2 term is equivalent to a more attractive potential at larger radii and comes closer to the desired effect of a more constant interior potential (see section 2.2.4). Fig. 2.1 shows the effects of adding the l^2 and $l \cdot s$ terms on the energy levels of the simple harmonic oscillator potential.

2.2 Deformed Shell Models

The existence of rotational motion in a nuclear system is related to the non-spherical shape of the nucleus or nuclear deformation. Over the years, considerable evidence for the presence of stable deformed nuclei have been collected. The nuclei studied in this work are all axially deformed (non-spherical) in their ground states; therefore, a largely qualitative look at the most successful deformed shell models (Nilsson and Woods-Saxon models) has been included in this chapter. For a discussion of nuclear deformation, a parameterization of the shape of the nucleus is introduced first.

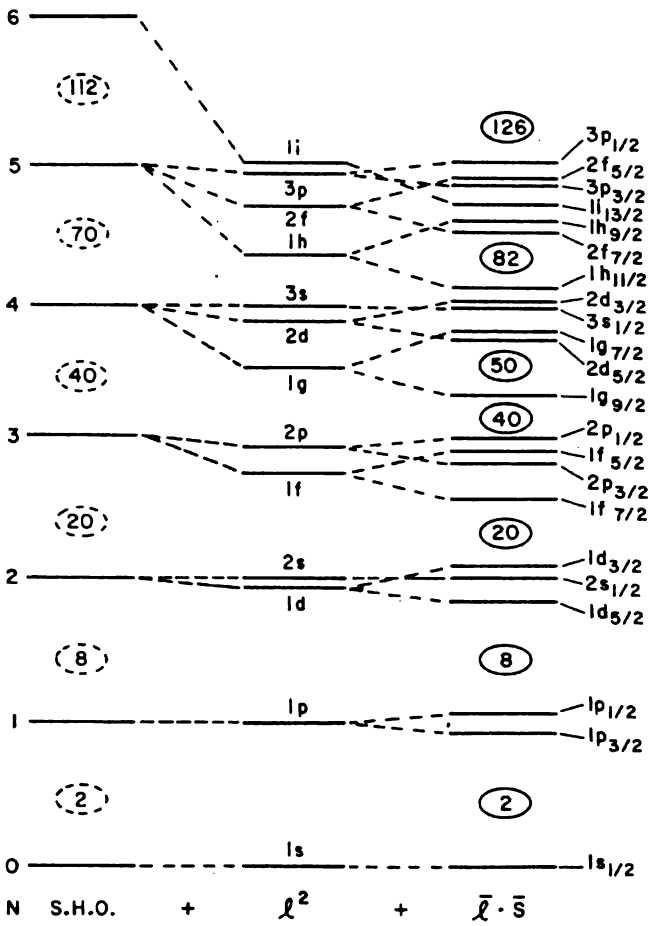


Figure 2.1: Single-particle energies for a simple harmonic oscillator (S.H.O.), a modified harmonic oscillator with l^2 term, and a realistic shell model potential with l^2 and spin orbit $(l \cdot s)$ terms. Reproduced from Ref. [7]

2.2.1 Nuclear Deformation Parameters

Nuclei in their ground states can assume a number of different spheroidal shapes: spherical, oblate (two semi-major axes equal), prolate (two semi-minor axes equal), and triaxial (all three principal axes are different). The nuclear shape is often parameterized by an expansion of the radial vector, R, in terms of the spherical harmonics,

$$R(\theta,\phi) = R_0\left[1 + \alpha_{00} + \sum_{\lambda=0}^{\infty}\sum_{\mu=-\lambda}^{\lambda}\alpha_{\lambda\mu}Y_{\lambda\mu}(\theta,\phi)\right], \tag{2.4}$$

where R_0 is the radius of a sphere with the same volume as the parameterized shape. The parameter α_{00} is determined by the requirement that the nuclear volume stay fixed for all deformations. Terms which include $\lambda = 1$ describe a shift of the whole system. The $\alpha_{\lambda\mu}$ constants are kept fixed by requiring that the origin coincides with the center of mass. In the realm of nuclear high spin, it is usually sufficient to include only the $\lambda = 2$ and $\lambda = 4$ degrees of freedom in the parameterization of Eq. 2.4. When the three planes defined by the principal axes are symmetric, the following simplification can be made

$$\alpha_{\lambda\mu} = \alpha_{\lambda-\mu}, \text{ and } \alpha_{\lambda\mu} = 0 \text{ for odd } \lambda \text{ or } \mu.$$

The radial vector for the nuclear surface to order $\lambda = 2$ can then be represented as

$$R(\theta,\phi) = R_0\left[1 + \alpha_{00} + \alpha_{20}Y_{20}(\theta',\phi') + 2\alpha_{22}Y_{22}(\theta',\phi')\right]. \tag{2.5}$$

Using the "Lund" sign convention, α_{20} and α_{22} become

$$\alpha_{20} = \beta_2\cos\gamma \tag{2.6}$$

and

$$\alpha_{22} = -\frac{1}{\sqrt{2}}\beta_2\sin\gamma, \tag{2.7}$$

where β_2 represents the amount the nucleus is stretched axially, and γ represents the degree of triaxiality. Fig. 2.2 illustrates the shape of the nucleus in relation to the deformation parameters β_2 and γ. Triaxial shapes are described by non-zero γ values, while prolate deformations are described by positive values of β_2. A spherical nucleus has zero β_2 and γ values.

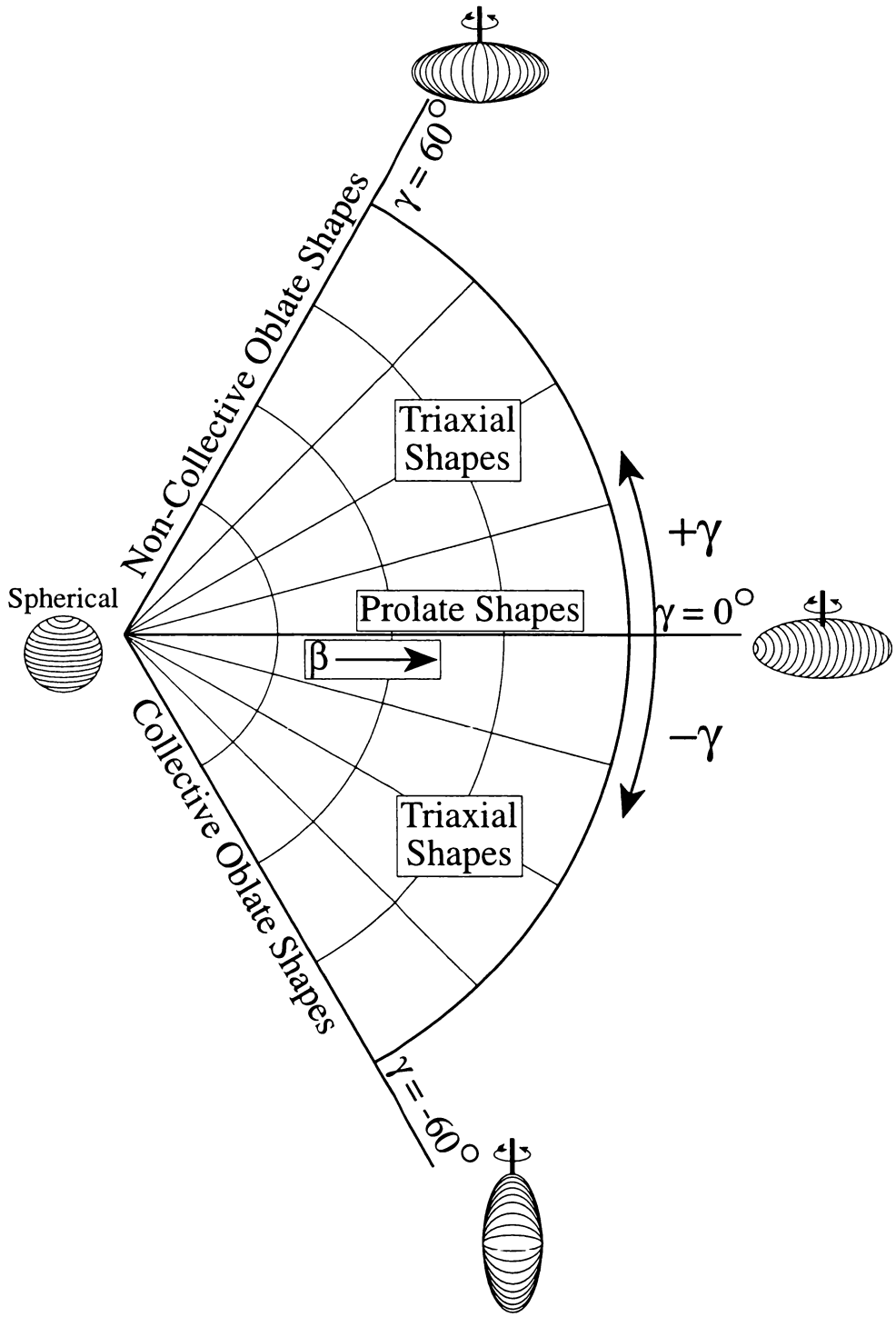


Figure 2.2: Nuclear shapes in relation to the parameters β_2 and γ. The parameters are expressed as polar coordinates. Reproduced from Ref. [9].

Another commonly used expansion is the Nilsson parameterization (ϵ_1, ϵ_2, γ, ...). It is based on modifying the the characteristic harmonic-oscillator frequencies (ω_1, ω_2, ω_3). For a detailed discussion of this parameterization the reader is referred to section 2.2.3.

2.2.2 Collective Model

The spherical shell model succeeded in predicting the magic numbers and in describing nuclei with even Z and N. However, it failed to describe nuclei with odd number of nucleons. Rainwater [10] proposed that, in odd-A nuclei, the motion of the odd nucleon could polarize the even-even core allowing all nucleons to move collectively and, thus, introduced the concept of spheroidal rather than spherical nuclear cores. This concept was further developed by Bohr and Mottelson [11] into a collective model for nuclei, the idea of which led to their sharing the Nobel prize for physics with Rainwater in 1975. In order to conserve the total angular momentum of odd-A nuclei, the core must have its angular momentum coupled to that odd nucleon. The quantization of the combined coherent motion of particle and deformed core forms the basis of the collective model. Other forms of collective excitations include vibrations and giant resonances. For a detailed treatment of the collective model and its applications, the reader is referred to Ref. [12].

2.2.3 Nilsson Model

This model accounts for most of the observed features of single-particle levels in many deformed nuclei and is always the first model to turn to when new experimental information on such levels is obtained. It also provides a microscopic basis for the existence of rotational and vibrational collective motion that is directly linked to the spherical shell model.

The Nilsson model [13] is based on an axially symmetric harmonic oscillator potential. The form of such an ellipsoidal potential can be written as

$$V_{h.o.} = \frac{m}{2}\left[\omega_x^2 x^2 + \omega_y^2 y^2 + \omega_z^2 z^2\right]. \tag{2.8}$$

The three frequencies ω_x, ω_y, ω_z have to be chosen proportional to the inverse of the half axes of the ellipsoid and should meet the condition for volume conservation, therefore,

$$\omega_x \omega_y \omega_z = const. = {\omega_0}^3 \tag{2.9}$$

In the case of axially symmetric shapes, one usually chooses the z-axis as the symmetry axis and introduces a deformation parameter ϵ by the following definition:

$$\begin{aligned} \omega_\perp^2 = \omega_x^2 = \omega_y^2 =: \omega_0^2(\epsilon_2)(1 + \frac{2}{3}\epsilon_2), \\ \omega_z^2 =: \omega_0^2(\epsilon_2)(1 - \frac{4}{3}\epsilon_2), \end{aligned} \tag{2.10}$$

where ϵ_2 is the only deformation parameter in this case, since $\omega_0(\epsilon_2)$ is determined in such a way that volume conservation is guaranteed.

Nilsson noted that by transforming the Cartesian coordinates x_i into the stretched coordinate system $x_{t_i} = (m\omega_i/\hbar)^{1/2} x_i$ the potential could be separated into a spherical and deformed component. In these coordinates the deformed potential (Eq. 2.8) has the form

$$V_{h.o.} = \frac{\hbar\bar{\omega}}{2}\left[r_t^2 - \epsilon_2 \frac{4}{3}\sqrt{\frac{\pi}{5}}\, r_t^2\, Y_{20}(\theta_t, \phi_t)\right], \tag{2.11}$$

where $\bar{\omega} \equiv (2\omega_\perp + \omega_z)/3$ is the average oscillator strength, and r_t, θ_t, and ϕ_t are spherical coordinates in the stretched frame. In this notation, only the second term within the square brackets depends on the deformation parameter ϵ_2.

As we have seen in section 2.1.1, the pure harmonic oscillator potential has two essential drawbacks. (i) A strong spin-orbit term must be added in order to reproduce the right magic numbers. (ii) For heavy nuclei, the realistic average potential is rather flat in the interior of the nucleus. In addition, nucleons at the surface (*i.e.* nucleons with higher l-values) feel a deeper potential in the real case, which is not accounted for in the harmonic oscillator potential. In order to include these effects, Nilsson added two terms to the deformed harmonic oscillator (2.8) and used the Hamiltonian:

$$H = \frac{\mathbf{p}^2}{2m} + \frac{1}{2}m\left[{\omega_\perp}^2(x^2 + y^2) + {\omega_z}^2 z^2\right] + C\mathbf{l}\cdot\mathbf{s} + D\mathbf{l}^2 \tag{2.12}$$

where C is a constant that gives the strength of the spin-orbit force, while $D\mathbf{l}^2$ shifts the levels with higher l-values downward. Later on, one observed that for states with large N quantum numbers, the corresponding shift is too strong and the following replacement was made [14]

$$D \cdot (\mathbf{l}^2 - \langle \mathbf{l}^2 \rangle_N), \tag{2.13}$$

where $\langle \mathbf{l}^2 \rangle_N$ is the expectation value of $\mathbf{l}^2$ averaged over one major shell with quantum number N. In this case, only the states within the shells are shifted. The center of gravity between different major shells remains unaffected.

Eq. 2.12 may be solved numerically as a function of deformation ϵ_2 to give the so-called Nilsson diagrams for neutrons (Fig. 2.3) and protons (Fig. 2.4). It should be noted that when $\epsilon_2 = 0$, that is the nucleus is spherical, the magic numbers are reproduced. One may notice that the nuclear deformation takes on both positive and negative values. Positive ϵ_2 refers to prolate shapes while negative ϵ_2 defines oblate shapes. These shapes are depicted in Fig. 2.5, where $\beta_2 \sim 0.95\epsilon_2$. Each Nilsson orbital is labeled by the following set of asymptotic quantum numbers that are good when deformation is nearly zero

$$[Nn_z|\Lambda|]\,\Omega^{(\pi)}, \tag{2.14}$$

where $N = n_z + n_\perp$ is the total oscillator quantum number, n_z is the number of quanta in oscillations (phonons) along the symmetry axis, $n_\perp = n_x + n_y$ is the number of oscillator quanta perpendicular to the symmetry axis, $\Omega = \Lambda + \Sigma$ is the component of total angular momentum along the symmetry axis (Σ is the component of spin along the symmetry axis, $\pm\frac{1}{2}$), and $\Lambda = \pm n_\perp, \pm(n_\perp - 1), \ldots, \pm 1$, or 0 is the component of orbital angular momentum along the symmetry axis. Note that for one-quasiparticle states Ω is often referred to as K, the intrinsic angular momentum of a state along the symmetry axis (usually $K = \Omega_1 + \Omega_2 + \ldots + \Omega_n$). A schematic illustration of the coupling of the angular momentum vectors for the case of a prolate deformed nucleus rotating perpendicular to its symmetry axis is shown in Fig. 2.6. The Nilsson levels may essentially be described by two good quantum numbers, the parity defined as $\pi = (-1)^l$, where l is orbital angular momentum, and the K value. The parities are denoted by solid lines for $\pi = +$, and dotted lines for $\pi = -$ as seen in Figs. 2.3 and

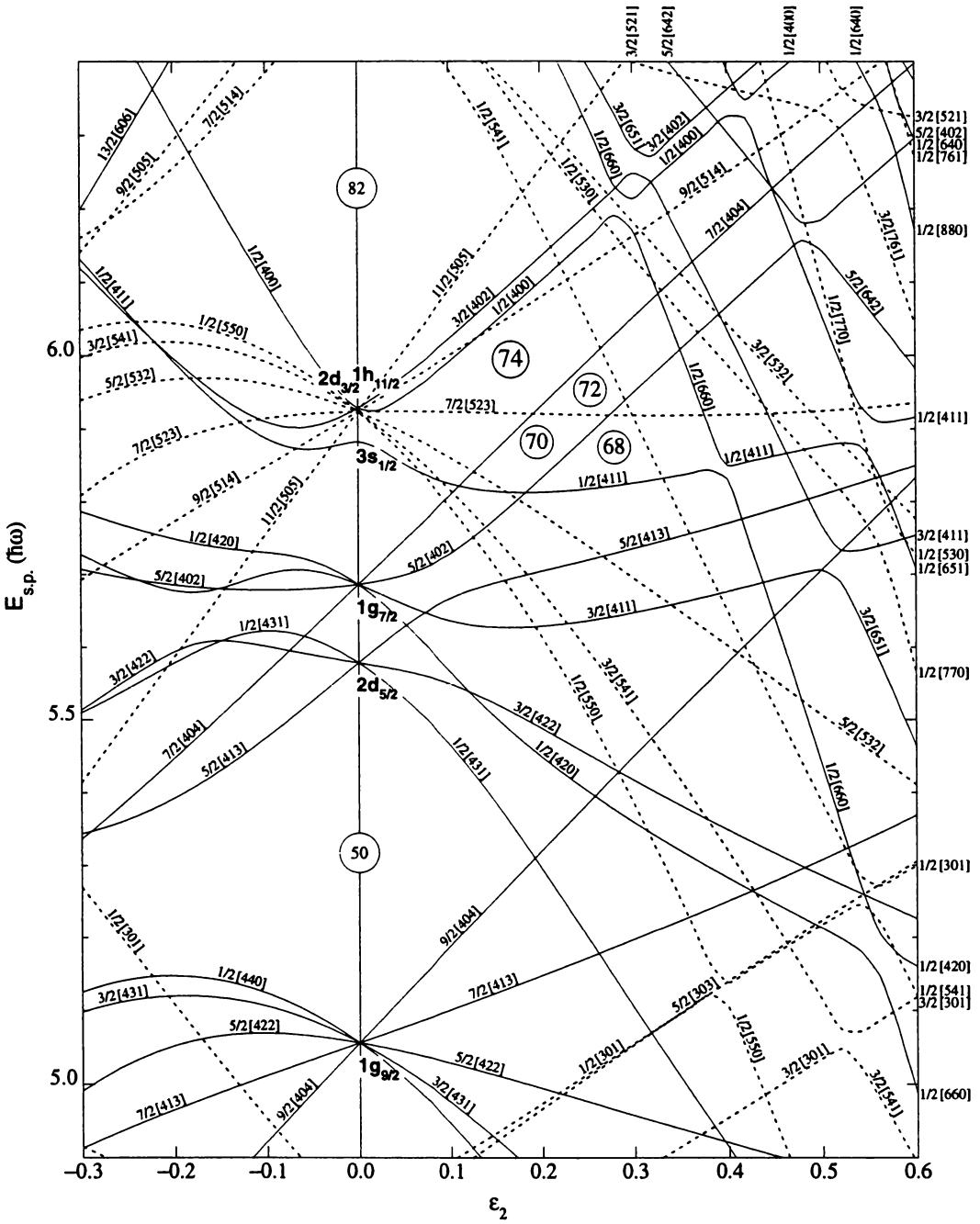


Figure 2.3: Nilsson diagram for neutrons, $50 \leq N \leq 82$ ($\epsilon_4 = {\epsilon_2}^2/6$). Reproduced from Ref. [8].

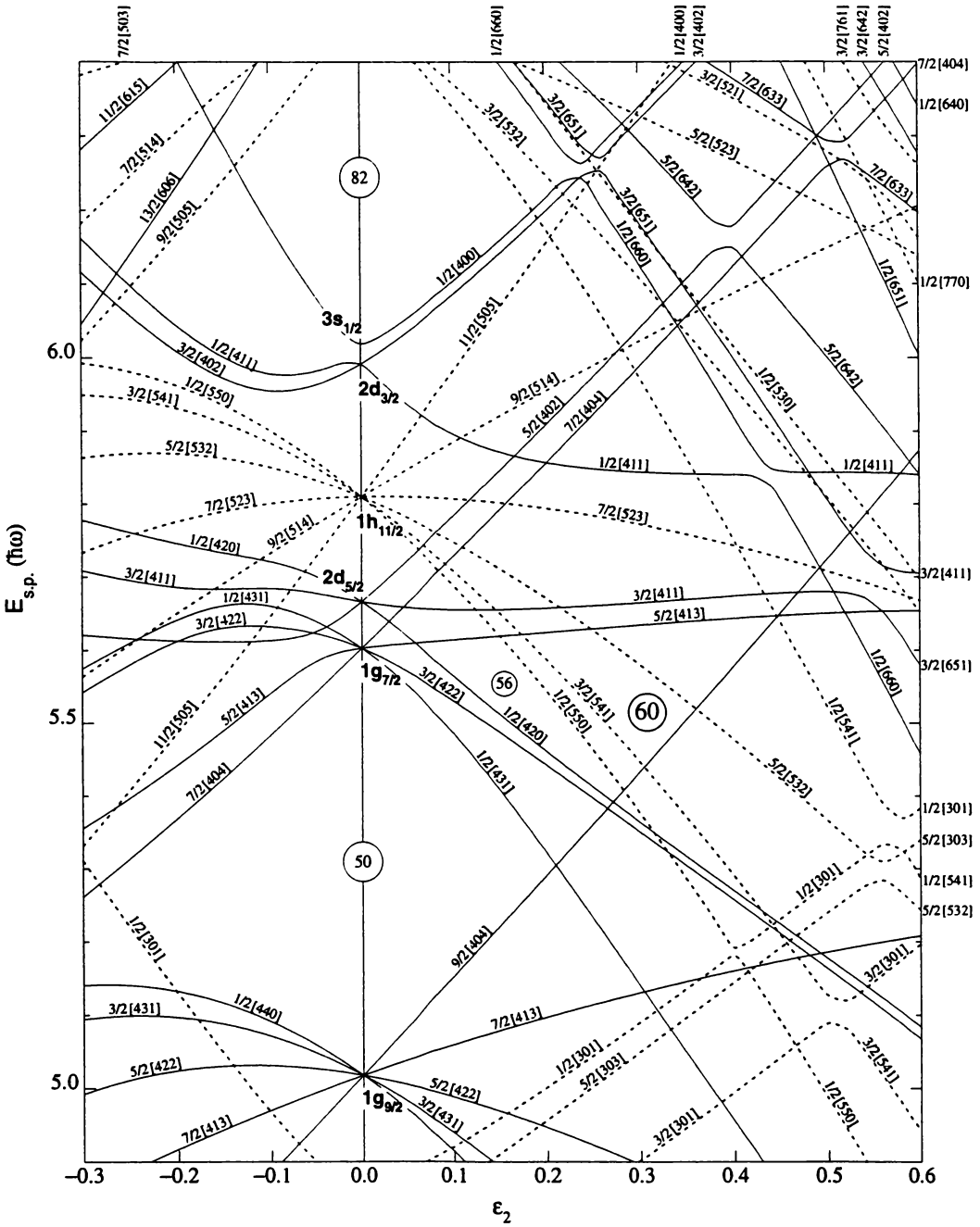


Figure 2.4: Nilsson diagram for protons, $50 \leq Z \leq 82$ ($\epsilon_4 = {\epsilon_2}^2/6$). Reproduced from Ref. [8].

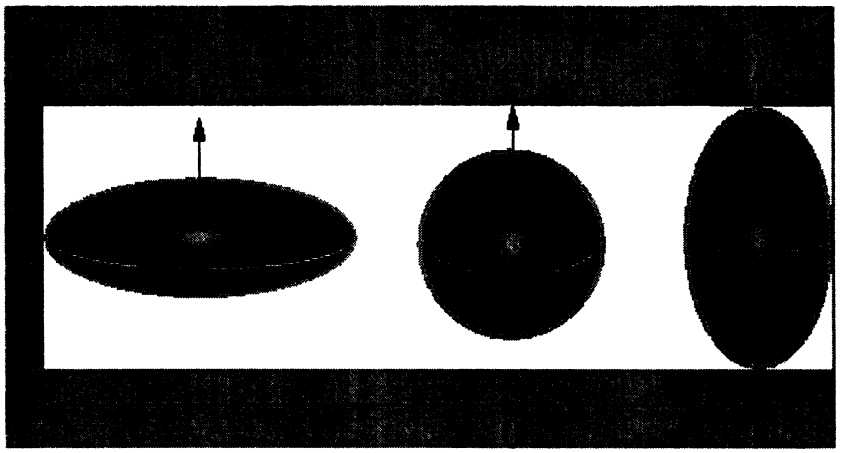


Figure 2.5: Diagram showing oblate, spherical, and prolate shapes. The arrows for the oblate and prolate shapes indicate the symmetry axis.

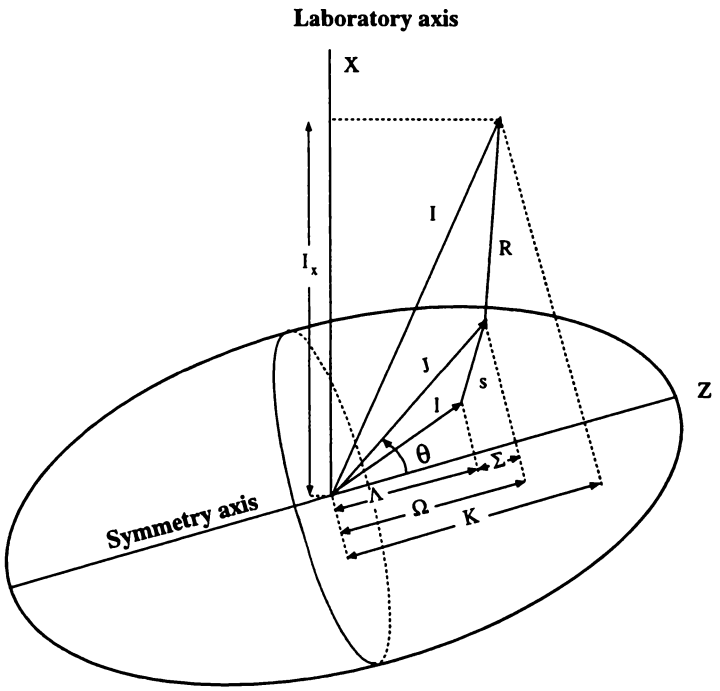


Figure 2.6: Asymptotic quantum numbers of the deformed Nilsson model. For odd-A nuclei, the intrinsic angular momentum J is the total angular momentum of the nucleon.

2.4. As two orbitals with the same π and K approach each other, they must repel. Past the inflection point, the mixing of the two wave-functions is the greatest and an exchange of "character" occurs.

Understanding of how to "read" the seemingly complicated Nilsson diagrams Figs. 2.3 and 2.4 is essential for one to identify the rotational bands observed in γ-ray spectroscopy. At $\epsilon = 0$, on Fig. 2.3 for example, several sub-shells exist between $50 \leq N \leq 82$ (*i.e.* $d_{5/2}$, $g_{7/2}$, $s_{1/2}$, and $h_{11/2}$). Each of these shells may hold $2j+1$ neutrons where j appears as the subscript labeling the shell. Each of these $2j+1$ sub-shells has a double degeneracy ($|K|$ and $|-K|$). The amount of splitting between adjacent K orbitals may be estimated classically using Fig. 2.6 again. The angle θ can be found by the expression $\theta = \sin^{-1}(K/j)$ and one will find that θ changes slowly for low-K values but rapidly for high-K values. This causes the fanning effect of the single-particle energies as the K orbitals protrude from the shell. The $h_{11/2}$ shell, for example, in Figs. 2.3 and 2.4 nicely shows this feature.

In these figures, it is evident that other shell gaps are possible at non-zero values of the quadrupole deformation. The presence of such gaps in the single particle energies indicates that the corresponding deformations are relatively stable. The approximate position of the Fermi surface in a Nilsson proton or neutron diagram for a given nucleus can be predicted from its theoretically predicted ground-state deformation. The ground-state deformation can also be extracted experimentally by measuring the intrinsic quadrupole moment Q_0[1] given by

$$Q_0 \approx \frac{3}{\sqrt{(5\pi)}} {R_{av}}^2 Z\beta_2(1+0.16\beta_2), \tag{2.15}$$

where $R_{av} = R_0 A^{1/3}$. Orbitals that are likely to be occupied by the valence nucleons are responsible for the observation of corresponding rotational bands. These "active" orbitals can be identified for a given nucleus by a knowledge of systematics. Therefore, the knowledge of which orbitals are occupied near or at the Fermi level in neighboring nuclei provides a guide to orbital assignment for rotational bands in the nucleus of interest.

[1]The intrinsic quadrupole moment is a measure of the extent to which the nuclear charge distribution deviates from spherical symmetry in the fixed frame of the nucleus.

2.2.4 Woods-Saxon Model

The choice of a "realistic" nucleonic potential is limited by the known properties of the nuclear force. A nucleon close to the center of the nucleus will feel the nuclear forces uniformly, *i.e.* there will be no net force [15]

$$\left(\frac{\partial V(\mathbf{r})}{\partial \mathbf{r}}\right)_{r=0} = 0. \tag{2.16}$$

The nuclear binding force gets stronger going from the surface ($r = R_0$) to the interior of the nucleus

$$\left(\frac{\partial V}{\partial r}\right)_{r<R_0} > 0. \tag{2.17}$$

Due to the finite range of the nuclear force

$$V(r) \simeq 0, r > R_0. \tag{2.18}$$

The Woods-Saxon potential [16] can represent the above nuclear conditions very well. The general form of the Woods-Saxon potential is expressed as

$$V = V_{s.o.} + V_{Coul} + V_{w.s.} \tag{2.19}$$

where $V_{s.o.}$ is the spin-orbit term, V_{Coul} is the Coulomb interaction, and $V_{w.s.}$ takes the form

$$V_{w.s.} = -V_0 \left[1 + \exp\left(\frac{r - R_0}{a}\right)\right]^{-1} \tag{2.20}$$

where $a \sim 0.5\ fm$ dictates the diffuseness of the potential surface, and $V_0 \sim 50$ MeV represents the depth of the potential well at $r = 0$.

This potential not only will reproduce the experimentally observed single-particle levels and the magic numbers, but the theoretical wavefunctions are also more realistic, allowing for the calculation of other nuclear properties such as transition probabilities and quadrupole moments. Woods-Saxon single-particle diagrams have very similar labeling to that of Nilsson diagrams. The K value in the Woods-Saxon formalism is placed to the right of the bracketed quantum numbers. Depending on the mass region, subtle differences between the two potentials, such as the relative placement of some orbitals, may occur. However, it is clear that if one wishes to

go beyond the predictions of the single-particle energy levels and examine properties associated with the wave functions, one should favor using the Woods-Saxon potential over the Nilsson potential.

2.3 Nuclear Rotation

2.3.1 Rotations of Axially Symmetric Deformed Nuclei

Nonspherical nuclei have a simple character of being able to undergo rotations about an axis perpendicular to the symmetry axis. In order to discuss rotational motion, we need to specify the deformed wavefunctions. In the particle plus rotor model picture, these wavefunctions must be able to accurately describe two aspects associated with nuclear rotation: intrinsic excitation (specified by the function χ_K) and rotational motion (specified by D matrices). The motion of a single nucleon in a deformed field is characterized by having a two-fold degeneracy corresponding to clockwise and counterclockwise motions which are distinguished by the projection, K, of their angular momenta on the symmetry axis. The nuclear wavefunction that describes a rotating deformed nucleons with nucleonic time-reversed orbitals is given by [7]

$$\Psi_{IM} = \left(\frac{2I+1}{16\pi^2}\right)^{1/2} \left[D_{IMK}\chi_K + (-1)^{I-K} D_{IM-K}\chi_{-K}\right], \tag{2.21}$$

where M is the projection of the total angular momentum on the z axis of the rotated coordinate system, and I is the total angular momentum of the nucleus. The intrinsic wavefunction χ_{-K} is the time-reversal state of χ_K and is obtained from χ_K by rotation of 180° around the z axis. The rotational band is then a sequence with

$$I = K, K+1, K+2, ... \tag{2.22}$$

In the case of $K = 0$, only even J values are allowed and we simply have

$$\Psi_{IM} = \left(\frac{1}{8\pi^2}\right)^{1/2} D_{I0}\chi_0. \tag{2.23}$$

If we assume that the ground state is $J^\pi = 0$, $K = 0$, and if all angular momentum can be ascribed to rotation (as is normally true for the low-lying, low-spin, positive-parity

states in deformed even-even nuclei) we obtain the famous symmetric top rotational energy expression

$$E_{rot}(I) = \frac{\hbar^2}{2\mathcal{J}} I(I+1), \tag{2.24}$$

where only even I's are allowed, and $\mathcal{J}$ is the moment of inertia of the core. Using the previous expression, one can extract the energy ratio $E_{(I=4)}/E_{(I=2)} = 3.33$ for even-even nuclei. This is one of the most famous results of the rotational model and still remains one of the big signatures for the deformed rotational motion of the atomic nucleus.

2.3.2 Cranked Shell Model

In order to account for collective rotation around an axis perpendicular to the symmetry axis, the procedure suggested by Inglis [17] known as the cranking model approximation is frequently employed. The cranking model is a very powerful tool to study nuclear structure at the vicinity of the yrast line[2] at high spin. A summary of this model and its application can be found in Refs. [18, 19].

The rotation of a deformed nuclear field with respect to the rotation axis introduces an explicit time dependence to the Schrödinger equation. This may, however, be reduced to a stationary equation of motion when the laboratory frame is transformed into the rotating frame. This transformation allows one to compare theoretical calculations directly with experimental data and has the added advantage of allowing for the extraction of the single-particle properties from the nuclear level scheme. By means of the rotation operator

$$R(\omega t) = e^{-i\omega t j_x}, \tag{2.25}$$

the transformation of the time-dependent Schrödinger equation for a single particle from the lab frame to the body fixed (intrinsic rotating frame) can be achieved

$$i\hbar \frac{\partial \Psi_{int}}{\partial t} = (h_0 - \omega j_x)\Psi_{int}, \tag{2.26}$$

[2]The yrast line is a sequence of all states that have the highest angular momentum for a given energy.

where $h_0 - \omega j_x$ is the one-particle Hamiltonian or Routhian in the rotating frame. The summation over all the independent particles in the system leads to the total cranking Hamiltonian

$$H^\omega = H_0 - \omega J_x \tag{2.27}$$

where ω is the angular frequency of the system, and J_x is the angular momentum operator along the axis of rotation x, which is perpendicular to the symmetry axis z. The term ωJ_x corresponds to the centrifugal and Coriolis forces that arise due to the non-inertial system of the rotating frame. An upper limit for the strength of the Coriolis force may be calculated [7]

$$V_{cor} = \frac{\hbar^2}{2\mathcal{J}} Ij \tag{2.28}$$

where I is the total angular momentum, j is the single-particle momentum, and $\mathcal{J}$ is the moment of inertia. It is apparent from this relationship that the Coriolis force is not only dependent on how fast the nucleus is rotating, but also which orbital a nucleon occupies. For typical inertial parameters (say 15 keV for rare-earth nuclei) and for I, $j = 11/2$, this attains 400 keV which is comparable with typical spacings between Nilsson orbits $\sim$ 150 keV and, thus, cannot be neglected. This is a significant effect specially on the high-j intruder orbitals in the mass $A \sim 130$ region (the proton and neutron $h_{11/2}$ orbitals) at high spins.

2.3.3 Symmetries in the Cranking Hamiltonian

The cranking routhian possesses several symmetries: time, space, and rotation by 180°. Of common interest are the time, space, and rotation by 180° about the rotation axis. However, time-reversal invariance is usually broken for single particle states except for non-collective rotations about the symmetry axis. This is due to the fact that rotation mixes states of different J and, thus, $[H^\omega, J_x] \neq 0$. Space symmetry is described by the parity (π), quantum number, while space reflection (rotation by 180°) is described by the signature (α) quantum number. The signature quantum number is defined as

$$R_x(\pi)\Psi_\alpha = e^{-i\pi j_x}\Psi_\alpha = e^{-i\pi\alpha}\Psi_\alpha \tag{2.29}$$

where Ψ_α is the wave function with signature α. The eigenvalue of R_x may be indicated in some literature as the signature and may be defined as

$$r = e^{-i\pi\alpha}, \tag{2.30}$$

and one finds (Bohr and Mottelson [12]) for integer I

$$r = (-1)^I, \tag{2.31}$$

where I is the total nuclear spin. Thus for systems with an even number of nucleons we have

$$\begin{aligned} r = \ +1 \ (\alpha = 0), \ I = \ 0, 2, 4, ... \\ r = \ -1 \ (\alpha = 1), \ I = \ 1, 3, 5, ... \end{aligned} \tag{2.32}$$

while for systems with odd particle number we have

$$\begin{aligned} r = \ -i \ (\alpha = +\frac{1}{2}), \ I = \ \frac{1}{2}, \frac{5}{2}, \frac{9}{2}, ... \\ r = \ +i \ (\alpha = -\frac{1}{2}), \ I = \ \frac{3}{2}, \frac{7}{2}, \frac{11}{2}, ... \end{aligned} \tag{2.33}$$

An advantage of using α as the signature quantum number rather than r is that α is an additive quantity. For example, in the case of an odd-odd nucleus, if the proton wavefunction is characterized by $I = 1/2$ ($\alpha = \frac{1}{2}$) and the neutron by $I = 7/2$ ($\alpha = -\frac{1}{2}$), then the signature of the resulting rotational band is $\alpha_r = \alpha_p + \alpha_n = 0$.

The effect of the models discussed so far on orbitals level structure and degeneracies is demonstrated in Fig. 2.7 for the $N = 2$ shell. The harmonic oscillator is altered by the Woods-Saxon potential which splits the angular momentum states with different l, levels of larger l having lower energy. A degeneracy of $2(2l + 1)$ is observed in each level resulting from the $2l+1$ magnetic substates and the two possible spin states. The introduction of the spin-orbit coupling ($\mathbf{l} \cdot \mathbf{s}$) in the shell model lifts the degeneracy of different j's such that each level can hold $2j + 1$ particles. In a deformed nuclear potential, the shells are split into doubly degenerate orbitals which reflect time-reversal symmetry. Finally, the Coriolis and centrifugal forces break the last degeneracy such that each level (and therefore the particle occupying that level) may be labeled by its own set of parity π and signature α.

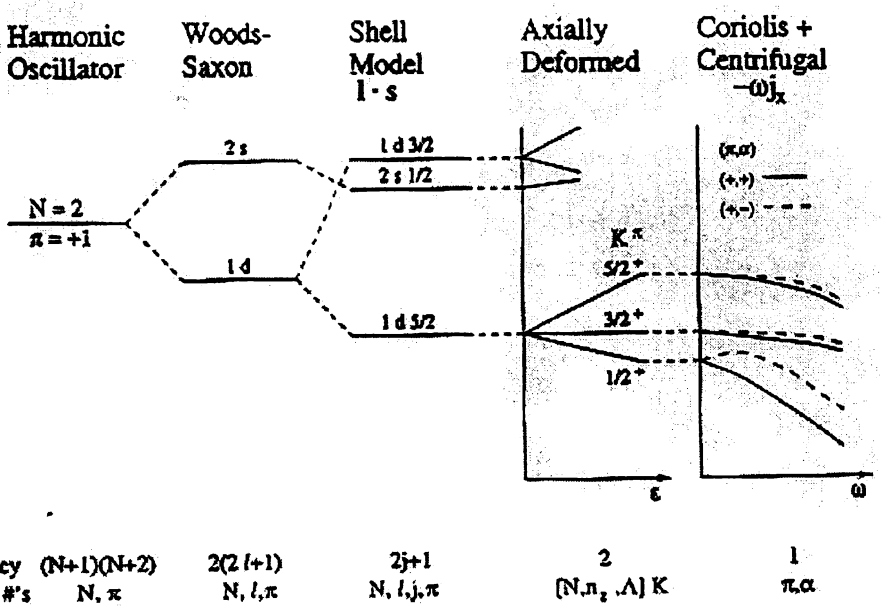


Figure 2.7: A schematic diagram of the energy spectrum under the influence of various nuclear potentials. The degeneracy and characteristic quantum numbers are given for each case. (Reproduced from Garret *et. al.* [20]).

2.3.4 Signature Splitting

The Hamiltonian for a collective rotation can be expressed using the notation for the different angular momenta in Fig. 2.6

$$H = \frac{\hbar^2}{2\mathcal{J}}R^2 = \frac{\hbar^2}{2\mathcal{J}}(I^2 + j^2 - 2I \cdot j), \tag{2.34}$$

where $R = I - j$. Using the raising (I_+, j_+) and lowering (I_-, j_-) operators, the above Hamiltonian can be rewritten as

$$H = \frac{\hbar^2}{2\mathcal{J}}\left[(I^2 + j^2 - (I_+ j_- + I_- j_+)\right]. \tag{2.35}$$

The last term in the above Hamiltonian is due to the Coriolis and centrifugal effects. This term connects states differing by $\Delta K = \pm 1$ and is diagonal for $K = 1/2$ states. The diagonalization of the Hamiltonian in Eq. 2.35 in a space of $\Omega = 1/2$ orbital gives rise to a decoupling parameter (a) in the rotational energy [7]

$$E_{rot}(I) = \frac{\hbar^2}{2\mathcal{J}}\left[I(I+1) + \delta_{K\frac{1}{2}} a(-1)^{I+\frac{1}{2}}(I + \frac{1}{2})\right], \tag{2.36}$$

where the decoupling parameter a is proportional to $(-1)^{j-1/2}(j+1/2)$. For $K = 1/2$, the decoupling parameter has the effect of lowering one signature in energy compared to the other, *i.e.* signature splitting. For pure-j orbitals, examination of Eq. 2.36 and the dependence of a on j reveals that the signature which contains the states with spin $I = j$ will be favored in energy. If the Hamiltonian 2.35 is diagonalized within a set of high-j states, the effects of the diagonal contribution to the $K = 1/2$ band are strongly propagated through the other rotational bands via the Coriolis term. This effect is clearly shown at the far right of Fig. 2.7, where the the amount of signature splitting decreases for higher-K values due to less mixing with the $K = 1/2$ level.

2.3.5 The Pairing Interaction

The nuclear models discussed so far were built on the assumption that single nucleons only interact with other nucleons by an average potential field created by all the other nucleons. However, experimental observations suggested the need for the existence of pairing correlations between nucleons to explain several nuclear structure features such as:

- The odd-even mass difference, which refers to larger gain in binding energy for an even-even nucleus compared to its neighboring odd-mass nuclei
- The ground states for all even-even nuclei have $I^{\pi} = 0^{+}$, and associated with this is the fact that excited particle states are $\sim$ 1-2 MeV above the ground state
- The reduction of nuclear moments of inertia compared to those of a rigid body
- The modification of the occupation probabilities near the Fermi surface.

Following the microscopic BCS [22] theory of superconductivity, Bohr, Mottelson and Pines [23] suggested a similar treatment for pairing correlations in atomic nuclei. Qualitatively, two particles pair by orbiting the same j shell and K orbitals, but in opposite directions (*i.e.* time reversed orbitals) which result in a maximum overlap of their wave functions.

A qualitative picture of the BCS application to nuclear physics is possible with the introduction of the particle-hole space representation. For that purpose, the ground state of even-even nuclei is considered as a vacuum. Denoting the vacuum by $|N\rangle$, then any particle or hole excitation with respect to the Fermi surface can be expressed as

$$\begin{aligned} \Psi^p_\nu &= a^+_\nu |N\rangle \\ \Psi^h_{\bar{\nu}} &= a^+_{\bar{\nu}} |N\rangle, \end{aligned} \tag{2.37}$$

where ν denotes any state above the Fermi level and $\bar{\nu}$ below the Fermi level. To conserve particle number, the Hamiltonian should include a Lagrangian multiplier proportional to the particle number operator $\hat{N}$,

$$H = H^\omega + H_{pair} - \lambda \hat{N}. \tag{2.38}$$

Here H^ω is the normal cranking Hamiltonian 2.27, H_{pair} denotes the pairing interaction, and the multiplier λ (chemical potential) is determined from condition for particle number conservation

$$N = \langle \Psi | \hat{N} | \Psi \rangle. \tag{2.39}$$

By combination of the two operations in Eq. 2.37, a particle-hole excitation in the N-particle system can be created

$$\Psi^{ph}_{\nu\bar{\nu}} = a^+_\nu a_{\bar{\nu}} |N\rangle. \tag{2.40}$$

Consequently, the corresponding excitation spectra can be written as

$$\begin{aligned} \varepsilon^p_\nu &= \varepsilon_\nu - \lambda, \ \varepsilon_\nu > \lambda \text{ particle state} \\ \varepsilon^h_{\bar{\nu}} &= \lambda - \varepsilon_{\bar{\nu}}, \ \varepsilon_{\bar{\nu}} < \lambda \text{ hole state} \\ \varepsilon^{ph}_{\nu\bar{\nu}} &= \varepsilon_\nu - \varepsilon_{\bar{\nu}}, \ \text{particle-hole excitation.} \end{aligned} \tag{2.41}$$

This particle-hole space representation is very useful when dealing with the pairing correlations. The pairing interaction can now be reduced to the excitation of a particle or a hole or a mixture of both (quasiparticles). In this representation, the quasiparticle

spectrum will possess reflection symmetry about the Fermi surface; for every state with energy ε_ν there is always an unoccupied state with energy -ε_ν.

Through the use of the creation and annihilation operators a^+ and a in Eq. 2.38, the new cranking Hamiltonian referred as the Hartree-Fock-Bogolyubov (HFB) cranking can be expressed as

$$H = \sum_{\mu\nu} e^{\omega}_{\mu\nu} a^+_\mu a_\nu - \sum_{\mu,\nu>0} G a^+_\mu a^+_{\bar{\mu}} a_{\bar{\nu}} a_\nu - \lambda \sum_\nu a^+_\nu a_\nu. \tag{2.42}$$

The second term represents the pairing interaction (H_{pair}) with the scattering strength represented by the factor G. It is mathematically complicated to deal with a two-body interaction and a reduction to a one-body problem is possible by using a linearized approximation of this interaction. By introducing the two operators

$$\begin{aligned} P^+ &= a^+_\nu a^+_{\bar{\nu}} \\ P &= a_{\bar{\nu}} a_\nu, \end{aligned} \tag{2.43}$$

which create or annihilate a time-reversed pair. The pairing term in the Hamiltonian (2.42) can then be expressed in a linearized form as

$$H_{pair} = -\Delta(P^+ + P) \tag{2.44}$$

where Δ is the so called pairing gap parameter. The above Hamiltonian is then transformed into a one-body operator using a transformation suggested by Bogolyubov [26]. In this transformation the pairing gap Δ, is expressed as

$$\Delta = G \sum_{i,j} U_i V_j, \tag{2.45}$$

where U and V are known as the emptiness and fullness factors, respectively. They are expressed by

$$\begin{aligned} U_i^2 &= \frac{1}{2}\left[1 + \frac{\varepsilon_i - \lambda}{E_i}\right] \\ V_i^2 &= \frac{1}{2}\left[1 - \frac{\varepsilon_i - \lambda}{E_i}\right], \end{aligned} \tag{2.46}$$

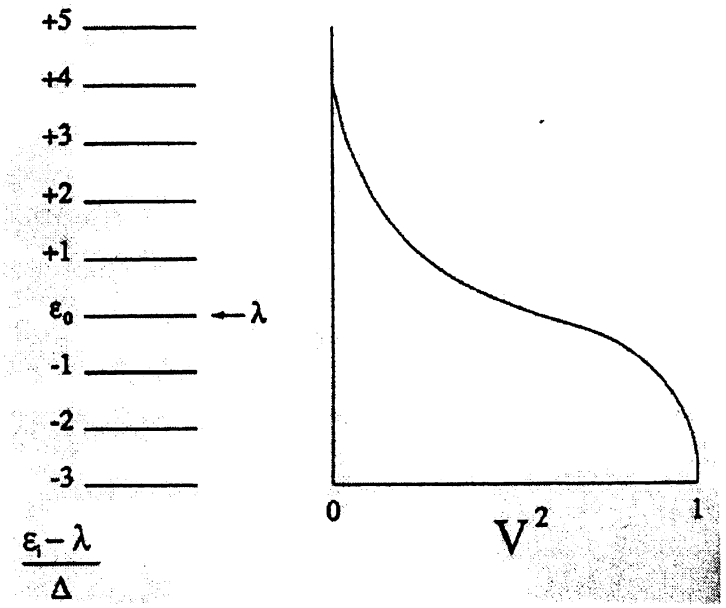


Figure 2.8: Depiction of partial occupancy due to pairing. The left hand side displays an idealized set of equally spaced single-particle levels. The right hand side shows how the occupancy V^2 partially fills the single-particle levels. Reproduced from Ref. [7].

where ε_i is the single-particle energy, and E_i is the energy necessary to excite a *quasiparticle* given by

$$E_i = \sqrt{(\varepsilon_i - \lambda)^2 + \Delta^2}. \tag{2.47}$$

It is more appropriate now to speak of quasiparticles partially filling the nuclear levels. Fig. 2.8 shows a plot of the ratio $(\varepsilon - \lambda)/\Delta$ versus V^2. One may note that $V^2 \to 1$ for $(\varepsilon_i \ll 0)$ and $V^2 \to 0$ for $(\varepsilon_i \gg 0)$. The emptiness and fullness parameters satisfy the normalization condition $U^2 + V^2 = 1$.

The large energy gap between the ground state and the first two-quasiparticle state in even-even nuclei can now be qualitatively explained with the use of Eq. 2.47. A two-quasiparticle state would require an excitation

$$E_{i,j}^{e-e} = \sqrt{(\varepsilon_i - \lambda)^2 + \Delta^2} + \sqrt{(\varepsilon_j - \lambda)^2 + \Delta^2}. \tag{2.48}$$

A minimum of 2Δ in energy is necessary before any simple two-quasiparticle excitation is observed in even-even nuclei. Typical values for Δ are 0.7 - 1.0 MeV for even-even nuclei and, thus, most two-quasiparticle structures occur at $\sim$ 1.5 - 2.0 MeV. For

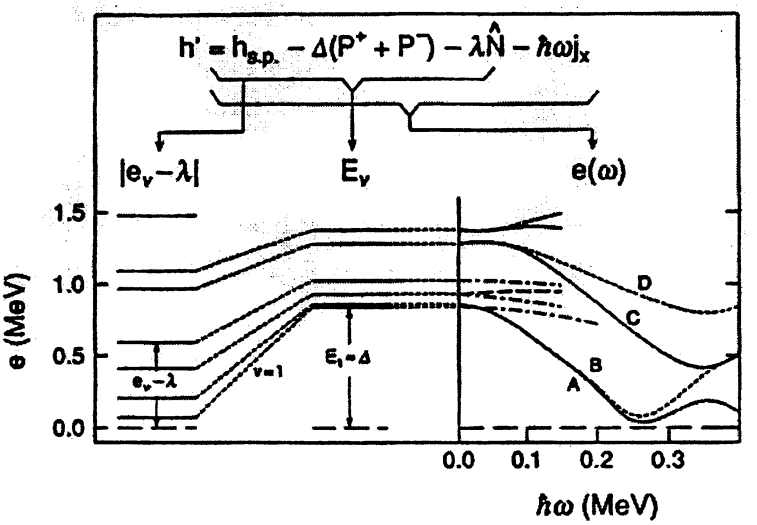


Figure 2.9: Illustration of the effect of pairing correlations and Coriolis interactions on a single-particle spectrum around the Fermi surface λ. The single-particle excitations are plotted on the left relative to λ, the pairing effect is included in central quasiparticle levels, and the Routhian $e(\omega)$ calculated from the cranked shell model are on the right. Reproduced from Ref. [21].

one-quasiparticle state, the excitation energy will be

$$E_i^o = E_i - E_0 = \sqrt{(\varepsilon_i - \lambda)^2 + \Delta^2} - \sqrt{(\varepsilon_0 - \lambda)^2 + \Delta^2} \tag{2.49}$$

where E_0 is the quasiparticle energy of the orbit nearest the Fermi level.

It is worth mentioning at this point the difference between the HFB and the CSM approach in solving the Hamiltonian Eq. 2.27. In the CSM calculations, the parameters [β_2 (quadrupole deformation), β_4 (hexadecapole deformation), γ (triaxial deformation), λ (chemical potential), and Δ (pairing gap)] are fixed at realistic values. This allows a condensed form representation of the quasiparticle energies versus ω. In HFB calculations, the determination of the field parameters (including shape and pairing) are done self-consistently. The quasiparticle Routhian calculated from the HFB cranking method as a function of rotational frequency is plotted in the right column of Fig. 2.9. Notice that the doubly-degenerate time-reversal states at zero frequency are split under the rotation. The closest two-quasiparticle levels to the Fermi surface (lowest excitations) are labeled by A and B, respectively.

2.3.6 Quasiparticle Diagrams, Band Crossings, and Alignment

The quasiparticle level energies (Routhians) plotted as a function of rotational frequency are often referred to as the quasiparticle diagram. The quasiparticle Routhians are calculated by the cranked Hartree-Fock-Bogolyubov (HFBC) method. For a thorough description of the HFBC solutions, the reader is referred to Ring and Schuck [25]. Fig. 2.10 shows these calculations for both quasiprotons and quasineutrons of ^{128}Nd ($Z = 60$, $N = 68$), which is one of the nuclei described in this dissertation work, using the deformations shown on the top of the figure. Pairing (Δ) values of 1.14 MeV and 1.09 MeV were used for protons and neutrons, respectively. All the deformation and pairing values used in this calculation were extracted from Total Routhian Surface (TRS) predictions at a rotational frequency $\omega \sim 0.06$ MeV [27]. The TRS calculations are HFBC calculations done self-consistently with respect to deformation. Detailed description of the TRS concept can be found in Refs. [27, 28, 29].

Each level on the Routhian plot is characterized by two good quantum numbers, parity π and signature α. As seen in Fig. 2.10, four possible combinations of (π, α), (+, +1/2), (+, -1/2), (-, +1/2), and (-, -1/2), are denoted in the diagrams by solid, short-dashed, dot-dashed, and long-dashed curves, respectively. The individual quasiparticle levels are labeled according to a scheme given in Table 2.1. One may notice in Fig 2.10 that every trajectory has an equal and opposite trajectory about $e' = 0$, but with opposite signature [30]. User's manual for the quasiparticle diagram can be found in Ref. [19].

We mentioned earlier that the ground state of even-even nuclei is built on the quasiparticle vacuum. The first excited two-particle state is formed when levels E_p and F_p are occupied (top diagram in Fig. 2.10). With increasing rotational frequency the energy of the quasiparticle level is lowered due to the Coriolis interaction. At a critical frequency, $\omega_{E_pF_p}$, the quasiparticle levels dive into the Fermi surface and become energetically favored. At this point the pairing gap for the two levels disappears and the two particles E_p and F_p consequently align their spins along the rotation axis, *i.e.* the pair is broken. The quasiproton levels E_p and F_p are discontinued after the rotational frequency point $\omega_{E_pF_p}$ as they are being crossed by the ground-state

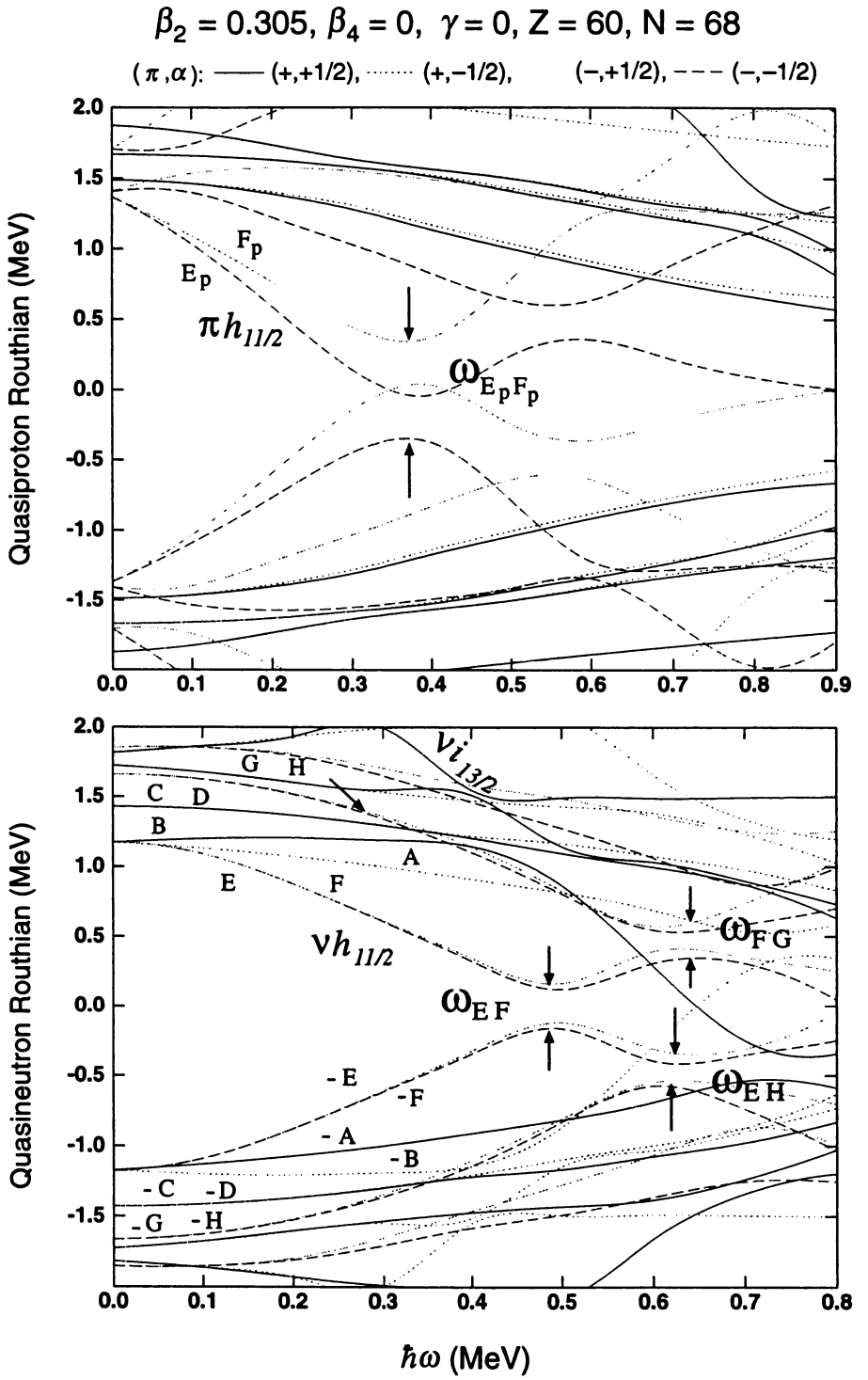


Figure 2.10: Quasiparticle Routhians calculated for both neutrons and protons in ^{128}Nd ($Z = 60$, $N = 68$).

Table 2.1: Convention used for labeling quasiparticle configurations. The subscript n indicates that the configuration is the nth lowest in energy within a particular set of quantum numbers (π, α).

Label (neutron, proton)	$(\pi, \alpha)_n$	Label (neutron, proton)	$(\pi, \alpha)_n$
A, A_p	$(+, +\frac{1}{2})_1$	B, B_p	$(+, -\frac{1}{2})_1$
C, C_p	$(+, +\frac{1}{2})_2$	D, D_p	$(+, -\frac{1}{2})_2$
E, E_p	$(-, -\frac{1}{2})_1$	F, F_p	$(-, +\frac{1}{2})_1$
G, G_p	$(-, -\frac{1}{2})_2$	H, H_p	$(-, +\frac{1}{2})_2$

band. Band crossings are represented by the inflection points where the trajectory of similar parity and signature repel from each other as seen in Fig. 2.10. After this crossing frequency, the two-quasiparticle band, called the s-band [31, 32], become the yrast structure based on the $\pi h_{11/2}$ configuration. The amount of aligned angular momentum i (alignmnet) that can be gained from a particular band crossing can be estimated from the negative slope of the Routhian trajectory

$$i = -\frac{de'}{d\omega}. \tag{2.50}$$

Since in the naive CSM picture alignment is an additive quantity, the total alignment from a crossing, say the E_pF_p crossing, is the sum of the negative slopes of the E and F trajectories. Therefore, one may observe from Fig. 2.10 that the $\pi h_{11/2}$ band should have more alignment than the $\nu h_{11/2}$ band. This is indeed found to be true as will be discussed in later chapters.

With increasing angular momentum, the two-quasiparticles occupying $\nu h_{11/2}$ become energetically favored (lower diagram in Fig. 2.10). At a critical frequency, ω_{EF}, a crossing with a two-quasiparticle $\pi h_{11/2}$ band occurs and a four-quasiparticle band is formed based on a $\pi(h_{11/2})^2 \otimes \nu(h_{11/2})^2$ configuration, where the superscript indicates the number of quasiparticles involved in this configuration. For odd-A nuclei such as ^{129}Nd ($Z = 60$, $N = 69$), the GS band is a one-quasiparticle configuration. The band crossing scenario still holds, where the GS one-quasiparticle band crosses with a two-quasiparticle band to form a three-quasiparticle band. If the odd particle,

in this case a neutron, occupies one of the E or F levels, the first neutron crossing at ω_{EF} will not appear and the crossing is *blocked* (Pauli blocking). However, a second crossing at higher rotational frequency ω_{EH} or ω_{FG} with a two-quasiparticle neutron band can occur (see lower diagram in Fig. 2.10) to form a three-quasiparticle band. For odd-odd nuclei like ^{130}La ($Z = 57$, $N = 73$), two configurations based one quasiproton and one quasineutron exist and experience either proton or neutron crossings at higher rotational frequencies to form four-quasiparticle configurations like $\pi h_{11/2} \otimes \nu(h_{11/2})^3$, ...etc.

The interaction strength between the GS band and higher excited bands at the crossing point can be estimated by the distance between the two-crossing levels on the Routhian diagram. On the alignment plot (I_x versus ω), the strength of the interaction on the yrast structure manifests itself as a curvature at the crossing frequency. A strong interaction (large level repulsion of the Routhians) shows as a smooth *upbend* at the crossing frequency on the alignment plot of a given band. On the other hand, a weak interaction results in the formation of a sharp *backbend* or S-shaped alignment plot. The backbending effect was discovered experimentally in 1972 by Johnson *et al.* [32].

2.3.7 Transformation of Experimental Observables into the Rotating Frame

In order to compare theoretical predictions of the CSM with experimental data in the laboratory frame, one has to express the experimental results in the rotating frame [18]. Let us consider a nucleus rotating about the x-axis which is perpendicular to the symmetry axis z. The excitation energy in the laboratory frame E_x, and in the rotating frame E', are related by

$$E' = E_x - \omega I_x \tag{2.51}$$

where I_x is the projection of the total angular momentum on the rotation axis. Using the vector relations in Fig. 2.6, a semiclassical expression for I_x can be obtained through geometrical arguments as

$$I_x(I) = \sqrt{I(I+1) - K^2} \approx \sqrt{(I+\frac{1}{2})^2 - K^2}. \tag{2.52}$$

The angular velocity about the x axis is given by the canonical relation

$$I_x(I) = dE(I)/dI_x, \tag{2.53}$$

where E is the excitation energy. Experimentally, the rotational frequency may be approximated by the method of finite differences

$$\omega(I) = \frac{E(I+1) - E(I-1)}{I_x(I+1) - I_x(I-1)} \tag{2.54}$$

which defines the rotational frequency $\omega(I)$ for angular momentum state I. The total Routhian E' contains contributions from the collective rotation and quasiparticle excitations. In order to extract the quasiparticle Routhian e', one has to subtract a reference routhian E'_{ref} that describes the collective rotation

$$e'(\omega) = E'(\omega) - E'_{ref}(\omega). \tag{2.55}$$

Similarly, the quasiparticle alignment $i(\omega)$ is defined as

$$i(\omega) = I_x(\omega) - I_x^{ref}(\omega), \tag{2.56}$$

where I_x^{ref} is the reference angular momentum of the rotating core.

Clearly, one collective parameter associated with a rotating body is its moment of inertia. Eq. 2.24 is an example of how the moment of inertia is used to parameterize the excitation energy of a nucleus as a function of angular momentum. Eq. 2.24 is valid provided the nuclear moment of inertia remain constant and the $I(I+1)$ rule is observed. However, nuclei are not perfect rotors, and while this parameterization gives a good fit for the first few energy levels along the yrast line, larger and larger deviations between calculated and observed nuclear energy levels occur as I increases. This is primarily due to the Coriolis anti-pairing effect. This fact led Harris [24] to parameterize the energy of rotational bands by an expansion in powers of ω^2

$$E = \alpha\omega^2 + \beta\omega^4 + \gamma\omega^6 + ... \tag{2.57}$$

Reducing the Harris model to two parameters yields the expression

$$E = \frac{1}{2}(\mathcal{J}_0 + 3C\omega^2)\omega^2 \tag{2.58}$$

where $\mathcal{J}_0$ and C are constants. The result of this model shows that the moment of inertia is not constant and varies as a function of rotational frequency

$$\mathcal{J} = \mathcal{J}_0 + \mathcal{J}_1\omega^2, \tag{2.59}$$

where $\mathcal{J}_1$ is proportional to C in Eq. 2.58. Classically, the total angular momentum is related to the moment of inertia by

$$I_x = \omega\mathcal{J}. \tag{2.60}$$

Combining this equation with the expression for the moment of inertia in the two parameter Harris formula (Eq. 2.58), yields

$$I_x^{ref} = \omega\mathcal{J}_0 + \omega^3\mathcal{J}_1. \tag{2.61}$$

Integrating I_x^{ref} with respect to ω yields the energy of the core in the rotating frame (reference Routhian)

$$E'_{ref} = -\int I_x^{ref}(\omega)d\omega = -\frac{\omega^2}{2}\mathcal{J}_0 - \frac{\omega^4}{4}\mathcal{J}_1 + \frac{1}{8\mathcal{J}_0}, \tag{2.62}$$

where $I_x^{ref} = -dE/d\omega$ is the canonical Hamilton relation. The last term in Eq. 2.62 is a constant of integration and has been added so that $E'_{ref} \sim 0$ at $I = 0$ [18]. Equations 2.61 and 2.62 are the phenomenological representations of the quasiparticle vacuum, and this translates into the ground band for even-even nuclei. The parameters $\mathcal{J}_0$ and $\mathcal{J}_1$ are chosen such that the ground-state band has zero initial alignment.

As mentioned previously, the energy of a rotational band does not usually follow the "$I(I+1)$" rigid rotor rule. The Harris model considers collective effects only and this is reflected in the smooth variation of the moment of inertia as a function of rotational frequency. Bohr and Mottelson [12] proposed two alternative definitions of the nuclear moment of inertia, which reflect the different aspects of nuclear dynamics. These definitions are referred to as the *kinematical* and *dynamical* moments of inertia. They are defined as follows

$$\begin{aligned} \text{Kinematical:} \quad & \mathcal{J}^{(1)} = I_x(dE/dI_x)^{-1} = I_x/\omega \\ \text{Dynamical:} \quad & \mathcal{J}^{(2)} = (d^2E/dI_x^2)^{-1} = dI_x/d\omega. \end{aligned} \tag{2.63}$$

The kinematical moment of inertia emphasizes its relation with the kinetic motion of the nucleus and, therefore, has information on the nuclear static properties like deformation and pairing. The dynamical moment of inertia expresses the response of the nucleus to a force and, therefore, dynamical effects like backbending will cause abrupt changes in $\mathcal{J}^{(2)}$. In the limit of a rigid rotor, $\mathcal{J}^{(1)} = \mathcal{J}^{(2)} = \mathcal{J}_{rig}$.

2.4 The Nuclear Electromagnetic Radiation

2.4.1 Multipole Radiations and Transition Probabilities

The electromagnetic field can be considered as a sum of multipole fields denoted by $\mathcal{M}(\sigma, \lambda)$, where σ represents E or M for electric or magnetic fields, and λ is the multipole order of the field. For example, electric quadrupole transitions are denoted by $E2$, and magnetic dipole transitions by $M1$, ... etc. When these fields are treated on the quantum level, certain restrictions apply on transitions between initial (I_i) and final (I_f) angular momentum states. The amount of angular momentum L carried by the photon propagating between these states is given in terms of the multipole order λ as $L = \lambda\hbar$, $\lambda = 1, 2, 3...$ etc. Multipole emissions of photons in quantal systems are governed by the following parity and angular momentum selection rules:
(1) Conservation of angular momentum dictates the following addition rule

$$\vec{I}_i = \vec{L} + \vec{I}_f. \tag{2.64}$$

This restricts the possible multipole orders to be $(I_i + I_f) > \lambda > |I_f - I_i|$. The radiation field observed would contain a mixture of these multipoles.
(2) Parity of the radiation field is dictated by:

$$\begin{aligned} \pi(E\lambda) &= (-1)^{\lambda} \\ \pi(M\lambda) &= (-1)^{\lambda+1}. \end{aligned} \tag{2.65}$$

From the above equation, it is obvious that a transition that is electric dipole in character would change the parity between the initial and final states, whereas a magnetic dipole would not.

In the so-called Weisskopf estimate [33], the reduced transition probabilities for different multipole transitions are deduced from the following relation [34]

$$B(\sigma\lambda) = f_\sigma(\lambda)\left(\frac{\hbar c}{E_\gamma}\right)^{2\lambda+1}, \tag{2.66}$$

where $f_\sigma(\lambda)$ is a complicated expression of λ with different functional form of λ for magnetic and electric multipoles, and E_γ is the γ-ray energy of the electromagnetic transition between two nuclear energy states in MeV. The Weisskopf estimate provides a rough and simple estimate for a single-particle transition probability for each multipolarity. It is a very useful unit with which γ-ray transition probability can be compared. For example, if the observed decay of a certain γ transition is many orders of magnitude smaller than the Weisskopf estimate, we might expect that a poor match-up of initial and final wave functions is slowing the transition. Similarly, if the transition were much greater than the Weisskopf estimate, we might guess that more than one single nucleon is responsible for the transition. In addition, the Weisskopf transition probability for a given nuclear transition provides an estimate on the degree of "collectivity" of the nuclear states connected by this transition. One should keep in mind, however, that the properties of specific nuclear states can modify these estimates by many orders of magnitude.

The Weisskopf reduced transition probabilities $B(\sigma\lambda)$, and the corresponding partial γ-ray half lives ($T_{1/2}$) for the first three multipolarities ($\lambda : 1 - 3$) are presented in Table 2.2 (reproduced from Ref. [34]). The reduced transition probabilities listed are functions of mass number A and γ-ray energy E_γ in MeV. From these transition probabilities, one can draw two immediate conclusions:

(1) The lower multipolarities are dominant. Increasing the multipole order by one unit reduces the transition probability by a factor of about 10^{-5}.

(2) For a given multipole order, electric radiation is more likely than magnetic radiation by about two orders of magnitude in medium and heavy nuclei. Therefore, it follows that the most commonly observed radiations are magnetic and electric dipole, and electric quadrupole.

For an in-depth treatment of the electromagnetic properties in nuclear spectroscopy, the reader is advised to consult the reference by Hamilton [34].

Table 2.2: Numerical values of Weisskopf estimates

Reduced single particle probability	γ-ray half life
$B(E1) = 0.064\ A^{2/3}\ e^2(fm)^2$	$T_{1/2} = 6.762\ A^{-2/3}\ E_\gamma^{-3}\times 10^{-15} sec$
$B(E2) = 0.059\ A^{4/3}\ e^2(fm)^4$	$T_{1/2} = 9.523\ A^{-4/3}\ E_\gamma^{-3}\times 10^{-9} sec$
$B(E3) = 0.059\ A^2\ e^2(fm)^6$	$T_{1/2} = 2.044\ A^{-2}\ E_\gamma^{-3}\times 10^{-2} sec$
$B(M1) = 1.790\ (e\hbar/2M_pc)^2$	$T_{1/2} = 2.202\ E_\gamma^{-3}\times 10^{-14} sec$
$B(M2) = 1.650\ A^{2/3}\ (e\hbar/2M_pc)^2(fm)^2$	$T_{1/2} = 3.100\ A^{-2/3}\ E_\gamma^{-3}\times 10^{-8} sec$
$B(M3) = 1.650\ A^{4/3}\ (e\hbar/2M_pc)^2(fm)^4$	$T_{1/2} = 6.655\ A^{-4/3}\ E_\gamma^{-3}\times 10^{-2} sec$

2.4.2 In-band Transition Rates

One of the most accurate tests to investigate the wave-functions of nuclear states is to compare the experimentally determined γ-ray transition probabilities between states versus theoretical predictions. This is often possible by measuring directly the ratio of the intensities of γ rays which deexcite collective states. Strongly coupled rotational bands with $K \neq 0$ are composed of two sequences of stretched quadrupole transitions ($I \rightarrow I-2$) which are linked by stretched dipole transitions ($I \rightarrow I-1$). Important quantities such as the deformation of the nucleus and what quasiparticles are associated with a given band can be deduced from these transition probabilities. The $E2$ transition is the most common transition in the deformed rotational structure of the rare-earth region. The reduced transition probability for a collective $E2$ transition from an initial state $|I_i\rangle$ to a final state $|I_f\rangle$ within a rotational band can be expressed in the rotational model [12] as

$$B(E2 : I_i \rightarrow I_f) = \frac{5}{16\pi} e^2 {Q_0}^2 |\langle I_i 2K0 | I_f K\rangle|^2\ (eb)^2. \tag{2.67}$$

The reduced transition probability for $M1$ transitions, $B(M1)$, can be estimated from the extended geometrical model devised by Dönau [36] and Frauendorf [37]

$B\,(M1 : I \rightarrow I-1) =$

$$\frac{3}{8\pi}\left[\sum_{m=\pi,\nu}(g_m - g_R)\left(\sqrt{1-\left(\frac{K}{I}\right)^2}K_m - \frac{K}{I}i_m + \frac{\Delta e'_m}{\omega}\right)\right]^2 \mu_N^2 \qquad (2.68)$$

where g_m are the single-particle g factors, K_m are the projections of the single-quasiparticle angular momenta on the symmetry axis, i_m are the quasiparticle alignments, and $\Delta e'_m/\omega$ are the signature splitting energies divided by the rotational frequency. Since $B(M1)$ transitions are orbital dependent, they can be used to help determine or confirm quasiparticle assignments for bands with intra-band $M1$ transitions.

In our data analysis, the experimental $B(M1)/B(E2)$ values were extracted from each experiment by estimating the intensity of each γ ray deexciting a given level. These intensities ($I_\gamma(M1)$ and $I_\gamma(E2)$) are then used in the following equation [35]

$$\frac{B(M1; I \to I-1)}{B(E2; I \to I-2)} = 0.693\frac{I_\gamma(M1)}{I_\gamma(E2)}\frac{E_\gamma^5(E2)}{E_\gamma^3(M1)}\left[\lambda(1+\delta^2)\right]^{-1}\left(\frac{\mu_N}{eb}\right)^2, \qquad (2.69)$$

where δ is the $E2$:$M1-$mixing ratio given by

$$\delta = \sqrt{0.7}E_\gamma\frac{\langle I|M(E2)|I-1\rangle}{\langle I|M(M1)|I-1\rangle} \qquad (2.70)$$

for $I \to I-1$ transition. The branching ratio, λ, is defined as

$$\lambda = \frac{I_\gamma(I \to I-2)}{I_\gamma(I \to I-1)}. \qquad (2.71)$$

It is apparent from Eq. 2.70 that for a pure $E2$ transition, δ goes to infinity, while for the case of a pure $M1$ transition, δ vanishes. The effect of the mixing ratio on the branching ratio is the following: when the mixing is dominated by $E2$, the mixing ratios are large, and when the $M1$ dominates, the $(1+\delta^2)^{-1}$ term has essentially no effect. The use of the experimental $B(M1)/B(E2)$ values for quasiparticle configuration assignment of the nuclei studied in this work is discussed in detail in later chapters.

CHAPTER 3

Experimental Techniques

3.1 Population of High-Spin States

3.1.1 Heavy-Ion Fusion Evaporation Reactions

In order to study high-spin states of a given nucleus, sufficiently large amounts of angular momentum must be imparted to it. Fusion evaporation reactions are the primary technique used to create nuclei with high angular momentum and excitation energy. The fusion process occurs when an accelerated heavy-ion projectile is captured by a stationary target nucleus to form a compound nucleus. The new composite nucleus decays by first emitting particles and then γ rays, which can be detected to identify and study the nuclei of interest. Fusion evaporation reactions allow the observation of unstable nuclei far from the line of stability which cannot be produced by other methods. This technique opened a new vista of interesting physics in the rare-earth region as nuclei near the proton drip line can be investigated.

In order for the fusion of beam and target to occur, the energy of the beam must be high enough to overcome the mutual Coulomb repulsion of the target and projectile. The Coulomb barrier is given in the center of mass system by

$$E_{CB} = 1.44 \, \frac{Z_i Z_t}{R_{it}} \text{ MeV}, \tag{3.72}$$

where Z_i and Z_t are the number of protons in the beam and target nuclei, respectively, and $R_{it} = R_i + R_t$ is the Coulomb radius in fm. Fig. 3.1 illustrates an accelerated nucleus on a collision path with a target nucleus. The angular momentum of the projectile is related to its linear momentum mv and the impact parameter b by $l = mvb$. The complete fusion reaction can occur for limited values of b. For instance, if

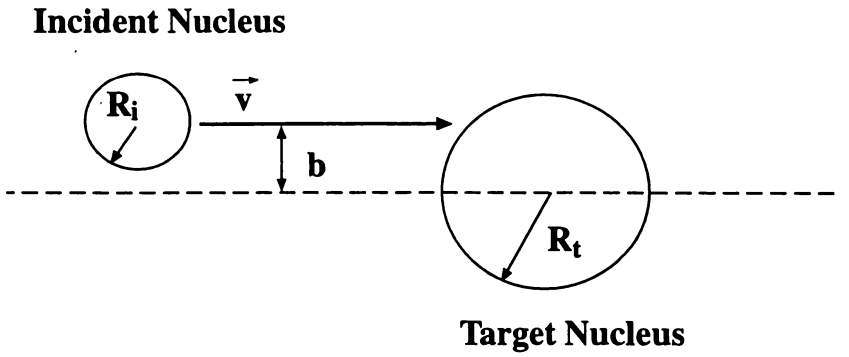


Figure 3.1: Schematic drawing of an incident nucleus impacting a target nucleus.

the geometrical impact parameter is greater than the combined radii of the two nuclei, they will only interact electromagnetically. In the case where the impact parameter is smaller than the combined radii and the energy of the incoming nucleus is greater than the Coulomb barrier, the two nuclei may overlap and complete fusion can occur. In such a reaction, the nucleons inside the resulting compound nucleus come to a thermal equilibrium such that the subsequent deexcitation will be essentially independent of the reaction mechanism.

After thermal equilibrium is reached, the compound nucleus is highly excited and usually has a very large angular momentum. The excitation energy of the compound nucleus is

$$E_{ex}^{max} = E_{CM} + (M_i + M_T - M_{c.n.})c^2, \tag{3.73}$$

where $E_{CM} = \frac{A_i}{A_i+A_T} E_i$ [MeV] is the center of mass energy of the system, and M_i, M_T, and $M_{c.n.}$ are the masses of the incident, target, and compound nuclei, respectively. The term $(M_i + M_T - M_{c.n.})c^2$ is often referred to as the Q value. Normally, in selecting a beam and target combination for high-spin studies, one wants to induce as much angular momentum into the nucleonic system as possible while still having a significant cross section for the nucleus of interest. Since the beam is responsible for imparting this angular momentum, the heaviest nucleus possible at the highest energy possible which will produce the desired isotope is the most advantageous beam selection. Pelte and Schwalm showed in Ref. [38] that the maximum angular

momentum contributing to fusion can be estimated from the sharp cut-off model as

$$\ell_{max}(\hbar) \approx 0.219\ R_{fus}\ [A_\mu(E_{CM} - E_{CB})]^{1/2}, \tag{3.74}$$

where R_{fus} is an empirically derived radius of fusion,

$$R_{fus} = 0.95\ (A_i^{1/3} + A_T^{1/3})\ [\text{fm}], \tag{3.75}$$

$A_\mu = \frac{A_i A_T}{A_i + A_T}$ [amu] is the reduced atomic mass, E_{CM} is the center of mass energy of Eq. 3.73, and E_{CB} is the Coulomb barrier energy defined by Eq. 3.72. The sharp cut-off model can also give an estimate on the total reaction cross section for $l \leq l_{max}$

$$\sigma = \pi\lambda^2(l_{max} + 1)^2, \tag{3.76}$$

with the reduced wavelength λ defined as

$$\lambda = \hbar/\sqrt{E_{CM}A_\mu}. \tag{3.77}$$

If the total reaction cross section is measured, the corresponding experimental value of l_{max} can be derived from Eq.(3.76).

3.1.2 Decay of Compound Nuclei

A compound nucleus is formed when the intermediate system survives fast fission. After a relatively short period of time ($\sim 10^{-19}$ seconds), the nucleus begins to release energy by particle emission. This process quickly lowers the excitation energy of the nucleus as the emitted particle carries away an amount of energy that is at least equivalent to its separation energy of $8 - 10$ MeV. However, an emitted particle carries only a small fraction of the angular momentum of the system ($\sim \hbar$ on average). Although protons and alphas are possible reaction exit channels, the Coulomb barrier is usually sufficiently strong such that the charged-particle emission probability is reduced. If the compound nucleus is on the neutron-deficient side of the β stability region, then the neutron binding energy begins to increase. When the number of neutrons is approximately 15% less than that near β stability, the binding energy of a neutron is likely equivalent to the proton binding energy *plus* its Coulomb barrier [39].

At this point protons and neutrons are evaporated with comparable probabilities. In our Gammasphere experiment (see next chapter), the compound nucleus was ^{132}Sm which has $\sim$ 20% fewer neutrons than stable ^{150}Sm. Therefore, in neutron-deficient regions, like the mass $A \sim 130$ region, the emission of charged particles is even favored over neutrons. In addition to the Coulomb barrier, compound nucleus particles like alphas carry a large angular momentum l, which means that it has to overcome the centrifugal barrier given by

$$E_l = \frac{l(l+1)\hbar^2}{2\mu R^2} \text{ MeV}, \tag{3.78}$$

where μ is the reduced mass of the emitted particle and R is the tunneling radius. Since in the $A \sim 130$ region protons and alphas will be evaporated with a large probability, the detection of charged particles is required as a means to distinguish the desired reaction channels from the unwanted channels.

After the emission of several particles and around 10^{-15} seconds, γ-ray emission begins to compete with particle emission when the excitation energy of the system is brought down to region of one neutron separation energy or less above the yrast line. At this point, the nucleus begins to "cool" through the emission of statistical γ rays. The level density is extremely high in this region, therefore, a continuum of γ rays (largely electric dipole in nature) is all that can be observed.

The very last stage of deexcitation is decay along the yrast line to the ground state through the emission of γ rays. Due to the low-level density near the yrast line, these γ rays appear as discrete lines in the spectrum. For most spectroscopic studies, only levels with spins up to $\sim$ 30-50 $\hbar$ receive enough intensity to be resolved. Studies of these discrete lines are important for understanding the underlying physics behind high-spin states and the interplay between single and collective particle motion, which is the main subject of this thesis. Fig. 3.2 schematically illustrates the various stages of decay of an excited compound nucleus. Included in this figure are approximate estimates of E_{ex} and I_{max} for the target-beam combination of two heavy evaporation reactions discussed in this thesis work.

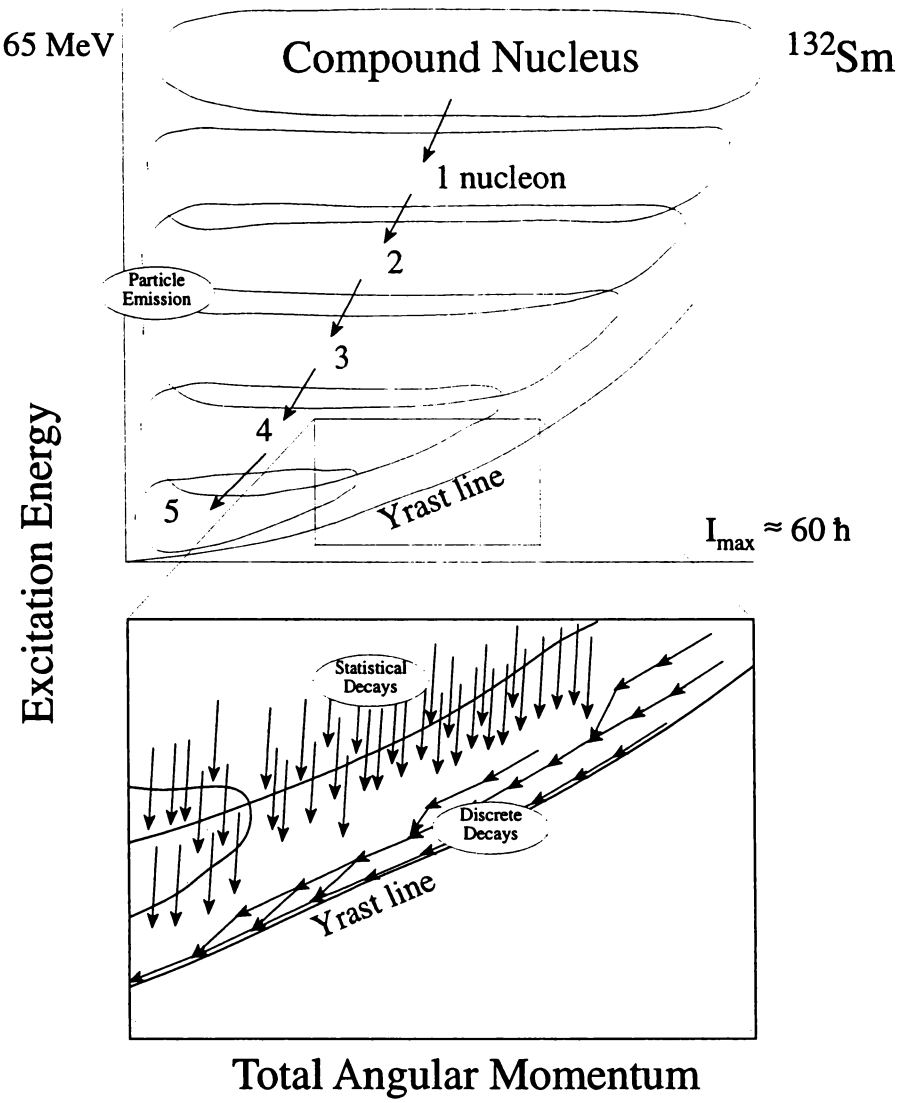


Figure 3.2: Angular momentum versus energy illustration of the decay of a compound nucleus. The nuclear excitation is plotted as total angular momentum versus excitation energy. The labels "$E \sim 65$ MeV" and "$I \sim 60\hbar$" indicate the excitation energy and maximum angular momentum for a compound nucleus with $A \sim 130$, $A_i = 40$, and $A_t \sim 90$.

3.1.3 Statistical Model Calculations for Reactions Cross Sections

Previous sections provided an overall qualitative understanding of the fusion evaporation process and the population of high-spin states. In reality, the reaction parameters are modeled in more detail via statistical model calculations. In one of these calculations, a commonly-used code named PACE (Projected Angular momentum Coupled Evaporation) [40], Monte-Carlo simulations of the formation and decay process of a compound nuclear system are performed.

The cross sections to produce the residual nuclei from the reaction ^{19}F + ^{116}Cd (which is used for one of the experiments described in this work) are shown Fig. 3.3. In this PACE calculation, the 5n channel (^{130}La), which is one of three nuclei studied in this work, is the strongest populated channel with maximum partial cross section of $\sim$ 550 *mb* at a beam energy of $\sim$ 90 MeV as seen in the top part of Fig. 3.3. The calculation also predicts the partial cross section of the maximum angular momentum that could be attained at that beam energy. The angular momentum for all species produced in this reaction at 90 MeV is $\sim 37\hbar$ as seen in the lower part of Fig. 3.3. Different neutron evaporation channels have cross section peaks at different beam energies. If one defines $E_m(\#\mathrm{n})$ as the corresponding beam energy of a channel at its largest cross section, it can be seen from Fig. 3.3 that $E_m(4n) < E_m(5n) < E_m(6n) < E_m(7n)$. This can be understood from the fact that more beam energy is needed to separate a larger number of particles from the bound nucleus.

It should, however, be stated that PACE is only a guideline for any high-spin experiment as its prediction accuracy of reaction cross sections depends on the mass region. Several versions of PACE have been developed, and one of these versions is a code called EVAPOR developed by Beene *et al.* [41], which gives better predictions than PACE for nuclei closer to the proton drip-line. For the reaction ^{40}Ca + ^{92}Mo, used in two of our experiments, EVAPOR predicted partial cross sections for more than 20 residual nuclei for a beam range of 140-260 MeV. The nuclei of interest ^{128,129}Nd had a maximum cross section of $\sim$ 58 and $\sim$ 28 *mb* at beam energies of $\sim$ 170 and $\sim$ 200 MeV, respectively. The fission probability is nearly zero up to a

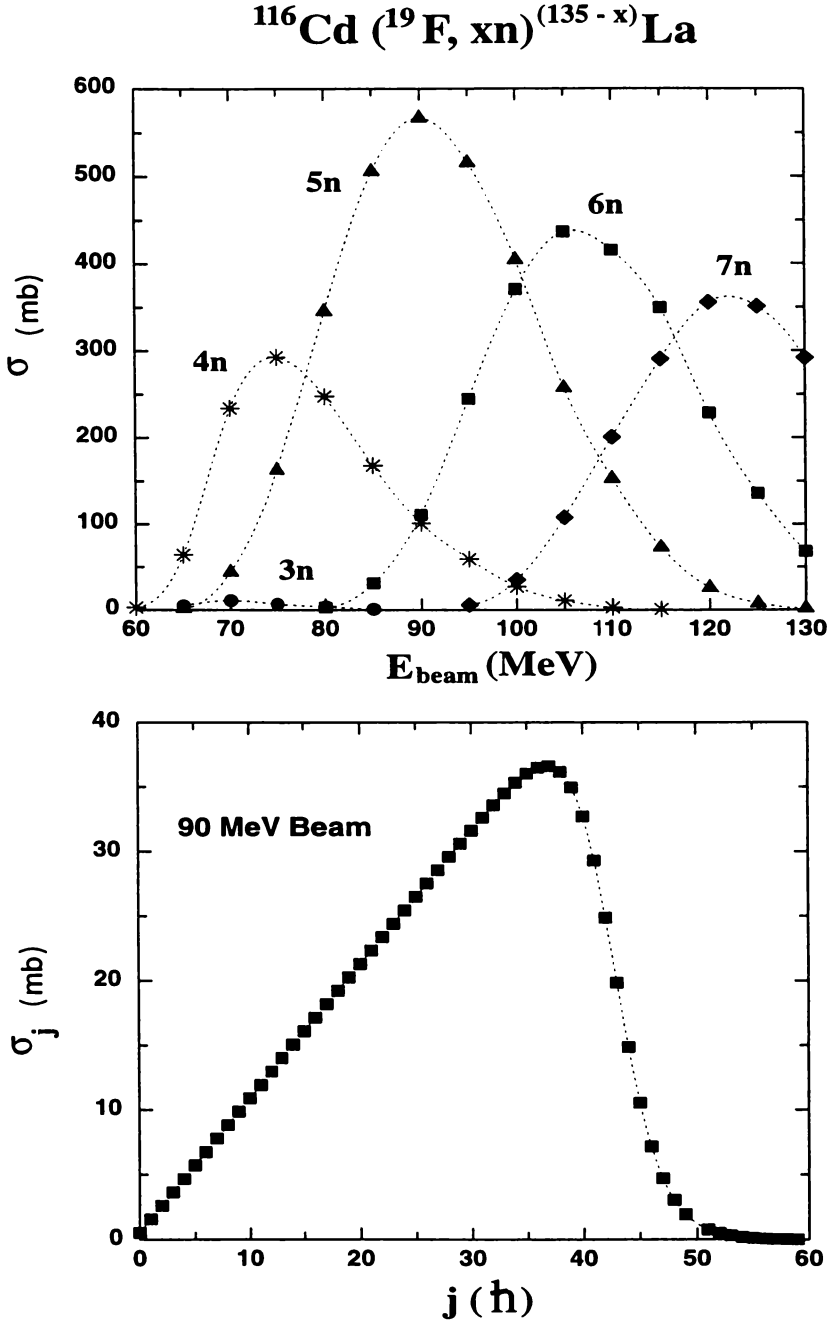


Figure 3.3: Calculated cross sections for residual nuclei as a function of beam energy (above). Calculated partial angular momentum cross sections versus angular momentum for the same reaction at a 90 MeV beam energy (below).

beam energy of $\sim$ 180 MeV after which it increases dramatically. The γ-ray decay from fission products creates a large background making the identification of γ rays associated with the nuclei of interest impossible with Ge-detectors alone. Therefore, a reasonable beam energy of 184 MeV was chosen for this reaction. Another Monte-Carlo simulation code called HIVAP [42] was used to give relatively accurate absolute cross sections for the different reaction exit channels for the reaction ^{40}Ca + ^{92}Mo. Results of HIVAP calculations are discussed in Chapter 5.

3.2 Experimental Devices

The data for this study were taken from three experiments. In one experiment, a ^{40}Ca beam was supplied by the 25 MV tandem accelerator at the Holifield Radioactive Ion Beam Facility (HRIBF) at Oak Ridge National Laboratory (ORNL). The emitted γ rays were detected by the Ge Clover detector array CLARION [43]. Light charged particles emitted by the deexciting compound nuclei were identified using the HyBall [43] array. The Recoil Mass Spectrometer (RMS) [44] and the Position Sensitive Avalanche Counter (PSAC) [43, 44] were used as external triggers for mass identification. In a second experiment emphasizing the highest spin states possible, a similar beam was provided by the ATLAS linear accelerator at Argonne National Laboratory (ANL). The emitted charged particles were detected with the Microball [45] detector array, and γ rays were detected with the Gammasphere [46] detector array surrounding the Microball. The third experiment was performed at the Wright Nuclear Structure Laboratory (WNSL) at Yale University. The ^{19}F beam was supplied by the 20 MV tandem, while the emitted γ rays were detected with the YRAST Ball [47]. The operation and detection capability of these experimental devices is briefly described below, but we introduce first the concept of γ-ray detection using Ge detectors.

3.2.1 Gamma-ray Detection and Properties of Germanium Detectors

There are two principal qualitative features of x rays and γ rays with regard to their detection: (1) x rays and γ rays are many times more penetrating in matter than

charged particles, and (2) a beam of photons is *not* degraded in energy as it passes through a thickness of matter, only attenuated in intensity. The interaction of x rays or γ rays with the detector material occurs through one of the following processes:

- Photoelectric Effect
- Compton Scattering
- Pair Production

The photoelectric effect involves the absorption of a photon by an atomic electron with the subsequent ejection of the electron from the atom. Since a free electron cannot absorb a photon and also conserve momentum, the photoelectric effect always occurs on bound electrons with the nucleus absorbing the recoil momentum. It is the most useful interaction for the purpose of detecting the complete energy of the photon. This process is dominant for low energy photons (150 keV or less). Compton scattering involves the scattering of a photon off free electrons. The scattered electron does not absorb the full energy of the γ ray, and if the photon escapes from the detector after being scattered, the total energy of the γ ray will not be deposited. The chance that a photon will be photoabsorbed is roughly dependent on Z^5 ($Z \equiv$ number of protons) of a given material, while the chance for Compton scattering is approximately linear in Z. Therefore, high-Z materials are desirable for γ-ray detection to favor the photoabsorption process. Photoabsorption and Compton scattering are the dominant interaction processes of photons with matter for photon energies up to $\sim$ 2 MeV. The process of pair production involves the transformation of γ rays with energies greater than 1.022 MeV into an electron-positron pair.

Two semiconductor materials are typically used in γ-ray detectors: silicon and germanium. For the purposes of γ-ray detection, germanium ($Z = 32$) is superior over silicon ($Z = 14$) because of the Z^5 dependence of the electromagnetic photoabsorption. In addition, semiconductor materials, like germanium, offer very good energy resolution[1] because of its low ionization energy. Thus, for experiments

[1]The energy resolution of the detector is conventionally defined as the full width at half maximum (FWHM) divided by the location of the peak centroid.

where good energy resolution of γ rays is of primary importance, detectors of Ge material are used. The number of free charge carriers (electrons and holes) created for a given energy of incident radiation is directly related to the resolution of the detector. Typical energy resolution for a High-Purity Ge detector (HPGe) is about 2 keV for the 1.33 MeV γ ray emitted by a ^{60}Co source. Under the influence of high electric fields in the detector material, the electrons and their resulting holes are swept to opposite contacts where a charge, which is proportional to the energy of the γ ray, can be measured. For germanium semiconductor material, the energy gap to create an electron-hole pair is $\sim$ 3 eV, which is a much lower energy gap compared with scintillator materials ($\sim$ 1 keV).

The low ionization energy of semiconductor detectors, however, has a disadvantage in that the probability to thermally excite electrons into the conduction band is quite high, which causes a leakage current. For Ge detectors to be useful in γ-ray spectroscopy, the detectors are cooled to liquid nitrogen temperature (77 K) which greatly reduces the leakage current. To enlarge the sensitive volume for radiation detection, an $n-p$ junction is typically created in the semiconductor material, and a reverse bias voltage is applied to the device. With the application of the reverse bias, the total collection time for electron-hole pairs created by an incident γ ray is $\sim$ 100 ns per 1 cm of detector material. This is a slow rise time compared to other types of detectors (*e.g.* NaI scintillators with rise time of few nanoseconds).

The different kinds of γ and x ray Ge detection systems implemented for the experiments discussed in this work are briefly discussed below. The reader is encouraged to refer to the following sources [48, 49] for in-depth coverage of Ge detectors and their use in γ-ray measurement techniques.

Low Energy Photon Spectrometers

Low-Energy Photon Spectrometers (LEPS) have a planar geometry that has a relatively small volume compared to the surface area facing the reaction. When fully depleted and operated with large overvoltage, the electric field in these detectors is almost uniform from one contact to the other. The result of this is that collection time

for charge carriers is relatively fast and the signal to noise ratio is comparatively large (due to a small detector capacitance). Therefore, these detectors have better time and energy resolution than coaxial Ge detectors (discussed below). However, these detectors have a small sensitive volume, and because of that high-energy γ rays pass through the detector with little interaction. Therefore, LEPS detectors are typically used for detecting γ and x rays with energies up to about 200 keV.

Coaxial and Segmented Ge Detectors

In order to present a larger detector volume for a given surface area, the coaxial detector was designed. This design provides a much wider range for an efficient γ-ray detection ($\sim$ 50 keV$-$10 MeV). The sacrifice is that the energy and time resolution are reduced compared to planar designs. The larger γ-ray energy detection range and the overall greater efficiency of the coaxial geometry makes it the most popular Ge detector for nuclear spectroscopic studies and, therefore, is found in all large γ-ray spectrometers around the world. These currently used large-volume, high-purity Ge (HPGe) detectors have relative efficiencies of $> 20 - 25\%$[2].

One of the problems with large-volume Ge detectors is that they have such a large angular acceptance that the Doppler shift of γ rays emitted from a recoiling nucleus degrades the resolution. One technique that has been used to effectively reduce the size of the angular acceptance without reducing efficiency is to electronically segment a detector [51]. In Gammasphere for example, some of the detectors have been electrically segmented into two D-shaped halves (see Fig. 3.4). The high-resolution, total-energy signal is still read from a common electrode at the center of the detector, while lower resolution signals can be read separately from each half, thus indicating which side of the crystal was hit first. Consequently, the effective angular size of the Ge detector is reduced by a factor of two. In typical experiments, this improves the resolving power of Gammasphere by a factor of two.

[2]The efficiency of a detector is defined as the number of counts in the 1332.5 keV peak from a ^{60}Co source placed 25 cm away, divided by the number of counts observed in a 3"$\times$3" NaI crystal under the same conditions.

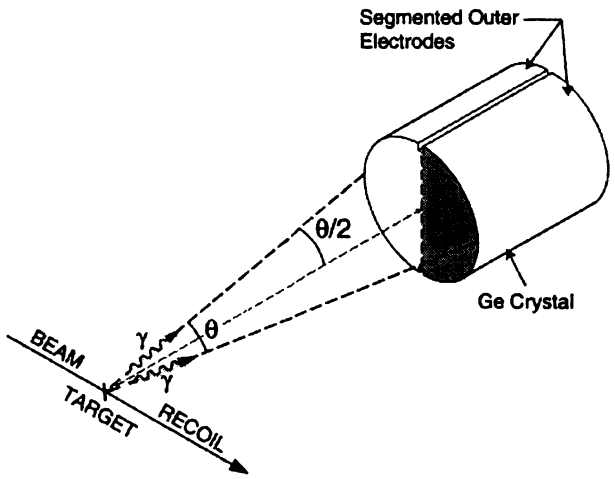


Figure 3.4: Schematics of an electrically-segmented detector.

Clover Ge Detectors

Another technique to increase the detector area presented to the target, while minimizing Doppler broadening, is to pack several coaxial detectors in a close configuration, thus getting a much larger detector with a resolution that is no worse than a single coaxial Ge detector. One design involves packing four detectors together in a common liquid nitrogen cryostat. Such a design is known as a clover detector (see bottom picture, Fig. 3.5). This feature of the design is advantageous, because one can add energies from nearly simultaneous events detected in adjacent segments of the same detector under the assumption that they are from the same γ ray ("add-back" mode). This technique is very effective when data rates are such that the chance of "true" events occurring in adjacent detectors is small. In "add-back" mode, one can gain in efficiency up to 50% of the value obtained in "singles" mode (*i.e.* when the four detectors are operated independently as single Ge detectors).

BGO Detectors

Bismuth germanate ($Bi_4Ge_3O_{12}$, commonly abbreviated as BGO), is a scintillation material in the form of crystals. A major advantage of BGO is its high density ($\sim$ 7.1 g/cm^3) and the large atomic number of the bismuth component ($Z = 83$).

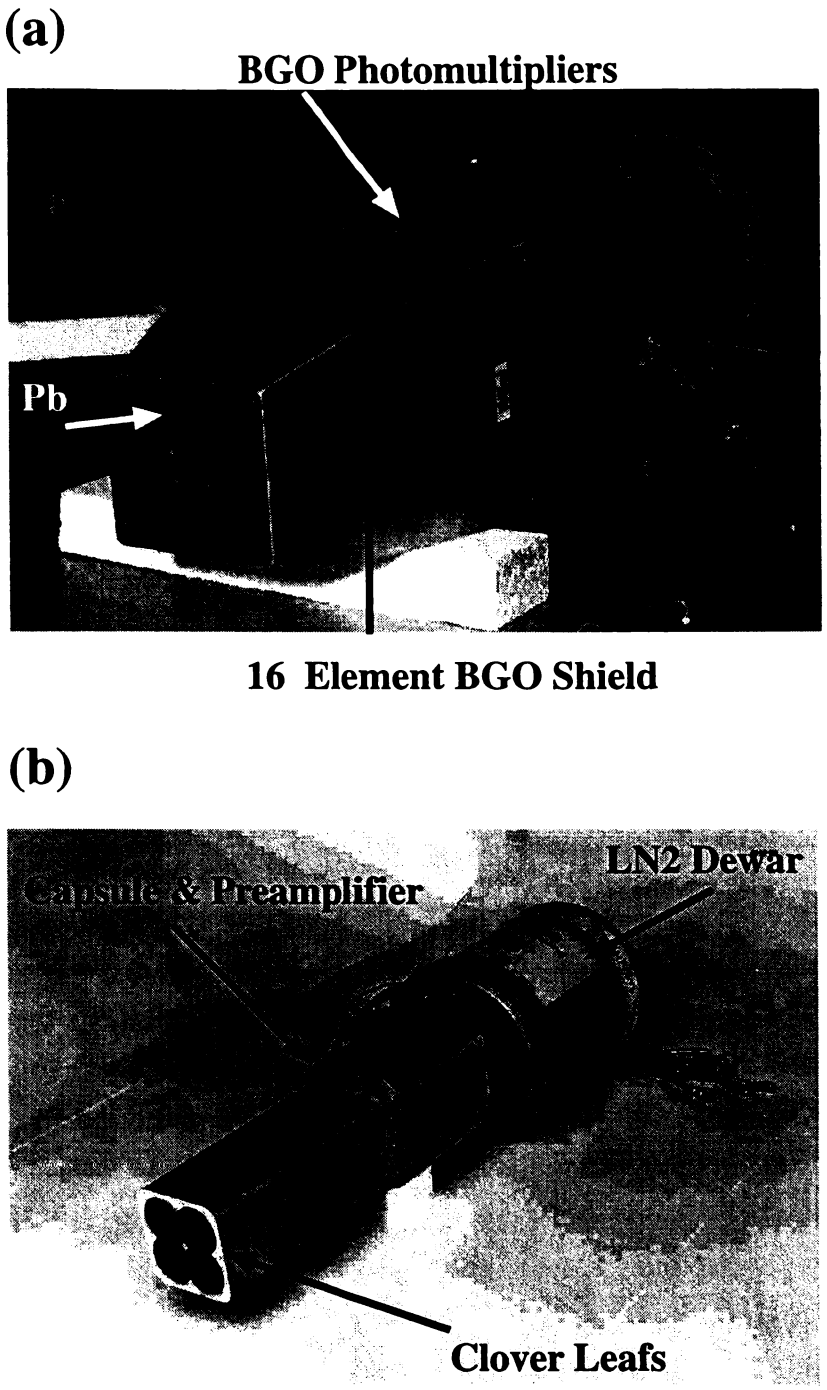


Figure 3.5: A CLARION clover with the BGO shield (a), and without the BGO shield (b).

These properties result in the largest probability per unit volume of any commonly available scintillation material for the photoelectric absorption of gamma rays [48]. Therefore, BGO is used as a shield material to detect the energetic γ rays scattered out of the Ge crystals, and thus reducing the Compton continuum and improving the Peak-to-total (P/T) ratio. The P/T ratio is defined as the ratio of the area of the full-energy peak to the total number of counts in the whole energy spectrum. For a given Ge-BGO setup, the P/T ratio can serve as a good indicator of the performance of the Compton-suppression shield. In γ-γ coincidence experiments, the highest achievable P/T is of critical importance since the efficiency of "good" γ-γ events goes as the square of the P/T ratios. A prototype Gammasphere detector with a BGO shield can achieve a P/T value of ~ 0.7 for a ^{60}Co source [52]. The use of BGO shields in large detector arrays and its suppression capability is presented in the following section.

3.2.2 Large Arrays of Escape Suppressed Spectrometers

Large Arrays of Escape Suppressed Spectrometers (ESS) have revolutionized the γ-ray spectroscopy study of the atomic nucleus. The unsurpassed sensitivity of the current generation of arrays is such that it is possible to study weak features, with an intensity of 10^{-5} of the total reaction cross section, associated with exotic phenomena at the extremes of nuclear spin and deformation. This allowed observation of γ-ray cascades that are well beyond the detection limits of previous generation arrays.

The most important properties of a γ-ray detector array are energy resolution, efficiency, and peak-to-background ratio. These arrays use large-volume Ge detectors to achieve good energy resolution and high peak efficiency. In addition, the detectors are surrounded by BGO shields for improving the peak-to-total ratio. A large number of detectors are used to keep the solid angle of each individual detector small and thus reduce both the probability of detecting of two different γ-rays and the Doppler broadening of the γ-ray lines. Another advantage of large arrays is the distance between the target and the detectors which allows auxiliary detectors to be placed in the target chamber. The current arrays all use a similar design to obtain the best performance from the available technology. Some of the parameters used in

describing the characteristics of an ideal array are:

- The **Gamma-Ray Multiplicity** M_γ is the number of γ rays produced in a single event. For rare-earth nuclei produced in heavy-ion fusion evaporation reactions, for example, M_γ is typically $\sim$ 25 to 30.

- The **Detection Fold** F_D in an event is $\sim M_\gamma \epsilon$, where ϵ is the *total* efficiency of the detector array, *i.e.* the efficiency including both photopeak and residual unsuppressed Compton-scattered γ rays.

- The **Number of Reactions** N_R produced during the experiment depends on beam current, target thickness and total reaction cross-section.

- The **Number of Events** N_E recorded during the experiment varies with the detected fold F_D as

$$N_E[F_D] \approx N_R^{M_\gamma} C_{F_D} \epsilon^{F_D} (1-\epsilon)^{M_\gamma - F_D}, \tag{3.79}$$

  where C_{F_D} is a constant representing the number of combinations.

With these different parameters describing the detection performance of large detector arrays in mind, a brief description of the three largest and most powerful ESS arrays in the US is presented. These arrays have been used in the three high-spin spectroscopy experiments for this dissertation project.

Gammasphere and Next Generation Arrays

Gammasphere is a spectrometer of unparalled sensitivity to nuclear electromagnetic radiation due to its high resolution, granuality, and efficiency. This powerful combination of features makes it the ideal device for studying nuclear spectroscopy of rare and exotic processes. Of particular current interest are studies at the very limits of nuclear stability, high angular momentum, unusual neutron-to-proton ratio, high mass, and high internal excitation energy.

Gammasphere has the capability of using 110 HPGe detectors. The peak to total ratio obtained in Gammasphere is 57% - 61% for ^{60}Co. The BGO shield has a

Table 3.1: Properties of Gammasphere

Number of Detectors	110 hexagonal units w/BGO
	40 unsegmented
	70 segmented
Ge Detector size	7.1 cm (D) × 8 cm (L)
Target to Ge distance	25.25 cm
Total Ge solid angle	46% of 4π
Total peak efficiency (1.33 MeV)	9.9%
P/T (1.33 MeV)	0.6
Energy resolution (1.33 MeV)	2.5 keV (FWHM)

tapered lip which gives a Ge solid angle of 0.418% of 4π and a half opening angle of the Ge detectors of 7.4°, which, for 110 detectors, gives a total Ge coverage of 46%. The full Gammasphere array with 110 detectors has a total photopeak efficiency of 9.9%. The detectors are mounted at the following angles (with a forward-backward symmetry) with respect to the beam axis: 10 detectors at 17.3°, 10 at 31.7°, 10 at 37.4°, 20 at 50.1°, 10 at 58.3°, 20 at 69.8°, 10 at 79.2°, 10 at 80.7°, and 10 at 90°. A summary of the characteristic parameters for Gammasphere are shown in Table 3.1 The mechanical system of Gammasphere consists of two hemispheres with support structures which can move away transversely from the beam line and rotate along an axis perpendicular to the beam for ease of detector mounting and dismounting. The Ge-BGO electronics are implemented on VXI modules, each containing two channels. There are six crates of Ge-BGO electronics and one crate of trigger and readout electronics. Interface with external detectors is provided in the trigger unit and units for controlling CAMAC crates and data readout via a FERA bus. The data are processed by six single-board computers in VME crates and can be sent to eight 8-mm tape units for recording at a maximum total rate of 40 Mbytes/sec. At the same time, data are sent to an array of workstations for analysis. A partial photograph of one of Gammasphere's hemispheres is provided in Fig. 3.6.

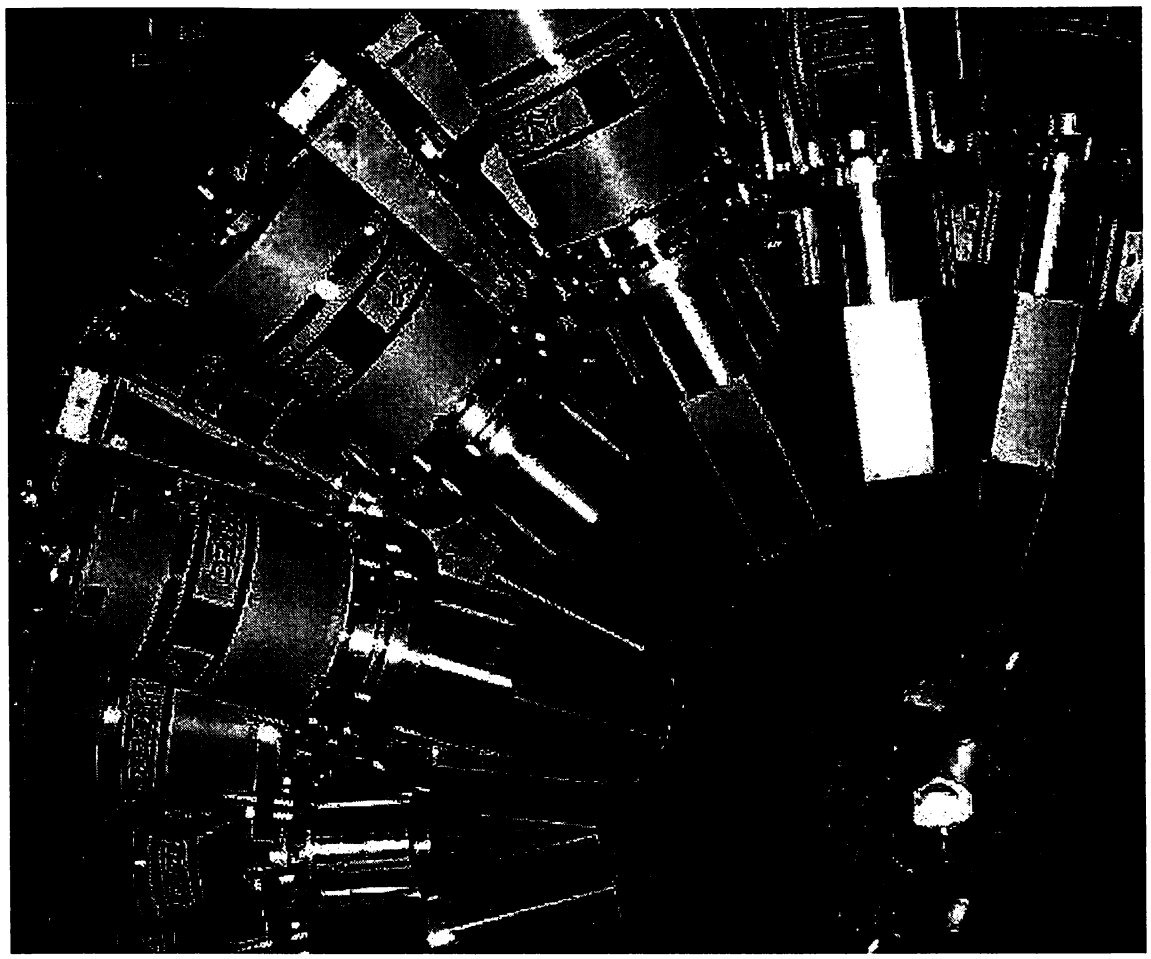


Figure 3.6: 1/4 view of Gammasphere showing the cavity which fits the target chamber that holds the Microball. Each of the Gammasphere Ge detectors is surrounded by a 6-element BGO suppression shield plus a cylindrical BGO backplug behind the Ge Crystal.

Using the parameters defined in the previous section, one can now consider examples of typical values for these quantities for any large detector array. In a typical high-spin experiment, using a fusion-evaporation reaction to produce rare-earth nuclei, with several pnA of beam current, one can expect a reaction rate of the order of 10^5 per second. A three-day experiment thus produces $N_R \sim 3\times10^{10}$ reactions with a typical γ-ray multiplicity of $M_\gamma \sim 25$. Gammasphere has an efficiency of $\epsilon \sim 0.15$, resulting in $N_E[F_D \geq 4] \approx 1.6 \times 10^{10}$ events which can be histogrammed in a three-dimensional cube (see section 3.4). Fig. 3.7 shows calculated sensitivity limits for Gammasphere used in conjunction with three different values of γ ray multiplicity and recoil velocity. Note that in all cases, the optimum calculated sensitivity occurs for fold 4.

It is worth mentioning that the next generation arrays, such as GRETA (Gamma Ray Energy Tracking Array), might have total detection efficiencies approaching $\epsilon \sim 0.6$, resulting in an average detection fold of about 15. The huge number of counts generated by such an array would require analysis in 6 or 7 dimensions [54]. A prototype of GRETA is currently being designed at Lawrence Berkeley National Laboratory. In this new detector array, the full 4π solid angle is covered by highly segmented germanium detectors. Events that would be rejected in Compton-suppressed arrays can be recovered using tracking, and thus increasing the efficiency compared to currently existing arrays.

CLARION

The Clover Array for Radioactive ION beams (CLARION) is a Ge array that consists of eleven segmented clover detectors and ten single-crystal Compton Suppressed Spectrometers (CSS). Each clover consists of four individual crystals sharing a common cryostat. By minimizing the dead layer between the adjacent crystals, the signals from all four crystals may be added together to obtain the total pulse height for an incident γ ray that scatters from one crystal to one or more of the other three crystals. This so-called add-back mode increases the photo efficiency of a clover detector from about 100% to more than 150% for ^{60}Co lines, and provides excellent efficiency for

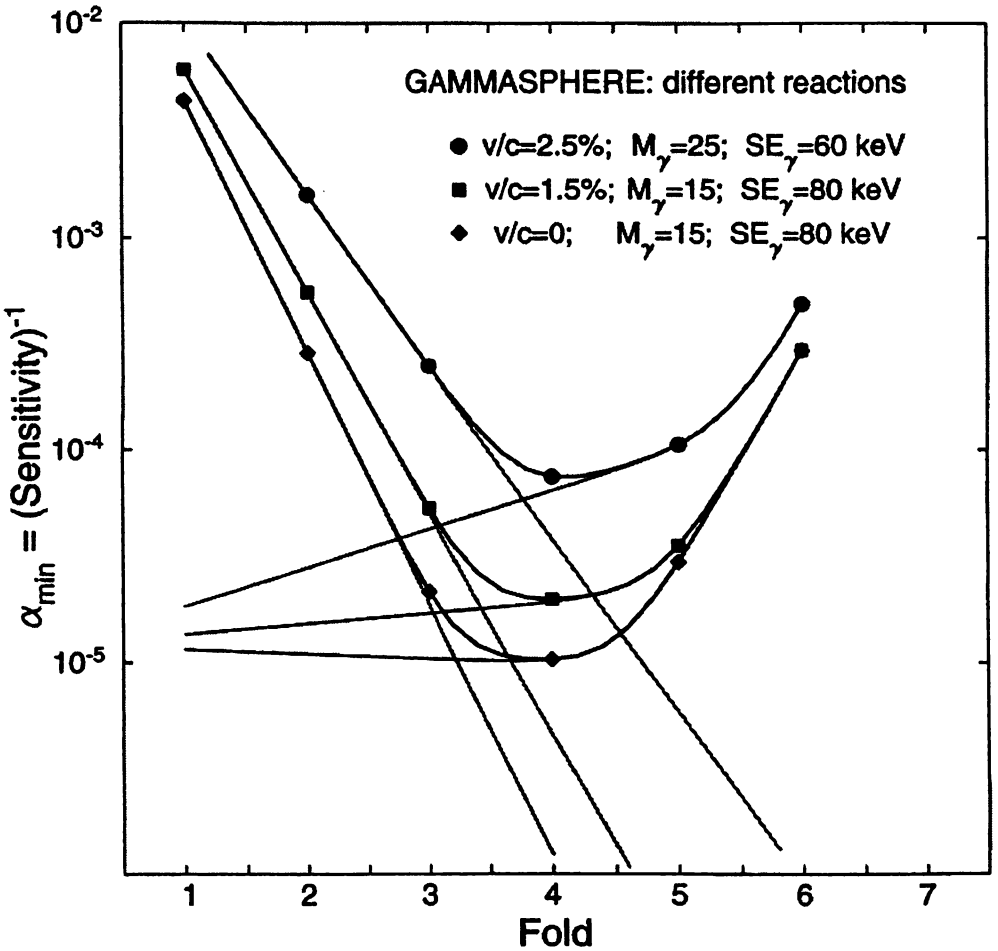


Figure 3.7: Calculated sensitivity for Gammasphere used in conjunction with three different values of γ-ray multiplicity M_γ, recoil velocity v/c, and average γ-ray energy separation SE_γ. The calculations are performed as described in Ref [53].

detection of high-energy γ rays. When operated in add-back mode, a single clover detector has a photopeak efficiency of 0.2% for detection of 1.33 MeV γ rays. Furthermore, the small effective width (2 cm) of segmented Ge detectors help reduce the effect of Doppler broadening. The peak-to-total ratio of the Compton-suppressed clover detectors, when operated in add-back mode, is approximately 55% for ^{60}Co. The four individual crystals of a clover detector can be used as a polarimeter.

The array is placed in front of the RMS beam line and surrounds a 15-cm radius target chamber. The combination of 10 single-crystal elements and 11 Clover detectors placed 22 cm from the target will have a total photopeak efficiency of about 2.6% for a 1.33 MeV γ ray. This large distance from the target reduces the Doppler broadening and allows the use of auxiliary detectors such as the HyBall (see section 3.2.3). Fig. 3.5 shows a picture of one of CLARION's clovers with and without the BGO shield. A lead mask is put in front of the shield to prevent γ rays originating from the target to interact directly with the BGO. The effect of suppression and add-back for CLARION clovers are shown in Fig. 3.8.

YRAST Ball

The Yale Rochester Array for SpecTroscopy (YRAST Ball) is the world's largest university-based Ge detector array, with 28 Ge detectors and a total photo peak efficiency of $\sim$ 2%. The detector arrangement is flexible to allow the use of a variety of auxiliary detectors with YRAST Ball. The detectors are mounted in four rings making angles of 163° (3 positions), 135° (8 positions), 90° (9 positions), 55° (8 positions) with respect to the beam axis. In our YRAST Ball experiment, we used four LEPS detectors, seven Clovers, and 15 single Ge detectors. Fig. 3.9 shows the detector component of the YRAST Ball inside one of the experimental vaults at the Wright Nuclear Structure Laboratory, Yale University.

3.2.3 Charged Particle Detection

The passage of charged particles through matter is generally characterized by a loss of energy by the particle and a deflection of the particle from its incident direction.

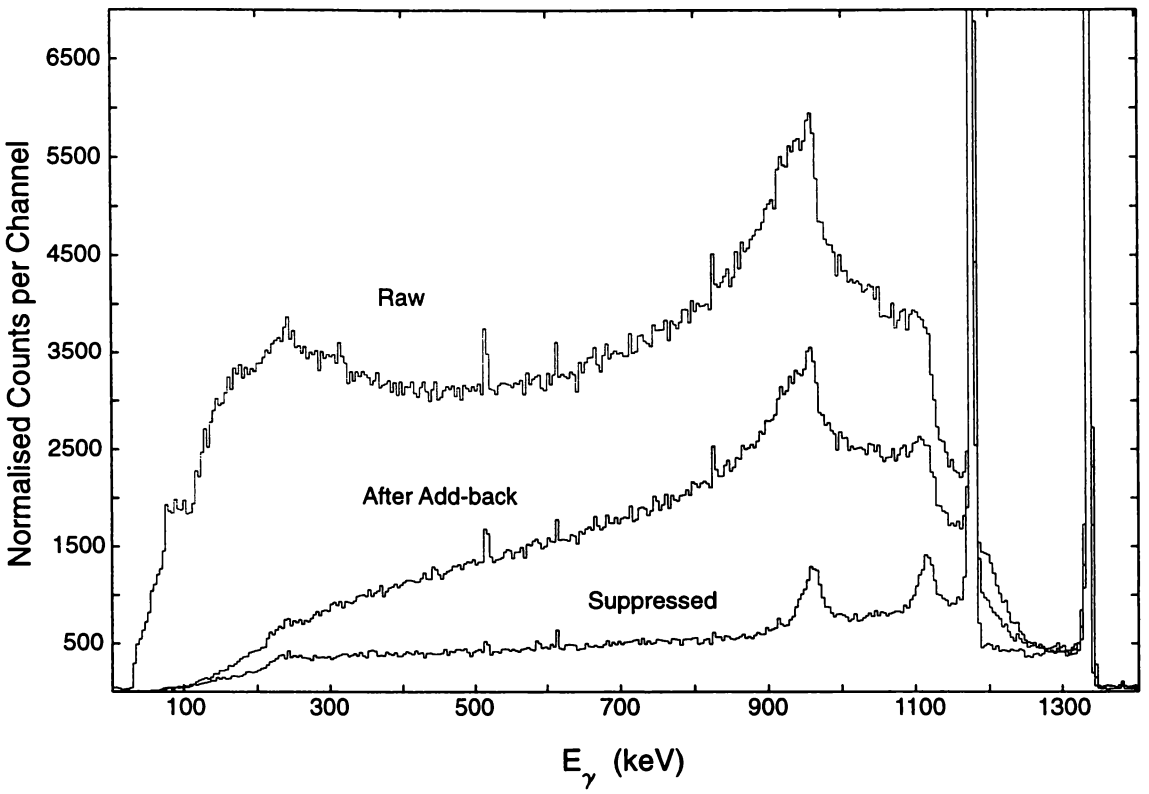


Figure 3.8: The effect of add-back and Compton suppression on clover spectra of a ^{60}Co source placed in the center of CLARION (see next section). These spectra are normalized so as to have the same areas for the truncated full-energy photo-peaks at 1173 keV and 1332 keV. The peaks in the suppressed spectrum at the Compton-edge energies can be ascribed to photons backscattered from the Ge crystal which escaped through the BGO shields.

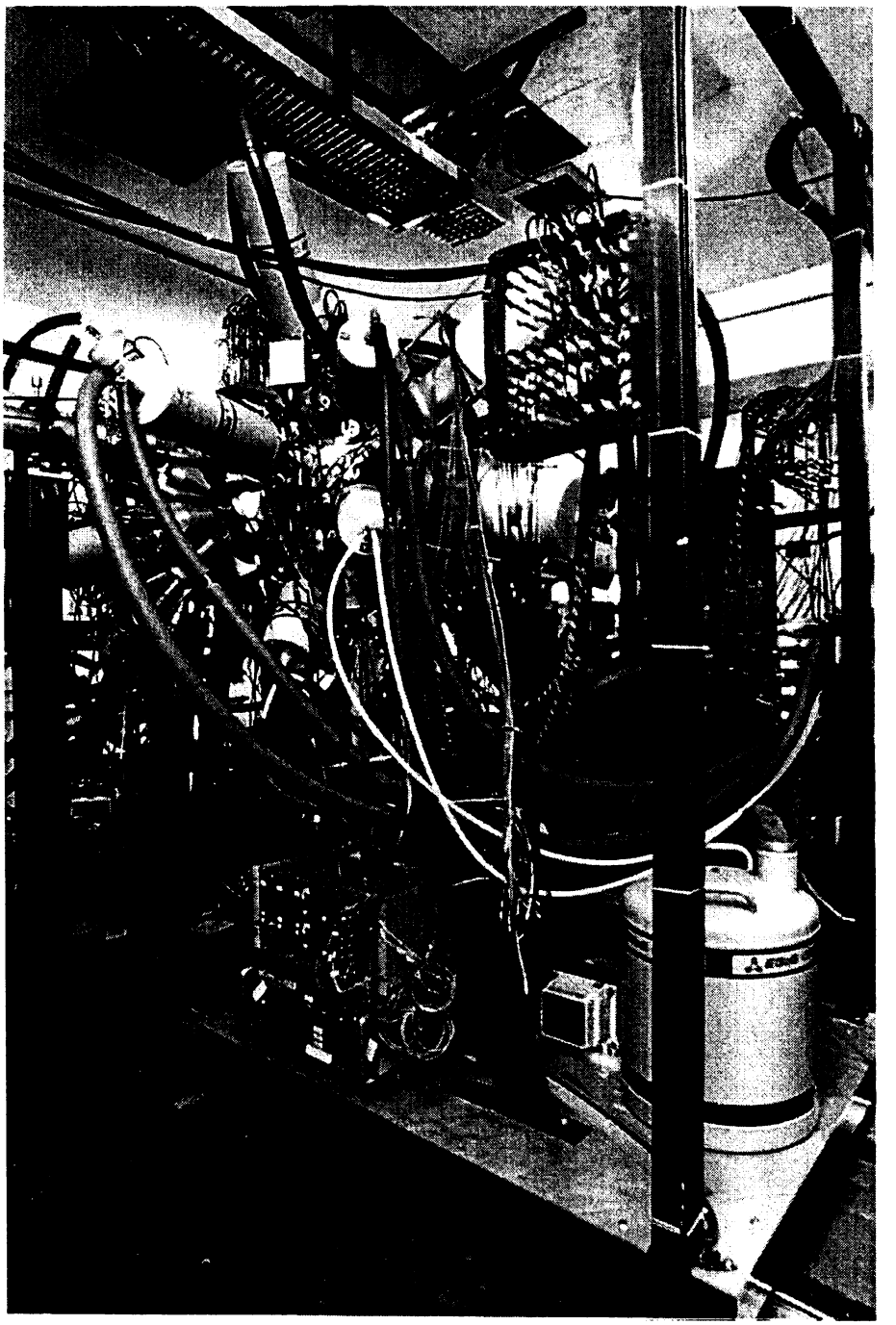


Figure 3.9: The YRAST Ball

These effects are primarily the result of two processes:
(1) Inelastic collisions with the atomic electrons of the material.
(2) Elastic scattering from nuclei.
Of the two electromagnetic processes, the inelastic collisions are almost solely responsible for the energy loss of heavy particles (particles heavier than the electron). In these collisions, energy is transferred from the particle to the atom causing an ionization or excitation of the latter. The generalized Bethe-Block formula [49] gives an expression for the energy loss per length of any charged particle in a given material

$$-\frac{dE}{dx} = z^2 M f(\beta), \tag{3.80}$$

where z is the charge of incident particle, M is the mass of the charged particle, and $f(\beta)$ is a function of the particle velocity. Thus the energy loss in any given material is dependent only on the mass, charge, and the velocity of the particle.

Charged particle detection systems like the Microball and HyBall use the scintillation properties of the CsI crystals to detect light charged particles emitted in fusion evaporation reactions or fragmentation reactions. CsI is an inorganic material, and when doped with some impurities like thallium iodide, called activators, it can emit visible photons when it absorbs energy from an incident charged particle. The light output of CsI can then be detected and amplified by photodiodes attached to the body of the CsI crystals. The advantage of inorganic crystals lies in their greater stopping power due to their higher density and higher atomic number. Among all the scintillators, CsI also gives one of the highest light outputs, which results in better energy resolution. A most useful property of CsI is its various decay times for different exciting particles. Pulse shape discrimination techniques can therefore be used to differentiate among various types of particles. Particularly clean separation can be achieved between charged particles such as protons and alphas. The Microball and HyBall are two CsI array detectors which have been used in conjunction with Gammasphere and CLARION, respectively, for two of the experiments described in this thesis. Their properties and detection capabilities are described in short below.

The Microball and HyBall

At one time, γ-ray spectroscopy in the very neutron-deficient nuclei of the mass 130 region was incredibly difficult due to the wide variety of charged-particle evaporation channels available to the compound nucleus. However, when small compact arrays of charged particle detectors, like the Washington University Microball, is used in conjunction with Gammasphere, this problem has been turned into an asset. By correlating γ rays detected in Gammasphere with protons and alphas detected in the Microball, the transitions may be associated with charged-particle emission channels. Thus, as many as twenty different nuclei may be studied from one experiment. In addition, charged particle arrays like Microball and HyBall allow kinematic reconstruction of the recoil momentum, and thus, event-by-event correction of the gamma-ray spectra for Doppler broadening introduced by particle emission.

The Microball is a highly-efficient charged-particle detection system designed to be used in conjunction with Gammasphere as seen in Fig. 3.10. The detector array consists of a 4π arrangement of CsI(TI) scintillators in the shape of a portion of a cone such that a large number of CsI crystals can be packed in a closed (ellipsoidal) geometry around the target. The scintillator crystals are arranged in 9 rings to cover the angular range from $4° - 172°$. Each CsI crystal is coupled to a Si photodiode for scintillation light readout. CsI was chosen as the Microball detector material since it satisfies several criteria:

(1) Good charged particle identification (PID).

(2) Large solid angle coverage for good channel identification. This requirement is important when a weak channel such as (HI,p2n) needs to be selected in the presence of a much stronger channels like (HI,3p).

(3) Small total mass to minimize degradation of the peak-to-total ratio of the Gammasphere Ge detectors.

(4) Excellent gain stability with counting rate, temperature, and time. Reasonably good energy resolution.

(5) Adequate Segmentation. This allows the device to keep up with the high event rate of Gammasphere.

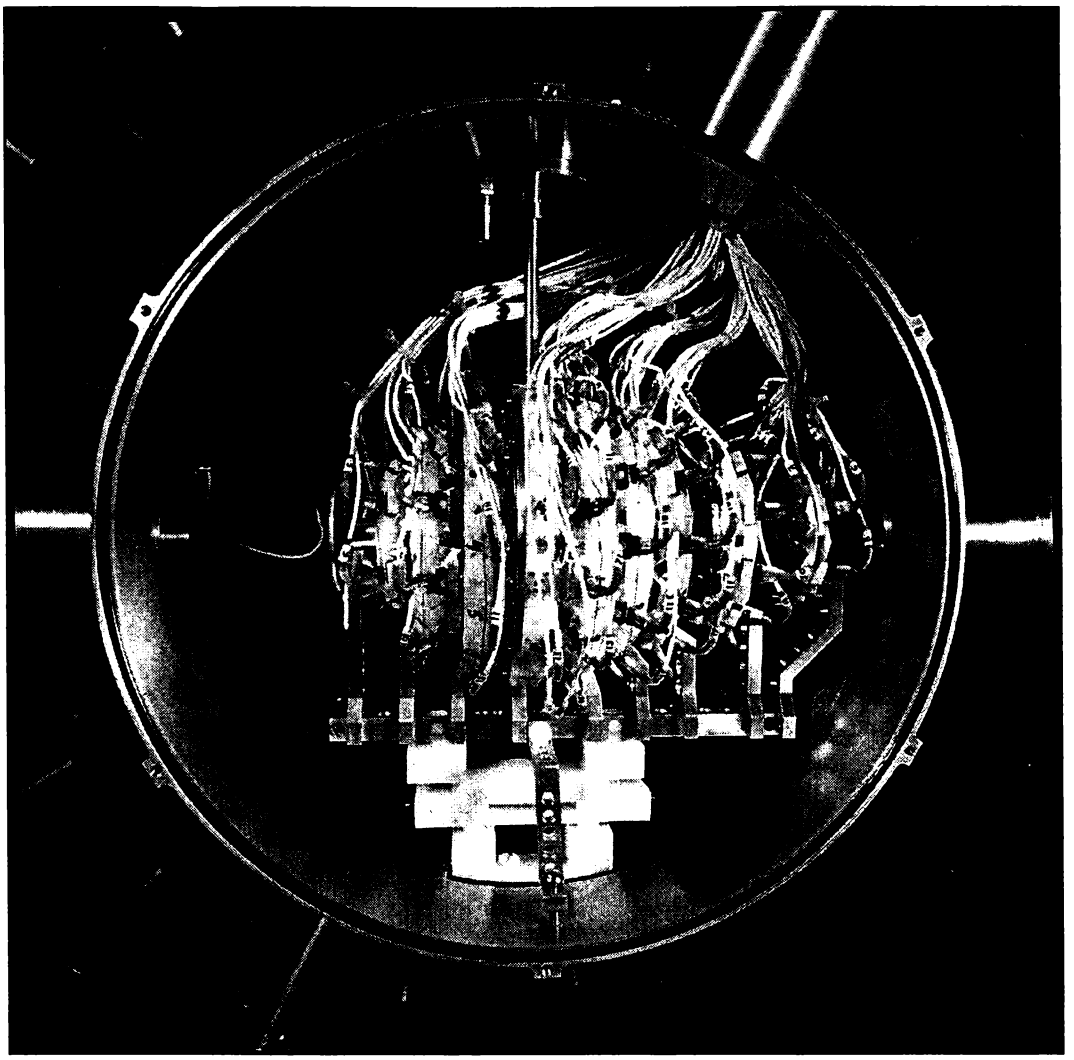


Figure 3.10: Close-up photograph of the Micoball installed in Gammasphere target chamber. The Microball detectors are supported by thin Derlin rings which are held by Aluminum legs. The supporting structure allowing 9 degrees of freedom (rotations and translations) is used to align the device to the chamber and the beam axis. The detectors are held by rectangular blocks that hold the two leads of the photodiode. The signal cables are thin shielded coaxial cables (75 Ω) with Teflon insulation and connect the diodes to their preamplifiers located outside the vacuum. Ring 6 is located at exactly 90° and it has an opening to allow the target to be inserted in position.

Table 3.2: Properties of Microball

Number of CsI detectors	95
Angular coverage	$\sim 97\%$ of 4π
	angular range from $(4 - 172)^\circ$
Maximum counting rate	~ 4500 counts/s per CsI detector
Energy resolution	$\sim 2.7\%$ for 8.78 MeV α's
Overall particle detection efficiency	~ 0.89

(6) CsI can be packed in small geometry to fit inside the target chamber of Gammasphere.

A summary of the characteristic parameters of the Microball is shown in Table 3.2. The most important feature of the Microball is its ability to distinguish charged particles. The signal generated by a charged particle stopped in a Microball detector has two decay components, a fast and a slow one. The first component typically has an amplitude and decay time, $\tau = 0.4 - 1.0\ \mu s$, that is dependent on the type of charged particle stopped by the detector. The second component has decay time, $\tau \sim 7\ \mu s$, independent of particle type. The ratio of these two components uniquely characterizes the type of charged particle or its PID. For the purpose of spectroscopy, it is important to recognize that for each reaction there is a distribution of cross sections in the various channels. If the channel of interest has a smaller production cross section than other channels with more charged particles, then one should be concerned with the fact that there is always a probability that one or more charged particles pass undetected and hence the correlated γ rays are associated with exit channels that has a lower charge particle number. For example, when three protons are emitted and two are detected, the event will then appear as a two proton event. This effect was clearly seen in our Gammasphere experiment where large intensity γ-ray transitions from ^{129}Pr and ^{128}Ce in the $3p$ and $4p$ channels, respectively, appeared in the $2p$-correlated γ-ray projection.

The effective detection efficiency of the Microball (for either protons or alphas) for a given reaction can be extracted using the statistics of strong γ-ray transitions (detected by Gammasphere) that belong to a certain charged-particle exit channel. For example, in our Gammasphere experiment, the ratio of γ-ray counts under the 238-keV transition in ^{129}Pr $\pi h_{11/2}$ band was measured in the $2p$ channel and the $3p$ channels, respectively. ^{129}Pr is created in the $3p$ evaporation channel, but is also observed as one of the strongest contaminants in the $2p$ channel, which was our channel of interest. The ratio of counts under this peak in the two channels was found to be $R_{(\frac{3p}{2p})} \sim 1.2$. Since the protons are indistinguishable Fermionic particles, one can use the following formula [50] to deduce the Microball efficiency for detecting protons ε_p

$$R_{(\frac{yp}{xp})} = \frac{\varepsilon^x}{\varepsilon^y(1-\varepsilon)^{(x-y)}(\frac{x!}{y!(x-y)!})}, \tag{3.81}$$

where xp represent the intensity of γ-rays detected for a given transition in the x-proton channel, y is the actual proton channel that the γ ray originated from, and ε^x is the detection efficiency of the Microball for the x channel. Using Eq. 3.81, a proton efficiency value $\varepsilon_p \sim 0.71$ was found for the Microball, which is smaller than the expected Microball efficiency ($\epsilon_p \sim 0.78$). However, some Microball events were lost in the experiment due to functional problems with the Fragment Mass Analyzer (FMA) at ANL which consequently affected the Microball data stream written to tape. Thus, the efficiency for detecting protons was artificially reduced.

The Hybrid-4-π (HyBall) array of 95 CsI detectors is very similar in its function and construction geometry to the Microball. It is operated as an inner ball inside the CLARION array at ORNL. Its use with CLARION and RMS allows excellent channel selection by simultaneous detection of light-charged particles emitted in heavy-ion-fusion-evaporation reactions with γ's and recoils. The HyBall is housed in an aluminum target chamber with a forward funnel which can also accommodate the microstrip-Si-detector for proton-alpha discrimination.

3.2.4 Mass Spectroscopy with the Recoil Mass Spectrometer

The Recoil Mass Spectrometer (RMS) is a zero degree device used to separate masses produced in nuclear reactions. The spectrometer is 25 m long and is comprised of a momentum separator for beam rejection and the traditional electric-magnetic-electric dipole mass separator. The most striking physical difference between the RMS and other mass spectrometers is the large size of the dipole elements in the mass separator. The large electric dipole radius of curvature (6 m) gives the RMS a much higher electrical rigidity than the other machines without increasing the electric field for the dipoles (the RMS can accommodate recoils with an electrical rigidity up to 15 MeV/Q). The RMS has acceptances of $\pm$ 10% in recoil ion energy and $\pm$ 5% in mass-to-charge ratio A/Q. There are two primary functions of the RMS:
(1) Separate the recoils leaving the target according to their mass-to-charge ratio A/Q. The location where this spatial dispersion of recoils into groups by A/Q is called the "focal plane".
(2) Prevent the beam particles that pass through the target without reaction from scattering into the focal plane where the recoils are separated.

An extremely useful feature of a recoil mass spectrometer is the short time scale on which it operates after the nuclei are generated in the target. This time scale is determined by the time-of-flight of recoils through the system, typically on the order of 1 or 2 μs. This feature means that the mass identification it provides can be applied to the study of very-short lived nuclei. Furthermore, this short time scale means that it is possible to preserve correlations between prompt events observed at the target and decay events occurring at the focal plane within a few μs. These timing advantages are not available in on-line isotope separators because of the time delay involved in extracting the nuclei produced in the thick target. A schematic sketch of the RMS is shown in Fig. 3.11. The A/Q separation and beam suppression capabilities alone offered by recoil mass spectrometers cannot provide the high channel selectivity necessary for studying nuclei very far from stability with production cross-sections lower than around 100 μb. This high sensitivity comes from the detector systems used

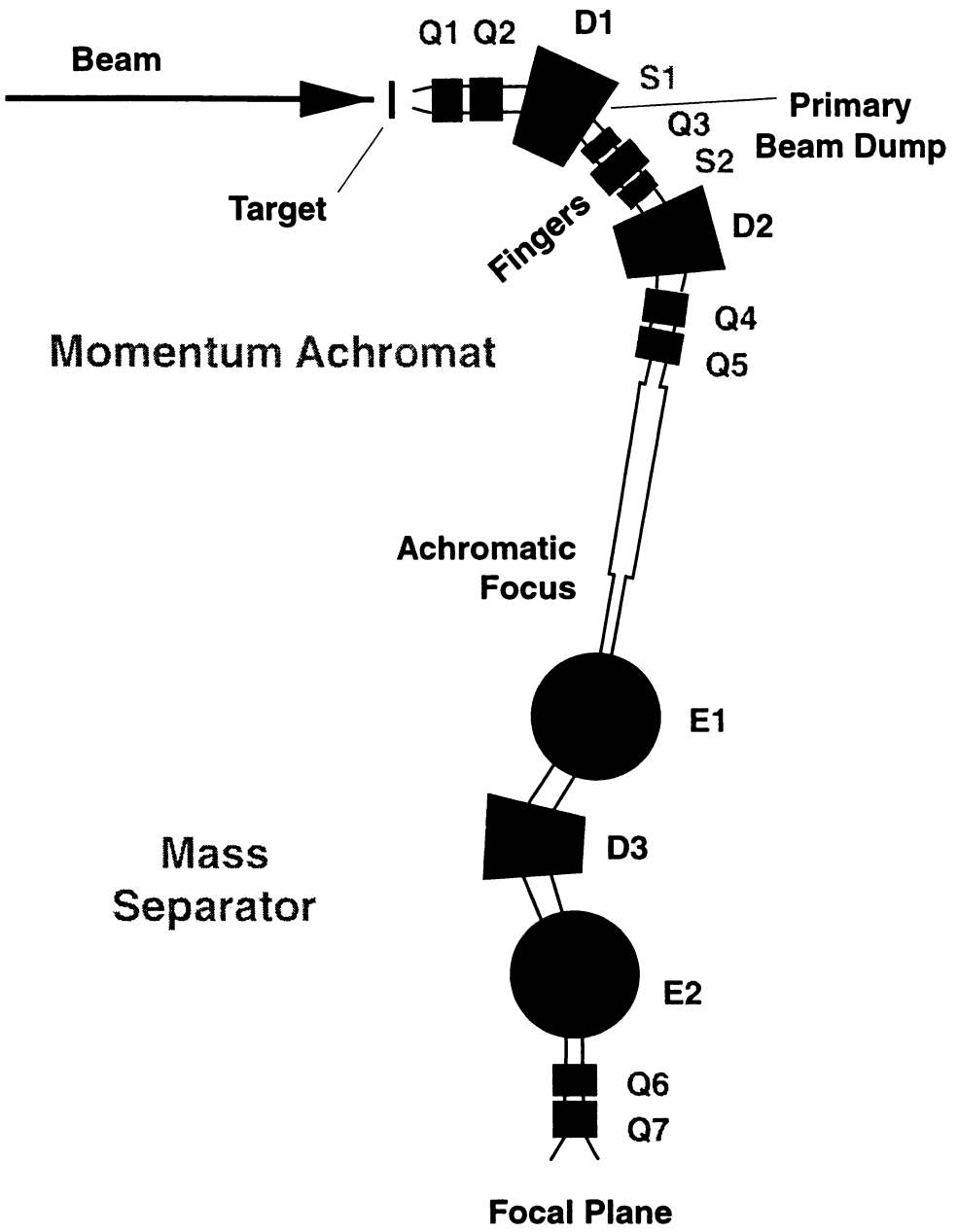


Figure 3.11: A schematic view of the HRIBF Recoil Mass Spectrometer. The beam enters the target shown at the top of the figure from the left. The recoils are dispersed according to their charge-to-mass ratio A/Q at the focal plane. The device consists of two electric dipoles (E1 and E2), three magnetic dipoles (D1-D3), seven magnetic quadrupoles (Q1-Q7), and two magnetic sextuploes (S1 and S2).

together with these devices. One such a device is the Position Sensitive Avalanche Counter, or PSAC for short, located at the RMS focal plane and is introduced briefly below.

The Position Sensitive Avalanche Counter

The Position Sensitive Avalanche Counter (PSAC) is housed in a chamber which is bolted into the larger focal plane housing (see Fig. 3.11). This detector provides mass identification of the spatially separated recoil products and arrival time information for the recoils. The PSAC has a 36×10 cm active area consisting of four wire planes which are stacked as closely as possible in order to provide a more uniform electric field and to minimize the gas volume. All wires are 20 micron gold-plated tungsten separated by 2 mm. Isobutane is constantly circulated through the chamber at a pressure of 3 torr. Although at such pressures the energy loss signal of the ion is expected to be small, these signals may be used to discriminate between the recoils of interest and any scattered beam which may somehow survive the RMS and strike the PSAC. Spatial sensitivity is achieved through time delays of signals from two of the wire planes called the X and Y plane. The signals are taken from both ends of the active area and the time difference between the signals is related to the position of the transversing ion. This arrangement of the detector enables it to handle higher counting rates and a transmission rate of $\sim 90\%$, and thus allowing the recoils to pass on to other detectors placed downstream.

3.3 Electronics and Data Acquisition Systems

3.3.1 Concept of Coincidence

Fusion evaporation reactions are characterized by the emission of copious number of γ rays. High-spin physicists are only interested in coincidence relations between different γ rays rather than detecting uncorrelated "single" γ-ray emissions. Therefore, the coincidence technique between two or more Ge detectors was devised to observe useful correlated events which greatly reduce the background in γ-ray spectra due

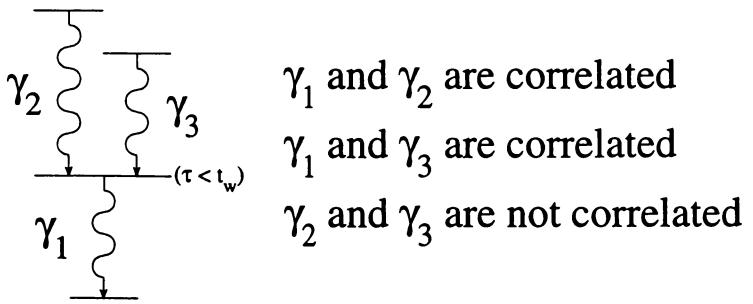


Figure 3.12: Schematic decay scheme illustrating correlated γ decays. The lifetime (τ) of the middle energy level is much less than the coincidence time window (t_w) of the detectors observing decay.

to random uncorrelated events. Fig. 3.12 illustrates the coincidence concept between three different γ rays. Each level shown in Fig. 3.12 has a half-life which is usually shorter than the coincidence gate used for the detectors in coincidence. By choosing a time window (t_w) greater than τ for the middle level, two detectors will observe γ_1 and γ_2 to occur in coincidence, likewise for γ_1 and γ_3. Since γ_2 and γ_3 are not correlated, observation of a coincidence between these two would be a random occurrence. By choosing t_w to be small enough (*e.g.* $\sim$ 50 ns), the random coincidence of γ_2 and γ_3 would be far less frequent than the correlated coincidences. After many decays, the γ_1-γ_2 and γ_1-γ_3 correlations will appear greatly enhanced over γ_2-γ_3 coincidences.

3.3.2 Compton-Suppression Electronics

The initial advance in the spectroscopy of high-spin states was taken at the Niels Bohr institute in the late 1970's when several Ge(Li) detectors were used in coincidence. Indeed, by using just two Ge(Li) detectors the phenomenon of back-bending (spin $\sim 15\hbar$) was discovered, and by using four detectors Riedinger *et al.* [56] established the detailed quasiparticle structure of ^{160,161}Yb up to spin 30 $\hbar$. Fig. 3.13 shows a schematic of a simple setup for two Ge detectors in coincidence with no suppression. The basic technique is to convert the analog signal from the detectors into a logic signal and then to send these pulses to a coincidence module. From the description of the circuit, it can bee seen that a coincidence output signal is produced if any part of the two incoming signals overlap. (This is the ideal case, of course. In a real circuit,

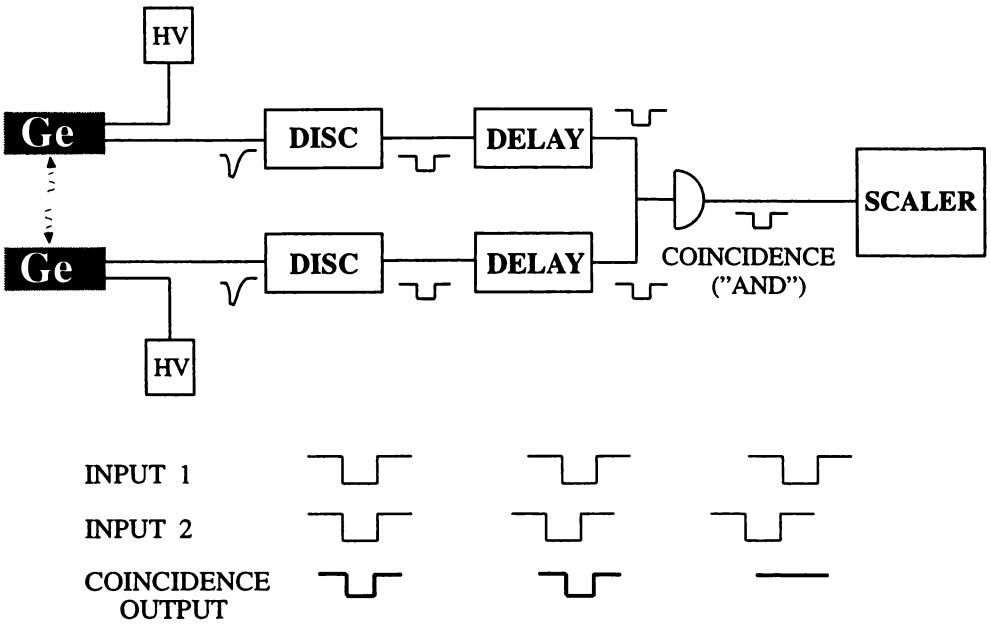


Figure 3.13: A simple coincidence circuit for two non-suppressed Ge detectors.

there is generally a minimum overlap necessary before it can be recognized as such. For the purpose of discussion, however, we will consider the coincidence circuit as ideal). Thus all pulses arriving within a time equal to the sum of the their widths are registered as coincident. Fig. 3.13 shows some examples of coincident and non-coincident pulses. In order for this setup to work, however, it is necessary that the electrical path of each branch leading to the coincidence module be of equal length. This can be ensured by adding adjustable delays to each line, as shown in Fig. 3.13. In principle, only a delay is needed on the faster branch, however, one on each branch provides a bit more flexibility when adjusting the circuit.

Although early coincidence experiments provided exceptional results, a major experimental problem remained; namely that of a poor peak-to-background ratio caused by incomplete energy collection in the Ge detector. Most of the counts ($\sim$ 75%) form a continuous background at lower energies caused mainly by γ rays Compton scattering out of the Ge crystal. The solution is to detect this scattered radiation in a surrounding detector (an escape-suppression shield) and to reject coincidence events between the Ge detector and the shield. A typical design for a Compton-suppression

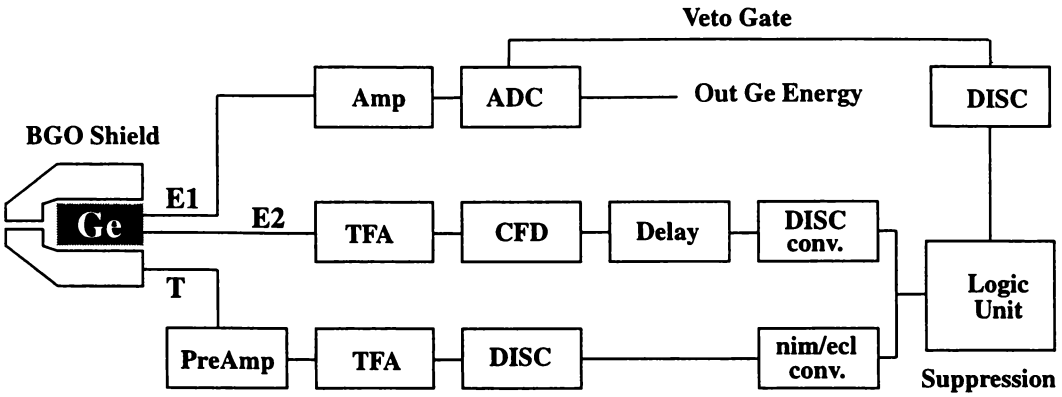


Figure 3.14: The schematics of a sample Compton-suppression setup of a single Ge detector with BGO shield.

setup is that shown in Fig. 3.14.

When an incident γ ray is completely absorbed in the Ge crystal, a detection signal is generated and split into two identical signals E1 and E2 for further processing (see Fig. 3.14). If a γ ray is completely absorbed in the BGO shield, then only one signal is generated (labeled T). However, when a γ ray is scattered between the two detector materials, then three signals E1, E2, and T are generated. The purpose of the circuit in Fig. 3.14 is to extract the timing and energy information of a "good" event (*i.e.* the γ ray is fully absorbed in the Ge crystal) and reject other events. The signal pulse generated in the Ge detector are characterized by a rise time (the time the event occurs), and energy (proportional to the area under the pulse).

For a bad event, the T signal from BGO is passed to a Time Filter Amplifier (TFA) which processes the rise time of the signal by quick amplification. The signal is then passed to a Constant Fraction Discriminator (DISC) which generate a logic signal with a width that is proportional to the rise time of the signal. The E2 signal from the Ge detector passes first through a TFA and then through a discriminator (CFD). The CFD generates a logic signal similar to a DISC, but is more suitable for handling Ge signals compared with BGO signals, as the latter need only simple discrimination due to their very fast rise time. The width of the CFD or DISC logic signal represent the "time window" of an event. E2 and T signals are then passed to a logic unit where their widths are compared. If the E2 signal time window falls in

the T signal time window then a "veto" signal is generated in the logic unit. This veto signal is then sent to the Analog to Digital converter (ADC) unit which stops the processing of the "energy" signal E1 (*i.e.* no event is written to tape). For a good event, no veto signal is generated and both timing and energy information of the event from E2 and E1 signal, respectively, are written to tape.

One should bear in mind that the electronic setup of multi-detector arrays is composed of multiplets of the Compton-suppression circuit shown in Fig. 3.14 with more sophisticated suppression and trigger system units.

3.3.3 Data Acquisition and Sorting

The function of a data acquisition system is complicated as it requires an integration of hardware and software components through an interface, usually CAMAC based. The analog energy and time signals from the detectors are handled by the NIM electronics first, then it is sent in logic format to a CAMAC event handler that performs low-level software manipulation of the data. The "processed" data are then sent to workstations for analysis and storage. Whether a given event is accepted is determined in the master gate (see output of logic unit in Fig. 3.14). The master gate can be programmed to trigger a good event based on a given condition of the input parameters. For example, in our ORNL experiment, the trigger condition was γ-γ-recoil which requires at least two Ge detectors in prompt coincidence with a recoil signal from the PSAC. For a good event, the ADC's (Analog to Digital Converters) and TDC's (Time to Digital Converters) are triggered to digitize the input signal, and the "event" logic pulse is sent to the event handler.

A typical event will contain information about the detectors that fired in coincidence. The event also contains information about the energy, time and any coincident events from auxiliary detectors like the Microball. To examine correlations between detectors, the event must be properly decoded and incremented into a format useful for analysis. There are many program packages available for handling event data and make it available for the user to manipulate as desired. The tape scanning package that was used for the analysis presented in this thesis was TSCAN [57]. The

TSCAN program will typically read data from magnetic tape and pass it to a function that is user defined. It is in this user defined function that the event is decoded and sorted.

3.4 Offline Data Analysis

This sections briefly introduces the analysis process of the experimental data that leads to the ultimate goal of any high-spin spectroscopy experiment: establishing a level scheme of the nucleus of interest. The analysis procedure starts by scanning the raw data tapes, followed by energy and efficiency calibration of the Ge detectors, and ends with building a coincidence cube or matrix. Several software packages and scanning routines are implemented at each level of the analysis process. The function and use of these software packages are also briefly described.

3.4.1 Charged Particle Data Analysis

The combination of light charged particles like the Microball and HyBall with large detector arrays like Gammasphere and CLARION, respectively, has considerable power for isolating and studying nuclei far from stability. This is achieved through channel enhancement by detecting emitted charged particles in heavy-ion reaction experiments. The basic strategy used to analyze charged-particle events involves the removal (gating out) events from electrons and γ-rays detected by the CsI crystals, while keeping the events due to protons and alphas.

The raw data tapes are scanned and 2-dimensional histograms of charged-particle events correlated with γ-ray events are constructed for each of the CSI detectors. These 2-dimensional histograms can be constructed in any of these forms: energy versus PID, energy versus time, and Ratio (energy/PID) versus time. Fig. 3.15 shows a plot of energy (E) versus PID for one of the forward HyBall detectors used in the ORNL experiment. The vertical and horizontal axes are *proportional* to the CsI energy and PID signals, respectively. One may observe that several distinct count regions appear in the 2-dimensional map. The lowest energy and PID counts correspond to random uncorrelated signals from x-rays and electrons. The next region of

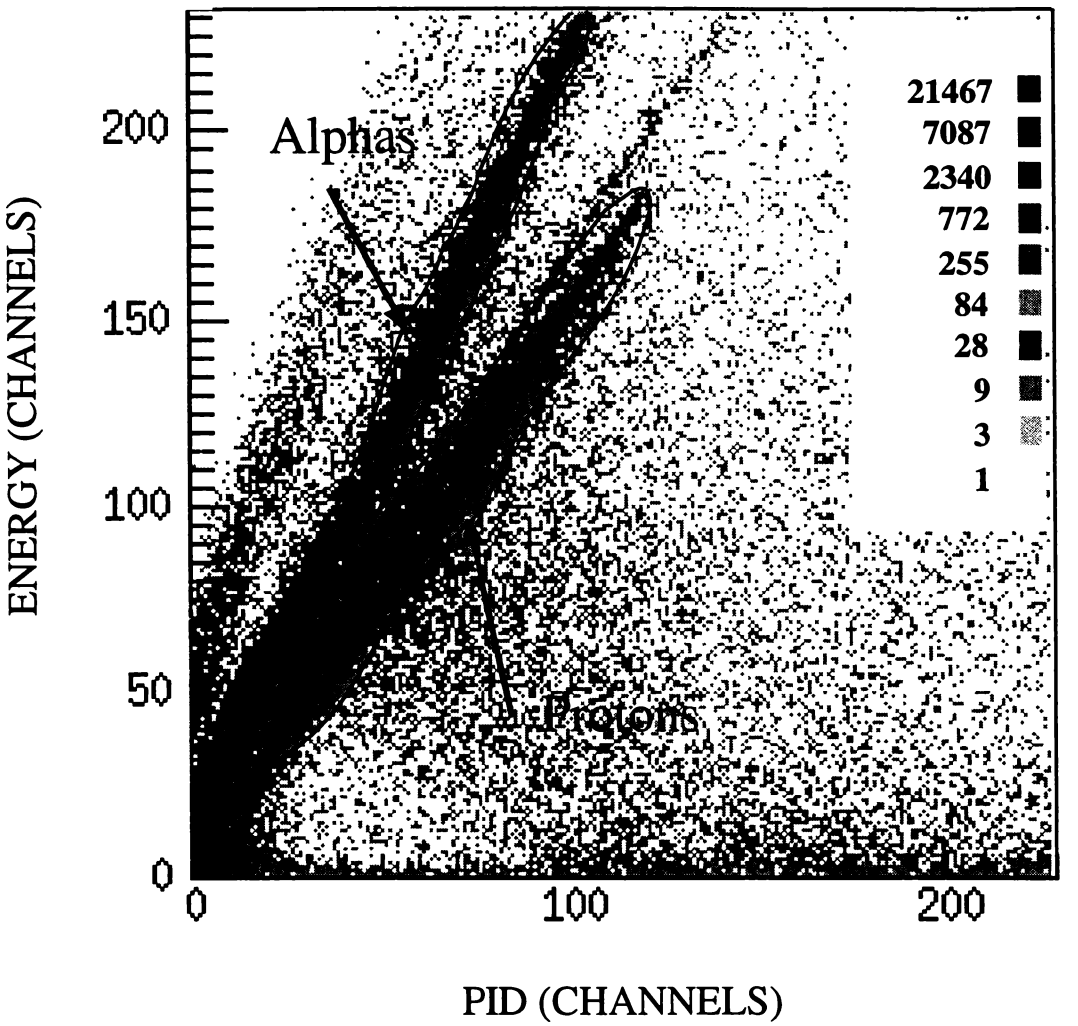


Figure 3.15: Energy versus particle identification ratio (PID) for one CSI detector in the forward ring of the HyBall. Alphas and protons are concentrated in well-separated count regions.

significant counts has roughly a shape of an elongated cigar which is due to detected protons that are in coincidence with γ-ray events. The next region of significant counts lies higher in energy to the proton region and represents detected alpha particles in coincidence with γ-ray events. It is apparent from this map that one can cleanly separate useful events due to protons or alpha's both by energy and PID. Free-form "banana" gates can be drawn by hand around these regions. The data are then sorted again and γ-ray events which are in coincidence with the charged-particle events within the banana-gated regions are histogrammed in matrices or cubes (see next section). One should be careful in making the banana-gates as tight as possible around the region of interest, but large enough to to include as many charged particle events as possible to maximize statistics. This procedure was performed for *all* of the Microball and HyBall detectors in ANL and ORNL experiments, respectively.

It is worth mentioning the energy calibration procedure of CsI detectors. Energy calibration for protons and alphas is different due to their different interaction strengths in the CsI crystal and absorbers. For protons, a linear equation of the form $E_p = A + Bx$ is used to determine the energy of protons, where x is the channel number. A and B are the calibration constants and represent the offset and gain, respectively. The α energy in CsI(Tl) for a given channel is given in terms of the proton energy in MeV for that channel

$$E_\alpha = aE_p + b\ln(1 + cE_p). \tag{3.82}$$

For our Gammasphere run, the parameters in Eq. 3.82 had the following values, a =0.93, b =1.29, c =2.59 [58]. For protons, two data points (energy peak positions) must be measured for each CsI detector. For alphas, only one data point is sufficient to find the calibration parameters.

3.4.2 Ge γ-ray Data Analysis

Energy and Efficiency Calibration of Ge Detectors

Ge detectors are generally expected to maintain a linear relationship between the energy deposited in the detector and the signal generated accordingly. Because of the

unique characteristics of the detectors and the electronic setup, the devices must be calibrated to determine this linear relationship. Electronics, namely the ADC's, are designed to produce a linear output such that $E = A + Bx$, where E is the height of the input pulse, x is the channel number, and A and B are constants which can be determined from common calibration standard spectra of the ^{152}Eu and ^{182}Ta sources. The x-ray and γ-ray energies of both these sources cover a wide energy range (57.5 keV in ^{182}Ta to 1408.0 keV in ^{152}Eu). The relative intensities of these energies are found in the Table of Isotopes [59]. Fig. 3.16 shows the spectra from both sources using all Gammasphere detectors in the setup of the ANL experiment.

The response of Ge detectors to fully absorbed γ rays varies with the γ-ray energy in a non-linear fashion. By fitting the intensities of the universally accepted γ transitions in the ^{152}Eu and ^{182}Ta, Radford [60] created a relative efficiency curve as seen in Fig. 3.17 so that peaks with similar energies from both sources are normalized to the same intensity. For the Ge detectors used in the Gammasphere experiment, Fig. 3.17 shows that the maximum efficiencies for these detectors occurs at $\sim$ 200-keV. The EFFIT program included with the Radware [60] software package, uses the following parameterization to fit the data:

$$\ln(\varepsilon) = \left\{ \left(A + Bx + Cx^2\right)^{-G} + \left(D + Ey + Fy^2\right)^{-G} \right\}^{-1/G} \tag{3.83}$$
$$x = \ln(E_\gamma/100),$$
$$y = \ln(E_\gamma/1000),$$

where ε is the efficiency , and the γ-ray energy E_γ is in keV. The first (second) term in parenthesis on the right hand side of Eq. 3.83 models the low (high) energy behavior of the Ge efficiency. The parameter G determines the shape of the turn-over region between the high and low energy efficiency curves. Fig. 3.17 shows the fit applied to data points from ^{152}Eu and ^{182}Ta sources in our Gammasphere experiment. The values of the parameters in Eq. 3.83 resulting from a fit to these data are, from A to G; 4.5, 7.0, -1.0, 6.0, -0.7, 0.0, 3.0.

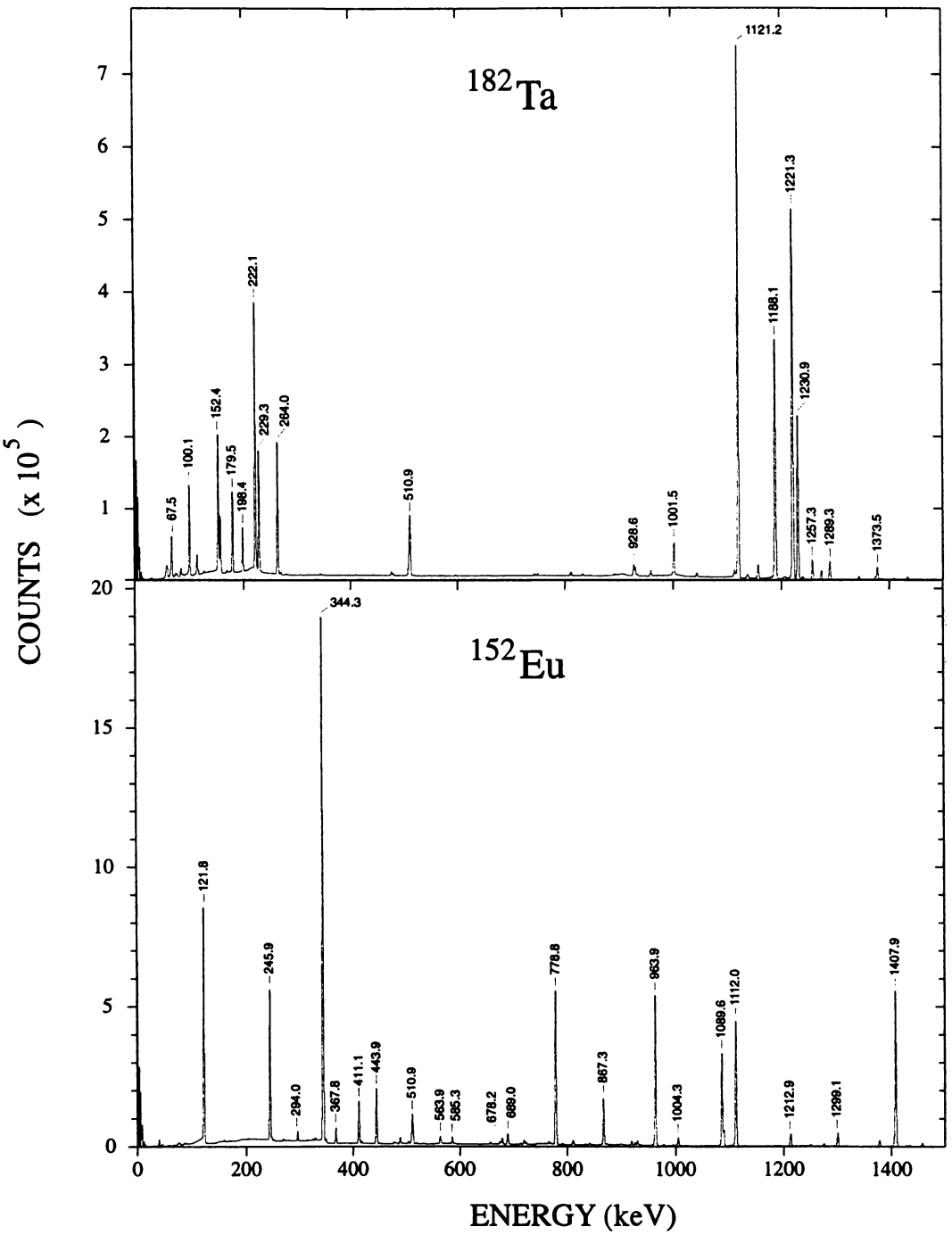


Figure 3.16: Calibration Spectra of ^{182}Ta and ^{152}Eu. Spectra for both sources are the sum of all Gammasphere Ge detectors singles spectra. The peak at 511 keV, observed in both spectra, is due to γ rays created from electron-positron annihilation.

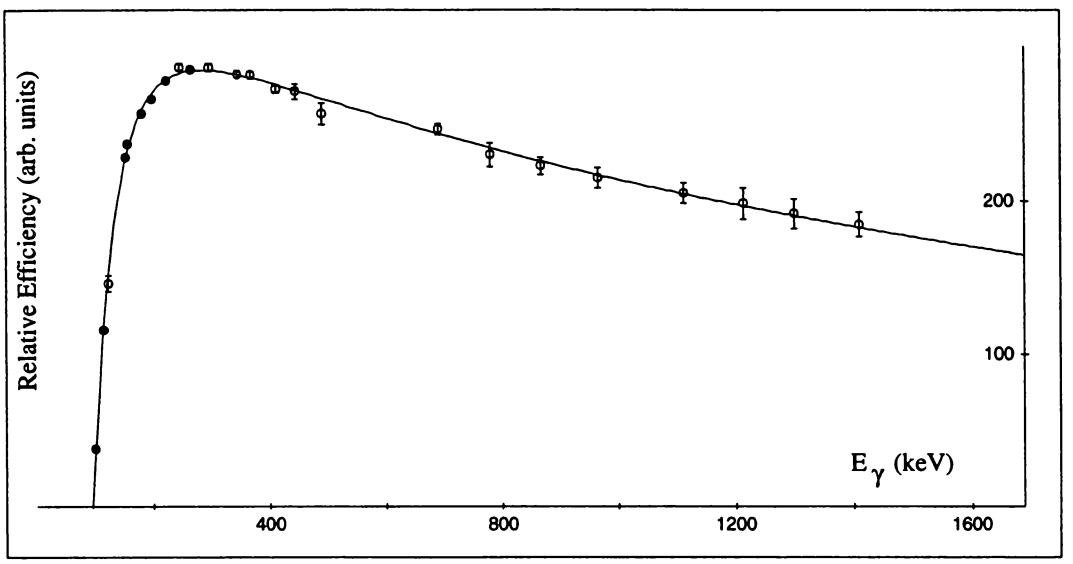


Figure 3.17: Efficiency calibration curve of Gammasphere detectors. The data points are taken from the ^{152}Eu and ^{182}Ta source spectra generated by all Ge detectors of Gammasphere. Data points with filled circles are taken from the ^{182}Ta source and open circle data points are taken from the ^{152}Eu source. Also shown is the efficiency function $\varepsilon(E_\gamma)$, fit to the data.

Building Matrices and Cubes

The data taken in our experiments were written to tape and scanned using the sorting routine TSCAN developed at Oak Ridge National Laboratory, University of Tennessee, and Rutgers University. For the analysis of prompt γ-decay cascades, the most common histograms are created by sorting γ-γ events into a two-dimensional energy spectrum (matrix). For example, when two γ rays γ_1 and γ_2 are detected simultaneously in a given event, then two histogram cells are incremented in the following way: (row, column) = (γ_1, γ_2) and (row, column) = (γ_2, γ_1). Therefore, scanning 2-fold γ-ray events using the previous procedure, results in a symmetric γ-ray matrix. An event containing three γ rays would be resolved into three pairs ([γ_1, γ_2], [γ_1, γ_3], and [γ_2, γ_3]), and so on. If the nucleus of interest is formed in a charged-particle exit channel of a fusion evaporation reaction, then the use of charged-particle detectors to associate the emitted γ-rays with the corresponding charged-particle exit channel is essential. In this case, *all* γ-ray events sorted into matrices or cubes are essentially correlated with the emission of the charged-particle channel of interest. Large detector arrays, such as Gammasphere, have so many detectors that three and higher-fold Ge coincidences are common. In this case, cubes (3-D histograms) of γ-γ-γ events are typically created.

The code ESCL8R [60] was used to analyze the γ-γ matrices from our three high-spin experiments. The code automatically keeps track of energy calibrations, efficiencies, and electron conversion coefficients. ESCL8R incorporates the background subtraction algorithm described in Ref. [60]. Once matrices are created, γ-γ coincidence relationships are studied by examining slices of these matrices. Slices, or gates, are created by summing the contents of a set of channels that represent a peak. The resulting one-dimensional histogram is then further analyzed to determine what events occurred in coincidence with the gated γ ray. For a symmetric γ-γ matrix, a gate can be placed on either axis of the matrix at a particular energy. At the gating energy, all counts in matrix channels sharing the same coordinate γ_x are projected on the other axis (y). The width in channels of a given gate, say γ_x for example, depend

on the full width at half maximum (FWHM) of the peak determined by

$$\mathrm{FWHM}(x) = \sqrt{f^2 + g^2\frac{x}{1000} + (h\frac{x}{1000})^2} \tag{3.84}$$

where x is channel number and f is a constant due to noise in the detectors and amplifiers, g is from the statistics of the charge collection process, and h is due to Doppler-broadening of the peaks from the emitted γ-rays of recoiling nuclei. Typical values for the parameters used in the above expression are approximately $f = 3$, $g = 1$, and $h = 4$ for an energy dispersion of 0.5 keV per channel and a recoil velocity of $\sim 2.5\%$ of the speed of light

The higher fold data ($F \geq 3$) from large detector arrays demand a more complex analytical tool than the γ-γ matrix to fully extract all the information provided. For the Gammasphere experiment, the 2p channel data were sorted in a γ-γ-γ cube, which adds an additional axis of correlation. The code LEVIT8R [60] was used to inspect the cube, which is a three dimensional version of ESCL8R and thus works in a similar way. LEVIT8R offers the option of fitting the energies and intensities to a two dimensional projection or directly to the cube. Using an additional γ ray for gating can, in most cases, significantly enhance the resulting gated spectra. This double-gating technique on a given cube works exceptionally well at resolving coincidence relationships when one of the gating γ rays is a multiplet, *i.e.* it appears in two or more bands. Fig 3.18 demonstrates the gating procedure in LEVIT8R on the 2p-cube from the Gammasphere experiment. Notice the tremendous improvement and increased selectivity of double gating compared to single gating which result in producing well-resolved coincidence spectra with no contaminant transitions and with excellent background reduction.

Kinematic Doppler Shift Corrections

In fusion evaporation reactions, the recoil nuclei travel away from the target with non-negligible velocities. In our Gammasphere experiment, for example, the emitted nucleus ^{128}Nd from the reaction ^{92}Mo(^{40}Ca,2p2n) at beam energy of 184 MeV were estimated to have a recoil velocity of $\beta \sim 0.028$. This β value is input as a parameter

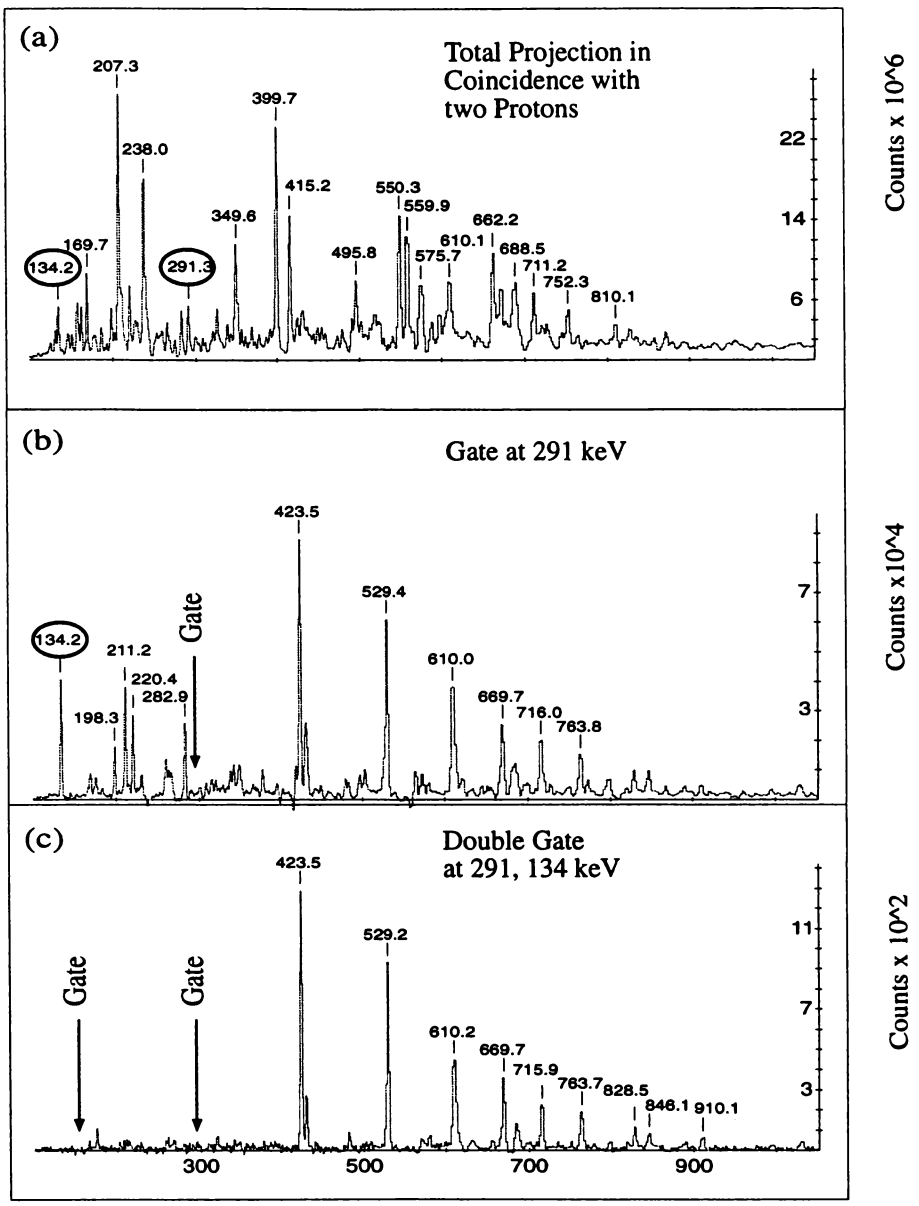


Figure 3.18: The spectrum in panel (a) show the total projection generated by LEVIT8R on the 2p-cube from Gammasphere experiment. Spectrum (b) shows a gate on the 291-keV γ-ray transition which belong to the ground-state band of ^{128}Nd. Spectrum (c) is the result of simultaneously double gating on the 134- and 291-keV transitions. All the labeled peaks in panel (c) belong to the ground state of ^{129}Nd.

in the sorting program which in turn calculates the correct γ-ray energies using the typical recoil correction

$$E_\gamma = E_{\gamma[Ge]}\,(1 + \beta \cos\theta)^{-1}\,, \tag{3.85}$$

where $E_{\gamma[Ge]}$ is the energy of a γ ray reported by a Ge detector located at an angle θ, relative to the beam axis. From the previous formula one can see that the Doppler correction increases with increasing γ-ray energies which limits the ability to identify higher energy transitions for a given γ-ray sequence due to large broadening in the peaks.

Determination of γ-ray Multipolarity

The use of large detector arrays allows one to measure γ-γ correlations and to determine spins and multipolarities of transitions. This is possible due to the different geometrical locations of the Ge detectors. A method based on the observation of Directional Correlations of deexciting states (DCO ratios) was adopted to determine the γ-ray multipolarities and spins of nuclear levels. The theory of DCO ratios is well developed and described in detail by Krane *et al.* [61]. The method of deducing the DCO ratios is described in Refs. [62, 63]. The angular correlation of γ rays emitted from oriented states depends on the spins of the levels, the multipolarities, mixing ratios of the γ transitions, and the m-substate population distribution of the initial state. The description of the DCO ratios is simplified in our experimental conditions due to the use of unpolarized beam and the fact that the detectors are insensitive to the polarization of the emitted γ-rays. An immediate consequence of these two experimental factors is that detectors placed at forward and backward angles with respect to the beam axis can be treated equally. This means that we can sum the γ spectra of detectors at the same angle θ and at the complementary angle 180°- θ to increase statistics.

Depending on the detector positions in the array, it is expected that transitions of $M1$ and $E1$ character to possess DCO ratios of $\sim$ 0.5 and $\sim$ 1.0 for $E2$ character transitions (see description of experimental setup in the next three chapters). A stretched $M1$ may have slightly larger DCO ratios (see definition in Chapter

4) if there is sufficient $M1/E2$ mixing. Some care must also be taken when a transition has a DCO value of ~ 1.0 because non-stretched dipoles ($\Delta I = 0$) are expected to have this value also. Since DCO ratios cannot distinguish the difference between $M1$ and $E1$ transitions, a difference in parity between the two connected states cannot be determined. However, very often the parities of the low-spin band members have already been determined. Thus identification of a stretched $E2$ transition allows the parity value of new higher lying in-band members to be continued.

CHAPTER 4

Experimental Results of and Discussion of ^{128}Nd

4.1 Overview

The region of nuclei with $Z \sim 60$, $N \sim 70$, has been predicted to have significant ground-state deformation ($\beta_2 \sim 0.3 - 0.4$) as the neutron Fermi surface is near mid-shell $N = 66$ [1]. Shape coexistence has been observed in the region as highly deformed bands are found in light $A \sim 130$ nuclei [64]. In addition, these neutron-deficient nuclei provide an important means of testing the standard Cranked Shell Model (CSM). The yrast structures of even-even nuclei near $A \sim 130$ show evidence for rotational alignment of $h_{11/2}$ quasiproton pairs at a well-defined rotational frequency in the range $\hbar\omega \sim (0.32 - 0.36)$ MeV, which is well reproduced by the standard cranking calculations. In contrast, the alignment of $h_{11/2}$ quasineutrons generally occurs over a much wider (0.5 to > 0.7 MeV), and higher, frequency range than predicted by the CSM. Possible explanations for these effects are sought in the systematics of these lightest neodymium ($Z = 60$), praseodymium ($Z = 59$), and cerium ($Z = 58$) isotopes. With these perspectives, we have investigated high-spin states in ^{128}Nd which is the lightest Nd nucleus with known excited states. In addition, the presence of octupole correlations is explored in this and other nearby even-even nuclei.

4.2 Experimental Details

In an experiment emphasizing the population of some of the most neutron-deficient nuclei in the $A \sim 130$ region, an 184 MeV ^{40}Ca beam from the ATLAS superconducting linear accelerator at Argonne National Laboratory (ANL) was delivered to a

0.625 mg/cm^2 thick, self-supporting ^{92}Mo target. Prompt γ rays were detected with 99 Compton-suppressed Ge spectrometers in the Gammasphere array [46]. Charged-particle evaporation residues were detected with the 95 CsI detectors of the Washington University Microball [45] array. Approximately 116 million five-fold (γ^5) or higher events were determined to have γ rays in coincidence with two protons (comprising $\sim$ 20% of the total events). These events were sorted into an $E_\gamma \times E_\gamma \times E_\gamma$ cube and were analyzed with the Radware [65] software package. The level scheme for ^{128}Nd from the present data is shown in Fig. 4.1.

Relative spin assignments proposed for the states in ^{128}Nd were determined through directional correlation of oriented states (DCO) analysis. To facilitate this analysis, we created an asymmetric matrix where the energy of γ rays observed in detectors located at $\sim$ 35° and $\sim$ 145° were histogrammed along one axis and coincident γ rays observed in detectors located at $\sim$ 90° were histogrammed along the other axis. DCO ratios were determined by the expression

$$R_{DCO} = \frac{I_{\gamma_1}(\text{at } \sim 35^\circ \text{ or } \sim 145^\circ;\ \text{in coincidence with } \gamma_2 \text{ at } 90^\circ)}{I_{\gamma_1}(\text{at } 90^\circ;\ \text{in coincidence with } \gamma_2 \text{ at } \sim 35^\circ \text{ or } \sim 145^\circ)},$$

where I_{γ_1} is the intensity of the γ ray of interest and γ_2 is a stretched $E2$ ($\Delta I = 2$) transition. With the detectors at the given angles, one expects R_{DCO} values of approximately 0.5 for pure dipole transitions ($M1$ and $E1$) and 1.0 for quadrupole transitions ($E2$). The measured DCO ratios are summarized in Table 4.1 along with the energy, spin, and parity of the states, as well as the energy and relative intensity of the depopulating γ rays. Weak transitions above states of determined spin, where reliable DCO analysis could not be performed, were assigned multipolarities assuming that the rotational behavior of the band persists.

In our Gammasphere experiment, nearly 15 different nuclei were populated with substantial intensity. These nuclei are indicated in Fig. 4.2 by blue stripes. It was expected that reasonable amounts of leak-through products would be present in our channel of interest, namely the $2p$ channel. Because of this leak-through problem, γ rays from nuclei in the $3pxn$ and $4pxn$ channels were observed in our $2p$ sorted data. However, using triplet coincidence gating on the Radware built $E_\gamma \times E_\gamma \times E_\gamma$ cube considerably reduced the contribution from these nuclei.

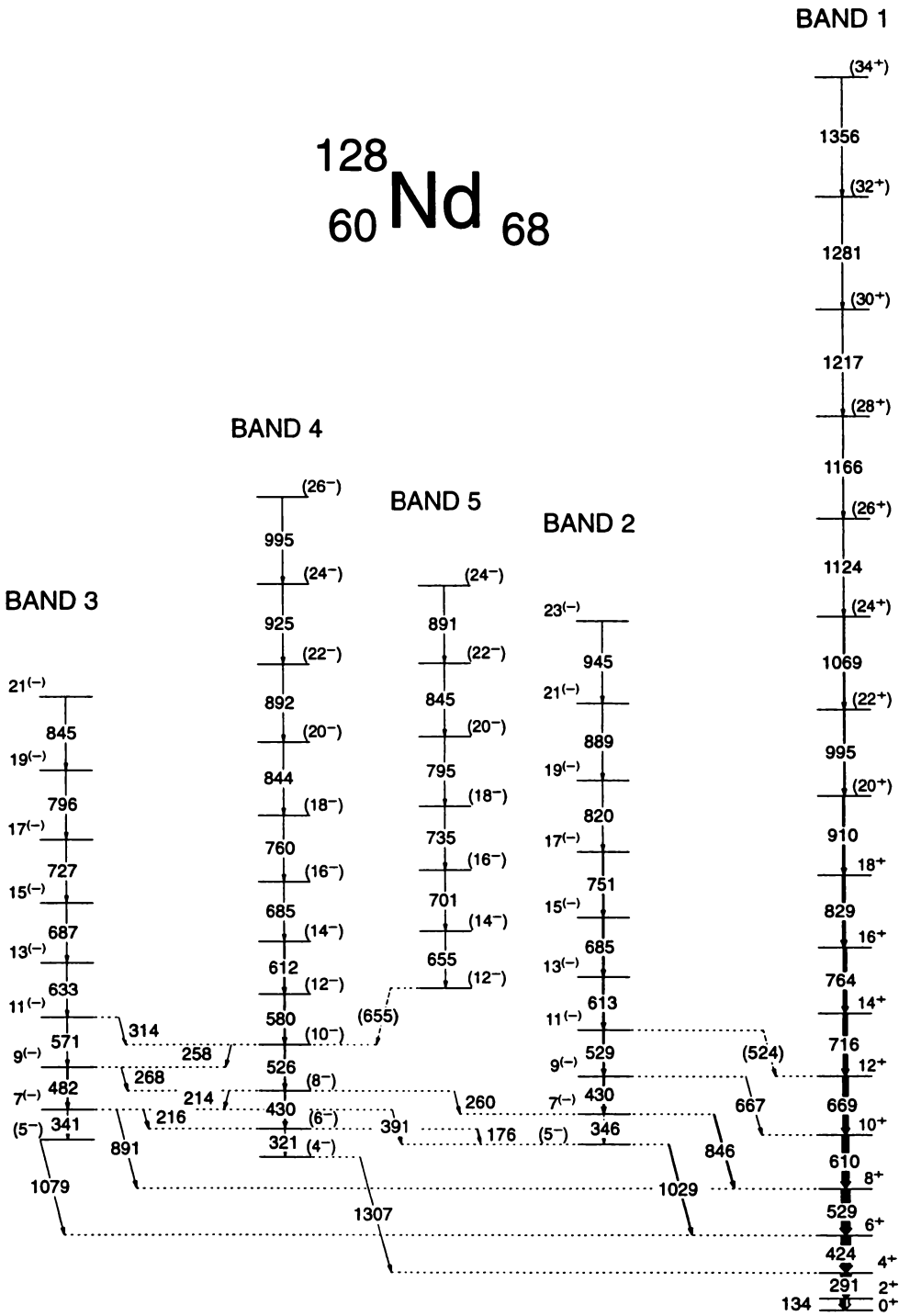


Figure 4.1: The level scheme for ^{129}Nd. The width of the arrows are proportional to the relative intensity of the transition. Tentative transitions are denoted by dashed lines. Spin and parity assignments are explained in the text.

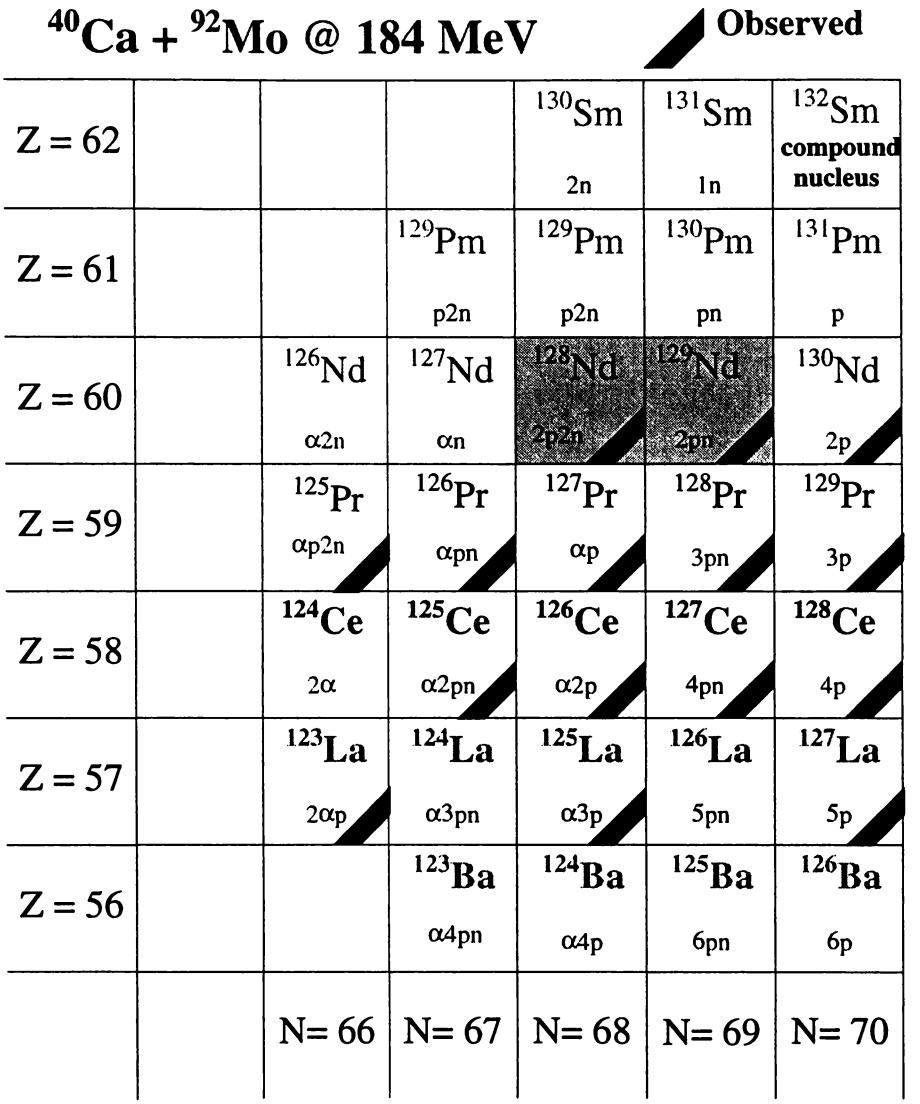


Figure 4.2: Map of the observed and possibly populated nuclei following particle evaporation from the ^{132}Sm compound nucleus. The charged particle channel is given below the isotopic symbol. Nuclei with black stripes were observed in one or more data sets. The gray boxes indicate the nuclei that has been analyzed in the $2pn$ and $2p2n$ channels, respectively.

Table 4.1: Data for levels and gamma rays in ^{128}Nd

$I_i^{\pi\,a}$	E_{level} (keV)	E_γ (keV)^b	$I_\gamma{}^c$	DCO	Multipolarity
		BAND 1			
2^+	133.7	133.7		0.93(7)	$E2$
4^+	425.0	291.3	≡100	0.97(4)	$E2$
6^+	848.5	423.5	96(5)	0.99(4)	$E2$
8^+	1377.9	529.4	85(5)	0.93(4)	$E2$
10^+	1988.0	610.1	67(4)	0.94(9)	$E2$
12^+	2657.4	669.4	53(4)	0.88(4)	$E2$
14^+	3373.4	716.0	40(2)	0.91(5)	$E2$
16^+	4137.2	763.8	32(2)	0.86(6)	$E2$
18^+	4965.9	828.7	26(2)	0.9(1)	$E2$
20^+	5875.7	909.8	15(1)		$E2$
22^+	6870.2	994.5	9(1)		$E2$
24^+	7939.5	1069.3	7.6(9)		$E2$
26^+	9063.0	1123.5	4.2(9)		$E2$
28^+	10229.3	1166.3	4.0(9)		$E2$
30^+	11446.0	1216.7	3.5(8)		$E2$
32^+	12726.7	1280.7	3.5(8)		$E2$
34^+	14083	1356	<3		$E2$
		BAND 2			
(5^-)	1877.5	1029.0	9.0(8)		$E1$
$7^{(-)}$	2224.3	346	<3		$E2$
		846.4	10(1)	0.58(6)	$E1$
$9^{(-)}$	2654.1	429.8	14(1)	0.91(6)	$E2$

Table 4.1 (continued).

$I_i^{\pi\,a}$	E_{level} (keV)	E_γ (keV)^b	$I_\gamma{}^c$	DCO	Multipolarity
		1275	<3		$E1$
		667	<3		$E1$
$11^{(-)}$	3183.3	529.2	13(1)	0.90(8)	$E2$
		523.5	<3		$E1$
$13^{(-)}$	3796.2	612.9	13(2)		$E2$
$15^{(-)}$	4481.3	685.1	11(2)		$E2$
$17^{(-)}$	5232.6	751.3	8(1)		$E2$
$19^{(-)}$	6053.0	820.4	6(1)		$E2$
$21^{(-)}$	6942.3	889.3	4(1)		$E2$
$23^{(-)}$	7888	945	<3		$E2$
		BAND 3			
(5^-)	1927.4	1078.9	<3		$E1$
$7^{(-)}$	2268.3	340.9	3.5(2)		$E2$
		890.8	5.6(7)	0.5(1)	$E1$
		215.6	3.8(7)		$M1/E2$
		391	<3		$E2$
$9^{(-)}$	2750.6	482.3	7(1)	0.98(5)	$E2$
		267.8	3.3(7)		$M1/E2$
$11^{(-)}$	3321.7	571.1	6(1)		$E2$
		314	<3		$M1/E2$
$13^{(-)}$	3954.9	633.2	5(1)		$E2$
$15^{(-)}$	4641.5	686.6	5(1)		$E2$
$17^{(-)}$	5368.6	727.1	4(1)		$E2$
$19^{(-)}$	6165	796	<3		$E2$
$21^{(-)}$	7010	845	<3		$E2$

Table 4.1 (continued).

$I_i^{\pi\,a}$	E_{level} (keV)	E_γ (keV)^b	$I_\gamma{}^c$	DCO	Multipolarity
		BAND 4			
(4^-)	1731.9	1306.9	<3		$E1$
(6^-)	2052.5	320.6	6.0(9)		$E2$
		176.1	7.6(9)	0.62(7)	$M1/E2$
(8^-)	2482.8	430.3	9(1)		$E2$
		259.8	4.6(6)		$M1/E2$
		214.2	3.5(6)		$M1/E2$
(10^-)	3008.8	526.0	8(1)		$E2$
		258	<3		$M1/E2$
(12^-)	3589.1	580.3	8(1)		$E2$
(14^-)	4201.3	612.2	7(1)		$E2$
(16^-)	4886.4	685.1	6(1)		$E2$
(18^-)	5646.2	759.8	4.2(1)		$E2$
(20^-)	6489.8	843.6	3.9(1)		$E2$
(22^-)	7381.8	892.0	4(1)		$E2$
(24^-)	8307	925	<3		$E2$
(26^-)	9302	995	<3		$E2$
		BAND 5			
(12^-)	3664.1	655.3	4(1)		$E1$
(14^-)	4319.1	655.0	4(1)		$E2$
(16^-)	5019.9	700.8	3.5(8)		$E2$
(18^-)	5755	735	<3		$E2$
(20^-)	6552	797	<3		$E2$

Table 4.1 (continued).

$I_i^{\pi\,a}$	E_{level} (keV)	E_γ (keV)^b	$I_\gamma{}^c$	DCO	Multipolarity
(22^-)	7398	846	<3		$E2$
(24^-)	8289	891	<3		$E2$

[a] Spin and parity of the initial state.

[b] Uncertainties in E_γ are 0.2 keV for most transitions except for relatively weak transitions which are 0.5 keV.

[c] Relative intensity of the transition where $I_\gamma(291.3) \equiv 100$.

4.3 The Level Scheme

Prior to our work, little was known about ^{128}Nd. The original identification of levels in the ground-state band was made by Lister *et al.* [66] using charged particle and neutron detection techniques. Moscrop *et al.* [67] confirmed the ground band in ^{128}Nd up to $I = 14^+$. The present data enabled the extension of this band (labeled as band 1 in Fig. 4.1) by ten more transitions to a maximum observed spin of $I = (34^+)$. A spectrum of the ground-state band is given in Fig. 4.3, which is a result of summing all coincidence spectra produced by double-gating on every combination of γ rays above the 8^+ state. For the transitions below the 18^+ level, DCO ratios were deduced (see Table 4.1) and the $E2$ nature of these transitions was confirmed. The ground state of ^{128}Nd is well-deformed as indicated by the calculations of Möller and Nix [1] ($\beta_2 = 0.321$) as well as a standard total Routhian surface (TRS) [28] calculation ($\beta_2 = 0.305$). The E_{4+}/E_{2+} ratio is equal to 3.17, suggesting that ^{128}Nd is a good rotor as the rigid body value of this ratio is 3.33.

In addition to confirming and extending the previously known ground-state sequence to higher spins, we observed four new side bands for the first time. Band 2 is the strongest side band observed in ^{128}Nd as indicated in Table 4.1 and a spectrum of the sequence is displayed in Fig. 4.4(a). A DCO ratio of 0.58(6) was measured for the

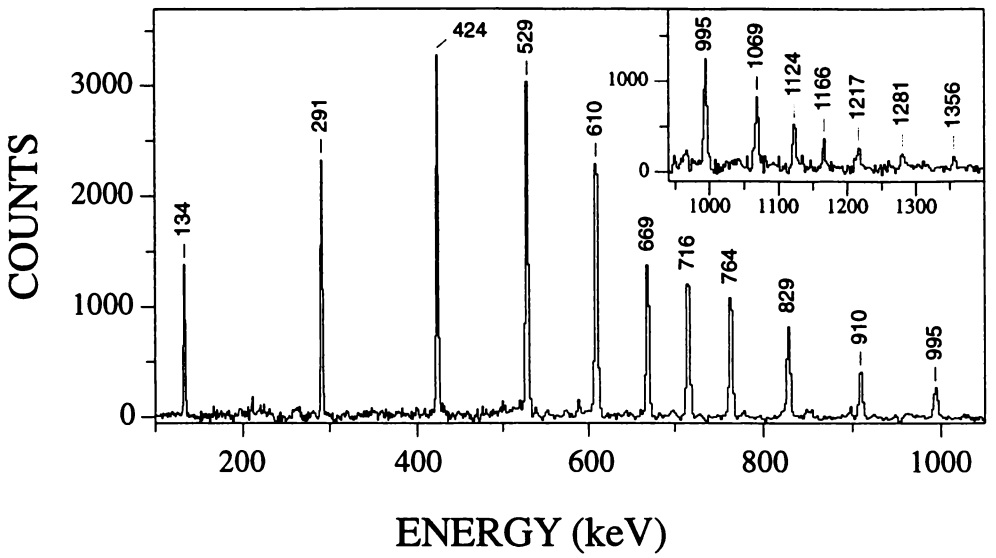


Figure 4.3: Spectrum of the ground-state band (band 1) in ^{128}Nd. The spectrum is a result of summing the coincidence spectra generated by double-gating on all possible combinations of γ rays above the 18^+ state in the band. The high-energy part of the spectrum is displayed in the inset.

846.4-keV linking transition from the $7^{(-)}$ state in band 2 to the 8^+ state of the ground-state structure, implying a change in spin of one unit of $\hbar$. An $I \rightarrow I-1$ assignment of this γ ray would make band 2 become yrast above the $17^{(-)}$ state, which contradicts the pattern of the measured intensities (see Table 4.1). An $I \rightarrow I+1$ assignment for the 846.4 keV γ ray provides a more consistent scenario with the observed intensities and, thus, the state that this transition deexcites has been assigned a spin of $I = 7$. Further supporting arguments for the $I \rightarrow I+1$ assignment follows in a later section. With this assignment, the sequence is observed up to spin of $I = 23\ \hbar$. However, a firm parity assignment cannot be made for this state or for band 2. The proposed configuration of this structure suggest negative parity, which agrees well with the systematics of the lowest side bands in even-even Nd nuclei [64, 68, 69].

Bands 3 and 4 are found to be interlinked by several weak transitions assumed to be of mixed $M1/E2$ nature. A DCO ratio of 0.5(1) was measured for the 890.8-keV linking transition from the $7^{(-)}$ state in band 3 to the 8^+ state of the ground-state structure, implying a change of spin of one unit of $\hbar$. Similar to the spin

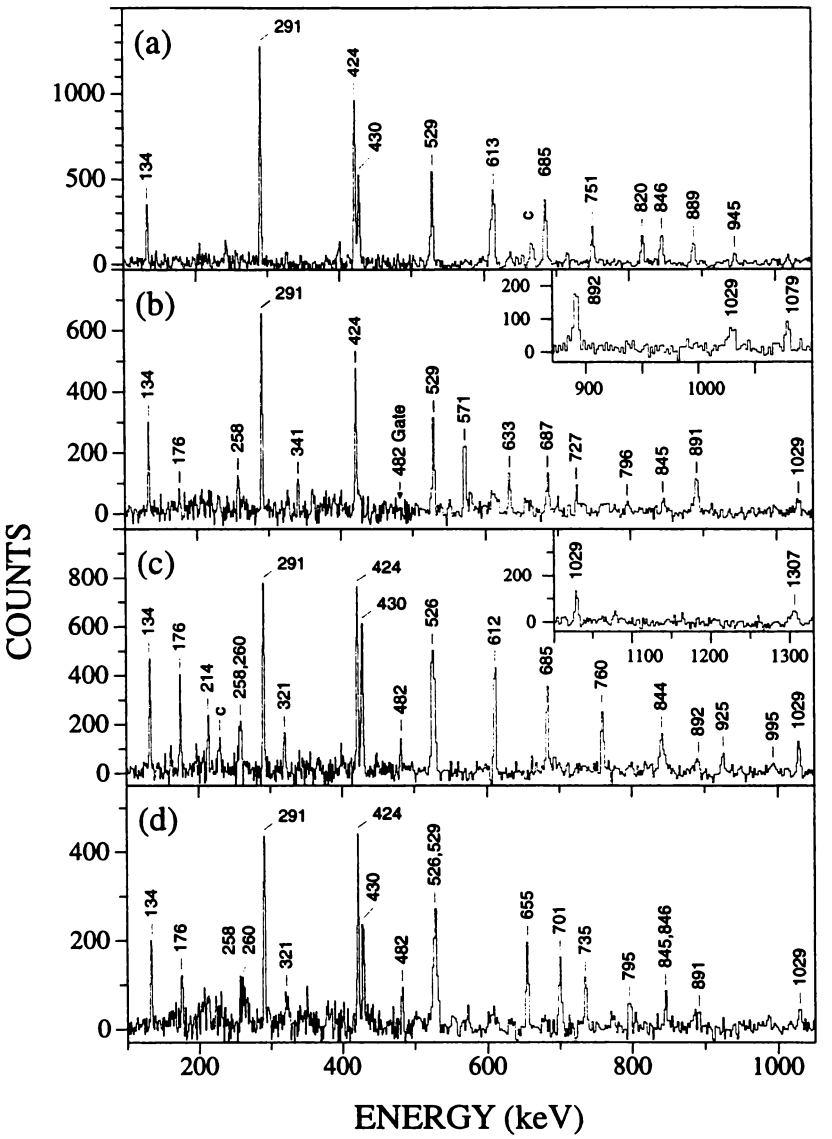


Figure 4.4: Spectra of the side bands in ^{128}Nd. The spectrum of band 2 shown in panel (a) is a result of summing several in-band coincidence gates. The peak marked with a "c" is a contaminant transition. (b) Spectrum of band 3 is produced by summing coincidence gates of the 482.3 keV with the lower four transitions of the ground-state band. (c) Spectrum of band 4 produced by summing many double-gated coincidence spectra and the inset show the linking transitions to the ground-state band. (d) Spectrum of band 5 is produced in a similar manner to (c) above. Peaks denoted by "c" are contaminant transitions.

assignment arguments for band 2, this level in band 3 is assigned a spin of $I = 7\ \hbar$. Decay into band 2 is also observed from both bands 3 and 4 at lower spins. Spectra of bands 3 and 4 are displayed in Fig. 4.4 (b) and (c), respectively.

A weak sequence, labeled band 5 in Fig. 4.1, was observed to feed the (10^-) state in band 4 by a tentative 655-keV linking transition. A sample spectrum of this band is shown in Fig. 4.4(d). Once again, firm spin assignments could not be made as DCO ratios could not be deduced. The spin assignment for band 5 is based on intensity and excitation energy considerations. The tentative negative-parity assignment is based on the arguments regarding its configuration given in the next section.

4.4 Rotational Alignments and Configuration Assignments

For a discussion of the ground-state band and the possible configurations of the linked side bands in ^{128}Nd, the rotational alignments of bands 1-5 are plotted in Fig. 4.5. Harris parameters [24] of $\mathcal{J}_0 = 22\ \hbar^2/\text{MeV}$ and $\mathcal{J}_1 = 17\ \hbar^4/\text{MeV}^3$ were used to subtract the angular momentum of the collective core. Cranked Shell Model (CSM) calculations [70] were performed using deformation parameters extracted from Total Routhian Surface (TRS) calculations [27], and the results are displayed previously in Fig. 2.10. The orbital labeling scheme is summarized in Table 4.2.

4.4.1 Band 1

A large alignment gain of $\Delta i \sim 8\hbar$ at a crossing frequency of $\hbar\omega_c \sim 0.35$ MeV is observed for band 1. The only nucleons that can align at this low frequency and give such a large increase in alignment are the low-K $h_{11/2}$ protons. This proton alignment (E_pF_p) is well known in the mass 130 region and the crossing frequency and alignment gain are similar to those observed in nearby nuclei [71]. CSM calculations predict the E_pF_p crossing to be near $\hbar\omega \sim 0.37$ MeV, which is in good agreement with our experimental observations. The next indication for a crossing in band 1 is observed at a frequency of ~ 0.57 MeV as seen in Fig. 4.5. An alignment of $h_{11/2}$ quasineutrons (EF) is likely responsible for this crossing, however, the CSM quasineutron diagram

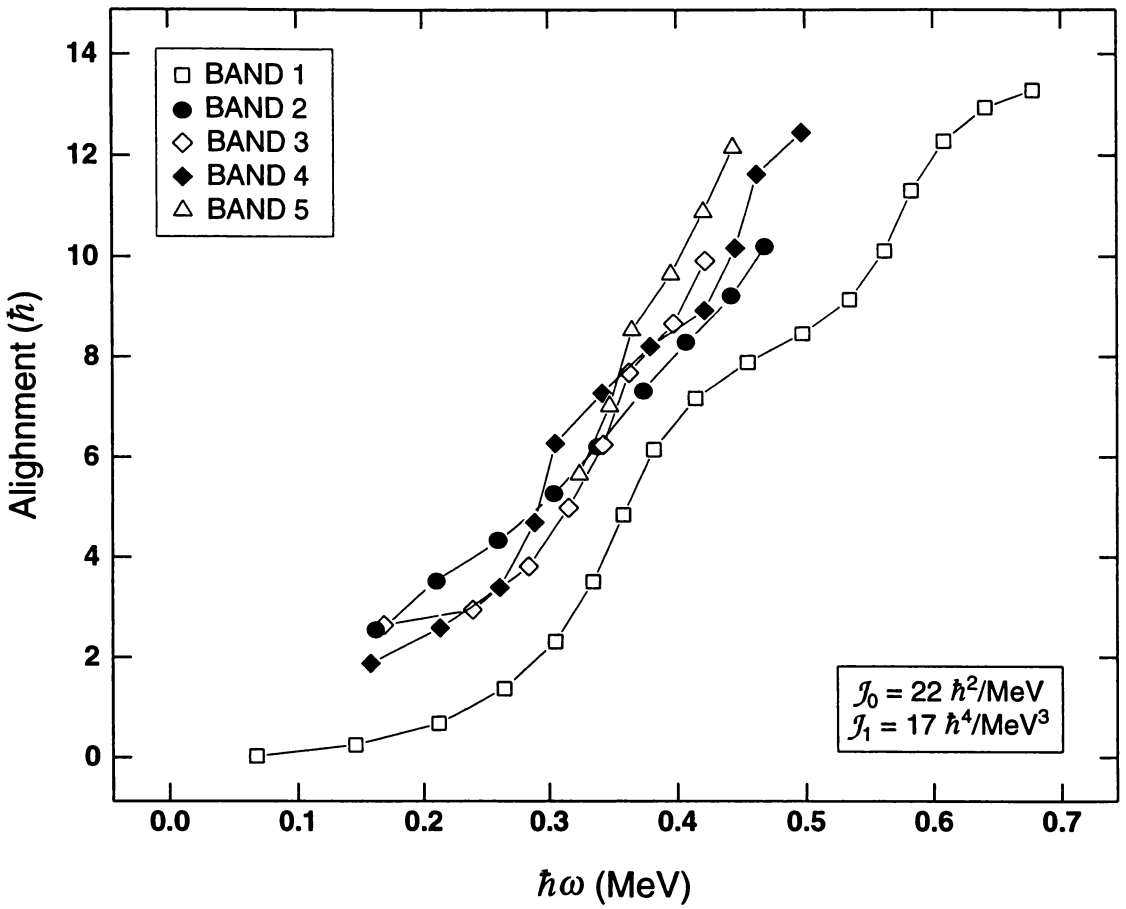


Figure 4.5: The alignment plotted versus rotational frequency for bands 1-4. Harris parameters of $\mathcal{J}_0 = 22\ \hbar^2/\text{MeV}$ and $\mathcal{J}_1 = 17\ \hbar^4/\text{MeV}^3$ were used to subtract the angular momentum of the collective core.

Table 4.2: Alphabetic quasiparticle labeling scheme for ^{128}Nd.

Label	$(\pi,\alpha)_n$*	Configuration **	Label	$(\pi,\alpha)_n$*	Configuration **
		Quasineutrons			
A	$(+,+\frac{1}{2})_1$	[411]1/2	B	$(+,-\frac{1}{2})_1$	[411]1/2
C	$(+,+\frac{1}{2})_2$	[402]5/2	D	$(+,-\frac{1}{2})_2$	[402]5/2
E	$(-,-\frac{1}{2})_1$	[523]7/2	F	$(-,+\frac{1}{2})_1$	[523]7/2
G	$(-,-\frac{1}{2})_2$	[541]1/2	H	$(-,+\frac{1}{2})_2$	[541]1/2
		Quasiprotons			
E_p	$(-,-\frac{1}{2})_1$	$h_{11/2}$	F_p	$(-,+\frac{1}{2})_1$	$h_{11/2}$

* Parity (π) and signature (α) of the orbital at $\hbar\omega = 0$ MeV. The subscript n numbers the quasiparticle's excitation of a specific signature and parity starting with the lowest in energy at $\hbar\omega = 0$ MeV.

** Configuration of the orbital at $\hbar\omega = 0$ MeV.

shown previously in Fig. 2.10 indicates that the EF alignment should occur near 0.47 MeV. Further discussion of this substantial delay in the EF crossing in ^{128}Nd and neighboring nuclei follows in a later section. Therefore, on the basis if these results it is possible to assign configurations as follows: for $I = 0 - 12\hbar$, band 1 is built upon the quasi-particle vacuum; for $I = 12 - 26\hbar$ it corresponds to the E_pF_p configuration; and for the $I = 26\hbar$ to the experimentally observed limit, it corresponds to the $E_pF_p \otimes E_nF_n$ configuration.

4.4.2 Band 2

Band 2 has an initial alignment of approximately 2.5 $\hbar$ and gains $\sim 8\hbar$ of alignment near $\hbar\omega = 0.36$ MeV (see Fig. 4.5), which is associated with the E_pF_p crossing. In the neighboring odd-Z isotone $^{127}_{59}$Pr [72], the band based on an $h_{11/2}$ proton is found to be the yrast sequence. Therefore, the lowest lying two-quasiproton band in ^{128}Nd would likely have this proton in its configuration and would Pauli block the $\pi h_{11/2}$ crossing. Since this is not the case for band 2, a two-quasineutron configuration is a more

reasonable possibility. At the lowest spin values, band 2 likely has a strong octupole vibartion admixture (see discussion in following section), but it has a more quasiparticle character at higher spins. From an inspection of the band structures observed in the neighboring odd-N ^{129}Nd [73] nucleus, one concludes that the neutron orbitals $d_{5/2}[402]5/2$, $d_{3/2}/s_{1/2}[411]1/2$, $h_{11/2}[523]7/2$, and $h_{9/2}/f_{7/2}[541]1/2$ are all likely near the neutron Fermi surface for ^{128}Nd. Among those, the [523]7/2 band is the most intensely populated structure in ^{129}Nd suggesting that this neutron is a constituent of the lowest lying two-quasineutron configuration in ^{128}Nd. Therefore, band 2 likely has the E neutron in its configuration (the E configuration is systematically found to be more energetically favored than its signature partner F). Since E has a signature of $\alpha = -\frac{1}{2}$ and band 2 has been determined to have $\alpha = 1$ (*i.e.* an odd-spin sequence), the second quasineutron must also have negative signature, leaving B, D, and G as possibilities. To reduce the number of possible configurations, one can consider the additivity of alignment for these quasineutrons. The experimental alignment values (in units of $\hbar$) at $\hbar\omega = 0.17$ MeV for the configurations observed in ^{129}Nd are as follows: A = 0.6, B = 1.0, C = 0.6, D = 0.5, E = 1.9, F = 1.8, G = 1.9, and H = 2.5. By adding the values for the E and G neutrons, one finds a larger alignment (3.8 $\hbar$) than that observed for band 2 ($\sim 2.6\hbar$ at $\hbar\omega = 0.17$ MeV). However, summing the alignments of the E neutrons with either the B or D neutrons gives a value close to the experimentally observed alignment of band 2. Bands involving the [402]5/2 orbital are normally strongly coupled with little signature splitting, therefore, if the ED configuration is observed, one would expect to see it coupled with its EC signature partner. In contrast, large signature splitting is expected with the $\alpha = -\frac{1}{2}$ signature being favored for the [411]1/2 orbital (see Fig. 2.10). Thus we suggest that band 2 is the EB configuration, which is consistent with the two lowest quasineutron orbitals predicted by the CSM in Fig. 2.10.

4.4.3 Bands 3 and 4

Similar to bands 1 and 2, the alignment gain of $\sim 6\hbar$ in bands 3 and 4 at $\hbar\omega = 0.35$ MeV is attributed to the E_pF_p crossing. The fact that both bands experience a proton

crossing indicates that these structures are built on two-quasineutron bands. The average of the initial alignments of bands 3 and 4 at $\hbar\omega \sim 0.17$ MeV is $\sim 2.3\ \hbar$. This is very close to the average of the EC and ED configurations ($\sim$2.3 $\hbar$) at $\hbar\omega \sim 0.17$ MeV. The exchange of low-energy $\Delta I = 1$ transitions between bands 3 and 4 at low spin is generally a feature of coupled signature partners. By inspecting Fig. 2.10, one can conclude that the CSM predicts that the EC, ED configuration would be the next lowest structure following EB. Bands involving the [402]5/2 orbital are strongly coupled, and therefore, one should observe both signatures, which is consistent with our experimental findings. Since the spin value for most of the levels in band 3 have been previously established to have an $\alpha = 0$ signature, then band 3 is assigned the ED configuration. Consequently, band 4 can be feasibly be assigned the EC configuration ($\alpha = 1$ signature).

As seen from Fig. 4.1, band 4 is more yrast than band 3 at higher spins due to the presence of a second crossing in band 4 at $\hbar\omega = 0.45$ MeV, as shown in Fig. 4.5. This crossing may be the EF crossing; however, this would suggest the force causing the delay in the ground-state band does not affect band 4. The alignment gain may also be caused by the adiabatic crossing of another negative-parity configuration. Therefore, the nature of this crossing is not clear at this time.

4.4.4 Band 5

Band 5 has an initial alignment of $\sim 5.7\ \hbar$ at $\hbar\omega = 0.33$ MeV and shows a strong alignment gain over the entire observed sequence. By inspecting Fig. 4.5, one can see an irregularity in the alignment of band 4 at $\hbar\omega \sim 0.28$ (12^- state). This irregularity is most probably caused by an interaction with band 4 which suggests that band 5 has a similar parity and signature to band 4. Due to its large initial alignmnet, we propose that band 5 is based on the BG configuration. The fact that no signature partner to band 5 was observed further supports our suggested assignment since this configuration involves the favored signatures of the [411]1/2 and [541]1/2 orbitals which normally have large signature splitting and would produce a decoupled band.

4.5 Octupole Correlations

A common property of nuclei exhibiting the features of reflection asymmetry (*e.g.* octupole shapes) is the occurrence of large $E1$ transition probabilities between the yrast positive- and negative-parity bands. However, enhanced $B(E1)$ rates can also be present in well-deformed reflection-symmetric nuclei, due to the coupling to low-lying octupole one-phonon states [74]. Enhanced $E1$ transitions feeding the ground-state band from the yrast negative-parity band have been reported in the nearby ^{130}Nd [64] and ^{126}Ce [75] nuclei. Nazarewicz *et al.* [76] pointed out that the tendency towards maximal octupole coupling occurs when orbitals with Nilsson quantum numbers (N, l, j) and ($N-1$, $l-3$, $j-3$) are located close to each other. This condition is satisfied in the light $A \sim 130$ region as the $h_{11/2}$ and $d_{5/2}$ orbitals are near both the proton and neutron Fermi surfaces. Enhanced $E1$ transitions are observed in the decay of band 2 of ^{129}Nd. The proposed $\nu(h_{11/2}, d_{3/2})$ configuration does not satisfy the $\Delta j = 3$ condition; therefore, one may not expect strong octupole correlations in this structure. However, the Coriolis interaction and deformation causes the neutron $d_{3/2}$ and $d_{5/2}$ orbitals to mix (indeed multiple transitions are observed between these structures in ^{129}Nd [73]) such that the presence of octupole vibrations may be observed in band 2. Of course, octupole correlations should also be strong in bands 3 and 4 ($\nu(h_{11/2}, d_{5/2})$ configuration), but as these bands were more weakly populated than band 2, we will focus on the latter structure.

The intrinsic electric dipole moment D_0, related to nuclear charge asymmetry, is a good measure of the strength of octupole correlation in a nucleus [74]. The relation between the $E1$ transition probability $B(E1)$ and D_0 is given by [12]

$$B(E1) = \frac{3}{4\pi} {D_0}^2 \langle IK10|(I-1)K\rangle^2 \ (efm)^2. \tag{4.86}$$

In most cases, absolute values of $B(E1)$ are not available, and D_0 has to be extracted from the known $B(E1)/B(E2)$ values deduced from

$$\frac{B(E1)}{B(E2)} = 0.77 \times 10^{-6} \frac{I_\gamma(E1)}{I_\gamma(E2)} \frac{E_\gamma^5(E2 : I \rightarrow I-2)}{E_\gamma^3(E1 : I \rightarrow I+1)} \ (fm^{-2}), \tag{4.87}$$

where E_γ is in MeV. The $B(E2)$ values are assumed with the rotational relationship

$$B(E2) = \frac{5}{16\pi} e^2 {Q_0}^2 |\langle I_i 2K0 | I_f K \rangle|^2 \ (eb)^2, \tag{4.88}$$

where Q_0 is the intrinsic quadrupole moment. Through the use of the above expressions, $B(E1)$ strengths were extracted for the 667- and 846.4-keV transitions deexciting band 2 levels assigned as $9^{(-)}$ and $7^{(-)}$, respectively. A range of K values ($K = 1 - 4$) have been used in the above expressions, together with a value of $Q_0 = 5.4$ eb from TRS calculations (corresponding to an axially deformed shape with $\beta_2 = 0.31$). Average values of the $B(E1)$ over the given range of K values were found to be 7.7×10^{-5} and 1.1×10^{-5} W.u. (corresponding to D_0 values of 0.04 and 0.01 e fm) for the 667- and 846.4-keV transitions, respectively. These $B(E1)$ values are very similar to measured $B(E1)$ strengths in odd-A rare-earth nuclei with octupole correlations [77]. For those nuclei, Hagemann *et al.* [77] managed to reproduce the experimental enhanced $E1$ strengths by invoking octupole softness in a theoretical model of one quasiparticle coupled to a rotor. Our intrinsic dipole moment values are smaller than measured enhanced dipole moments for heavy even-even nuclei in the Ba-Sm region with stable axially symmetric octupole deformations [74]. This is expected, however, since there has been no evidence so far that neutron-deficient, quadrupole-deformed even-even $A \sim 130$ nuclei possess a stable ground-state octupole deformation.

Enhanced $E1$ transitions feeding out of negative-parity bands have been also observed in $A \sim 170$ nuclei ($^{176-180}$Os [79], ^{178}Pt [80], and ^{180}Pt [78]) where octupole vibrations are prevalent. The negative-parity bands were based on a single-phonon octupole vibration at low spin crossed by two-quasiparticle excitations at higher angular momentum. The interband $E1$ transitions of $I \rightarrow I + 1$ character were found to be favored over the competing $I \rightarrow I - 1$ despite the larger energy of the latter [79, 78]. The $I \rightarrow I + 1$ enhancement was interpreted to be due to a phase difference arising for transitions with $\Delta K = 0$ and 1 [79]. Therefore, $I \rightarrow I + 1$ transitions are expected to be favored in the presence of octupole correlations, as is seen in ^{128,130}Nd, where the $I \rightarrow I - 1$ transitions are not observed. Thus band 2 in ^{130}Nd can be correlated with an octupole vibration at lower spins where strong $E1$

transitions occur.

To further expand the search for possible octupole correlations in other even-even $A \sim 130$ nuclei, we considered the nearby nucleus ^{126}Ce. If an octupole vibrational state exists in ^{126}Ce, one would expect to observe similar enhanced $E1$ transition(s) of $I \rightarrow I+1$ type. Instead, an enhanced 574-keV transition of $I \rightarrow I-1$ character was reported feeding the ground state-band from the proposed (9^-) in the yrast negative-parity band of ^{126}Ce [75]. In addition, a weak 1185-keV transition of $E3$ character was also reported feeding the ground-state band from the same state. The observation of an $E3$ transition in the experimental data is usually indicative of the presence of a *static* octupole deformation (β_3), and is experimentally found feeding the ground state from the 3^- state in even-even nuclei [81]. However, ^{126}Ce is likely a well-deformed nucleus ($\beta_2 = 0.293$, $\beta_3 = 0.0$) [1]. The Weisskopf partial life time estimate [34] for a 1185-keV level in ^{126}Ce would be of the order of ~ 0.5 μs, which suggests such a transition would not be observed in prompt spectroscopy. However, Wilson *et al.* [75] proposed, as a second but unlikely possibility, to lower the spin assignment of the negative-parity band by 2 $\hbar$. This spin assignment would make the 574-keV an $I \rightarrow I+1$ transition and, hence, in agreement with observed enhanced $E1$ transitions of similar character in ^{128,130}Nd nuclei. In addition, it would make the 1185-keV transition an $E1$ transition of $I \rightarrow I-1$ character which is an unfavored transition according to our arguments, and is consistent with their experimental observations [75].

4.6 Systematics of the $\nu h_{11/2}$ Crossing in $A \sim 130$ Nuclei

Band crossing frequencies are a valuable tool in exploring several nuclear features such as deformation and pairing. The ability to correctly predict various crossings in the rare-earth region has made the Cranked Shell Model (CSM) a standard for describing observed alignments. A particularly common band crossing in the rare-earth region is based on $\nu h_{11/2}$ alignment. However, partially due to the predicted γ softness of the heavier nuclei in this mass region [73, 82], a clear picture of the alignments and crossing frequencies is not easily obtained. Therefore, by focusing on the neutron

deficient nuclei near $N = 70$ and $Z = 60$, which are less γ soft due to their larger deformation [1], one can gain a better understanding of how the alignments depend on the deformation and Fermi levels. Surprisingly, large deviations have been observed between the experimental crossing frequencies and the predicted CSM values. For instance, Paul *et al.* [83] observed that the experimental $\nu h_{11/2}$ crossing for even-even Ce nuclei ($N = 66 - 74$) occurs at higher frequencies than the predicted CSM values and reaches a maximum ($\hbar\omega_c > 0.69$ MeV) for $N = 70$ (^{128}Ce). This crossing value is much larger than the CSM predicted value at $\hbar\omega_c \sim 0.44$ MeV. However, CSM predictions of the proton $h_{11/2}$ crossing in even-even, neutron-deficient Ce and Nd nuclei are in excellent agreement with the experimental values.

We have extended the systematics of the $\nu h_{11/2}$ crossing to include even-even, odd-A, and odd-odd nuclei in the most neutron deficient $A \sim 130$ nuclei ($N = 68 - 74, Z = 57 - 60$). Table 4.3 lists the nuclei of interest, the bands in which a $\nu h_{11/2}$ crossing has been observed, the crossing frequency values, and the sources of the experimental data. The bands were chosen such that for even-even nuclei the ground-state band (GSB) was used, and the most yrast structures not involving an $h_{11/2}$ neutron in the odd-A and odd-odd nuclei. For discussion purposes, the crossing frequencies of the $\nu h_{11/2}$ alignment for all the nuclei in Table 4.3 are plotted versus the neutron number N in Fig. 4.6.

Several trends can be identified when examining Fig. 4.6. Starting with the lowest Z isotope chain (La nuclei), a steady increase in crossing frequency with N is observed for both odd-A and odd-odd La nuclei . The neutron Fermi surface becomes increasingly higher in the $\nu h_{11/2}$ shell as N increases. Quasiparticles from high-K orbitals require more energy to align, and hence, an increase in rotational frequency with N is an expected trend. The neutron crossing in odd-odd $\pi h_{11/2} \otimes \nu d_{5/2}$ bands is seen at a noticeably lower frequency as compared with the odd-A $\pi h_{11/2}$ bands, causing an observed staggering. Hartley *et al.* [84] suggested that this may be due to a reduced pairing field caused by the blocking of a neutron orbital in odd-N versus even N nuclei. However, it is also possible that the oblate driving $h_{11/2}$ neutrons couple with the oblate driving $d_{5/2}$ neutron to create a shape change and thus influence the crossing frequency.

Table 4.3: The experimental neutron $h_{11/2}$ crossing frequency for rotational bands in $^{128-134}$Nd, $^{127-133}$Pr, $^{126,128-132}$Ce. Except for ^{128}Nd, the experimental data on these nuclei were compiled from the sources listed in the last column.

Nucleus	Configuration	Neutron Crossing	Reference
^{128}Nd	GSB	0.57 (1)	
^{129}Nd	$\nu d_{5/2}[402]5/2^+$	> 0.58	[73]
^{130}Nd	GSB	> 0.66	[64]
^{131}Nd	$\nu d_{5/2}[402]5/2^+$	0.48 (2)	[85]
^{132}Nd	GSB	0.50 (3)	[86]
^{133}Nd	$\nu g_{7/2}[404]7/2^+$	0.46 (2)	[87]
^{134}Nd	GSB	> 0.62	[69]
^{127}Pr	$\pi h_{11/2}[541]3/2^-$	0.55 (2)	[88]
^{128}Pr	$\pi h_{11/2}[541]3/2^- \otimes \nu d_{5/2}[402]5/2^+$	0.63 (3)	[89]
^{129}Pr	$\pi h_{11/2}[541]3/2^-$	0.66 (0)	[90]
^{130}Pr	$\pi h_{11/2}[541]3/2^- \otimes \nu d_{5/2}[402]5/2^+$	> 0.65	[91]
^{131}Pr	$\pi h_{11/2}[541]3/2^-$	0.57 (1)	[92]
^{132}Pr	$\pi h_{11/2}[541]3/2^- \otimes \nu g_{7/2}[404]7/2^+$	> 0.53	[93]
^{133}Pr	$\pi_{11/2}[541]3/2^-$	0.52 (1)	[94]
^{126}Ce	GSB	0.50 (1)	[75]
^{128}Ce	GSB	> 0.69	[83]
^{129}Ce	$\nu d_{5/2}$ $[402]5/2^+$	> 0.59	[95]
^{130}Ce	GSB	0.66 (3)	[96]
^{131}Ce	$\nu g_{7/2}$ $[404]7/2^+$	> 0.57	[97]
^{132}Ce	GSB	0.62 (0)	[98]

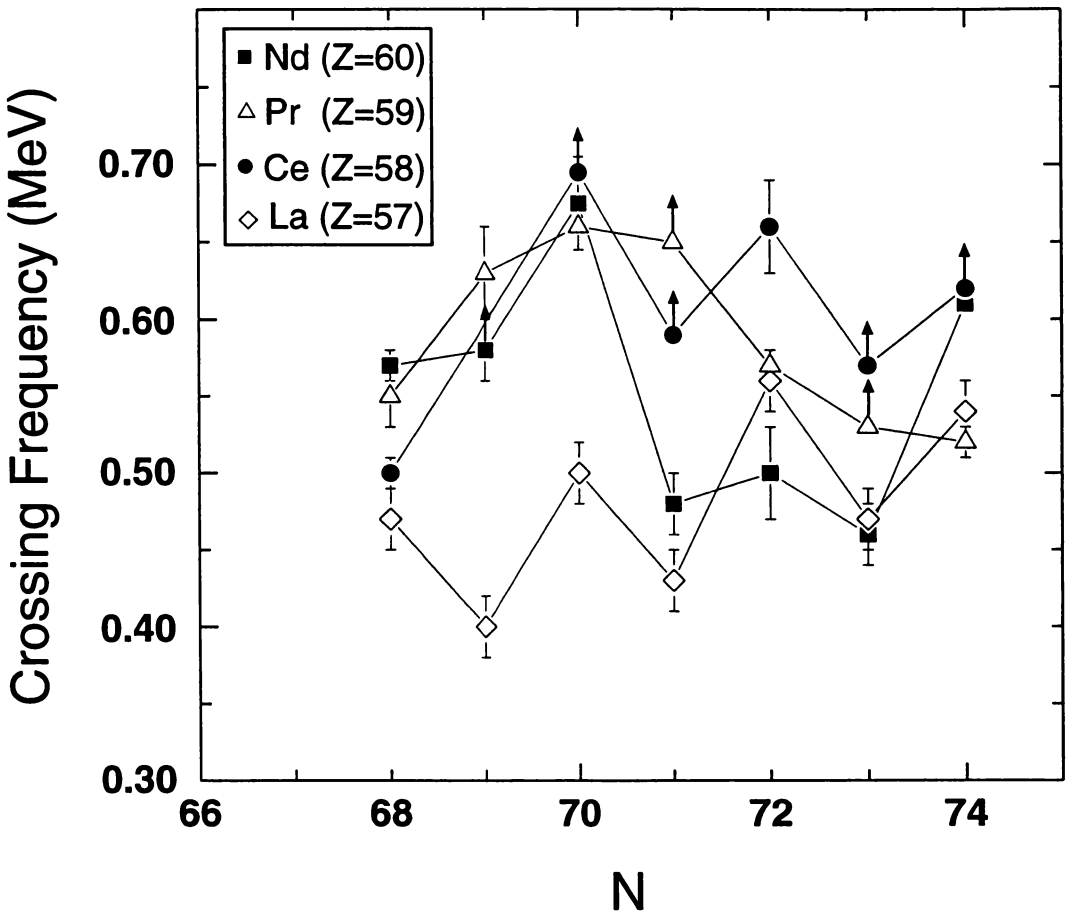


Figure 4.6: Experimental neutron $h_{11/2}$ crossing frequencies for lanthanum ($Z = 57$), cerium ($Z = 58$), praseodymium ($Z = 59$), and neodymium ($Z = 60$) nuclei.

Table 4.3 (continued).

Nucleus	Configuration	Neutron Crossing	Reference
^{125}La	$\pi h_{11/2}[550]1/2^-$	0.47 (2)	[84]
^{126}La	$\pi h_{11/2}[550]1/2^- \otimes \nu d_{5/2}[402]5/2^+$	0.40 (2)	[99]
^{127}La	$\pi h_{11/2}[550]1/2^-$	0.50 (2)	[100]
^{128}La	$\pi h_{11/2}[550]1/2^- \otimes \nu d_{5/2}[402]5/2^+$	0.43 (2)	[101]
^{129}La	$\pi h_{11/2}[550]1/2^-$	0.57 (2)	[102]
^{130}La	$\pi h_{11/2}[550]1/2^- \otimes \nu g_{7/2}[404]7/2^+$	0.46 (2)	[103]
^{131}La	$\pi h_{11/2}[550]1/2^-$	0.54 (2)	[104]

In contrast to La nuclei, the other isotope chains do not have a consistent systematic behavior. In most of the Ce nuclei, the $\nu h_{11/2}$ crossing is delayed to such a large extent that it is not seen up to the highest observed frequencies. Thus, only lower limits are shown in Fig. 4.6 and definitive trends cannot be extracted. However, it should be emphasized that no neutron alignment is seen in the $N = 70$ ^{128}Ce nucleus up to $\hbar\omega = 0.69$ MeV. The crossing frequency in the praseodymium nuclei increase with decreasing N (which is opposite to that of the La nuclei) and appears to peak at $N = 70$ or $N = 71$. The $N = 71 - 73$ Nd nuclei have $\nu h_{11/2}$ crossing frequencies at approximately where the CSM predicts their occurrence, but a sharp jump in the frequency is seen at $N = 70$ with decreasing values for the $N < 70$ nuclei. These trends suggest that the crossing is maximally delayed near $N = 70$ for the latter three chains. The presence of an $N = 70$ neutron subshell gap at high rotational frequency might influence the pairing interaction and, consequently, the crossing frequency. In order to investigate this possibility, single-particle CSM calculations for ^{130}Nd were performed, as shown in Fig. 4.7. The calculations show a gap at $N = 70$ at low rotational frequency, but it diminishes gradually with increasing rotational frequency.

In order to see what parameters or force may cause delays of 40% with

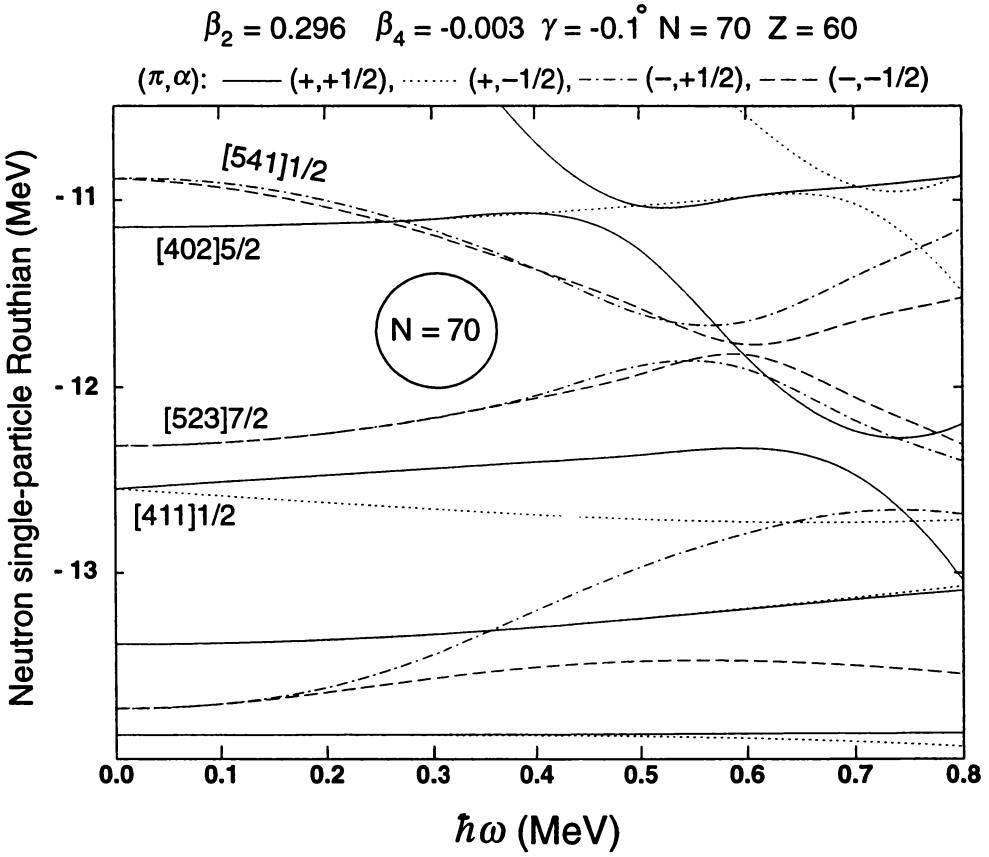


Figure 4.7: Single-particle Cranked Shell Model calculations for quasineutrons in ^{130}Nd. The deformation parameters (shown at the top of the figure) were determined from TRS calculations. Interpretation of the lines is displayed at the top of the figure. Explanation of the orbital labeling scheme is given in Table 4.2.

respect to predicted values, we performed CSM calculations for the nuclei in Fig. 4.6. First, the CSM input parameters (quadrupole deformation (β_2), triaxial deformation (γ), hexadecapole deformation (β_4), and pairing (Δ)) were determined from TRS calculations. For a given isotopic chain, the CSM predicts a relatively constant value of the crossing frequency for all the nuclei over the neutron range of interest. The average value of CSM neutron crossing predictions (in MeV) were as follows: ~ 0.48 for Nd, ~ 0.44 for Pr, ~ 0.42 for Ce, and ~ 0.42 for La nuclei. These values increase with Z, which is a product of the increasing β_2 deformation with Z. Good agreement is generally seen for the La and heavy Nd ($N \geq 71$), but large discrepancies are found for the other nuclei. In addition, CSM calculations failed to reproduce the unexpected "jump" in crossing frequency at $N = 70$. However, the CSM depends on several input parameters and we investigated whether a variation of these parameters might reproduce the high experimental crossing frequencies. Therefore, we performed CSM calculations for ^{128}Ce since it has the largest difference between experimental and predicted crossing frequencies (see Table 4.3). In each calculation, three of the CSM input parameters were fixed at a given value and the fourth was varied in small steps. This procedure was repeated many times for all the input parameters over the following parametric range: $0.24 < \beta_2 < 0.48$, $-30° < \gamma < +30°$, $-0.1 < \beta_4 < 0.1$, and $0.6 < \Delta_n < 1.4$ MeV. For this parametric range, the calculations show a smooth increasing trend of crossing frequency with increasing β_2 and Δ_n with maximum achievable values at γ, $\beta_4 \sim 0$. Fig. 4.8 displays three-dimensional plots of predicted neutron crossing frequency for ^{128}Ce versus three of the CSM parameters β_2, γ, and Δ_n. The plots in Fig. 4.8 clearly show that, between the three parameters used, variations of β_2 has the greatest influence on the crossing frequency, and large values of the crossing frequency can be achieved with the use of large β_2 values. In fact, we were able to reproduce the large experimental crossing frequency in ^{128}Ce (*i.e.* ~ 0.69 MeV) with only unrealistically large value of $\beta_2 \sim 0.46$. Thus, we are in agreement with Paul *et al.* [83] that the CSM alone cannot describe the delay.

The influence of quadrupole pairing was mentioned as a possible reason for the observed delay in even-even Ce nuclei [83]. Quadrupole pairing is not included in the CSM, but it is in the Projected Shell Model [105, 106]. ^{130}Nd ($N = 70$) was

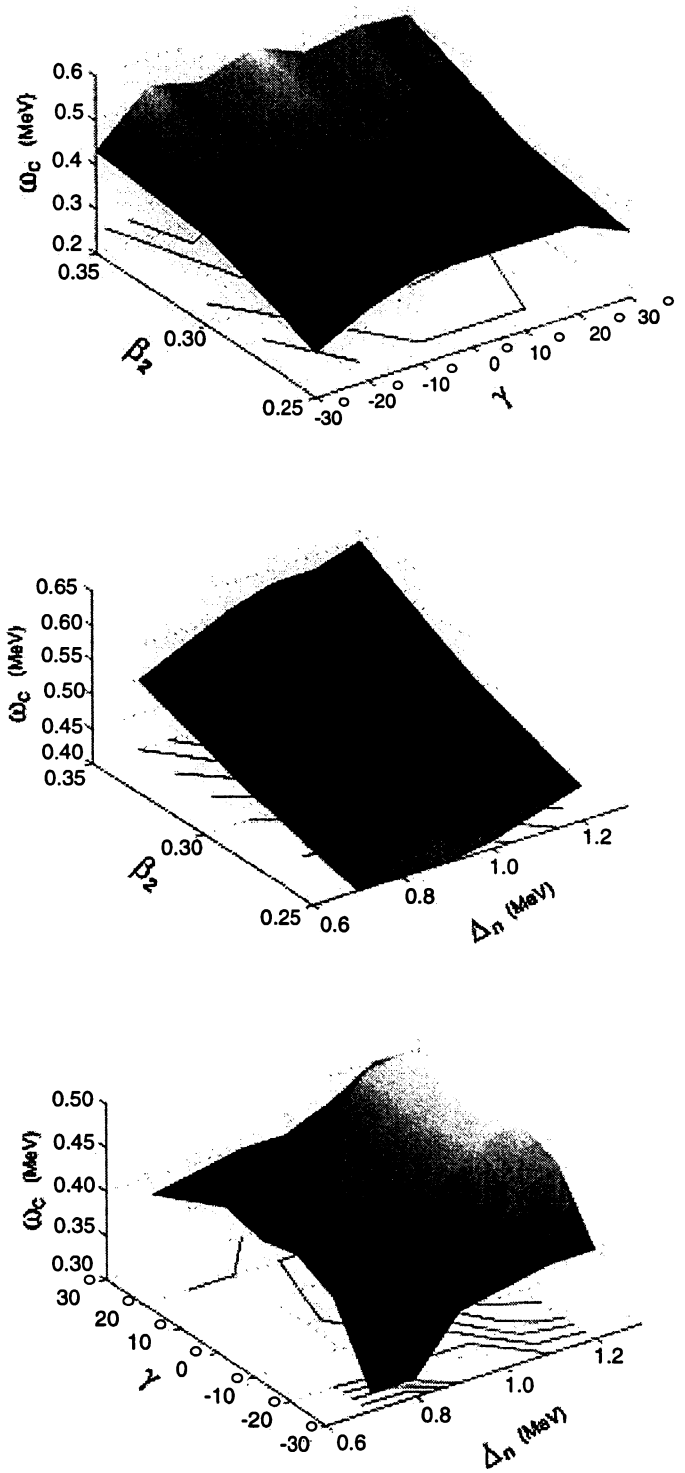


Figure 4.8: Three-dimensional plots of neutron crossing frequency ω_c for ^{128}Ce versus CSM parameters β_2, γ, Δ_n.

chosen as a test case and the quadrupole pairing force was varied substantially with little effect on the neutron crossing. Therefore, quadrupole pairing does not seem to be a reasonable explanation for the delay. Having ruled out the pairing interaction and the parameters of the CSM as possible causes of this "shift" in neutron crossing frequency, further theoretical work is needed to reveal the presence of certain subtle effects that give rise to large crossing frequencies and maximum values at $N = 70$ for neutron-deficient Nd, Pr, and Ce nuclei. Another puzzling observation is that other neutron-deficient nuclei in $A \sim 130$ region (La and Ba [84, 83] nuclei) do not seem to experience large crossing frequencies over the neutron range of interest, nor experience a "jump" at $N = 70$.

CHAPTER 5

Experimental Results of and Discussion of ^{129}Nd

5.1 Overview

The mass 130 region, with $Z \sim 60$ and $N \sim 74$, is well known for shape competition between weakly prolate and oblate bands at low spin [108] and for the occurrence of highly deformed bands at higher spins [109, 72, 110, 68, 111, 112]. This is due to the soft core which is susceptible to shape driving forces of the valence nucleons. Occupation of the $\nu i_{13/2}$ or of a hole in the $\pi g_{9/2}$ orbitals enhances the deformation of these nuclei from $\beta_2 \sim 0.2$ to $\beta_2 \sim 0.3 - 0.4$ [113, 114]. The alignment of two high-K $h_{11/2}$ neutrons has been associated with driving the nucleus to oblate shapes [115], while the occupation of one neutron in a $\nu h_{11/2}$ orbital, outside the even-even core, may produce stable triaxial deformation [82].

Although the $N \sim 74$ nuclei have been well studied through the use of Xn reaction channels, the lighter nuclei with $N \leq 70$ are not as well known. This is mainly due to lower cross-section reactions and the fact that the neutron-deficient compound nuclei favor multiple charged-particle reaction channels, which can produce over 20 different species of nuclei. However, with the sensitivity of Gammasphere [46] and the selectivity of the Microball [45], it is now possible to explore these nuclei which are far from stability.

In an experiment designed to populate high-spin states in the mass 130 region, a ^{92}Mo target was bombarded with ^{40}Ca. Theoretical calculations [1] predict large ground-state deformations $\beta_2 \sim 0.3$ for $Z \sim 60$, $N \leq 70$ nuclei, which is nearly as large as the highly deformed bands found in the heavier $A \sim 130$ region. Therefore, it is of interest to look for bands with the same highly-deformed configuration (namely the $\nu i_{13/2}$ structure) in the lighter nuclei to compare with those observed near $N \sim 74$.

The large ground-state deformation essentially eliminates the possibility of seeing oblate bands at low spin; however, one can track the shape driving influence of the $h_{11/2}$ neutron as N is decreased and β_2 is increased.

This Chapter will focus on the nucleus $^{129}_{60}Nd_{69}$, which is the lightest odd-A neodymium nucleus known. Significant extension of the level scheme was achieved by adding over 140 new transitions and three new structures to the previous work [116]. Evidence of the intruder $i_{13/2}$ band is indeed observed in ^{129}Nd as it adiabatically crosses a normal deformed sequence. Signature splitting in the energy levels of the $\nu h_{11/2}$ band was observed and compared with other $\nu h_{11/2}$ bands in the region. As signature splitting in these high-K bands is thought to be a result of significant γ deformation, cranked shell model calculations were performed in order to reveal approximate magnitudes and trends of triaxiality as a function of proton and neutron number. In addition, signature inversion in the neutron $h_{9/2}[541]1/2$ band was also observed and compared to signature inversion in the same band for the ^{131,133}Nd nuclei.

5.2 Experimental Details

Ions of ^{129}Nd were produced in two experiments using the reaction ^{92}Mo(^{40}Ca,2pn). In one experiment, the 170 MeV ^{40}Ca beam was supplied by the 25 MV tandem accelerator at the Holifield Radioactive Ion Beam Facility (HRIBF) at Oak Ridge National Laboratory (ORNL). The self-supporting ^{92}Mo target had a thickness of $\sim$ 450 μg/cm^2. A charge reset-foil was placed $\sim$ 10 cm behind the target in order to improve the detection of recoils with highly-converted transitions near the ground state, normally from short-lived ($\leq$ 10 ns) isomeric states. The emitted gamma rays were detected by the Ge Clover detector array CLARION [43]. Protons and α particles emitted by the deexciting compound nuclei were identified using the HyBall [43] array. Reaction products recoiling from the target foil were separated by the Recoil Mass Spectrometer (RMS) [44] at the focal plane according to their mass-to-charge ratio. A multiwire, gas-filled position sensitive avalanche counter (PSAC) [43, 107] was used to observe the spatial distribution of the mass groups at the focal plane. The

RMS was tuned for central recoils of mass $A = 129$, with energy of 40.5 MeV, and charge state $Q = 20.5^+$. The data were taken using a γ-γ-recoil trigger that required at least two HPGe detectors in prompt coincidence with a recoil signal from the PSAC. Gamma rays associated with mass 129 were sorted into a symmetric $E_\gamma \times E_\gamma$ matrix and were subsequently analyzed with the Radware software package [65]. A matrix of E_γ versus charged-particle multiplicity, with the same mass-gated condition, was also sorted such that gamma-charged particle coincidences could be investigated. A total of $\sim$ 4.2 million γ-γ coincidences were observed in the $A = 129$ mass-gated matrix.

The highest spin states in ^{129}Nd were achieved in the Gammasphere experiment described in detail in Chapter 4. Relative cross-sections (with respect to the strongest channel ^{129}Pr) were determined in the ORNL experiment (see Table 5.1). The experimental cross-sections were also compared with theoretical predictions from HIVAP [42] as shown in Fig. 5.1. Good agreement was found for most of the channels and, therefore, the calculated cross-section of $\sim$50 mb is likely a reasonable estimate for the $2pn$ channel leading to ^{129}Nd.

5.3 Analysis of ^{129}Nd

5.3.1 The Level Scheme and Spin Assignment

Before the present work, little was known about ^{129}Nd. Watson *et al.* [116] reported observing a strongly coupled sequence and assigned it to ^{129}Nd. In addition to confirming and extending the previously known sequence to higher spins (labeled as band 1 in Fig. 5.2), over 140 new transitions and three new structures were observed. A spectrum of $A = 129$ transitions from the ORNL data is presented in Fig. 5.3. Transitions in coincidence with both $A = 129$ recoils and three protons (^{129}Pr) have been subtracted from the spectrum leaving possible transitions from ^{129}Nd ($2pn$), ^{129}Pm ($p2n$), and ^{129}Sm ($3n$). However, no evidence of the latter two nuclei was observed and all the transitions in Fig. 5.3 were placed in the level scheme of ^{129}Nd (see Fig. 5.2).

One may see in Fig. 5.2 that the positive-parity structures, bands 3 and 4,

Table 5.1: Experimental and calculated relative cross sections for ^{40}Ca + ^{92}Mo reaction at E_{lab} = 170 MeV.

Channel*	Nucleus	Experimental Relative Cross Section**	Calculated Relative Cross Section**	Calculated Absolute Cross Section (mb)
$2pn$	^{129}Nd	40(6)	35.9	48.1
$2p2n$	^{128}Nd	3.0(5)	2.6	3.5
$3p$	^{129}Pr	≡100	≡100	134
$3pn$	^{128}Pr	30(4)	28.1	37.7
αp	^{127}Pr	<3	4.6	6.2
αpn	^{126}Pr	2(1)	1.9	2.5
$4p$	^{128}Ce	44(2)	47.2	63.2
$4pn$	^{127}Ce	<5	1.1	1.4
$\alpha 2p$	^{126}Ce	77(4)	17.0	22.8

* Charged-particle emission channel from the ^{132}Sm compound nucleus. p, n, and α denote emitted proton, neutron, and alpha particles, respectively.

** Relative cross section with respect to ^{129}Pr.

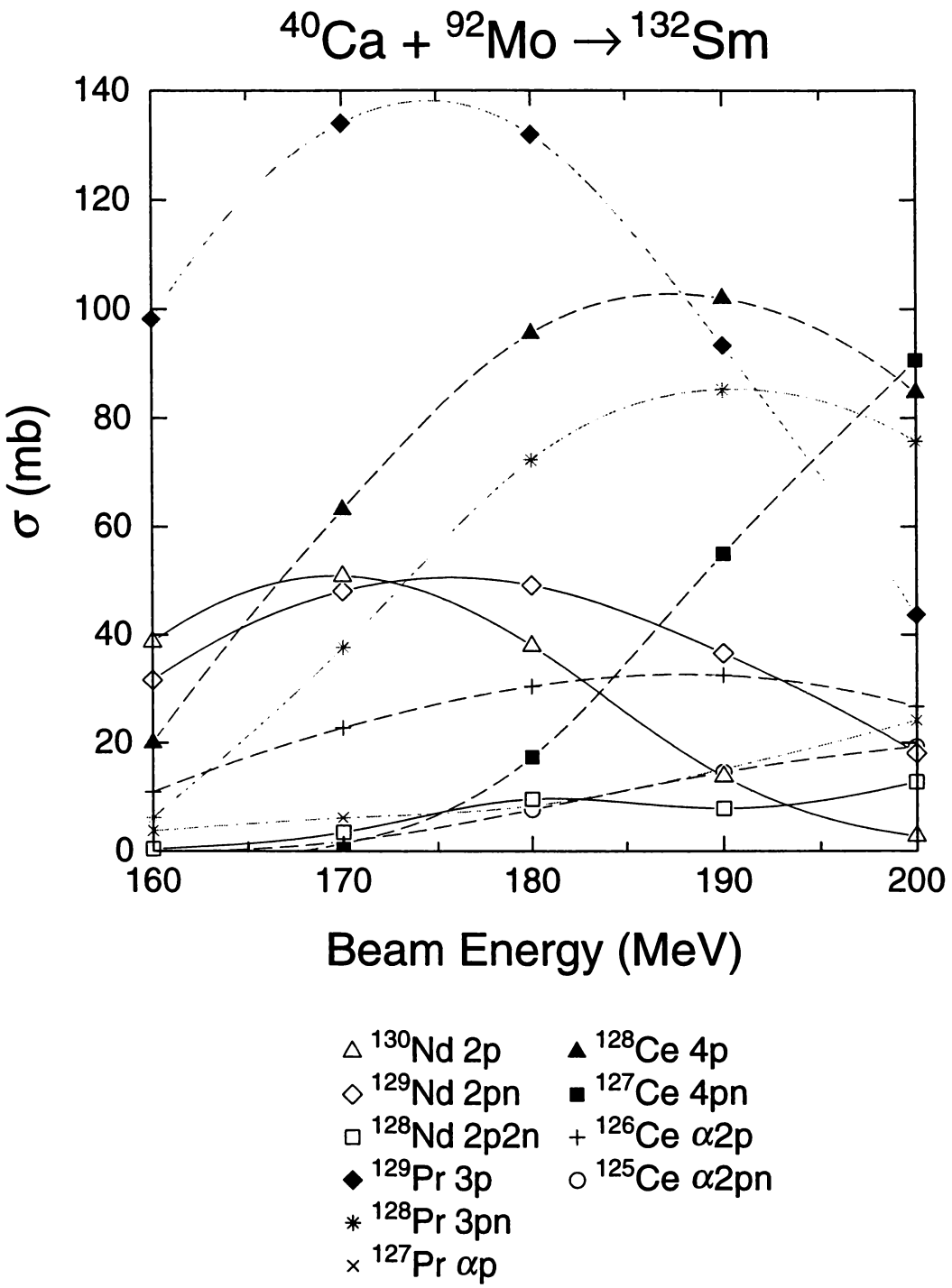


Figure 5.1: HIVAP theoretical predictions of reaction cross sections.

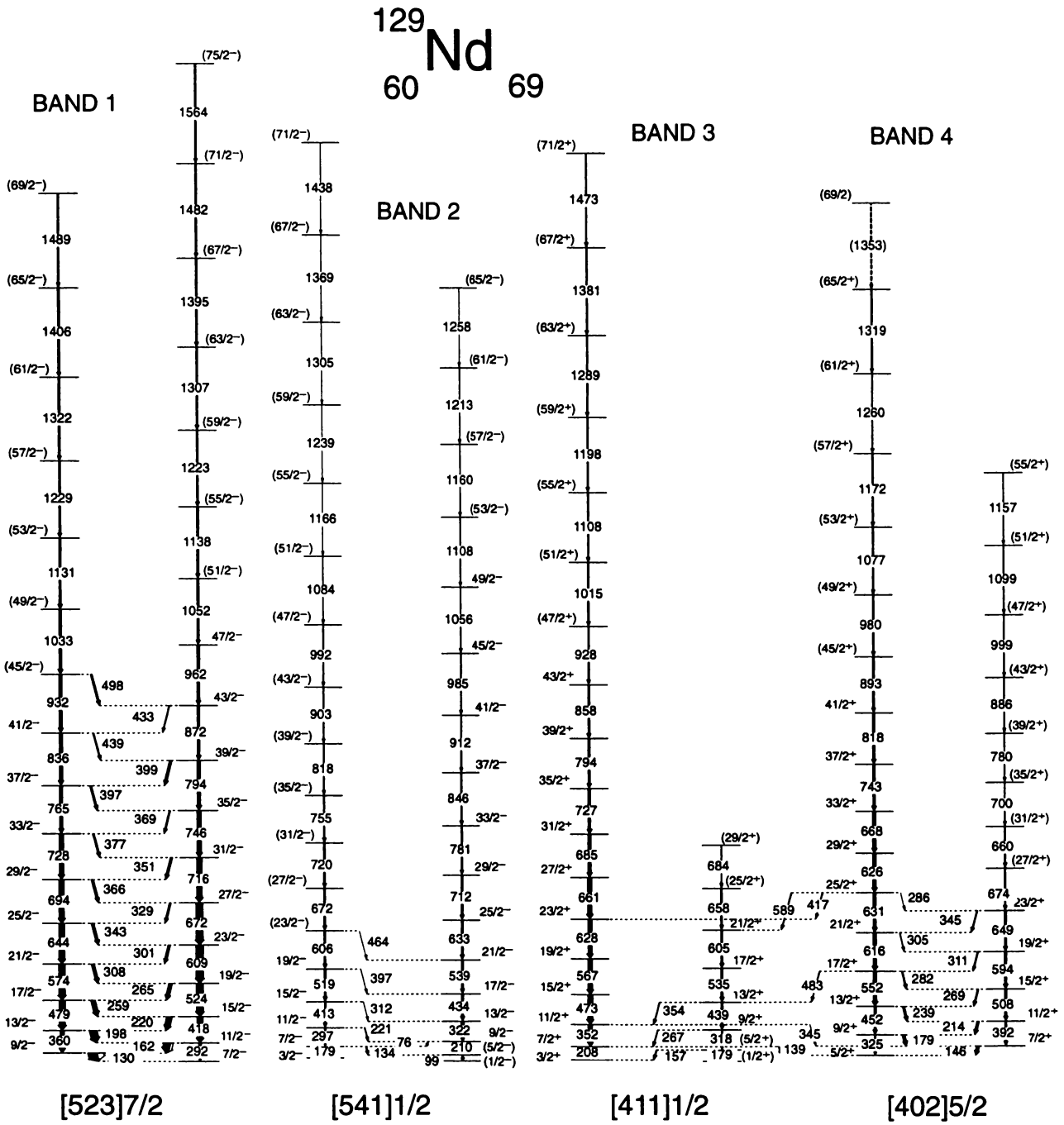


Figure 5.2: The level scheme for ^{129}Nd. The width of the arrows is proportional to the relative intensity of the transition. Tentative transitions are denoted by dashed lines. Spin and parity assignments are explained in the text. The proposed band-head configurations are also given.

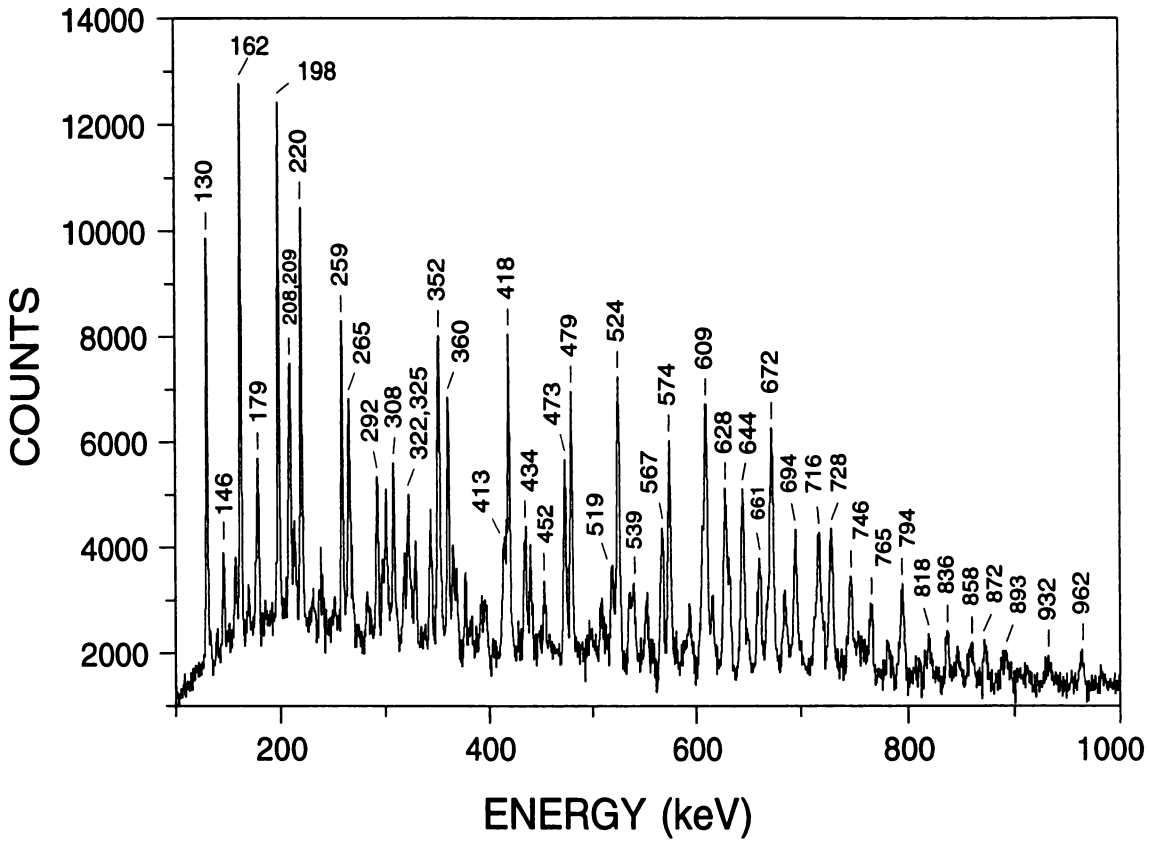


Figure 5.3: Transitions from $A = 129$ recoils in the ORNL experiment. Transitions in coincidence with three protons and $A = 129$ (^{129}Pr) were subtracted leaving ^{129}Nd γ rays (see text for details).

are linked with each other, while the negative-parity structures, bands 1 and 2, are not connected to any of the observed sequences. Previous decay works [117, 118] have suggested a ground-state spin of $(\frac{5}{2}^+)$ as well as a $(\frac{7}{2}^-)$ or $(\frac{9}{2}^-)$ isomeric state. From our analysis of the high-spin states, it is not clear whether any of the observed structures feeds the ground state, and therefore, firm excitation energies, spins, and parities cannot be assigned. However, the four structures have in-band characteristics that are similar to the four strongest bands in ^{131}Nd [85]. Thus, spin and parity assignments are largely based on systematics and similarities with ^{131}Nd and with the $N = 69$ isotones ^{127}Ce [119, 120] and ^{125}Ba [121, 122].

Relative spin assignments proposed for the states in ^{129}Nd were determined through directional correlation of oriented states (DCO) analysis. The asymmetric DCO matrix described in Chapter 4 for the analysis of ^{128}Nd was also used to extract DCO values for the transitions in ^{129}Nd. The measured DCO ratios are summarized in Table 5.2 along with the energy, spin, branching ratio, and parity of the states, as well as the energy and relative intensity of the depopulating γ rays. Weak transitions above states of determined spin, where reliable DCO analysis could not be performed, were assigned multipolarities assuming that the rotational behavior of the band persists, and the spins are shown in parentheses in Fig. 5.2.

Negative-parity Structures

The identification of structures in ^{129}Nd was derived from the γ-γ-recoil data in the ORNL experiment. Fig. 5.4(a) shows a summed coincidence spectrum from a mass 129 gated γ-γ matrix. By examining the γ-charged particle matrix, we were also able to determine that the strongest and cleanest transitions in this band were associated with a $2p$ evaporation. This additional information allows for the structure to be unequivocally associated with ^{129}Nd as it is the only $A = 129$ nucleus which can be produced by the emission of two protons. This confirms the preliminary results reported by Watson *et al.* [116], where this same band was observed up to a spin of $\frac{39}{2}$. In Ref. [116], mass-gating techniques similar to those described above were used, but without a charged-particle detector. This structure has been extended up to spin

Table 5.2: Data for levels and γ rays in ^{129}Nd

$I_i^{\pi\,a}$	E_{level} (keV)^b	E_γ (keV)^c	$I_\gamma{}^d$	DCO	λ^e	Multipolarity
		BAND 1 : [523]7/2 $\alpha = +\frac{1}{2}$				
$\frac{9}{2}^-$	X + 130.5	130.5	N/D^f	0.63(4)		$M1/E2$
$\frac{13}{2}^-$	X + 491.0	360.5	53(3)	1.0(1)	0.51(3)	$E2$
		198.6	96(5)	0.56(3)		$M1/E2$
$\frac{17}{2}^-$	X + 969.6	478.6	78(4)	0.91(8)	1.17(7)	$E2$
		259.0	58(3)	0.47(5)		$M1/E2$
$\frac{21}{2}^-$	X + 1542.8	573.2	76(4)	0.96(7)	1.8(1)	$E2$
		308.1	42(2)	0.45(2)		$M1/E2$
$\frac{25}{2}^-$	X + 2187.0	644.2	75(4)	1.14(8)	2.1(1)	$E2$
		343.4	29(2)	0.57(3)		$M1/E2$
$\frac{29}{2}^-$	X + 2881.4	694.4	71(4)	0.99(4)	3.7(4)	$E2$
		365.6	23(1)			$M1/E2$
$\frac{33}{2}^-$	X + 3609.5	728.1	59(4)	1.04(4)	2.5(2)	$E2$
		377.1	22(1)			$M1/E2$
$\frac{37}{2}^-$	X + 4374.1	764.6	38(2)	1.1(1)	3.3(4)	$E2$
		396.0	13.7(6)			$M1/E2$
$\frac{41}{2}^-$	X + 5210.3	836.2	33(2)	0.9(1)	5.3(8)	$E2$
		438.3	8.8(9)			$M1/E2$
$(\frac{45}{2}^-)$	X + 6142.4	932.1	22(2)		2.6(3)	$E2$
		498.5	6(1)			$M1/E2$
$(\frac{49}{2}^-)$	X + 7175.5	1033.1	18(2)			$E2$
$(\frac{53}{2}^-)$	X + 8306.8	1131.3	12(1)			$E2$
$(\frac{57}{2}^-)$	X + 9535.1	1228.3	8(1)			$E2$
$(\frac{61}{2}^-)$	X + 10857.1	1322.0	6(1)			$E2$
$(\frac{65}{2}^-)$	X + 12263.0	1405.9	5(1)			$E2$
$(\frac{69}{2}^-)$	X + 13746	1483	<4			$E2$

Table 5.2 (continued).

$I_i^{\pi\,a}$	E_{level} (keV)^b	E_γ (keV)^c	$I_\gamma{}^d$	DCO	λ^e	Multipolarity
		BAND 1 : [523]7/2 $\alpha = -\frac{1}{2}$				
$\frac{7}{2}^-$	X					
$\frac{11}{2}^-$	X + 292.5	292.5	30(2)	0.72(6)	0.40(2)	$E2$
		162.5	124(7)	0.51(3)		$M1/E2$
$\frac{15}{2}^-$	X + 710.6	418.1	75(4)	0.94(7)	1.12(6)	$E2$
		219.8	77(4)	0.47(4)		$M1/E2$
$\frac{19}{2}^-$	X + 1234.9	524.3	≡100	0.99(9)	1.88(7)	$E2$
		265.6	47(2)	0.40(7)		$M1/E2$
$\frac{23}{2}^-$	X + 1843.7	608.8	91(5)	0.98(5)	4.0(2)	$E2$
		300.9	32(2)	0.43(5)		$M1/E2$
$\frac{27}{2}^-$	X + 2516.0	672.3	84(5)	1.04(7)	3.0(2)	$E2$
		329.0	24(1)			$M1/E2$
$\frac{31}{2}^-$	X + 3232.2	716.2	72(4)	0.94(4)	3.5(3)	$E2$
		351.0	24(2)			$M1/E2$
$\frac{35}{2}^-$	X + 3978.5	746.3	51(3)	0.92(6)	4.4(5)	$E2$
		368.6	21(1)			$M1/E2$
$\frac{39}{2}^-$	X + 4772.0	793.5	38(2)	0.91(7)	2.1(3)	$E2$
		398.0	13(1)			$M1/E2$
$\frac{43}{2}^-$	X + 5644.5	872.5	24(2)	0.92(3)		$E2$
		433.0	6.7(7)			$M1/E2$
$\frac{47}{2}^-$	X + 6606.6	962.1	19(2)	0.91(6)		$E2$
$(\frac{51}{2}^-)$	X + 7658.5	1051.9	13(1)			$E2$
$(\frac{55}{2}^-)$	X + 8796.9	1138.4	12(1)			$E2$
$(\frac{59}{2}^-)$	X + 10019.6	1222.7	9(1)			$E2$
$(\frac{63}{2}^-)$	X + 11326.6	1307.0	7(1)			$E2$
$(\frac{67}{2}^-)$	X + 12720.6	1394.0	5(1)			$E2$

Table 5.2 (continued).

$I_i^{\pi\,a}$	E_{level} (keV)^b	E_γ (keV)^c	$I_\gamma{}^d$	DCO	λ^e	Multipolarity
$(\frac{71}{2}^-)$	X + 14202	1482	<4			$E2$
$(\frac{75}{2}^-)$	X + 15765	1563	<4			$E2$
		BAND 2 : [541]1/2 $\alpha = +\frac{1}{2}$				
$\frac{1}{2}^-$	Y					
$\frac{5}{2}^-$	Y + 99.0	99.0	18(9)	1.0(1)		$E2$
$\frac{9}{2}^-$	Y + 308.5	209.5	37(7)	0.96(7)	13.0(1)	$E2$
		76.0	4(1)			$M1/E2$
$\frac{13}{2}^-$	Y + 630.9	322.4	38(3)	0.87(7)		$E2$
$\frac{17}{2}^-$	Y + 1064.9	434.0	30(2)	1.01(7)		$E2$
$\frac{21}{2}^-$	Y + 1604.0	539.1	28(2)	1.12(4)		$E2$
$\frac{25}{2}^-$	Y + 2237.1	633.1	26(2)	0.93(7)		$E2$
$\frac{29}{2}^-$	Y + 2949.4	712.3	25(2)	0.94(7)		$E2$
$\frac{33}{2}^-$	Y + 3730.6	781.2	17(1)	1.09(7)		$E2$
$\frac{37}{2}^-$	Y + 4575.9	845.3	12(1)	1.05(6)		$E2$
$\frac{41}{2}^-$	Y + 5487.7	911.8	9(1)	1.06(5)		$E2$
$\frac{45}{2}^-$	Y + 6472.3	984.6	8(1)	0.99(8)		$E2$
$\frac{49}{2}^-$	Y + 7528.3	1056.0	6(1)	1.1(1)		$E2$
$(\frac{53}{2}^-)$	Y + 8637	1108	<4			$E2$
$(\frac{57}{2}^-)$	Y + 9797	1160	<4			$E2$
$(\frac{61}{2}^-)$	Y + 11010	1213	<4			$E2$
$(\frac{65}{2}^-)$	Y + 12266	1256	<4			$E2$

Table 5.2 (continued).

$I_i^{\pi\,a}$	E_{level} (keV)^b	E_γ (keV)^c	$I_\gamma{}^d$	DCO	λ^e	Multipolarity
		BAND 2 : [541]1/2 $\alpha = -\frac{1}{2}$				
$\frac{3}{2}^-$	Y + 54					
$\frac{7}{2}^-$	Y + 178.8	178.8	12(2)	1.0(2)	2.92(4)	$E2$
		133.6	14(9)	0.9(2)		$M1/E2$
$\frac{11}{2}^-$	Y + 476.3	297.5	18(2)	1.1(1)	4.5(3)	$E2$
		221.50	9(1)			$M1/E2$
$\frac{15}{2}^-$	Y + 888.9	412.6	20(2)	1.0(1)	19(3)	$E2$
		312.0	<4			$M1/E2$
$\frac{19}{2}^-$	Y + 1407.7	518.8	25(2)	1.0(3)	10(1)	$E2$
		397.2	5(1)			$M1/E2$
$(\frac{23}{2}^-)$	Y + 2013.5	605.8	22(2)		12(1)	$E2$
		464.0	<4			$M1/E2$
$(\frac{27}{2}^-)$	Y + 2685.2	671.7	21(3)			$E2$
$(\frac{31}{2}^-)$	Y + 3405.2	720.0	19(2)			$E2$
$(\frac{35}{2}^-)$	Y + 4160.3	755.1	16(1)			$E2$
$(\frac{39}{2}^-)$	Y + 4978.3	818.0	10(1)			$E2$
$(\frac{43}{2}^-)$	Y + 5881.2	902.9	9(1)			$E2$
$(\frac{47}{2}^-)$	Y + 6873.1	991.9	8(1)			$E2$
$(\frac{51}{2}^-)$	Y + 7956.8	1083.7	7(1)			$E2$
$(\frac{55}{2}^-)$	Y + 9122.8	1166.0	5(1)			$E2$
$(\frac{59}{2}^-)$	Y + 10361.9	1239.1	4(1)			$E2$
$(\frac{63}{2}^-)$	Y + 11667	1305	<4			$E2$
$(\frac{67}{2}^-)$	Y + 13036	1369	<4			$E2$
$(\frac{71}{2}^-)$	Y + 14474	1438	<4			$E2$

Table 5.2 (continued).

$I_i^{\pi\,a}$	E_{level} (keV)^b	E_γ (keV)^c	$I_\gamma{}^d$	DCO	λ^e	Multipolarity
		BAND 3 : [411]1/2 $\alpha = +\frac{1}{2}$				
$\frac{1}{2}^+$	Z					
$\frac{5}{2}^+$	Z + 178.8	178.8	6(1)		0.51(4)	$E2$
		157.0	14(2)	0.55(5)		$M1/E2$
$\frac{9}{2}^+$	Z + 497.2	318.4	13.7(9)	1.02(9)	1.23(9)	$E2$
		267.5	8(1)	0.9(1)		$M1/E2$
$\frac{13}{2}^+$	Z + 936.3	439.1	25(2)	0.91(7)	3.53(3)	$E2$
		354.3	9(1)			$M1/E2$
$\frac{17}{2}^+$	Z+ 1471.7	535.4	25(2)	0.9(1)		$E2$
$\frac{21}{2}^+$	Z + 2076.4	604.7	23(2)	1.1(2)		$E2$
$(\frac{25}{2}^+)$	Z + 2734.7	658.3	16(2)			$E2$
$(\frac{29}{2}^+)$	Z + 3418.4	683.7	<4			$E2$
		BAND 3 : [411]1/2 $\alpha = -\frac{1}{2}$				
$\frac{3}{2}^+$	Z + 22					
$\frac{7}{2}^+$	Z + 208.2	208.2	53(9)	0.95(5)	5.92(7)	$E2$
		138.8	13(4)	0.43(6)		$M1/E2$
$\frac{11}{2}^+$	Z + 559.8	351.6	75(4)	0.94(5)	7.09(7)	$E2$
		344.8	5.7(6)	0.71(9)		$E2$
$\frac{15}{2}^+$	Z + 1032.5	472.7	65(4)	1.09(7)		$E2$
$\frac{19}{2}^+$	Z + 1599.1	566.6	57(3)	0.97(6)		$E2$
$\frac{23}{2}^+$	Z + 2227.1	628.0	54(3)	0.95(6)		$E2$
$\frac{27}{2}^+$	Z + 2888.4	661.3	48(3)	1.10(5)		$E2$
$\frac{31}{2}^+$	Z + 3573.1	684.7	33(2)	0.93(5)		$E2$
$\frac{35}{2}^+$	Z + 4299.9	726.8	32(2)	1.05(5)		$E2$
$\frac{39}{2}^+$	Z + 5094.5	794.6	21(1)	1.10(6)		$E2$

Table 5.2 (continued).

$I_i^{\pi\,a}$	E_{level} (keV)^b	E_γ (keV)^c	$I_\gamma{}^d$	DCO	λ^e	Multipolarity
$\frac{43}{2}^+$	Z + 5952.3	857.8	15(1)	1.05(6)		$E2$
$(\frac{47}{2}^+)$	Z + 6879.9	927.6	9.9(4)			$E2$
$(\frac{51}{2}^+)$	Z + 7895.1	1015.2	8.7(9)			$E2$
$(\frac{55}{2}^+)$	Z + 9002.7	1107.6	7.1(8)			$E2$
$(\frac{59}{2}^+)$	Z + 10200.9	1198.2	4.9(7)			$E2$
$(\frac{63}{2}^+)$	Z + 11489.8	1288.9	4.5(2)			$E2$
$(\frac{67}{2}^+)$	Z + 12871	13801	<4			$E2$
$(\frac{71}{2}^+)$	Z + 14344	1473	<4			$E2$
		BAND 4 : [402]5/2 $\alpha = +\frac{1}{2}$				
$\frac{5}{2}^+$	Z+91					
$\frac{9}{2}^+$	Z + 415.5	324.5	28(2)	0.97(6)	0.84(7)	$E2$
		179.1	32(3)	0.43(7)		$M1/E2$
$\frac{13}{2}^+$	Z + 868.2	452.7	32(2)	0.88(6)	1.3(1)	$E2$
		239.3	22(2)	0.72(5)		$M1/E2$
$\frac{17}{2}^+$	Z + 1419.5	551.3	36(3)	1.00(8)	2.5(1)	$E2$
		282.1	17(1)	0.72(9)		$M1/E2$
		482.6	<4	0.9(1)		$E2$
$\frac{21}{2}^+$	Z + 2034.6	615.1	34(3)	1.15(9)	2.9(2)	$E2$
		304.7	9.9(8)	0.69(9)		$M1/E2$
$\frac{25}{2}^+$	Z + 2665.7	631.1	38(3)	1.01(6)	8.0(9)	$E2$
		286.9	5.5(7)	0.5(1)		$M1/E2$
		417.8	5.0(9)	0.63(7)		$M1/E2$
		589.2	9(1)	0.9(1)		$E2$
$\frac{29}{2}^+$	Z + 3292.3	626.6	36(3)	0.88(5)		$E2$
$\frac{33}{2}^+$	Z + 3960.2	667.9	25(2)	0.87(3)		$E2$

Table 5.2 (continued).

$I_i^{\pi\,a}$	E_{level} (keV)^b	E_γ (keV)^c	$I_\gamma{}^d$	DCO	λ^e	Multipolarity
$\frac{37}{2}^+$	Z + 4703.6	743.4	20(2)	0.89(8)		$E2$
$\frac{41}{2}^+$	Z + 5521.9	818.3	20(2)	1.03(5)		$E2$
$(\frac{45}{2}^+)$	Z + 6415.1	893.2	15(1)			$E2$
$(\frac{49}{2}^+)$	Z + 7395.3	980.2	11(1)			$E2$
$(\frac{53}{2}^+)$	Z + 8471.4	1076.1	7(1)			$E2$
$(\frac{57}{2}^+)$	Z + 9643.2	1171.8	4(1)			$E2$
$(\frac{61}{2}^+)$	Z + 10903	1259	<4			$E2$
$(\frac{65}{2}^+)$	Z + 12222	1319	<4			$E2$
$(\frac{69}{2}^+)$	Z + 13576	1354	<4			$E2$
		BAND 4 : [402]5/2 $\alpha = -\frac{1}{2}$				
$\frac{7}{2}^+$	Z + 237.1	146.1	38(13)	0.47(2)		$M1/E2$
$\frac{11}{2}^+$	Z + 629.4	392.3	21(1)	1.09(9)	0.76(5)	$E2$
		213.7	29(2)	0.65(3)		$M1/E2$
$\frac{15}{2}^+$	Z + 1136.8	507.4	30(2)	0.92(9)	1.45(9)	$E2$
		268.5	14(1)	0.57(5)		$M1/E2$
$\frac{19}{2}^+$	Z + 1730.2	593.4	30(2)	1.1(1)	2.4(2)	$E2$
		311.0	8(1)			$M1/E2$
$\frac{23}{2}^+$	Z + 2378.9	648.7	32(2)	1.0(1)	4.2(7)	$E2$
		344.8	9(1)			$M1/E2$
$(\frac{27}{2}^+)$	Z + 3053.5	674.6	22(2)			$E2$
$(\frac{31}{2}^+)$	Z + 3712.6	659.1	14(2)			$E2$
$(\frac{35}{2}^+)$	Z + 4413.1	700.5	10(1)			$E2$
$(\frac{39}{2}^+)$	Z + 5192.5	779.4	7(1)			$E2$
$(\frac{43}{2}^+)$	Z + 6078.9	886.4	4(1)			$E2$
$(\frac{47}{2}^+)$	Z + 7078	999	<4			$E2$

Table 5.2 (continued).

$I_i^{\pi\,a}$	E_{level} (keV)^b	E_γ (keV)^c	$I_\gamma{}^d$	DCO	λ^e	Multipolarity
$(\frac{51}{2}^+)$	Z + 8178	1100	<4			$E2$
$(\frac{55}{2}^+)$	Z + 9337	1159	<4			$E2$

[a] Spin and parity of the initial state.

[b] (X,Y,Z) are unknown constant energy values which should be added to the listed energy levels since the real excitation energies of the configurations are not known.

[c] Uncertainties in E_γ are 0.2 keV for most transitions except for relatively weak transitions which are 0.5 keV.

[d] Relative intensity of the transition where $I_\gamma(524.3) \equiv 100$.

[e] Branching Ratio (=$I(E2)/I(M1)$) was extracted by gating above the level of interest.

[f] Intensity could not be determined.

$\frac{75}{2}$ from the Gammasphere data (see inset of Fig. 5.4(a)) and is the most intensely populated sequence in ^{129}Nd. The in-band properties (alignments and $B(M1)/B(E2)$ ratios) indicate a negative-parity configuration and this band is likely the yrast structure built on the $\frac{7}{2}^-$ isomeric state observed in Ref. [118]. The yrast sequence in ^{125}Ba, ^{127}Ce, and ^{131}Nd also have $\frac{7}{2}^-$ band-head states, which is consistent with our assignment.

A second sequence of transitions was identified in the $A = 129$ matrix and is shown in Fig. 5.4(b). Similar to band 1, the strongest transitions were associated with the $2p$ channel. Thus, this new structure can also be firmly assigned to ^{129}Nd even though no linking transitions were observed. The Gammasphere data allowed for the extension of the sequence up to $I = \frac{71}{2}$ as seen in the inset of Fig. 5.4(b) and Fig. 5.2, where the structure is labeled as band 2. Additionally, the signature partner of band 2 was identified in the Gammasphere data and a representative spectrum is displayed in Fig. 5.4(c). From Fig. 5.2, one may notice that band 2 is weakly coupled with one signature lying lower in energy than its partner. Analysis of the in-band

properties (*e.g.*, alignment and signature splitting, see below) of band 2 indicates a negative-parity assignment is appropriate, and the similarities with a structure in ^{131}Nd (where spins and parities are known) suggest a band-head spin of $\frac{1}{2}^-$ for band 2.

Positive-parity Structures

The sequence displayed in Fig. 5.5(a) was observed in the ORNL data, and in a similar manner to bands 1 and 2 discussed above, it was firmly assigned to ^{129}Nd. The structure is labeled as band 3 in Fig. 5.2 and it was extended to $I = \frac{71}{2}$ from the Gammasphere data as shown in the inset of Fig. 5.5(a). A short sequence of transitions was also found in the Gammasphere data (see Fig. 5.5(b)), which was identified as the signature partner of band 3. One may notice in Fig. 5.2 that the latter sequence lies much higher in excitation energy than its partner, which is why it could not be extended to higher spins. Band 3 has similar in-band properties as a low-K, positive-parity structure in ^{131}Nd and, therefore, it has been assigned even parity and a band-head spin of $\frac{1}{2}^+$.

A new strongly-coupled band, which interacts with band 3 at low spins, has been observed in the Gammasphere data. Spectra of both signatures are given in Figs. 5.5(c) and (d) and the band is labeled as band 4 in Fig. 5.2. A DCO ratio of 0.43(6) was found for the 138.8-keV transition depopulating the $\frac{7}{2}^+$ state in band 3 to the band-head of band 4, indicating a change in spin of 1 $\hbar$. The 482.6 and 589.2 keV linking transitions from band 4 to 3 were determined to have an $E2$ nature (see Table 5.2), which establishes that bands 3 and 4 have the same parity and the 138.8-keV transition must correspond to a $I \rightarrow I - 1$ deexcitation. Therefore, a band-head spin of $\frac{5}{2}^+$ is assigned, which is consistent with the configuration (see below) and systematics observed for similar structures in ^{131}Nd and ^{127}Ce.

5.4 Configuration Assignments

In order to help identify the active orbitals nearest to the Fermi surface at $N = 69$, we provide a neutron single-particle diagram in Fig. 5.6. Total Routhian surface

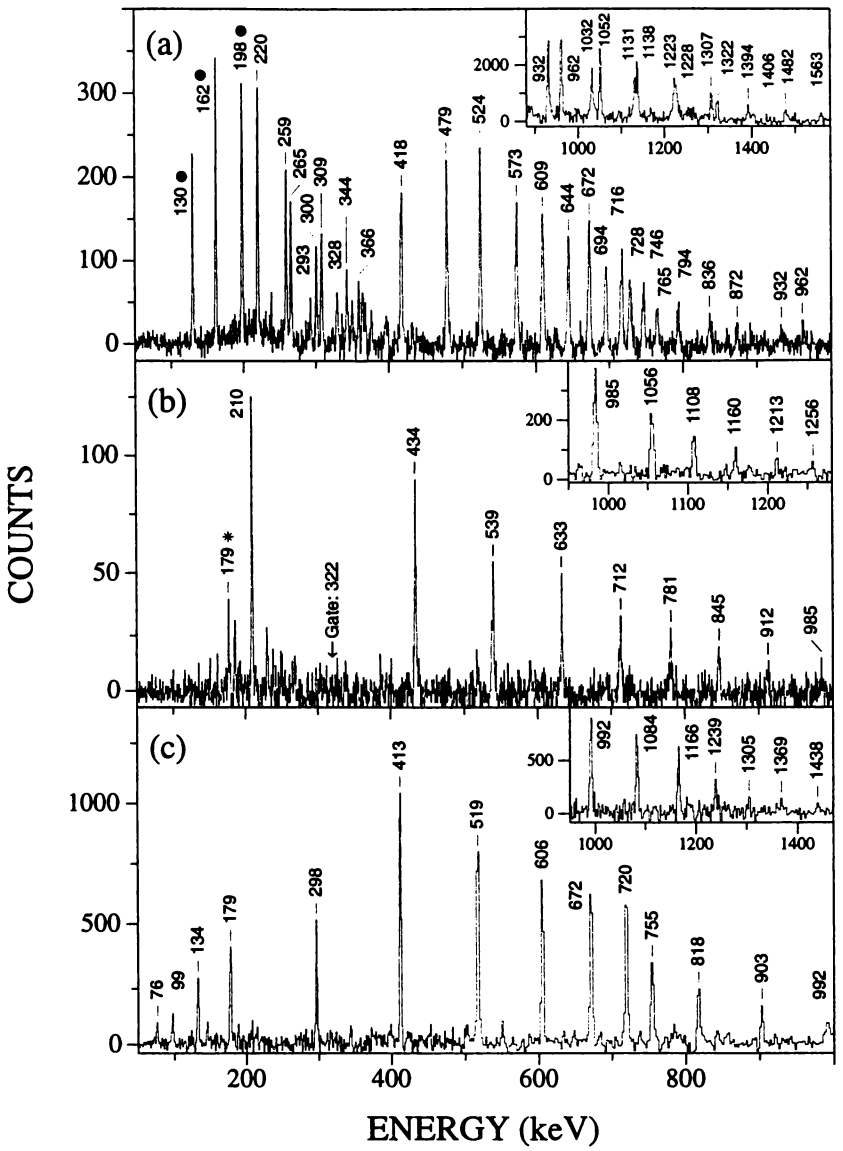


Figure 5.4: Spectra of the negative-parity configurations: (a) both signatures of band 1, and (b) $\alpha = +\frac{1}{2}$ and (c) $\alpha = -\frac{1}{2}$ of band 2. The main spectra in panels (a) and (b) are ORNL mass-gated spectra. The main spectrum in panel (a) is produced from the sum of the individual gated spectra of the peaks denoted by a filled circle. The spectrum produced in the main panel (c) and all the insets in the figure are the the sum of many double-gated coincidence spectra from Gammasphere data. Peaks denoted by $*$ are associated with γ rays from signature partners.

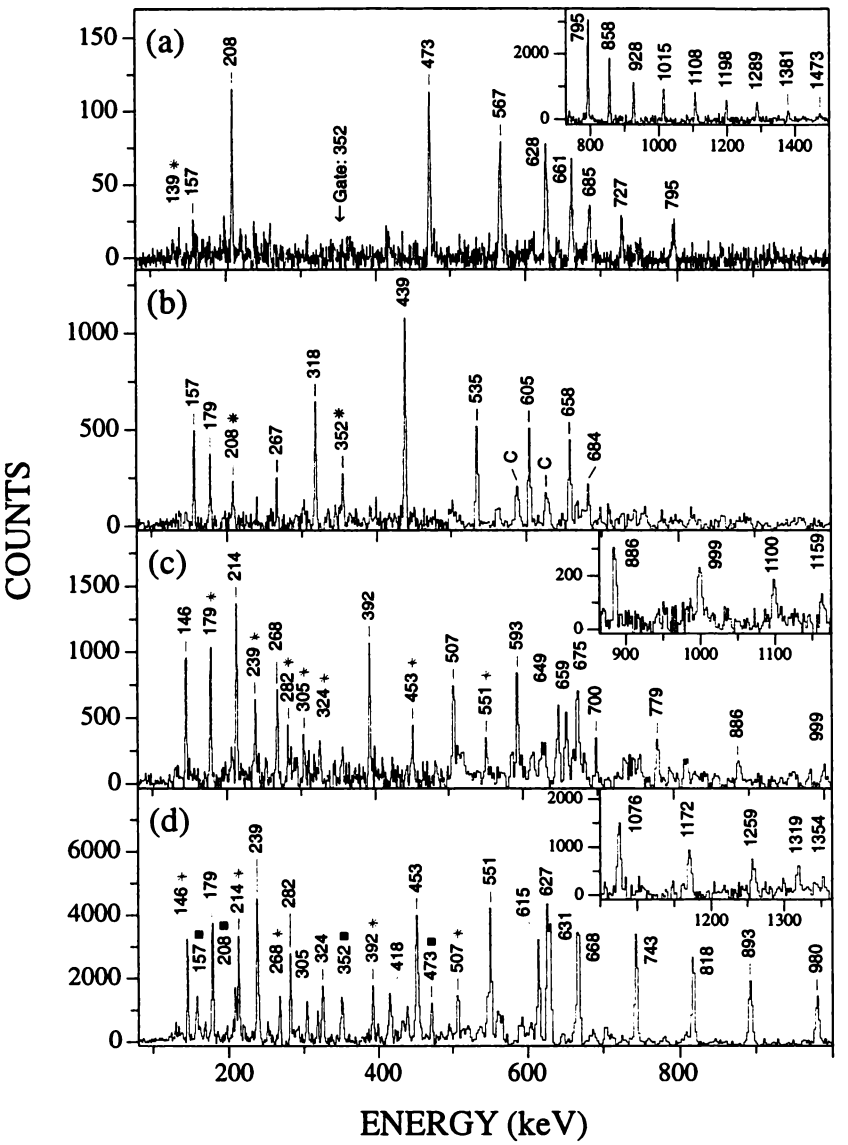


Figure 5.5: Sample spectra of the positive-parity configurations: (a) $\alpha = -\frac{1}{2}$, (b) $\alpha = +\frac{1}{2}$ of band 3, and (c) $\alpha = -\frac{1}{2}$, (d) $\alpha = +\frac{1}{2}$ of band 4. The insets in panels (a), (c), (d) and the spectra in main panels (b), (c), (d) are the result of summing many double-gated coincidence spectra from Gammasphere data. The main spectrum in panel (a) is an ORNL mass-gated spectrum. Peaks denoted by $*$ are associated with γ rays from signature partners, and peaks denoted by "c" are contaminant γ rays. Peaks denoted by filled squares in panel (d) belong to band 3.

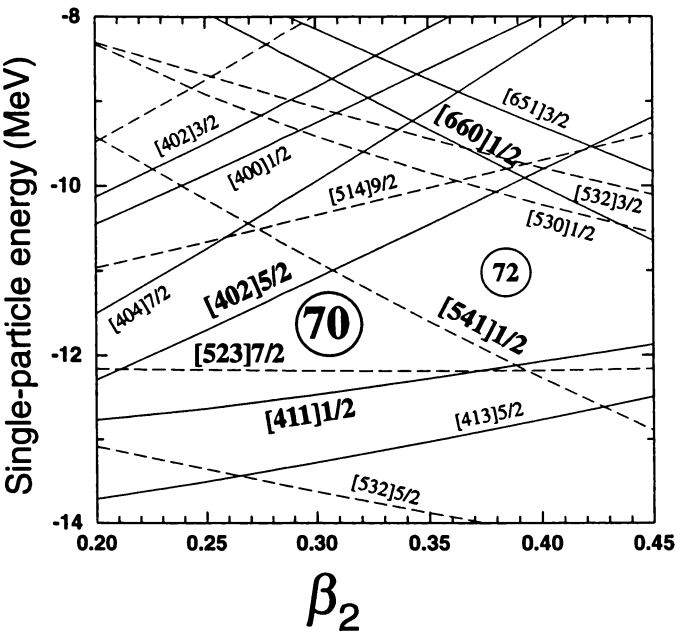


Figure 5.6: Neutron single-particle levels as a function of quadrupole deformation (where $\beta_4 = 0$ and $\gamma = 0°$) calculated using the Woods-Saxon potential [123, 124] with parameters given in Ref. [125].

(TRS) calculations [27] predict a ground-state deformation near $\beta_2 = 0.305$ for ^{129}Nd. For a prolate deformation of this size, one can deduce from Fig. 5.6 that bands based on the $h_{11/2}[523]7/2$, $d_{3/2}[411]1/2$, $d_{5/2}[402]5/2$, and $(h_{9/2}/f_{7/2})[541]1/2$ orbitals should be observed at relatively low excitation energies. Band characteristics such as the alignment behavior, the $B(M1)/B(E2)$ ratios, and the signature splitting were considered to associate the observed bands in ^{129}Nd with the orbitals mentioned above.

5.4.1 Alignments and band crossings

We introduce below supporting arguments for the quasiparticle assignments in ^{129}Nd based on CSM predictions of alignments and band crossings. The alignments of the bands in ^{129}Nd are plotted versus rotational frequency in Fig. 5.7. Harris parameters [24] of $\mathcal{J}_0 = 22\ \hbar^2/\text{MeV}$ and $\mathcal{J}_1 = 17\ \hbar^4/\text{MeV}^3$ were used to subtract the angular momentum of the collective core. These parameters were chosen such that $\mathcal{J}_0$ gives

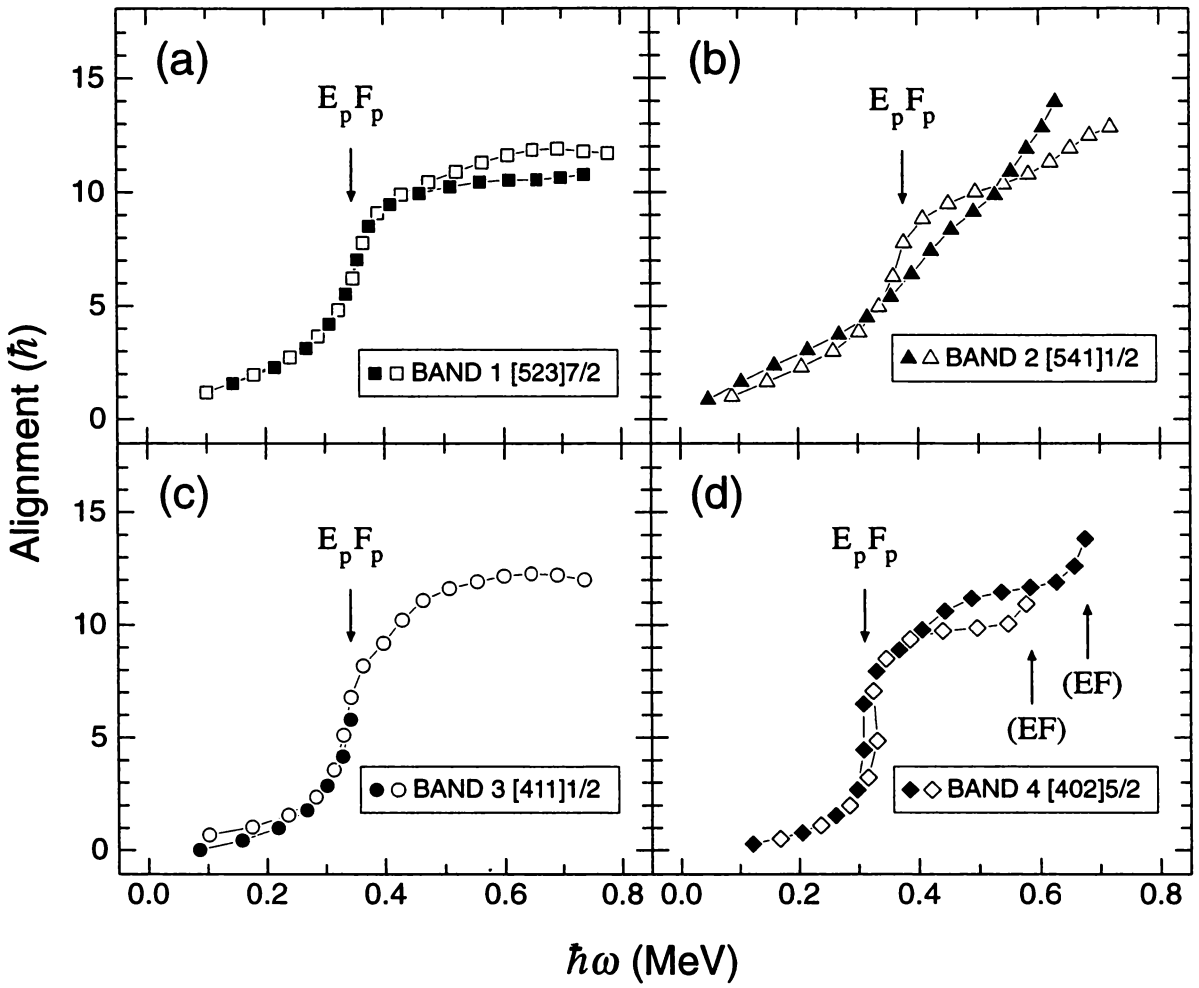


Figure 5.7: The alignment plotted versus rotational frequency for bands 1-4. Harris parameters of $\mathcal{J}_0 = 22\ \hbar^2/\text{MeV}$ and $\mathcal{J}_1 = 17\ \hbar^4/\text{MeV}^3$ were used to subtract the angular momentum of the collective core. The positive and negative signatures are denoted by filled and open symbols, respectively. Proposed band-head configurations are also given in the legends.

an initial zero alignment in the ground-state band of ^{128}Nd, and $\mathcal{J}_1$ value is chosen to give a rather flat alignment curve above the band crossing for the yrast [523]7/2 band in ^{129}Nd. The observed crossings are labeled in Fig. 5.7 using the standard alphabetic quasiparticle labeling scheme [126], which was summarized previously in Table 4.2 in terms of the orbital's parity, signature (π, α), and configuration at zero rotational frequency.

Negative-parity structures

Watson *et al.* [116] suggested that band 1 is based upon an $\nu h_{11/2}$ orbital, but due to limited information, they were not able to propose a definitive configuration. The band undergoes an alignment at $\hbar\omega_c \sim 0.35$ MeV and has an alignment gain of $\Delta i \sim 9$ $\hbar$. The only quasiparticles near the Fermi surface that can align at this low frequency and produce the large alignment gain are the lowest $h_{11/2}$ quasiprotons (E_p and F_p). The E_pF_p band crossing is well known in the mass 130 region and the alignment gain and crossing frequency are consistent with the first proton crossings observed in other $A \sim 130$ nuclei. Cranked Shell Model (CSM) [70] calculations for the protons and neutrons in ^{129}Nd were performed using the deformation parameters taken from a TRS calculation for the E and F neutron configurations at a frequency of $\hbar\omega \sim 0.30$ MeV. A predicted E_pF_p crossing occurs at $\hbar\omega_c \sim 0.36$ MeV which is in good agreement with the first observed crossing in band 1. In the quasineutron diagram, shown in Fig. 5.8, the first neutron crossing is predicted to occur at $\hbar\omega_c \sim 0.49$ MeV, but no crossings are experimentally observed up to high frequencies of ~ 0.8 MeV. The blocking of this crossing implies that band 1 is based upon a $\nu h_{11/2}$ orbital, which is most likely [523]7/2 as it is the nearest $\nu h_{11/2}$ orbital to the ^{129}Nd Fermi surface (see Fig. 5.6). Thus, the negative-parity and band-head spin assignments shown in Fig. 5.2 are consistent with similar bands in nearby nuclei. The CSM predicts two other neutron crossings, *i.e.* the FG and EH crossings at ~ 0.6 MeV as seen in Fig. 5.8; however neither crossing is observed in band 1. This behavior is contrary to ^{131}Nd where both of these crossings are observed near the predicted CSM frequency of ~ 0.6 MeV [85]. These crossings may be delayed in a manner similar to the delayed

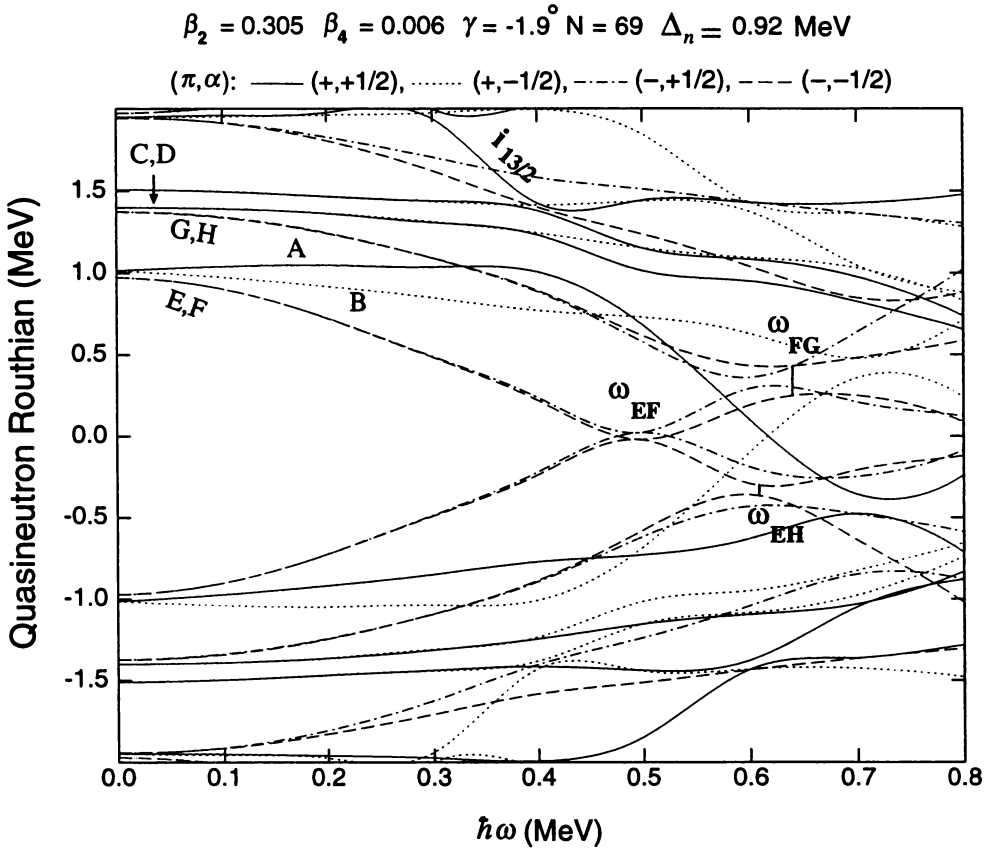


Figure 5.8: Cranked shell model calculation for quasineutrons in ^{129}Nd. The deformation parameters (shown at the top of the figure) were determined from TRS calculations. Interpretation of the lines is displayed at the top of the figure. Explanation of the orbital labeling scheme is given in Table 4.2.

EF crossings observed in even-even Ce and Nd nuclei (see discussion in Chapter 4), and also in other bands in ^{129}Nd (see below).

As seen from Fig. 5.7(a), the negative signature of band 1 has $\sim 1-2\ \hbar$ more alignment than its signature partner after the proton alignment. The small magnitude of this alignment indicates that it is not likely due to the FG crossing as $4-5\ \hbar$ has been associated with this alignment in nearby nuclei. TRS calculations were done for both signatures of the $\nu h_{11/2}$ configuration in ^{129}Nd for the frequency range (0.24 - 0.59 MeV) in order to test whether signature dependent deformation effects can account for this behavior. However, the calculations show little difference in potential depth or quadrupole deformation between the two signatures over the frequency range, indicating that this gain of alignment is likely not due to different deformations. The cause(s) of this interaction is not clear at this time.

Band 2 is associated with a low-K configuration as large signature splitting is initially observed (see Fig. 5.2). The gradual increase of alignment at low frequency is similar to that observed in the [541]1/2 bands of ^{131,133}Nd [115, 85]. Also, the apparent differing interaction strengths in the E_pF_p crossing region are strikingly similar to those seen in the $\nu h_{9/2}/f_{7/2}$ bands of ^{131,133}Nd; therefore, band 2 is assigned the [541]1/2 configuration. Rotational bands based on this orbital are known to have an intermediate deformation (between normal and highly deformed) [110]; thus, the chosen Harris parameters may be less appropriate for band 2 causing the gradual increase of alignment at low frequency seen in Fig. 5.7. The differing interaction strengths in the E_pF_p crossing region are unusual as no such signature dependent behavior is observed in the other ^{129}Nd bands. For a more detailed discussion of the [541]1/2 proton crossing the reader is referred to section 5.5.3.

A crossing is observed near 0.54 MeV in the positive signature, while the negative signature shows a crossing near 0.65 MeV. The next possible proton crossing is not predicted to occur until very high frequencies ($\hbar\omega > 1$ MeV); therefore, this second crossing is likely the result of a pair of neutrons aligning. The EF crossing is predicted to occur near 0.5 MeV (see Fig. 5.8); however, one would expect both signatures of the [541]1/2 band to experience this neutron alignment at approximately the same frequency. Therefore, an interpretation of these crossings is at present

lacking.

Positive-parity structures

In Fig. 5.7(c), a large gain in alignment ($\Delta i \sim 9\ \hbar$) can be observed at a crossing frequency of $\hbar\omega_c \approx 0.33$ MeV for the favored signature ($\alpha = -\frac{1}{2}$) of band 3. Once again, the $h_{11/2}$ quasiproton alignment is responsible for this gain. This structure exhibits a significant amount of signature splitting at lower spin (see Fig. 5.2) indicating that it likely corresponds to a low-K sequence. As stated previously, bands 3 and 4 have the same parity and from arguments given below, band 4 most likely has positive parity. Inspection of Fig. 5.6 indicates that the nearest positive-parity, low-K orbital is the [411]1/2 level, and, thus, band 3 is assigned this configuration. A second alignment in band 3 occurs near 0.43 MeV inducing a gain of $\sim$ 2-3 $\hbar$. While it is possible this is the EF crossing, it appears to be at a crossing frequency lower than expected by CSM calculations and much lower than that observed in band 4 (see below). The EF crossing is also known to be delayed in this region, rather than to occur at lower than expected frequencies (see discussion in Chapter 4). Perhaps this is a crossing with a "more-deformed" band as is seen at $\hbar\omega \sim 0.2$ MeV in the [411]1/2 band of ^{131}Nd. The more-deformed sequence is caused by a pair of neutrons scattering into the deformation driving [541]1/2 orbital. Once again, similar to ^{131}Nd, the [411]1/2 band is the only sequence to experience this crossing, which Hartley *et al.* [85] suggested to be a result of blocking and Fermi level position effects for the other bands. The higher crossing frequency in ^{129}Nd as compared with ^{131}Nd is due to the [541]1/2 orbital likely lying higher in energy for the former nucleus.

The lack of signature splitting in band 4 (up to spin $\frac{23}{2}$), as shown in Fig. 5.2, suggests a configuration with high K. The [402]5/2 and [413]5/2 orbitals are possible candidates, but the $B(M1)/B(E2)$ ratios, discussed in the following section, clearly indicate that band 4 should be associated with the [402]5/2 orbital. This assignment is consistent with a similar structure found in the $^{127}_{58}$Ce [119] isotone and in ^{131}Nd. Wilmarth *et al.* [117] suggested an $I^{\pi} = (\frac{5}{2}^{+})$ assignment for the ground state of ^{129}Nd. If this is correct, we can rule out the possibility that the ground state is based on

the [402]5/2 configuration since the [402]5/2 band lies higher in energy relative to the [411]1/2 orbital, as seen in Fig. 5.2. Inspection of Fig. 5.6, as well as the observed intensities, indicates that the [411]1/2 and the [523]7/2 orbitals are much closer to the Fermi surface than any other $K = \frac{5}{2}$ state. Therefore, either the $\frac{1}{2}^+$ or the $\frac{7}{2}^-$ state from bands 3 and 1, respectively, should also be considered as possible candidates for the ground state of ^{129}Nd.

The alignment of the negative signature of band 4, shown in Fig. 5.7(d), indicates that the sequence undergoes the E_pF_p crossing at $\hbar\omega_c \approx 0.31$ MeV. The upbend near 0.6 MeV is likely the EF neutron crossing. An additional gain of $\sim 2\hbar$ in alignment occurs in the positive signature after the proton alignment, as compared with the negative signature, at $\hbar\omega_c \sim 0.43$ MeV. A crossing with a more-deformed band, as seen in band 3, is unlikely since both signatures would be expected to experience an alignment gain. Instead, an adiabatic crossing with the $\nu i_{13/2}$ orbital may cause the additional alignment gain in the positive signature of band 4. This is reminiscent of an $i_{13/2}$ crossing in ^{131}Nd [85] and ^{135}Sm [127]. The occupation of the $i_{13/2}$ neutron intruder orbitals is known to be a prominent factor in driving the nuclear shape towards higher deformation for nuclei in the $A\sim130$ region [110, 113]. By inspecting the CSM calculations in Fig. 5.8, one can see that the $\nu i_{13/2}$ [660]1/2 intruder orbital interacts with the C configuration ([402]5/2 orbital) at $\hbar\omega_c \sim 0.43$ MeV, which is remarkably consistent with the experimental observations. The alignment gain near 0.7 MeV is likely the EF crossing, which is delayed in comparison with observations in the negative signature. Such a delay is consistent with the positive signature having larger deformation due to the exchange of character from $d_{5/2}$ to $i_{13/2}$. Thus, there is evidence to suggest the observation of the intruder $i_{13/2}$ orbital; however, further experimental verification of the larger deformation is required to confirm the assignment.

5.4.2 $B(M1)/B(E2)$ transition strength ratios

Further support for the quasiparticle configuration assignments can be derived from the analysis of measured $B(M1)/B(E2)$ ratios for each of the observed configurations

in ^{129}Nd. Experimental $B(M1)/B(E2)$ ratios were extracted using the observed γ-ray energies and branching ratios $[\lambda = I_\gamma(I \rightarrow I-2)/I_\gamma(I \rightarrow I-1)]$ according to the standard formula [35]

$$\frac{B(M1: I \rightarrow I-1)}{B(E2: I \rightarrow I-2)} = 0.693 \frac{E_\gamma^5(I \rightarrow I-2)}{E_\gamma^3(I \rightarrow I-1)} \times \frac{1}{\lambda(1+\delta^2)} \left(\frac{\mu_N}{e\mathrm{b}}\right)^2,$$

where E_γ is in MeV. To determine the magnitude of the mixing ratios δ for the $\Delta I = 1$ transitions, rotational model calculations [12] were performed using the measured branching ratios and assuming pure K. The resulting $B(M1)/B(E2)$ ratios are plotted in Fig. 5.9 along with theoretical predictions for possible configurations.

Theoretical calculations of $B(M1)/B(E2)$ ratios were performed with the rotational model form of the $B(E2)$ transition strength [12] and an extended formalism [128] of the geometrical model from Dönau [129] and Frauendorf [37] to determine the $B(M1)$ strength. An intrinsic quadrupole moment of $Q_0 = 5.32$ eb was assumed for ^{129}Nd from TRS calculations. The collective gyromagnetic ratio was given by $g_R = Z/A$ and the g_K values were calculated using a Woods-Saxon potential [123, 124] with the following results for the possible active orbitals shown in Fig. 5.6: $g_K([402]5/2) = -0.49$, $g_K([413]5/2) = 0.40$, $g_K([411]1/2) = 1.90$, $g_K([523]7/2) = -0.32$, and $g_K([541]1/2) = -0.54$.

The $B(M1)/B(E2)$ ratios for the negative- and positive-parity configurations are shown in Figs. 5.9(a) and (b), respectively. Arguments were previously given that band 1 is based upon an $h_{11/2}$ neutron and a good fit is found for the $B(M1)/B(E2)$ ratios with the predicted [523]7/2 values. A good agreement is observed between the experimental values for band 3 and the theoretical calculations for the [402]5/2 orbital. The calculated values for the [413]5/2 configuration are an order of magnitude lower than those found for band 3, so this configuration can be confidently ruled out. Bands 2 and 4 have small $B(M1)/B(E2)$ ratios, as shown in Figs. 5.9(a) and (b), which is expected for low-K structures. Good agreement between the calculated and observed ratios is found for our assignments of bands 2 and 4 as the [411]1/2 and [541]1/2 structures, respectively.

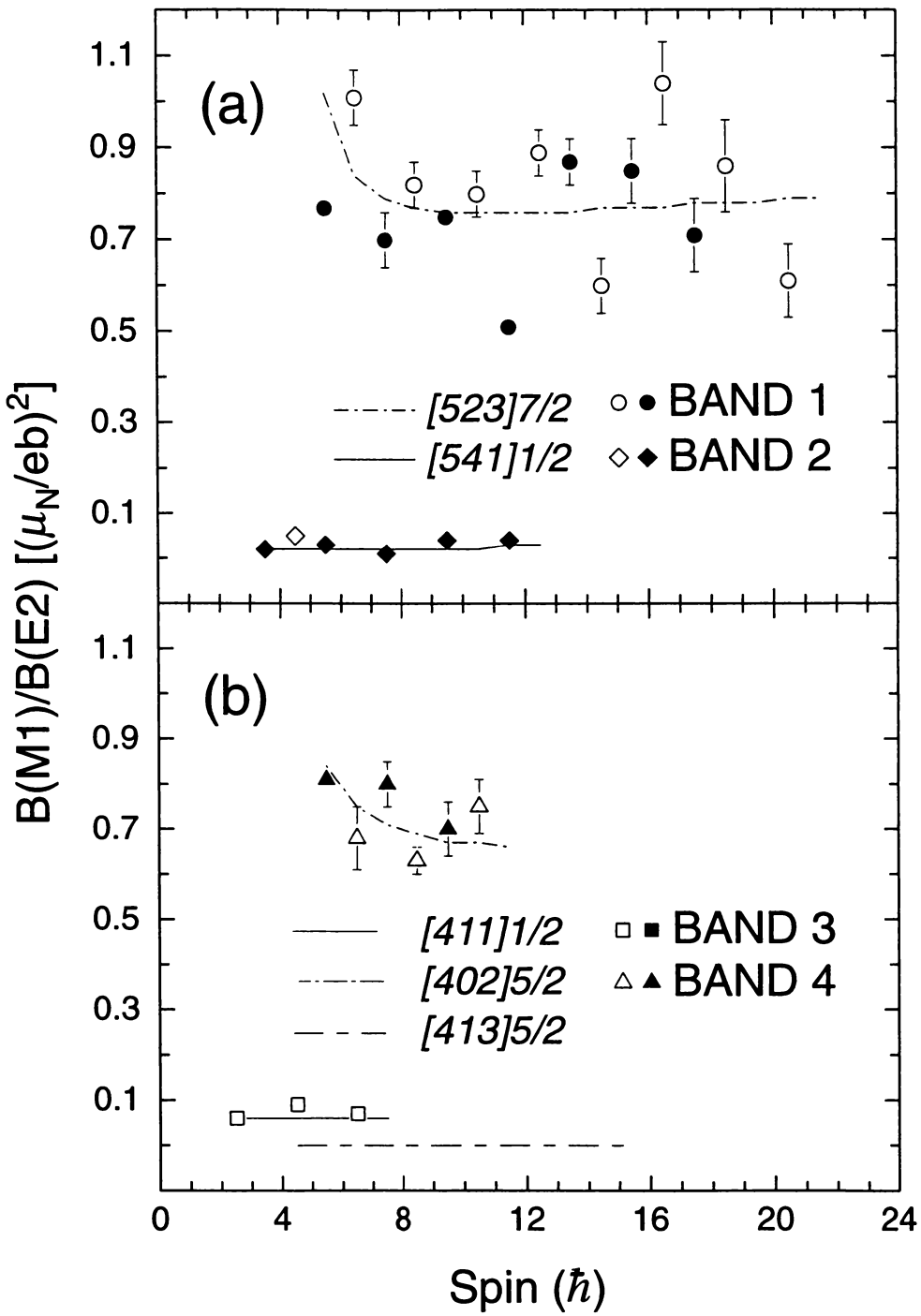


Figure 5.9: The experimental (symbols) and theoretical (lines) $B(M1)/B(E2)$ ratios for (a) bands 1 and 2 and (b) bands 3 and 4. The positive and negative signatures are denoted by filled and open symbols, respectively.

5.5 Discussion of Signature Splitting in $A \sim 130$ Nuclei

Signature splitting is generally measured by determining the difference in Routhian between signature partners of a rotational band at a particular value of the rotational frequency. Two alternate methods that amplify the effects of signature splitting are employed in this present work. In the first method, energy difference between two levels $E(I)$ and $E(I-1)$ is computed and normalized by dividing by $2I$. In the second method, the difference in energy between a level, $E(I)$, and the average of the next higher and lower levels is computed and the result is plotted versus the spin. This energy difference is referred to as the "staggering parameter," $S(I)$, and is given by the following equation:

$$S(I) = E(I) - \frac{1}{2}\,[E(I+1) - E(I-1)]. \tag{5.89}$$

This form of the staggering function has been used by Riedinger *et al.* [130] to study signature inversion in several different doubly-odd nuclei in different mass regions. When these indicators are applied to the energy levels in a rotational band, an alternating pattern (staggering) emerges in which the favored (unfavored) signature has the lowest (highest) values (see discussion in the following section).

This method of examining the difference between the energy levels of signature partner bands can provide a means of testing the deformation character of a given band. Using the technique outlined above, signature splitting for the lightest odd-A ($Z = 56 - 62$) nuclei has been studied and deformation trends have been established which reveal the dependence of signature splitting on triaxial deformation. Similarities with signature splitting in the $\pi h_{11/2}$ bands of the $A \sim 160$ mass region is also presented. We conclude the discussion of signature splitting with a comparison of signature inversion in the $\nu h_{9/2}$ [541]1/2 bands in ^{129,131,133}Nd nuclei. Before introducing the systematics of signature splitting, we present an overview of the quasiparticle deformation-driving effects on the nuclear shape.

5.5.1 The Deformation-Driving Forces in the $h_{11/2}$ Subshells

The ground-states of most deformed nuclei are either prolate or oblate; however, with increasing rotational frequency triaxial shapes in many nuclei are expected due to the deformation-deriving effects of quasiparticles. To determine these effects on the nuclear shape, Leander *et al.* [131] have calculated the quasiparticle energies for a single proton $h_{11/2}$ shell as a function of γ deformation. Cranked shell model calculations were done for different values of the Fermi energy (λ) using a modified oscillator potential and fixing the remaining parameters. Fig. 5.10 summarizes the results for these calculations by showing the Routhian for the lowest lying quasiparticle of opposite signature as a function of γ for nine different values of the Fermi energy. Fig. 5.10(b) shows the energy in oscillator units of each Fermi level used in the calculation along with the non-rotating $h_{11/2}$ single-particle levels at two γ-values, 0° and 60°. Two general features are observed in Fig. 5.10(a):
(1) The minimum of the quasiparticle trajectories for the favored signature has a relatively smooth γ dependence as the Fermi level moves through the shell.
(2) The different signatures of the $\pi h_{11/2}$ may drive the nucleus to different γ deformations with different strengths, where the strength is proportional to the slope of quasiparticle trajectory. The calculations show that the valence quasiparticle orbitals exert strong γ-driving forces on the core. As the Fermi surface rises through a high-j shell, the γ deformation to which the orbitals drive changes smoothly from γ = 0° (prolate) towards γ = -60° (oblate collective).

Quasiparticles also exert an axial-driving force on the nuclear core. Chen and Leander [132] have investigated this effect in the $\pi h_{11/2}$ quasiparticle orbitals as was done for the γ degree of freedom discussed above. Fig. 5.11 shows the axial-driving force, $-de'/d\epsilon_2$, generated by the $\pi h_{11/2}$ quasiparticle orbits as a function of quadrupole deformation (ϵ_2) for several values of the Fermi level. Positive values of $-de'/d\epsilon_2$ indicate that the deformation driving force drives the core to prolate shapes, while negative values drive it to oblate shapes, and in the middle of the shell, the deformation-driving force leads to spherical shapes. In short, Fig. 5.10 shows that the deformation-driving force is greatest (largest slopes) for the low-lying $h_{11/2}$

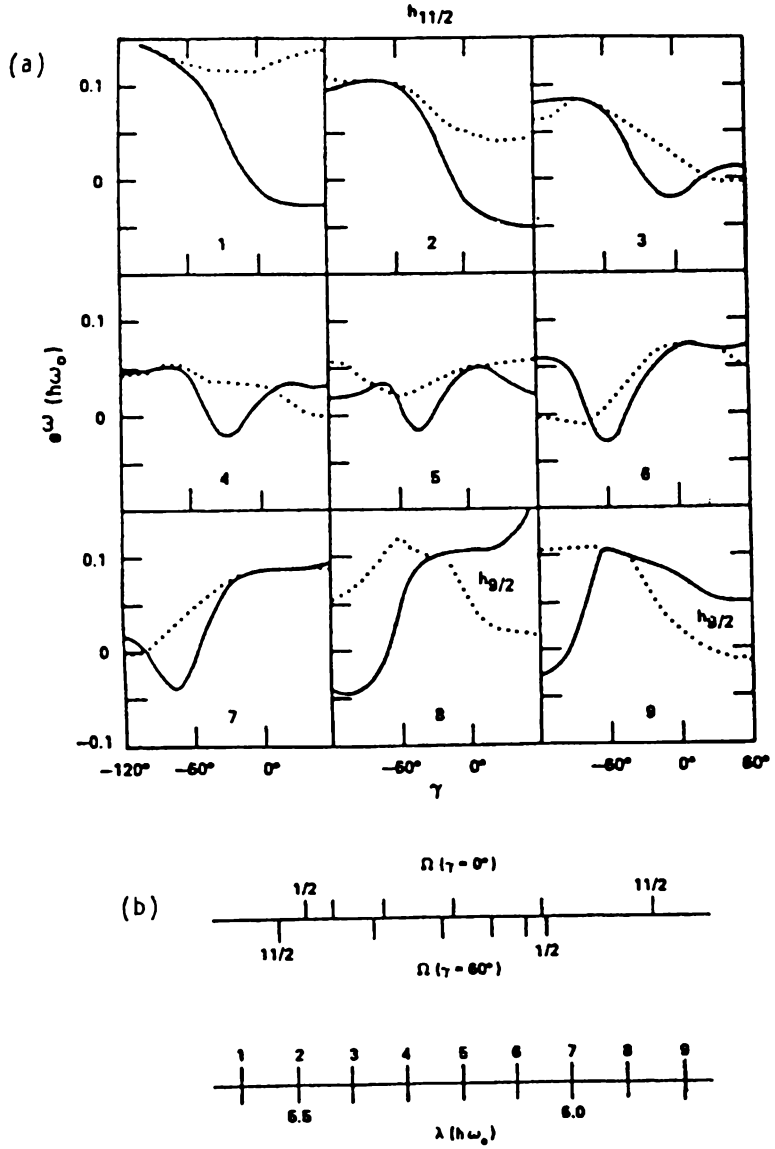


Figure 5.10: The quasiparticle energies as a function of the γ deformation of the lowest favored (solid lines, $\alpha = -1/2$) and unfavored (dashed lines, $\alpha = +1/2$) signatures of the $\pi h_{11/2}$ subshell for nine different values of the Fermi level. Part (b) of the figure shows the value of the Fermi energy used for each diagram in oscillator units. Also pictured are the non-rotating $\pi h_{11/2}$ single-particle levels at two γ-values, 0° and 60°. Reproduced from Leander *et al.* [131].

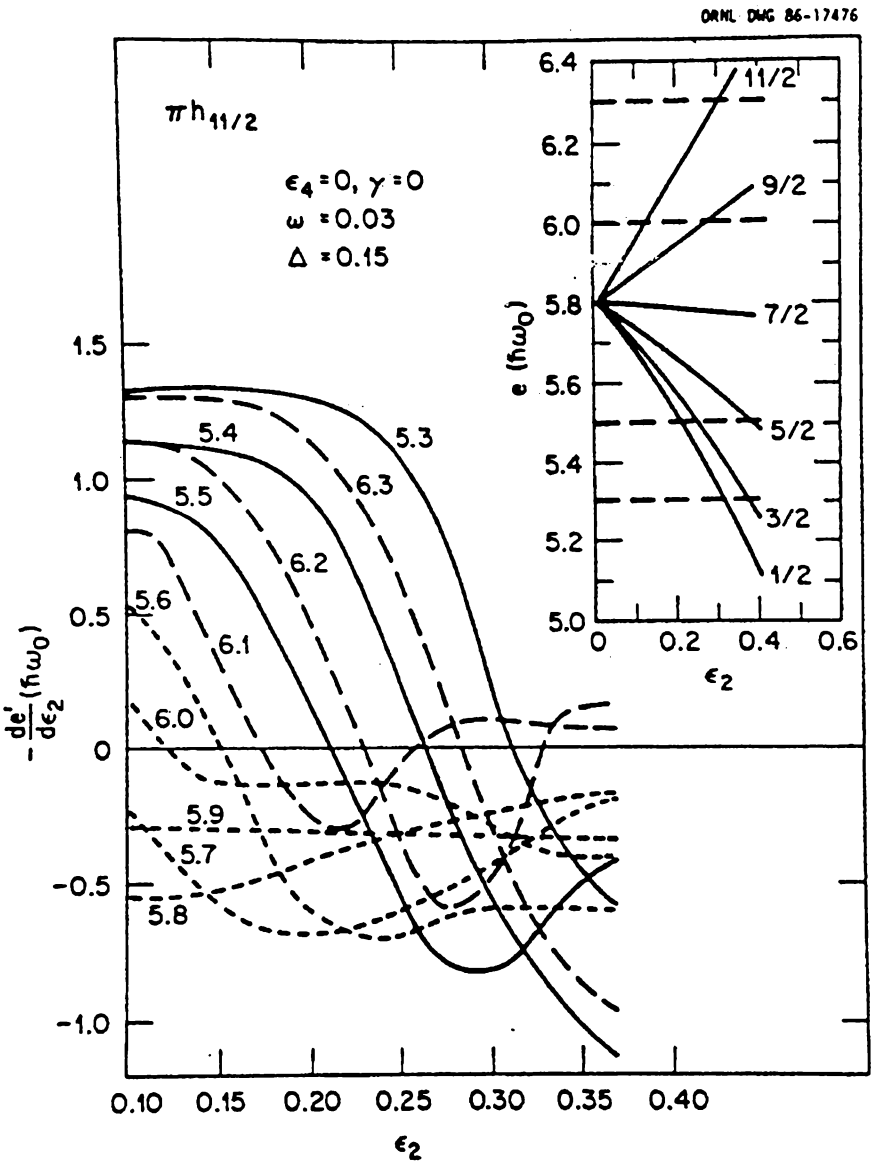


Figure 5.11: The quadrupole-driving force versus ϵ_2 for the $\pi h_{11/2}$ quasiparticles for various values of the Fermi level. The solid curves represent Fermi levels low in the $h_{11/2}$ shell (see inset). Short-dashed lines represent Fermi levels in the middle of the shell and long-dashed lines represent Fermi levels high in the shell. Reproduced from Ref. [133].

quasiparticle orbitals, however, mid to upper members may also influence the shape of the core towards oblate deformations. It is interesting to see that in analogy to the restoring force of a classical spring, the different orbitals have different equilibrium minima (stable points), where $-de'/d\epsilon_2 = 0$.

It is worth mentioning that the discussion presented above for γ and axial deformation-driving effects can be generalized for the neutron $h_{11/2}$ subshells and other proton or neutron high-j subshells as well. Thus, figures 5.11 and 5.10 can also be used as a qualitative guide for determining the γ- and quadrupole-driving forces of high-j quasiparticles.

5.5.2 Signature Splitting Systematics of the $\nu h_{11/2}$ Bands in Odd-$A \sim 130$ Nuclei

Signature is the symmetry quantum number related to the invariance of a nucleonic state under a rotation by 180° about the rotation axis. Odd-A nuclei possess two values of the signature (α) according to the equation $\alpha_I = \frac{1}{2}(-1)^{I-1/2}$, where I is the spin of a given state. Similarly, the energetically favored signature of a coupled band can be determined by $\alpha_f = \frac{1}{2}(-1)^{j-1/2}$. Therefore, in the $\nu h_{11/2}$ bands, the $\alpha = -\frac{1}{2}$ signature is expected to be favored. The degree of signature splitting in a band usually relates to the admixture of the $K = \frac{1}{2}$ component in its wavefunction which has the decoupling parameter [12] separating the two signatures. Therefore, small signature splitting is expected in mid- to high-K orbitals, where only a small component of $K = \frac{1}{2}$ is expected. However, large signature splitting has been observed in $K = (\frac{7}{2}, \frac{9}{2})$ $\pi h_{11/2}$ bands in $N \sim 90$ ($A \sim 160$) nuclei [134], and this was suggested to be the result of negative triaxial deformations [135]. While high-K orbitals tend to drive the soft nuclear core towards oblate shapes, the core prefers a prolate deformation. These two opposing forces can create stable triaxial shapes [82]. Large signature splitting in the $A \sim 130$ region is also observed as the analogous neutron $h_{11/2}$ orbitals are occupied. In our analysis, we investigate the degree of triaxiality needed to achieve the energy splitting within the framework of the CSM and define any observed trends.

The signature splitting of the energy levels for the proton rich Ba-Ce-Nd-

Sm nuclei is displayed in Fig. 5.12. Data for the nuclei, other than ^{129}Nd, were compiled from the following sources: ^{123}Ba [136], ^{125}Ba [35], ^{127}Ba [137], ^{129}Ba [138], ^{131}Ba [139], ^{125}Ce [140], ^{127}Ce [119], ^{129}Ce [95], ^{131}Ce [97], ^{133}Ce [141], ^{131}Nd [85], ^{133}Nd [142], ^{135}Nd [143], ^{133}Sm [144], ^{135}Sm [127], ^{137}Sm [145]. The convention $[E(I)$-$E(I\text{-}1)]/2I$ was used to display the energy splitting, where $E(I)$ is the energy of a state with spin I. For discussion purposes, the calculated quadrupole deformation (β_2) from Ref. [1] has been given in Fig. 5.12 for each nucleus. The large region of deformation covered by these nuclei varying from N=67 ($K = \frac{7}{2}$) to 75 ($K = \frac{9}{2}$), will reveal the signature splitting dependence on β_2 and on the neutron Fermi surface.

Low-Spin Region $I < \frac{27}{2}$

As seen from Fig. 5.12, two general trends are observed:
(1) The signature splitting *increases* with N for a given isotopic chain. This is contrary to what is expected if only Coriolis coupling is involved, as K increases with N. It is also seen that β_2 *decreases* with N, which is related to the proximity of the $N = 82$ spherical shell gap.
(2) The signature splitting *increases* as Z decreases in a given isotone chain, while β_2 *decreases* along the chain due to the $Z = 50$ shell gap.

The decrease in β_2 deformation makes the nuclei more susceptible to the oblate-driving forces of the high-K, $\nu h_{11/2}$ orbitals, and this can produce γ deformation. The signature splitting dependence on γ and β_2 can be investigated within the CSM to reveal which type of deformation plays the dominant role. The nucleus ^{129}Ba was used as an example, since large splitting was observed for the expected high-$K(\frac{9}{2})$ $\nu h_{11/2}$ band. The results of our calculations are presented in Fig. 5.13, where one can see the experimental energy difference in the Routhian ($\Delta e'$) is 200 keV at a frequency of 0.3 MeV. If a small amount of γ-deformation is assumed and held constant, the signature splitting does increase with decreasing β_2 (Fig. 5.13). However, unrealistically low β_2 values must be used to reproduce the experimentally observed splitting in ^{129}Ba, implying that β_2 alone cannot describe the splitting. The experimentally observed splitting can be reproduced using the predicted quadrupole

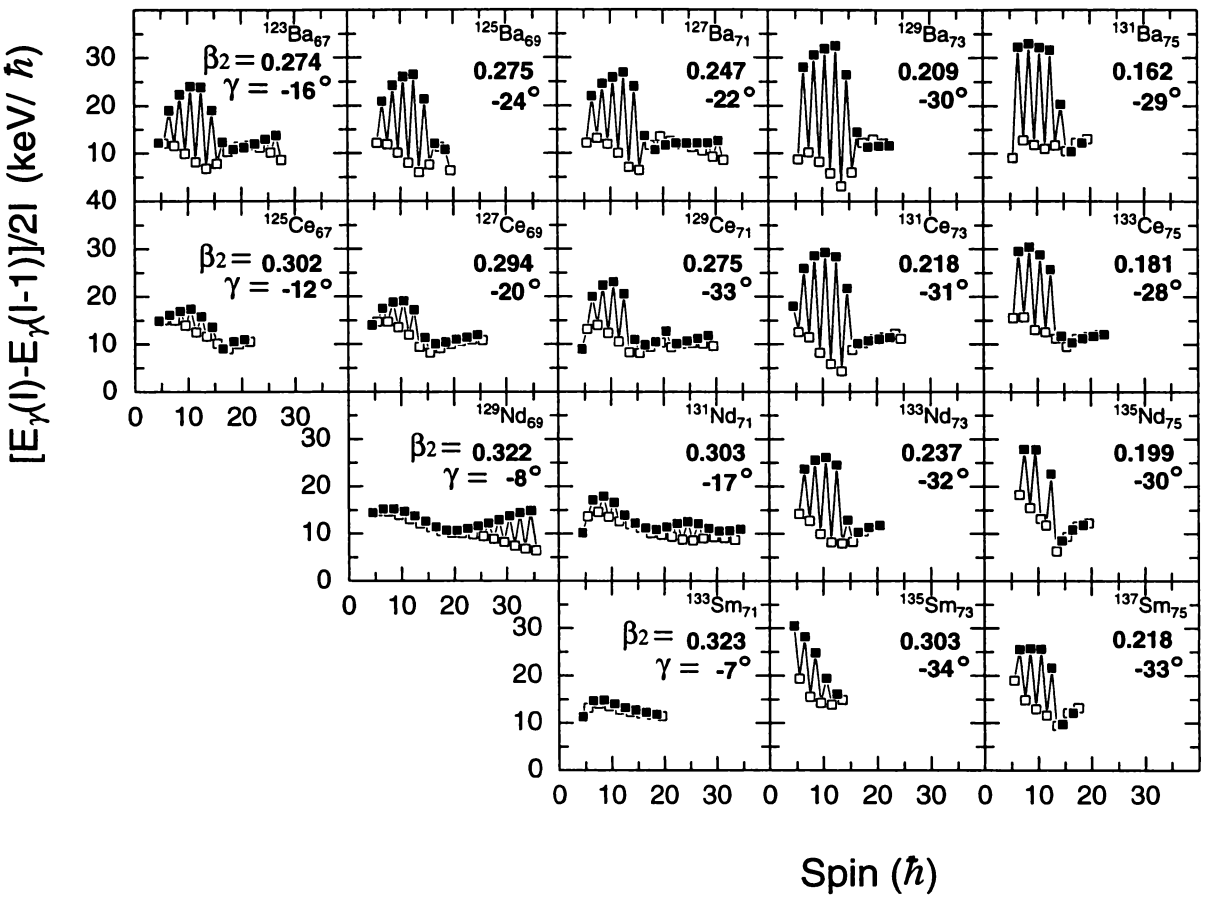


Figure 5.12: Signature splitting for the $\nu h_{11/2}$ bands as a function of spin in odd-A Ba ($Z = 56$), Ce ($Z = 58$), Nd ($Z = 60$), and Sm ($Z = 62$) nuclei. The $\alpha = +\frac{1}{2}$ ($\alpha = -\frac{1}{2}$) signature is denoted by filled (open) squares. K values of $\frac{7}{2}$ and $\frac{9}{2}$ for the $\nu h_{11/2}$ bands are assumed for $N = 67 - 71$ and $N = 73 - 75$, respectively. The quadrupole deformation (β_2) shown for each of the nuclei is taken from Ref. [1]. The γ deformation values shown are evaluated from the CSM as discussed in the text.

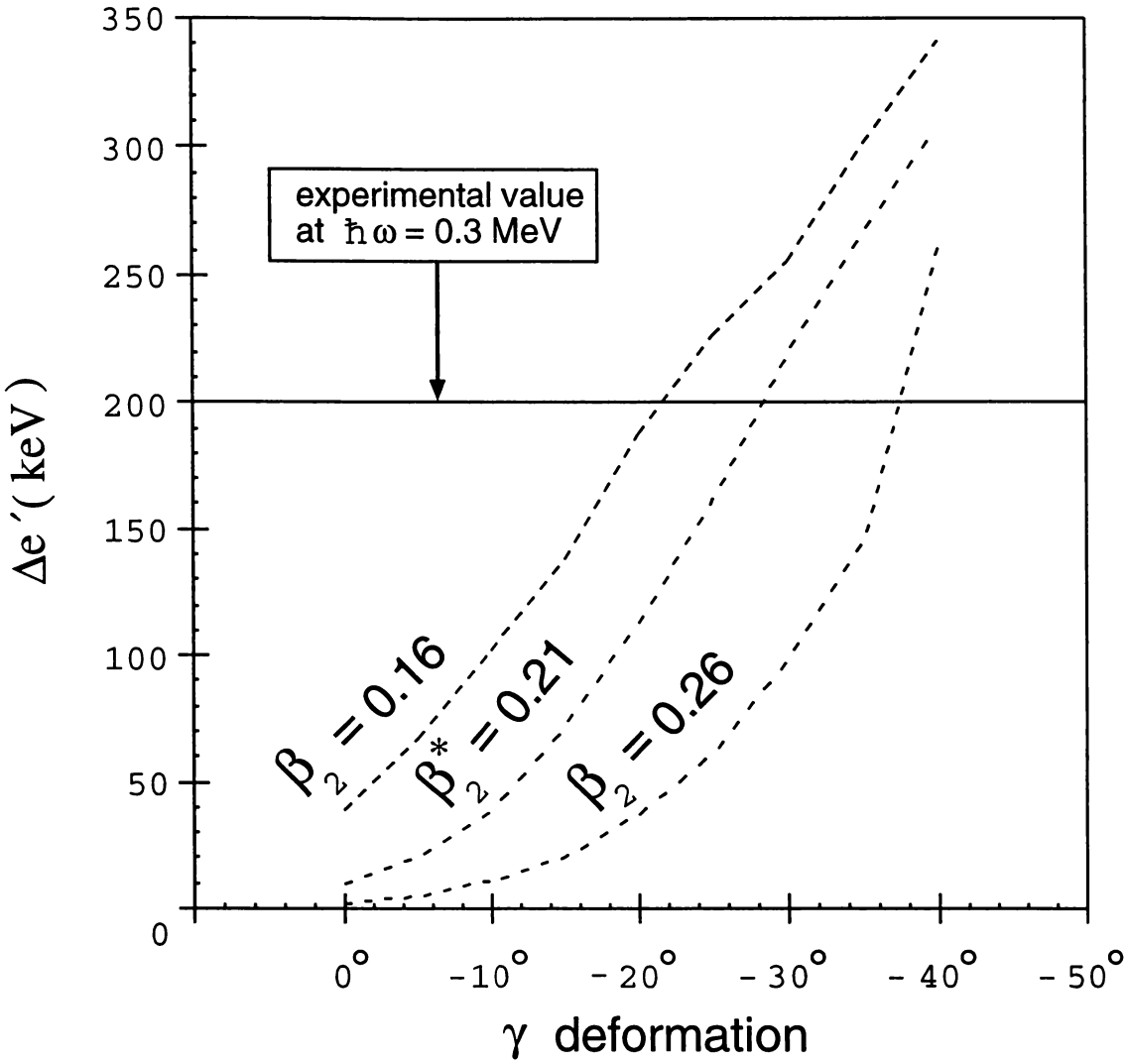


Figure 5.13: Theoretical CSM calculations of signature splitting in the $\nu h_{11/2}$ band versus γ deformation for ^{129}Ba. The calculations were carried out for three different β_2 values at $\hbar\omega = 0.30$ MeV. The β_2 value denoted by an asterisk is taken from Ref. [1].

deformation from Möller *et al.* [1] $\beta_2 = 0.21$ and a reasonable γ value of $-28°$. The experimental crossing frequency can also be reproduced for $\beta_2 = 0.16$ and $\beta_2 = 0.26$ using γ values of $\sim -20°$ and $\sim -36°$, respectively. Therefore, appreciable triaxial deformations appear to be a crucial parameter in CSM calculations in order to reproduce the unusually large splitting in ^{129}Ba.

Using β_2 values from Ref. [1], we performed CSM calculations in a similar manner for every nucleus in Fig. 5.12 in order to investigate the magnitude and the trends in γ deformation. The derived values for the triaxial deformation are shown in Fig. 5.12. A range of negative γ values was found, from $\gamma \sim -10°$ in the lightest nuclei to $\gamma \sim -30°$ in the heaviest. The amount of γ deformation generally increases with N along an isotopic chain, which corresponds to an increase in the observed signature splitting and decrease in β_2. The γ deformation decreases with increasing Z along an isotonic chain, which corresponds to a decrease in the observed signature splitting and increase in β_2. The more neutron-deficient nuclei generally have small γ deformation as well deformed, prolate minima are expected. TRS calculations by Granderath *et al.* [82] show also a significant increase in negative γ deformation with increasing N for the $\nu h_{11/2}$ configurations in Xe-Ba-Ce isotope chains. However, their calculations suggest that extremely large γ values of $\sim -70°$ were necessary to reproduce the signature splitting of the heavier nuclei. In contrast, the CSM predicts more modest triaxial deformation values that can also explain the large signature splitting.

High-Spin Region $I > \frac{27}{2}$

All of the $\nu h_{11/2}$ bands in Fig. 5.12 show a distinctive band crossing at $I \sim 15$, which is due to the alignment of two low-K $h_{11/2}$ protons. Although signature splitting is present at lower spins ($I < \frac{35}{2}$), it is greatly reduced above the crossing. Since signature splitting is a sensitive probe of the deformation, this can be taken as an indication that the three-quasiparticle band above the band crossing has a different deformation than the one quasi-particle band below it. The low-K protons tend to drive the nucleus towards prolate ($\gamma = 0°$) shapes in contrast to the high-K neutrons [82]. The much smaller energy splitting found in the $\pi h_{11/2}\nu h_{11/2}$ bands of

neighboring odd-odd nuclei [146] suggest that the deformation driving force of the proton is greater than that of the neutron. Thus, after the proton alignment in the $\nu h_{11/2}$ bands of the odd-A nuclei, the triaxial deformation may indeed change and have a value closer to $\gamma \sim 0°$. This is a behavior similar to that seen in $A \sim 160$ region, where the splitting is quenched after the alignment of low-K $i_{13/2}$ neutrons.

Not only is the splitting reduced after the $\nu i_{13/2}$ alignment in the $A \sim 160$ nuclei, but in many cases the normally unfavored signature lies lower in energy above the crossing. This phenomenon is known as signature inversion and is also seen in the $\pi h_{11/2}\nu h_{11/2}$ bands of the odd-odd $A \sim 130$ nuclei [146] and in the $\pi h_{11/2}$ bands of odd-A $A \sim 160$ nuclei [134]. The cause of the inversion in the $\pi h_{11/2}\nu(i_{13/2})^2$ structures has been suggested to lie in the $i_{13/2}$ neutron driving the shape of the nucleus to a small, positive γ value [147]. Signature inversion is also seen in the $\nu h_{11/2}$ bands of ^{123,127,129,131}Ba, ^{131,133}Ce, ^{135}Nd, ^{137}Sm after the proton crossing, as seen in Fig. 5.12. While the inversion lasts for a large spin range in $A \sim 160$ nuclei, normal ordering of the signatures is restored within a few units of spin for the $\nu h_{11/2}$ bands in $A\sim130$ nuclei. This suggests that the normal Coriolis effects supersede the force responsible for inversion at higher spins and, thus, that this force is weaker in the $A \sim 130$ nuclei as compared with the $A \sim 160$ region.

The change in shape from negative γ deformation before the crossing to positive γ deformation after the crossing may be the cause for the observed signature inversion in $A \sim 130$ nuclei. However, the role of a p-n interaction may also need to be considered as there is evidence to suggest that it is the cause of inversion in nearby odd-odd nuclei [148]. Clearly, theoretical work is needed to fully understand this inversion process.

5.5.3 Signature Splitting in the $\nu h_{9/2}$[541]1/2 Band

As part of our discussion of signature splitting systematics in $A \sim 130$ nuclei, we turn our attention to signature splitting in the [541]1/2 band in ^{129}Nd. A comparison with energy signature splitting of the same band in ^{131,133}Nd is presented in this section. The reader is reminded that the favored signature α_f of a given structure can be

determined by the j of the shell, where $\alpha_f = \frac{1}{2}(-1)^{j-1/2}$. Since energy splitting is largest for $K = 1/2$ orbitals [12], one would expect to observe large signature splitting in the [541]1/2 band. In some cases the splitting is so large that only the favored signature of the $K = 1/2$ band is observed as seen in the case of the proton [541]1/2 in odd-A ^{165,167,169}Lu [149, 150, 151] nuclei.

As single-particle neutron diagrams suggest (see Chapter 2), the parentage of the [541]1/2 orbital is mixed between the $h_{9/2}$ and $f_{7/2}$ shells. Therefore, the favored signature at low spin can help determine which shell contributes the largest component to the [541]1/2 wavefunction. In order to amplify signature effects in the [541]1/2 band in ^{129,131,133}Nd, Fig. 5.14 plots the energy of a given spin state (I) minus the average of the energies from the states $I + 1$ and $I - 1$ (staggering) versus spin. An inspection of Fig. 5.14 reveals the presence of several trends in signature splitting of the [541]1/2 band. First, the positive signature is found to be initially favored in ^{129}Nd , and little splitting is observed in ^{131}Nd [85]. However, the negative signature is initially favored in ^{133}Nd [115]. Using the definition of the α_f mentioned earlier, the $h_{9/2}$ orbital component will favor the $\alpha = +1/2$ signature and the $f_{7/2}$ orbital component will favor the $\alpha = -1/2$ signature. Therefore, when $h_{9/2}$ component is most dominant, the $\alpha = +1/2$ signature is favored in ^{129}Nd [Fig. 5.14(a)]. In ^{133}Nd [Fig. 5.14(c)], where $\alpha_f = -\frac{1}{2}$ initially, it appears that the $f_{7/2}$ shell is dominant and in ^{131}Nd [Fig. 5.14(b)] there is apparently an equal mixture of both components in the wavefunction. The likely cause of this signature favoredness is deformation, which increases from ^{133}Nd to ^{129}Nd as the nuclei become more neutron deficient. Since the [541]1/2 orbital originates from the $f_{7/2}$ shell, then at lower deformations (*e.g.* in ^{133}Nd) one expects this shell to be favored over the $h_{9/2}$. As deformation is increased, the $K = 1/2$ orbital from the $h_{9/2}$ shell crosses the [541]1/2 orbital such that the dominant component is changed. Therefore, Fig. 5.14 displays a nice experimental verification of the "parentage evolution" for the [541]1/2 orbital with deformation.

As angular momentum is increased, the signature splitting increases, reaches a maximum and then gradually starts to decrease until an inversion point is reached. After this inversion point the negative signature becomes favored for all spins in all

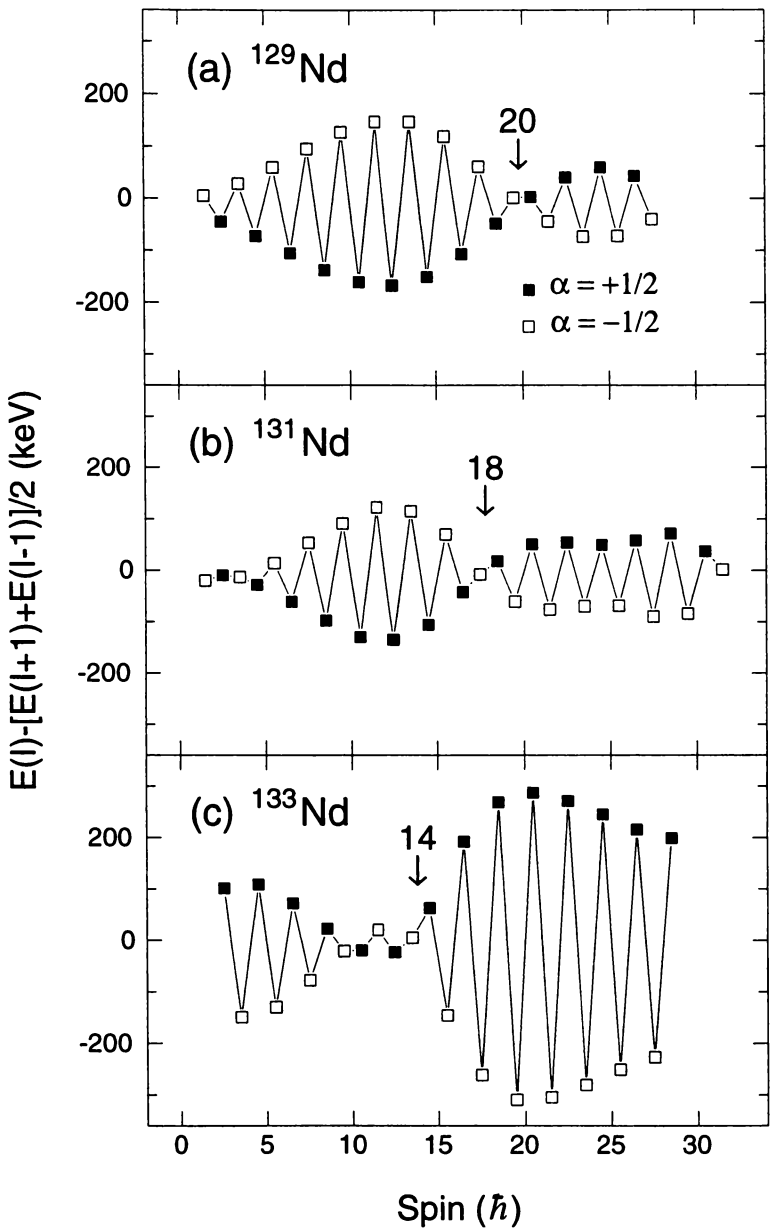


Figure 5.14: Signature splitting of the $\nu h_{9/2}[541]1/2$ bands in (a) ^{129}Nd, (b) ^{131}Nd, and (c) ^{133}Nd. The inversion point is marked in each panel with an arrow. The positive and negative signatures are denoted by solid and open symbols, respectively.

three nuclei. Figure 5.14 labels where these inversion points approximately occur for each of the nuclei. It can be observed that with increasing N, the inversion happens at a lower spin, and the amplitude of the splitting after the inversion also increases with N. None of the other bands in ^{129}Nd (or ^{131,133}Nd) show similar signature effects after the proton crossing. Perhaps the cause of this effect is an interaction of the negative signature of the [541]1/2 band with another three-quasiparticle band. However, there are only a few negative-parity orbitals to consider which may interact with the [541]1/2 band. One possible orbital is the down-sloping [530]1/2 intruder , but in order to have a strong interaction the two negative-parity $K = 1/2$ orbitals has to be closer (at least for ^{129}Nd) than the calculation in Fig 5.6 suggest. However, without the knowledge of the band-head energies of these structures it is difficult to verify this statement.

CHAPTER 6

Experimental Results of ^{130}La

6.1 Overview

The rotational configurations in odd-odd $A \sim 130$ nuclei are often characterized by the occupation of high-j, high-K neutron orbitals coupled to high-j, low-K proton orbitals. These orbitals are known to drive the nucleus towards different shapes leading to shape coexistence [104]. The properties of nuclear states at low and medium spins are dominated by the interplay between single-particle and collective motion, making the study of doubly-odd nuclei in this mass region most interesting. In this chapter we present new experimental results on ^{130}La where high-spin states of this nucleus were populated through a fusion evaporation reaction of a ^{19}F beam on a ^{116}Cd target. These results will be discussed in terms of the Cranked Shell Model (CSM) to propose new configuration and spin assignments to previously known structures in ^{130}La.

For odd-odd $A \sim 130$ nuclei, the Fermi surfaces of both protons and neutrons are located close to several single-particle orbitals with different parity and K. Therefore, there are different possibilities of orbital couplings which produce a multitude of quasiparticle states at low excitation energies. These states are expected to have very different values of I and K, resulting in isomers and increasing the difficulty of prompt spectroscopy. These isomers prevent the observation of prompt transitions to the ground state with known parity and spin. Thus high-spin rotational bands cannot be assigned firm spins and parities, and we must rely on systematics for such assignments. Here we present arguments that isomeric states exist at low spins in ^{130}La and, hence, we will partially rely on energy level systematics of the nearby odd-odd nuclei to assign relative spins of the configurations for this nucleus.

Recent experimental results on some odd-odd nuclei in this mass region show strong evidence for the presence of the so-called chiral-twin bands [152]. The proper conditions for observing chiral bands are satisfied in these nuclei due to the angular momentum coupling of the valence proton and neutron $h_{11/2}$ orbitals to a triaxial core. In this chapter we introduce the concept of chirality and show that ^{130}La does satisfy some, yet not all the conditions of nuclear chirality. However, our analysis on this nucleus dismisses recent experimental results which claim the observation of a chiral-twin band feeding at low spins the previously known $\pi h_{11/2}\nu h_{11/2}$ band in ^{130}La.

6.2 Experimental Details

High-spin states of ^{130}La were populated using the ^{116}Cd (^{19}Fl,5n) reaction at a range of beam energies (95 - 105 MeV). Ions of ^{19}F were delivered by the Wright Nuclear Structure Lab tandem accelerator at Yale University. The self-supporting target consisted of 1.7 mg/cm^2 of enriched ^{116}Cd. The calculated maximum achieved reaction cross section for the 5n reaction channel was $\sim$ 550 mb at a 90 MeV beam energy. Approximately 10^9 three-fold (γ^3) or higher events were detected by the Yrast Ball [47]. These events were sorted into an $E_\gamma \times E_\gamma \times E_\gamma$ coincidence cube and were subsequently analyzed with the Radware [65] software package. An asymmetric $E_\gamma \times E_\gamma$ coincidence matrix of γ-ray energies detected by the LEPS detectors versus γ-ray energies detected by Ge detectors was also sorted. A total of $\sim$ 21 million LEPS versus Ge coincidences events were observed. The level scheme from the present data is shown in Fig. 6.1

The multipolarities of most of the transitions in bands 1 and 2 were previously identified up to spins of (15^+) and (16^-), respectively (see Fig. 6.1) through angular distribution measurements [153]. In order to confirm the multipolarity nature of these transitions, we performed a directional correlation of oriented states (DCO) analysis. An asymmetric matrix was sorted from the Yrast Ball data, where the energy of γ rays observed in detectors located at 50° and 126° with respect to the beam axis were histogrammed along one axis, and coincident γ rays observed at

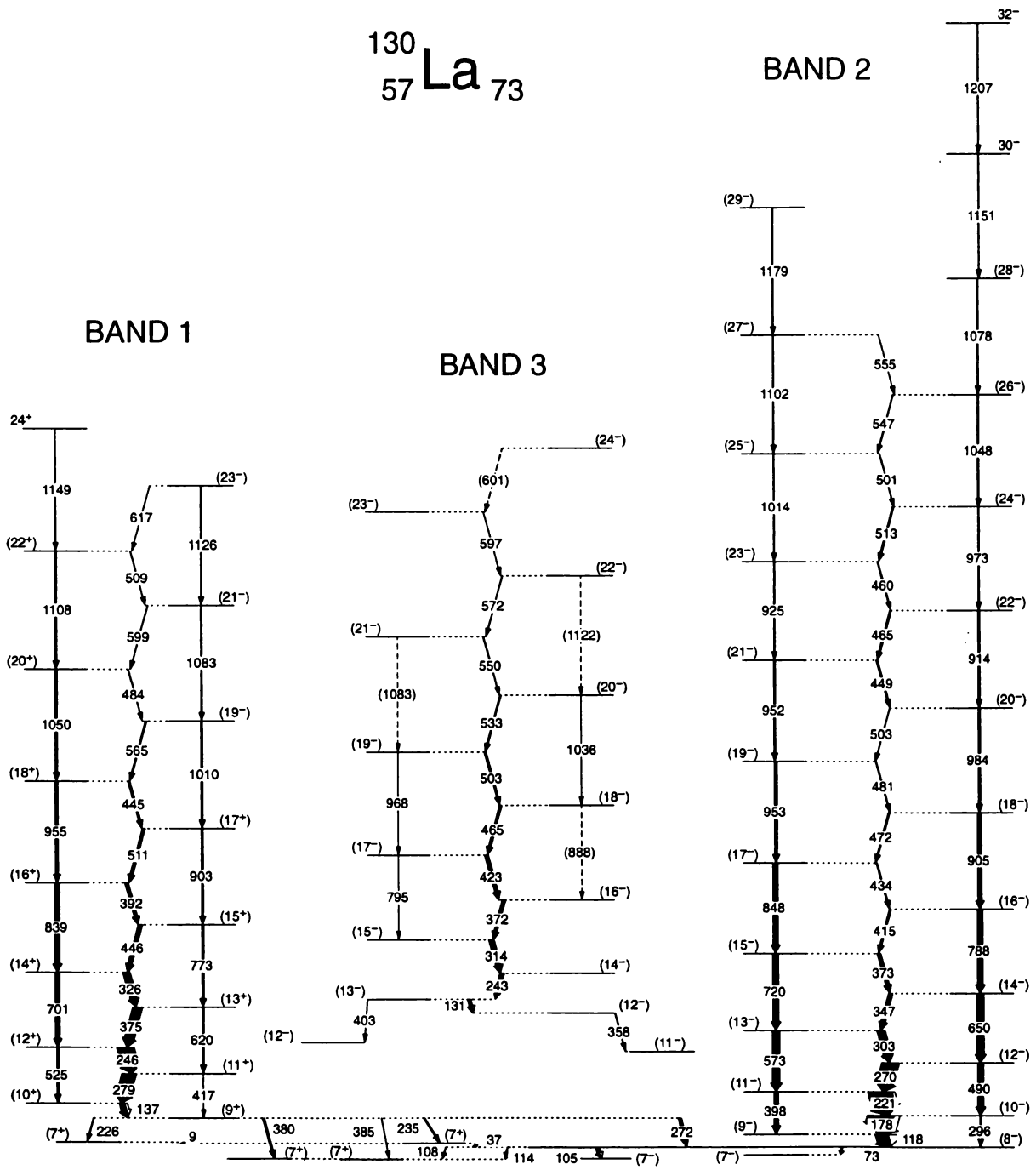


Figure 6.1: The level scheme of ^{130}La. The width of the arrows is indicative of the relative intensities of the transitions. Tentative transitions are denoted by dashed lines. Spin and parity assignments are explained in the text. The proposed band-head configurations are also given.

90° were histogrammed along the other. With the detectors at the given angles, one expects DCO values of $\sim$ 0.6 for pure dipole transitions ($M1$ and $E1$) and $\sim$ 1.0 for quadrupole transitions ($E2$). Through our DCO analysis, we were able to confirm the previously published multipolarities in bands 1 and 2. However, the multipolarities of the transitions below the (9^+) and (8^-) states in bands 1 and 2, respectively, were never measured before. Multipolarity information on these transitions are crucial to confirm the relative spins of bands 1 and 2. The measured DCO values for the transitions 105-, 114-, 226-, 235-, 380-, and 385-keV were as follows: 0.49(4), 0.44(4), 0.88(8), 0.86(1), 0.77(8), and 0.91(9), respectively. Unfortunately, we were unable to deduce a reliable DCO ratio for the 272-keV transition as it forms a partially resolved doublet with a contaminant transition of very similar energy. However, angular distribution measurements in Ref. [153] assigned a stretched $E1$ character to the 272-keV transition.

6.3 The Level Scheme

A ground-state spin and parity of $3^{(+)}$ for ^{130}La have been measured by Shuwei *et al.* [156] through the β^+ decay of ^{130}Ce. The original identification of high-spin states in ^{130}La was made by Paul *et al.* [153] where they observed two strongly coupled structures and assigned them as the $\pi h_{11/2}\nu h_{11/2}$ and $\pi h_{11/2}\nu g_{7/2}$ configurations. These configurations are labeled as bands 1 and 2 in Fig. 6.1, respectively. The band-head assignment of (9^+) for band 1 in Ref. [153] was based on similarities with other $\pi h_{11/2}\nu h_{11/2}$ bands in nearby odd-odd nuclei. A spin value of (8^-) was assigned to the band-head level of band 2, as a stretched $E1$ linking transition was observed between the two band heads [153]. Later work by Godfrey *et al.* [154] extended the previous configurations to higher spins and proposed new spin assignments by lowering the previously assigned spin values of the $\pi h_{11/2}\nu h_{11/2}$ configuration by two units of $\hbar$ and the spin assignment of the $\pi h_{11/2}\nu g_{7/2}$ configuration by three units of $\hbar$. In addition, they found a coupled band at higher excitation energies consisting of strong $M1$ transitions and very weak $E2$ transitions which they proposed to have an oblate structure [155]. However, they could not confirm the nature of this band as no linking

transitions to either bands 1 or 2 were found.

Our data analysis confirmed the previous high-spin structures [154, 155], extended the $\pi h_{11/2}\nu g_{7/2}$ configuration (band 2) by three transitions, and modified the highest energy transitions of band 1. We confirmed most of the transitions previously published in band 3 and modified the energies of the last two $M1$ transitions. In addition, we were able to to investigate the γ-ray energy sequences below bands 1 and 2, and proposed new spin assignments for these bands as shown in Fig. 6.1. Also, new spin and configurational assignments were made for the previously assigned oblate band (labeled as band 3 in Fig. 6.1). A detailed discussion of the spin assignments follows in the next section. Weak transitions above states of determined spin, where reliable DCO analysis could not be performed, were assigned multipolarities assuming that the rotational behavior of the band persists. Spectra of all the bands are shown in Fig. 6.2, which are the result of summing all coincidence spectra produced by double-gating on many combinations of γ rays at low spins.

Bands 1 and 2

By inspecting the spectra of bands 1 and 2 in Figs. 6.2 (a) and (b), one can clearly see that both bands are in coincidence with 73-, 105- and 114-keV transitions. This is an indication that both bands feed common states at low spins. With the help of the LEPS-Ge matrix, one can explore the possible coincidence correlations of γ-ray lines (detected by Ge) with low-energy γ rays (<100 keV) that are well resolved by the LEPS. Fig. 6.3 shows two sample LEPS spectra generated by gating on the Ge axis (137- and 118-keV transitions) and projecting on the LEPS axis of the LEPS-Ge matrix. Surprisingly, the spectra clearly show a very limited number of low-energy γ rays that are in coincidence with bands 1 and 2. In addition, it clearly confirms that both bands are in coincidence with the 73-, 105-, and 114-keV transitions in agreement with the Ge spectra in Figs 6.2 (a) and (b).

Before our present work, the latest spectroscopic information on these two bands was reported by Godfrey *et al.* [154]. Although we confirmed all the γ-ray transitions depopulating the 9^+ state in band 1, we did not observe any of the γ-ray

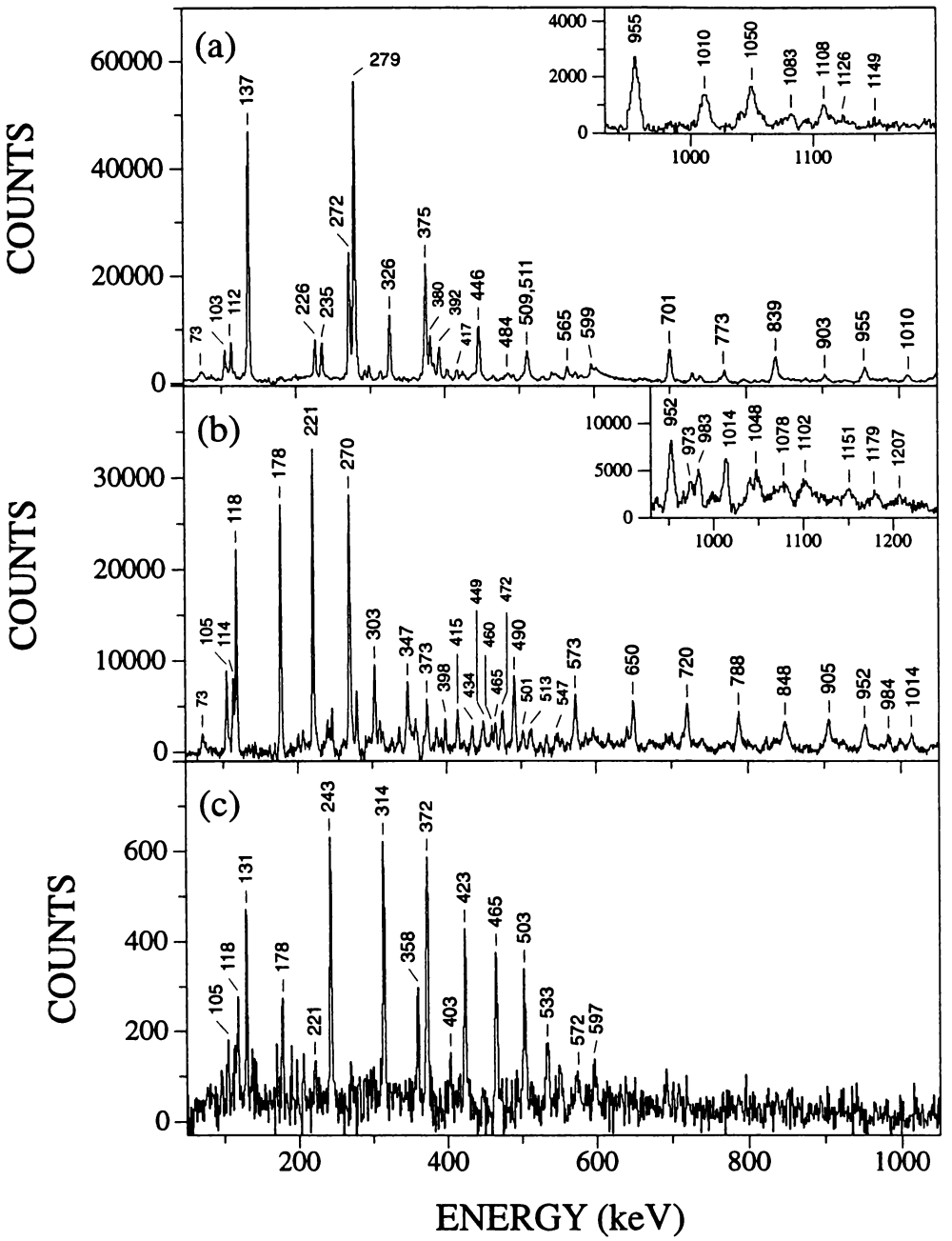


Figure 6.2: Spectra of the bands in ^{130}La generated by summing many coincidence gates. The spectra of bands 1 and 2 are shown in the main panels (a) and (b), respectively. The insets show the high-energy part of the spectra in the main panels. Panel (c) displays the spectrum of band 3 which is generated by summing many combinations of in-band $M1$ double gates.

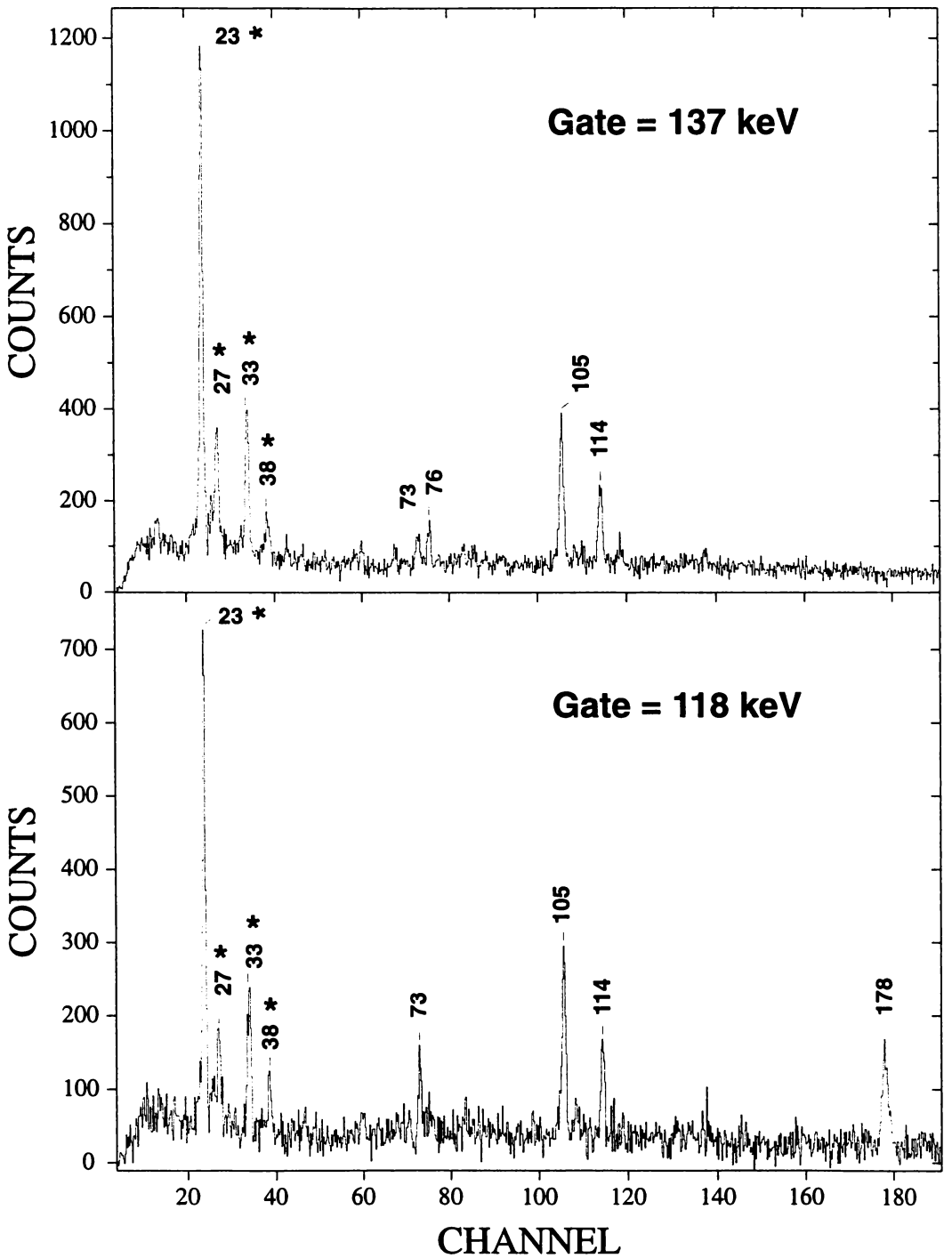


Figure 6.3: LEPS spectra of Ge-gated transitions. The 137- and 118-keV transitions from Ge data are the lowest-spin transitions in ^{130}La bands 1 and 2, respectively (see Fig. 6.1). Peaks denoted by an asterisk are contaminant x-rays which belong to ^{119}Cd and ^{130}La.

transitions they proposed feeding out of the 8^- level in band 2. In addition, our analysis shows some important differences between our γ-ray coincidence sequence with theirs for the γ rays observed below the states mentioned previously. First, we propose that bands 1 and 2 are linked through the 272-keV transition as seen in Fig. 6.1 (in agreement with Paul *et al.* [153]) rather than by 108- and 46-keV transitions proposed by Godfrey *et al.* [154]. Secondly, we propose that the 118-keV transition feeds the 105- and 114-keV transitions directly. Previous work shows a coincidence of the 118- with the 114-keV transition through a 46-keV transition. However, the LEPS spectrum in Fig. 6.3 shows no evidence for a 46-keV transition. We also argue that the apparent coincidence of the 118- and 73-keV transitions as seen in Fig 6.3 is not real and supporting arguments follow below. Thirdly, the 272-keV transition does see both the 105- and 114-keV transitions rather than the 114-keV transition only, as reported previously [154]. Fourthly, we could not confirm the presence of a 191-keV transition ($= 118 + 73$ keV) as was previously claimed [154]. Fifthly, we assign the 73-keV transition as tentative since it appears in all coincidence gates taken for all combinations of γ rays at low spins in bands 1 and 2.

Band 3

Careful inspection of the spectrum of band 3 in Fig. 6.2 (c) shows that its transitions are in coincidence with the 105-, 118-, and 221-keV transitions which are the lowest $M1$ transitions in band 2. In-band gating on the strong $M1$ transitions provides a strong indication that band 3 has no coincidence correlations with band 1 which contradicts a previous observation [155] that claims 13% of band 3 intensity feeds band 1 at low spins. For comparison purposes, our experimental data had nearly 14 times more coincidence events than that earlier measurement, which clearly rules out the statistics issue as a reason for not observing any linking transitions between these two bands.

The observation of the 118- and 221-keV transitions from in-band sum gates of band 3 transitions indicates that bands 1 and 3 do interact at low spins. As a result of this interaction one should be able to observe linking transitions between the two

bands in prompt spectroscopy. When generating spectra of band 3 by in-band gating, the presence of prompt linking transitions would feed out most of the intensity of band 3 into band 1 and, hence, the 105-, 118-, and 221-keV lines will appear more strongly in the spectrum. However, this is not the case as seen in Fig. 6.2 (c) where most of the band intensity is "contained" in the band itself and band 2 transitions appear much weaker than band 3 transitions. One possible cause for this weak coincidence between the two bands is the presence of one or more isomeric states below band 3 which decay by slightly delayed (but not too much longer than the coincidence window) and, hence, very weak linking transitions.

6.4 Configuration and Spin Assignments

Calculations by Möller *et al.* [1] predict a ground-state deformation of $\beta_2 \sim 0.22$ for ^{130}La. Using this quadrupole deformation value, one can refer to the single-particle diagrams in Chapter 2 to approximately locate the active orbitals nearest the Fermi surface at $N = 73$ and $Z = 57$. One expects to observe configurations in ^{130}La based on combinations of proton and neutron orbitals with low excitation energies in the nearby odd-N and odd-Z nuclei. Table 6.1 summarizes these neutron and proton orbitals and their expected excitation energies for ^{130}La. The excitation energy of a given orbital is taken as the average of the excitation energy of the same orbital from $(N+1, N-1)$ nuclei for the proton orbital, and from $(Z+1, Z-1)$ nuclei for the neutron orbitals. Before we start discussing the configuration and spin assignments of ^{130}La bands, it is helpful to present first several criteria that aid in identifying the quasiparticle structure of these bands with the orbitals in Table 6.1. These criteria are introduced below and include $B(M1)/B(E2)$ ratios, CSM calculations, and alignment plots. Detailed discussion of the use and interpretation of these plots and calculations for each of the bands will follow later in this section.

The experimental and theoretical $B(M1; I \rightarrow I-1)/B(E2; I \rightarrow I-2)$ values for bands 1-2 are plotted versus spin in the top part of Fig. 6.4, and for band 3 in the lower part of the same figure. Intrinsic quadrupole moment Q_0 values of 3.59 eb were assumed for the three bands, and the collective gyromagnetic ratio was given

Table 6.1: Alphabetic quasiparticle labeling scheme for ^{130}La. The excitation energy (E_x) is deduced from the average of the excitation energy of the same orbital from nearby nuclei (see text).

Label	$(\pi,\alpha)_n$*	Configuration **	Label	$(\pi,\alpha)_n$*	Configuration **	$E_x(keV)$
			Quasineutrons			
A	$(+,+\frac{1}{2})_1$	[404]7/2	B	$(+,-\frac{1}{2})_1$	[404]7/2	4.2
C	$(+,+\frac{1}{2})_2$	[411]1/2	D	$(+,-\frac{1}{2})_2$	[411]1/2	~ 5
E	$(-,-\frac{1}{2})_1$	[514]9/2	F	$(-,+\frac{1}{2})_1$	[514]9/2	172
			Quasiprotons			
A_p	$(+,+\frac{1}{2})_1$	[411]3/2	B_p	$(+,-\frac{1}{2})_1$	[411]7/2	0
C_p	$(+,+\frac{1}{2})_2$	[413]5/2	D_p	$(+,-\frac{1}{2})_2$	[413]5/2	187
E_p	$(-,-\frac{1}{2})_1$	[550]1/2	F_p	$(-,+\frac{1}{2})_1$	[550]1/2	238

* Parity (π) and signature (α) of the orbital at $\hbar\omega = 0$ MeV. The subscript n numbers the quasiparticle's excitations of a specific signature and parity starting with the lowest in energy at $\hbar\omega = 0$ MeV.

** Configuration of the orbital at $\hbar\omega = 0$ MeV.

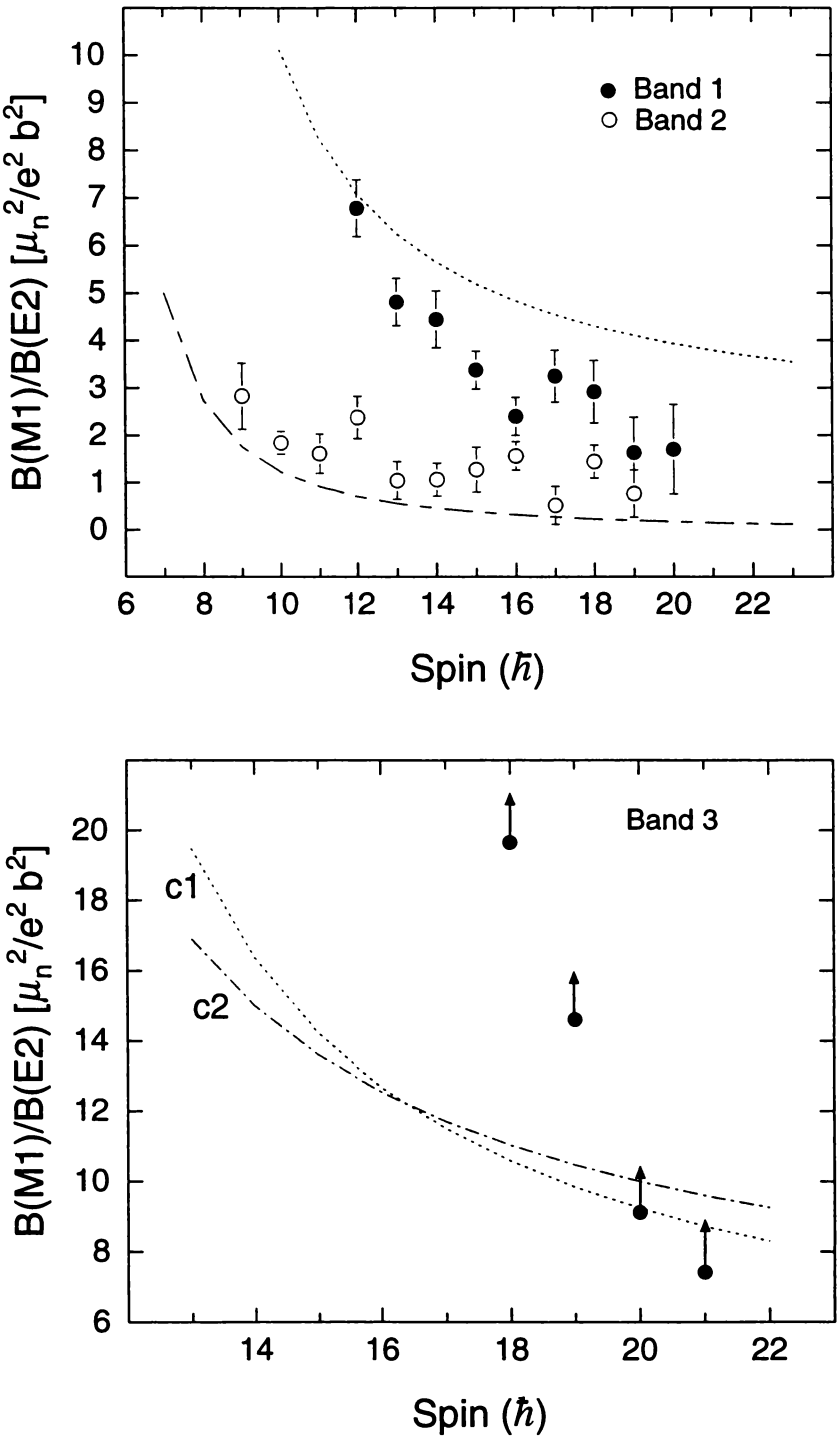


Figure 6.4: The experimental (symbols) and theoretical (lines) $B(M1)/B(E2)$ ratios for the three bands in ^{130}La. The arrows in the lower figure indicate that the experimental points are only a lower limit to the actual $B(M1)/B(E2)$ for band 3. The reader is referred to the text for an explanation of the theoretical lines shown.

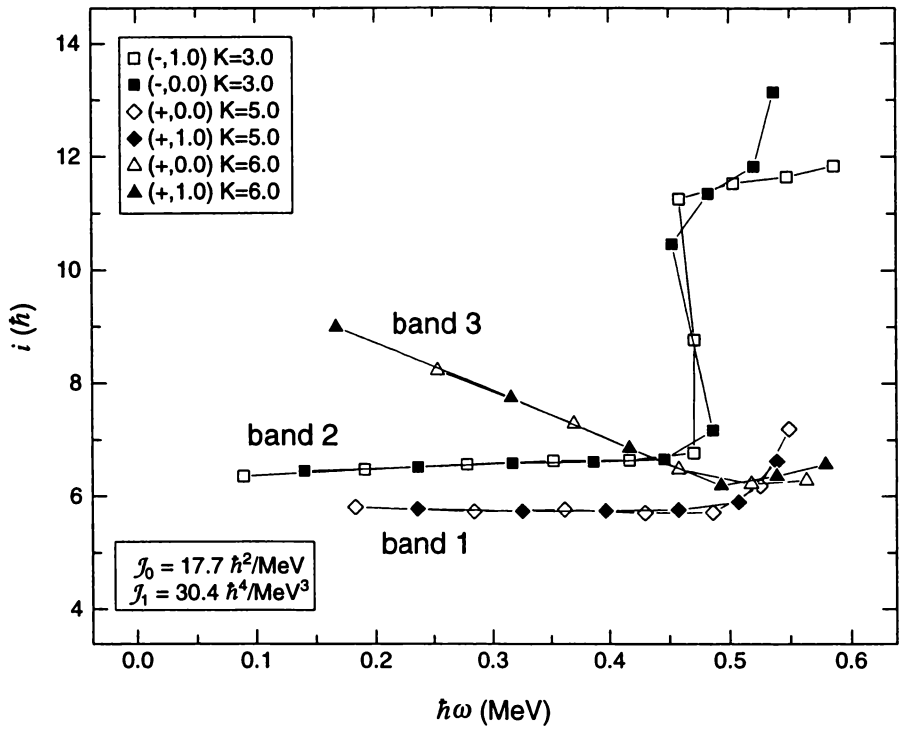


Figure 6.5: The alignment as a function of rotational frequency for bands 1-3 in ^{130}La.

by $g_R = Z/A$. The g_K values were calculated using a Woods-Saxon potential [123] with the following results for the orbitals discussed below: $g_K(\pi[550]1/2) = 1.44$, $g_K(\nu[404]7/2) = 0.35$, and $g_K(\nu[514]9/2) = -0.27$.

Rotational alignments of all ^{130}La bands are shown in Fig. 6.5. Fitted Harris parameters for band 1 of $\mathcal{J}_0 = 17.7\ \hbar^2/\text{MeV}$ and $\mathcal{J}_1 = 30.4\ \hbar^4/\text{MeV}^3$ were used [153] to subtract the angular momentum contribution of the core. However, the alignment I_x depends on the projection of the total spin on the rotation axis (K) as defined semi-classically by $I_x = \sqrt{(I+1/2)^2 - K^2}$. For now, we will use K values of 5, 3, and 6 for bands 1, 2, and 3 respectively, and will justify our choice of these K values in the discussion below.

CSM calculations for protons and neutrons were performed using the deformation parameters taken from TRS calculations for the E proton and neutron at zero rotational frequency. The result of the calculation is shown in Fig. 6.6 with approximate locations of the the predicted neutron and proton crossings. Comparison between the observed crossings in ^{130}La bands with CSM predictions offers clues with

regard to the configuration of the sequences.

6.4.1 Bands 1 and 2 : $\pi h_{11/2}\nu h_{11/2}$ and $\pi h_{11/2}\nu g_{7/2}$

Configuration Assignment

Band 1 has an initial alignment of $\sim 5.9\ \hbar$ with no gain in alignment up to $\hbar\omega \sim 0.54-$ MeV. Band 2 has a larger initial alignment of $\sim 6.3\ \hbar$ and gains $\sim 5.0\ \hbar$ of alignment at $\hbar\omega \sim 0.47$ MeV as seen from Fig. 6.5. Neither band experiences any alignment gain caused by the proton E_pF_p crossing predicted by CSM to occur at $\hbar\omega \sim 0.35$ MeV (see Fig. 6.6). This implies that both bands have an $h_{11/2}$ proton in their initial configuration which blocks the E_pF_p alignment. The only proton orbitals which are close to the proton Fermi surface are the highly-mixed low-K $h_{11/2}$ orbitals, namely $\pi[550]1/2$ and $\pi[541]3/2$, and rotational structures based on these low-K orbitals have been observed in the nearby odd-Z isotopes ^{129,131}La [157, 104]. The single-particle neutron diagram shows that the neutron orbitals closest to the $N = 73$ Fermi surface are $h_{11/2}[514]9/2$, $g_{7/2}[404]7/2$, and $h_{11/2}[523]7/2$. We can rule out the $h_{11/2}[523]7/2$ orbital since no such rotational structures in the nearby nuclei have been observed, and it would have a higher excitation energy than the orbitals listed in Table 6.1. With the $\nu[514]9/2$ and $\nu[404]7/2$ left as possible active orbitals, one would expect to observe a positive-parity band based on the $\pi h_{11/2}\nu h_{11/2}$ configuration and a negative-parity band based on the $\pi h_{11/2}\nu g_{7/2}$ configuration.

From the Gallagher-Moszkowski (GM) coupling rules [159], the energetically favored coupling for the $\pi[550]1/2 \otimes \nu[514]9/2$ configuration is $K = \Omega_p + \Omega_n = 5^+$ since the single-particle spins of these particles are aligned parallel. The favored coupling for the $\pi[550]1/2 \otimes \nu[404]7/2$ configuration is $K = 3^-$ as the spins of both particles are anti-parallel. These K values together with the corresponding g_K values for the above orbitals were used to calculate $B(M1)/B(E2)$ values for the two configurations. Fig. 6.4 (top) shows the result of these calculations, with the dotted line representing the theoretical predictions for the $\pi h_{11/2}\nu h_{11/2}$ and the dashed line representing the $\pi h_{11/2}\nu g_{7/2}$ calculation. Good agreement between the experimental results and theoretical predictions is observed for band 2, and for band 1 the

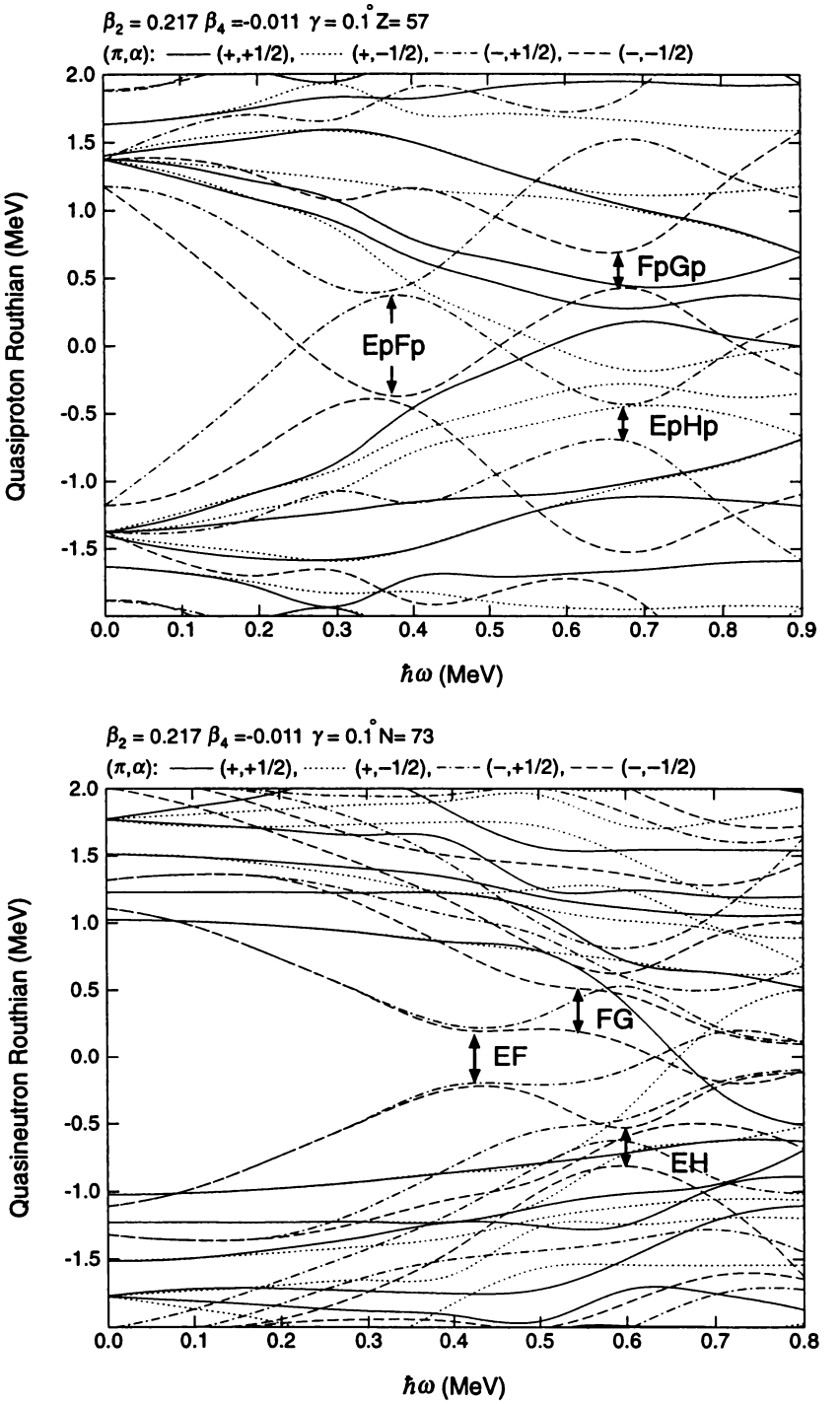


Figure 6.6: Cranked Shell Model calculations for quasiprotons and quasineutrons in ^{130}La. The deformation parameters were determined from TRS calculations at zero rotational frequency.

experimental values fall off faster with increasing spin than predicted.

The alignment plot of both bands shows that they experience a crossing at higher rotational frequencies. For band 1 an indication of an upbend is observed at $\hbar\omega \sim 0.54$ MeV, and for band 2 one can see a crossing (upbend) at a rotational frequency of ~ 0.47 MeV with an alignment gain of $\sim 5\ \hbar$. Since we argued previously that both bands have the $\pi h_{11/2}$ in their configuration, then one would expect that the observed alignment gains mentioned above are due either to the next available proton crossing after E_pF_p or to a neutron crossings. An inspection of the $\nu h_{11/2}$ crossing in ground-state bands of nearby even-even nuclei will give an indication of the approximate location of this crossing in ^{130}La. An average crossing frequency of ~ 0.47 MeV was found for the EF crossing in even-even $^{124-128}$Ba nuclei [84] which is similar to the crossing frequency found in band 2. Therefore, it is reasonable to assume that band 2 crossing is the neutron EF crossing which is consistent with CSM predictions of this crossing at $\sim$0.43 MeV (see Fig. 6.6). Band 1 has a neutron $h_{11/2}$ in its configuration and, therefore, will not experience the first neutron EF crossing. However, band 1 can experience either the second available proton or neutron crossings. Fig. 6.6 shows that the second available neutron crossing (FG) occurs at $\hbar\omega \sim 0.54$ which is similar to the observed crossing of band 1, while the second proton (F_pG_p or E_pH_p) crossing occurs at $\hbar\omega \sim 0.67$ MeV. Based on CSM predictions it seems more reasonable to assume that the observed gain of alignment is due to the neutron FG crossing, but we cannot rule out the second proton crossing as a possibility. Therefore, based on the analysis discussed so far, we assign $\pi h_{11/2}\nu h_{11/2}$ as the band-head configuration for band 1 and $\pi h_{11/2}\nu g_{7/2}$ as the band-head configuration for band 2, in agreement with previous assignments [153, 154].

The alignment for the $\pi h_{11/2}\nu g_{7/2}$ band (band 2) was found to be ~ 0.5 $\hbar$ less than that of the $\pi h_{11/2}\nu h_{11/2}$ band (band 1) as shown in Fig. 6.5. However, one would expect that the initial alignment of band 2 to be less than band 1 as the $\nu h_{11/2}$ orbital will have higher initial alignment than the $\nu g_{7/2}$. The alignment of band 1 is even less than the combined alignment of the proton $h_{11/2}$ ($\sim 5\ \hbar$) and the neutron $h_{11/2}$ ($\sim$ 1-2 $\hbar$) orbitals in neighboring odd-Z and odd-N nuclei, respectively. One possible cause for this alignment reduction is a residual interaction suggested by

Frauendorf *et al.* [160] to occur between the same high-j excited quasiparticles. This interaction affects pairing directly which is incorporated in the reference parameter $\mathcal{J}_1$ and leads indirectly to a decrease in alignment [160]. Band 1 is based on the $\pi h_{11/2}\nu h_{11/2}$ configuration (*i.e.* both neutron and proton quasiparticles occupy the same j) and so the alignment of this configuration could be reduced by a residual interaction.

Spin Assignment

We pointed out previously that the measured ground state of ^{130}La is $3^{(+)}$ [156]. Using the LEPS spectra in Fig. 6.3, we were able to conclude that there are only a few transitions that exist below the band-head of bands 1 and 2. Since each of these transitions carry 1-2 units of $\hbar$, the lowest observed states below the main configurations have a spin value of 7 $\hbar$, as seen in Fig. 6.1. In order to reach the $3^{(+)}$ ground state would mean that our band-head spin assignments for bands 1 and 2 would have to be decreased substantially. The band-head spin assignments would then be similar to those of Godfrey *et al.* [154] (6^+ for band 1 and 3^- for band 2). However, having lower band-head spins than we propose in Fig. 6.1 would not be consistent with the expected alignments of bands 1 and 2 (see discussion below). We therefore conclude that there are isomeric states between the unobserved ground state and the lowest spin states in Fig. 6.1. It is not uncommon to have low-lying isomeric states in doubly-odd $A \sim 130$ nuclei, as for example ^{128}Cs [161] and ^{130}Cs [158].

There are several reasons for our choice of the spin values shown in Fig. 6.1. The proposed configurations for bands 1 and 2 ($\pi h_{11/2}\nu h_{11/2}$ and $\pi h_{11/2}\nu g_{7/2}$) have initial alignments of $\sim$ 6 $\hbar$. The corresponding band-head spins for these configurations must be at least 6 $\hbar$ assuming K= 5, 3 for bands 1 and 2, respectively. However, DCO measurements indicate that the 272-keV linking transition is dipole and, therefore, the band-head spin of band 1 should be one unit of spin higher than the band-head spin of band 2. The experimental fits of $B(M1)/B(E2)$ ratios to the theoretical $B(M1)/B(E2)$ curves is usually a good indication of the accuracy of the spin assignments. Using our spin assignments, Fig. 6.4 shows that the best theoret-

ical fits of the experimental $B(M1)/B(E2)$ ratios of band 2, for example, occur for the spin range of 7 to 9, indicating that the band-head spin of band 2 is likely in that range and, consequently, band 1 will have a band-head spin range of 8 to 10, since they are linked (see Fig. 6.1). In fact, energy level systematics (see discussion below), leads to a band-head spin of 9^+ for band 1 in good agreement with our fits of $B(M1)/B(E2)$ ratios for this band and band 2. The spin assignments of Godfrey *et al.* [154] do not fit any theoretical $B(M1)/B(E2)$ curves.

To further strengthen our spin assignments, we refer to the energy level systematics of the $\pi h_{11/2}\nu h_{11/2}$ bands in doubly-odd $A \sim 130$ nuclei performed by Liu *et al.* [162]. The study included the following odd-odd nuclei: $^{120-130}$Cs, $^{124-134}$La, $^{130-136}$Pr, and $^{134-138}$Pm. According to the arguments of level systematics, the excitation energy of the $\pi h_{11/2}\nu h_{11/2}$ levels with the same spin follows a smooth trend with N for a given isotopic chain. After the spin adjustment of the levels for some of the La isotopes, a smooth curve for both signatures of the $\pi h_{11/2}\nu h_{11/2}$ was reproduced [162], as shown in Fig. 6.7. Using the systematics of Fig. 6.7(a), a band-head spin of 9^+ is assigned to the $\alpha = 1$ signature of band 1 in ^{130}La ($N = 70$). Similarly, a spin of 10^+ is assigned to the $\alpha = 0$ of band 1.

Therefore, based on our analysis and on the systematics of Liu *et al.* [162], we assign a band-head spin of (9^+) to band 1 and a band-head spin of (8^-) to band 2. However, absolute spins for these bands cannot be assigned without linking both configurations to the ground state. This can be done only through measuring the delayed γ-ray transitions that we propose to exist. Hence, all of the spin values shown in the level scheme of ^{130}La are designated as tentative.

6.4.2 Band 3: Oblate Structure

The first evidence for the observation of an oblate band in $A \sim 130$ region was reported by Paul *et al.* [104] in ^{131}La. They suggested that the rotational alignment of a pair of neutrons from the upper part of the $h_{11/2}$ shell drives the nucleus from prolate ($\gamma = 0°$) to collective oblate ($\gamma = -60°$) shape. In later experimental work on the doubly-odd ^{128,130}La nuclei, Godfrey *et al.* [155] identified band structures that

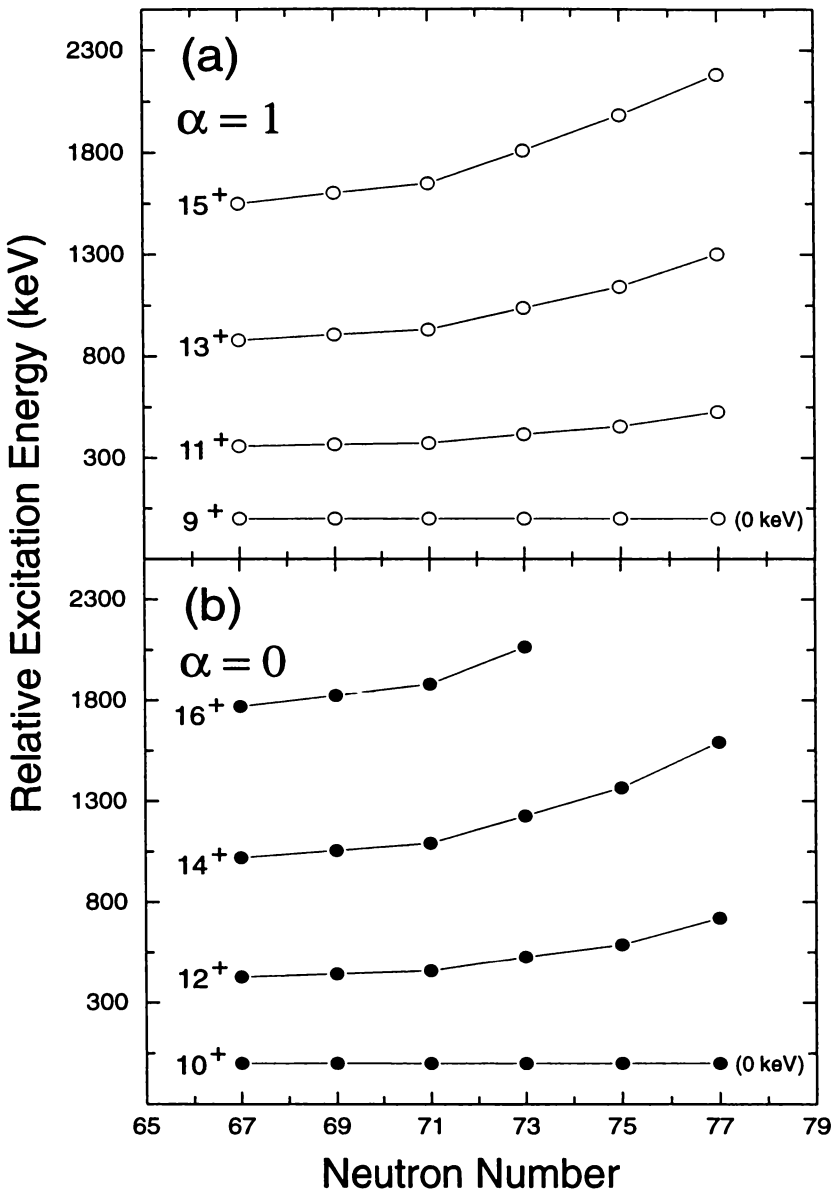


Figure 6.7: Energy level systematics of the $\pi h_{11/2}\nu h_{11/2}$ band signatures in $^{124-134}$La. Following the procedure of Liu *et al.* [162], the $I = 9^+$ in (a) and the $I = 10^+$ in (b) were set to 0 keV such that the relative level energies can be compared.

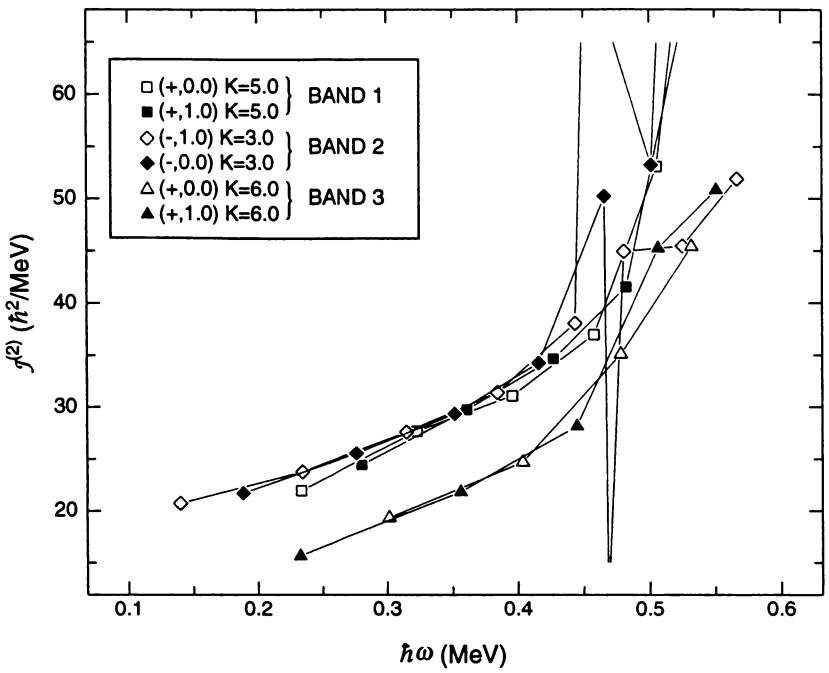


Figure 6.8: The dynamical moment of inertia $\mathcal{J}^{(2)}$ as a function of rotational frequency for bands 1-3 in ^{130}La.

shared many features of the oblate bands in ^{131}La. Based on spectroscopic similarities and theoretical CSM and TRS calculations, these bands in ^{128,130}La were classified as oblate structures. We present below supporting evidence for the oblate nature of this band and propose a new configuration and spin assignment based on our experimental findings.

One of the most striking features of this band is its large $B(M1)/B(E2)$ ratios (Fig. 6.4) which are nearly one order of magnitude larger than the $B(M1)/B(E2)$ ratios for bands 1 and 2. The presence of strong $\Delta I = 1$ transitions, leading to $B(M1)/B(E2)$ values of $\sim 10\ (\mu_N/eb)^2$ or larger are characteristic of collective rotational oblate bands in $A \sim 130$ mass region [164]. Another important property of this band is its relatively low dynamic moment of inertia $\mathcal{J}^{(2)}$. Fig. 6.8 shows that $\mathcal{J}^{(2)}$ for band 3 is nearly 65% less than that for prolate ($\gamma = 0°$) structures (bands 1 and 2), which is a very similar ratio for the oblate and prolate bands reported in ^{131}La [104]. The low dynamic moment of inertia indicates a different collective shape than bands 1 and 2, and is possibly associated with oblate deformations due to

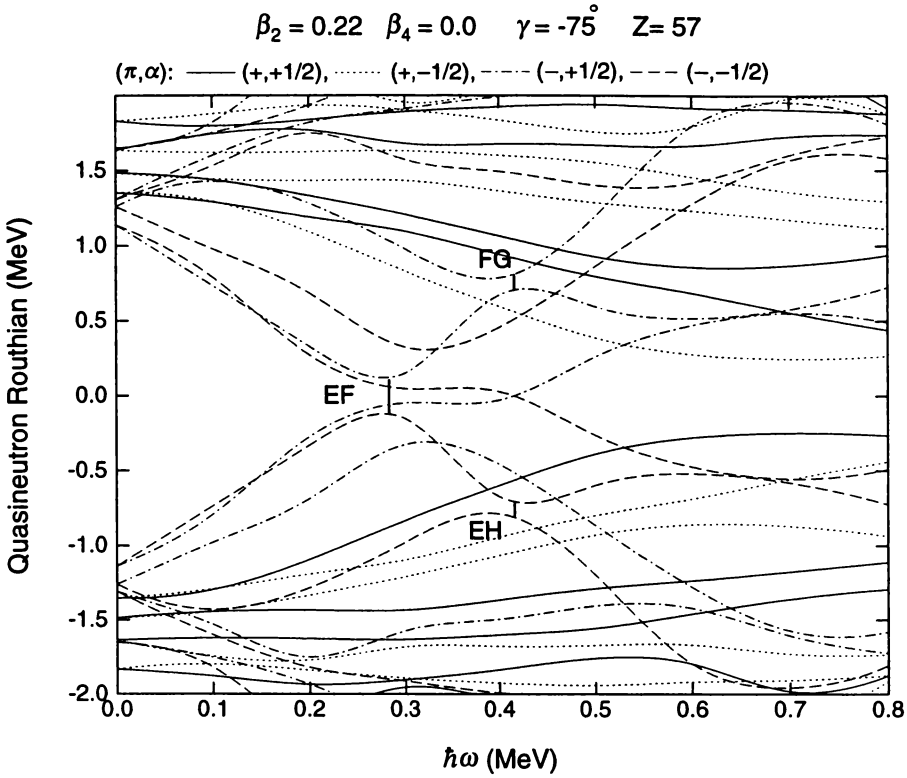


Figure 6.9: Cranked Shell Model calculations for quasineutrons in ^{130}La assuming an oblate deformation of $\gamma = -75°$, and quadrupole deformation of $\beta_2 = 0.22$.

the deformation-driving [505]$11/2^-$ proton orbital towards negative β_2 deformations (oblate) at $\gamma \sim 60°$ [164].

Since band 3 is in coincidence with band 2 as discussed previously, one would expect band 3 to be based on a quasiparticle excitation similar to $\pi h_{11/2}\nu g_{7/2}$ of band 2. The presence of a $\pi h_{11/2}$ quasiparticle in band 3 configuration blocks any quasiparticle excitations based on the first proton $h_{11/2}$ crossing (E_pF_p). An inspection of the CSM calculation in Fig. 6.9 shows that the first neutron EF crossing occurs at low rotational frequency of $\sim$ 0.27 MeV, and the next available neutron crossing is the FG or EH crossing predicted by CSM to occur at $\hbar\omega \sim 0.42$ MeV. Therefore, it is reasonable to assume that band 3 is a four-quasiparticle configuration based on the alignment of two $h_{11/2}$ neutrons (EF alignment). This is consistent with the assignment of $\pi h_{11/2} \otimes (\nu h_{11/2})^2$ for the oblate band in the nearby odd-Z ^{131}La [104]. For ^{130}La the extra neutron above the $\pi h_{11/2} \otimes (\nu h_{11/2})^2$ "core" is based on the neutron $g_{7/2}$

orbital. The third contributing neutron can be also an $h_{11/2}$ neutron which will then make band 3 based on the $\pi h_{11/2} \otimes (\nu h_{11/2})^3$ configuration. However, our experimental data show no cross talking between band 3 and band 1 ($\pi h_{11/2} \nu h_{11/2}$) which weakens this assumption. In addition, the CSM calculation shows that the neutron $g_{7/2}$ is the next most reasonable choice, and therefore, we propose that band 3 is based on the quasiparticle configuration $\pi h_{11/2} \otimes (\nu h_{11/2})^2 \otimes \nu g_{7/2}$. Theoretical $B(M1)/B(E2)$ predictions for the $\pi h_{11/2} \otimes (\nu h_{11/2})^3$ and $\pi h_{11/2} \otimes (\nu h_{11/2})^2 \otimes \nu g_{7/2}$ configurations mentioned are shown in Fig. 6.4, and are denoted by c1 and c2, respectively. Unfortunately, due to the weak intensity of the $E2$ transitions in band 3, only a lower limit for the actual $B(M1)/B(E2)$ ratio can be extracted. Therefore, no conclusive results can be obtained from this plot, but it shows that the theoretical and experimental results are most probably at the same order of magnitude.

To further strengthen our configuration assignment, a discussion of the alignment plot for band 3 is necessary. However, we need to use a proper K value for this band first. For an oblate shape ($\gamma = -60°$) the Fermi surface for the odd proton lies nearest the proton $h_{11/2}[550]11/2$ orbital. For small oblate deformations, the closest positive-parity orbital to the neutron Fermi surface is the $s_{1/2}[411]1/2$ which is strongly mixed with the $g_{7/2}[420]1/2$ orbital. Therefore, using the GM coupling rule, band 3 has either a K value of 5 or 6. We choose to use the $K = 6$ value for the alignment plot of this band as shown in Fig. 6.5. Band 3 has an initial alignment of $\sim 9\ \hbar$ which is larger than either band 1 or 2 as a result of its four quasiparticle nature. An estimate on the contribution of single-particle orbitals towards the initial alignment of band 3 can be obtained by summing the individual alignment of all contributing orbitals. However, the oblate band in ^{131}La is based on the $\pi h_{11/2} (\nu h_{11/2})^2$ configuration which acts like a "core" to band 3, and hence its intrinsic alignment is equivalent to the contribution of three quasiparticles. The remaining alignment contribution comes from either the neutron $[411]1/2$ or $[420]1/2$ which is most probably a small contribution ($\sim 1 - 2\hbar$). Indeed, we found the initial alignment of the oblate band in ^{131}La to be equal to $\sim 8.7\ \hbar$ and assuming a contribution of $\sim 1.7\ \hbar$ from the "valence" $g_{7/2}$ neutron, a total of $\sim 9\ \hbar$ can be easily achieved. Fig. 6.5 shows a continuous decrease in band 3 alignment with rotational frequency, which is

due to improper Harris parameters. This alignment behavior is also another indication that band 3 possesses a different deformation character than bands 1 and 2. At large rotational frequency ($\hbar\omega \sim 0.53$ MeV), an indication of a crossing is seen as a slight upbend in alignment is observed. The most reasonable crossing that could be responsible for this alignment upbend is the next available neutron GH crossing.

Therefore, based on the new configuration assignment, we tentatively assign negative parity to band 3. However, no definite spin assignment for band 3 can be assigned as no linking transitions with measured multipolarities to band 1 were observed. Assuming that multiple linking transitions to band 2 carry 2-3 units of $\hbar$, then one can possibly assign a band-head spin of (12 $\hbar$) for band 3 as shown in Fig. 6.1. This spin assignment is 3 $\hbar$ higher than previously proposed [155], and very similar to the band-head spin of 12.5 $\hbar$ of the oblate band in ^{131}La.

6.5 Overview of Nuclear Chirality

The phenomenon of chirality has long been observed in nature and originally referred to describe two objects which are mirror images of each other. Chirality can take several forms depending on the system it describes. Biomolecules for instance have a static chirality related to the different arrangements of atoms in the molecule, while in particle physics it has a "dynamic" character that describes the orientation of spin in massless fermions. Frauendorf and Meng recently [165] proposed the presence of chiral symmetry in atomic nuclei under certain nuclear conditions. Recent experimental results by Starosta *et al.* [152] has found the first evidence for chirality in atomic nuclei.

A triaxial nucleus is shaped rather like a kiwi fruit which if sliced lengthwise or perpendicular has an elliptical cross-section with three axes of different length. In order to describe a triaxial nucleus that possesses a chiral symmetry, three principal axes (PA) are used to describe the triaxial nuclear system. The three PA are denoted by l, i, and s, which stands for long, intermediate, and short, respectively. The top section of Fig. 6.10 illustrates the simplest possibility, which appears in odd-odd triaxial nuclei. The angular momentum vector J introduces chirality by selecting one

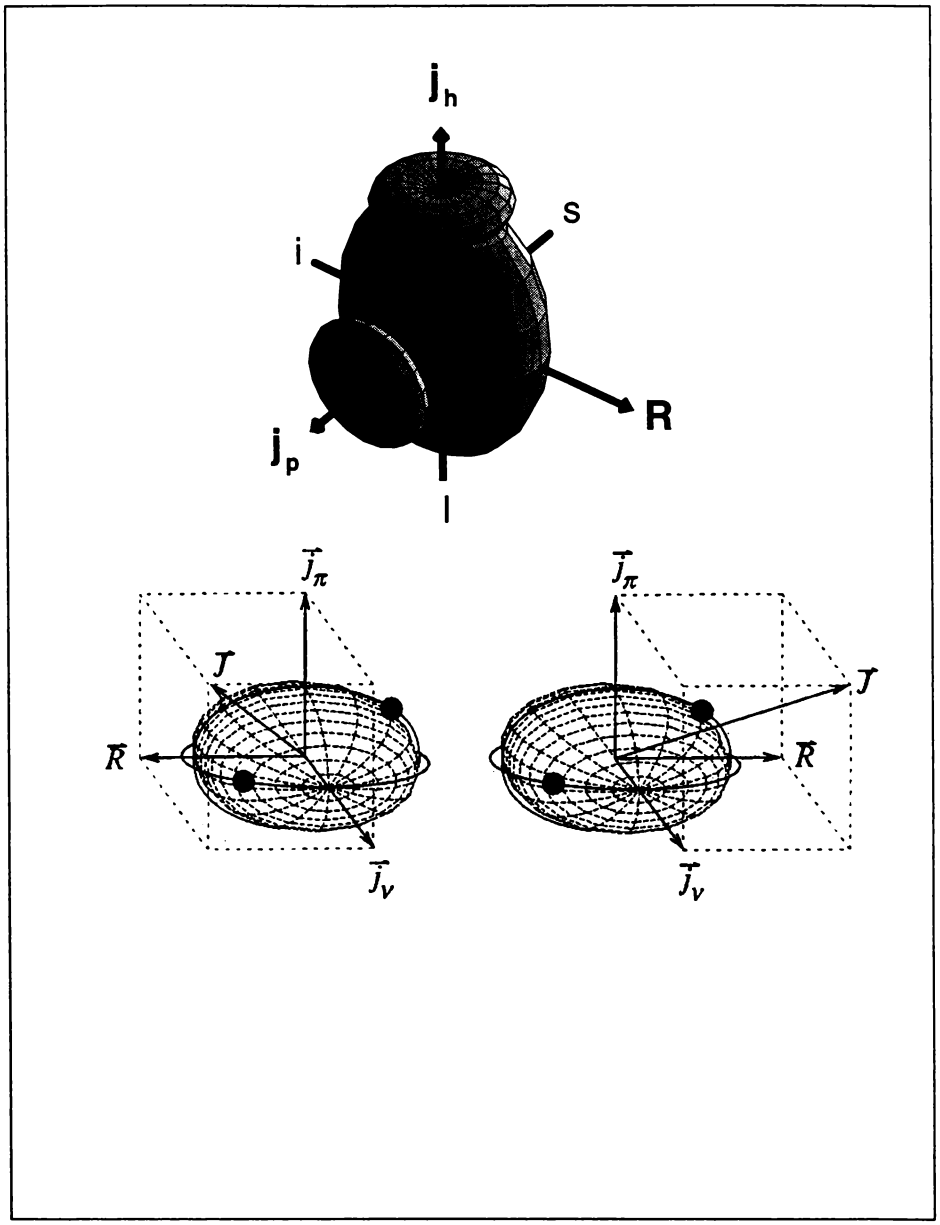


Figure 6.10: The upper part of the figures shows orbitals of a high-j proton and a high-j neutron hole coupled to the triaxial density distribution. The collective angular momentum R of the rotor prefers the intermediate axis., which has the largest moment of inertia. The total angular momentum $J = R + j_p + j_h$ points out of the plane of drawing. The short (s), intermediate (i), and long (l) form a right-handed screw with respect to J. The lower part of the figure shows left- and right-handed chiral systems for a triaxial odd-odd nucleus.

of the octants defined by the PA. In four of the octants the axes l, i, s form a left-handed system (an example is shown in the lower left section of Fig. 6.10), and in the other four a right-handed system (see lower right of Fig. 6.10). This gives rise to two degenerate rotational bands because all octants are energetically equivalent. Hence the chirality of nuclear rotation results from a combination of dynamics (angular momentum) and geometry (the triaxial shape).

The left- and right-handed systems are related by the chiral operator $TR_y(\pi)$ which has a value of one when the rotation occurs in any of the three planes spanned by the PA. However, when the axis of rotation is out of the three planes defined by the PA, the operation $TR_y(\pi)$ changes the chirality of the PA with respect to the axis of rotation J, and a *spontaneous* breaking of the chiral symmetry occurs in the nuclear-fixed frame. The required restoration of the broken symmetry for the lab system yields nearly degenerate double $\Delta I = 1$ bands. It should be noted, however, that the doublet bands do not represent pure right- or left- handed states, but rather combinations of the two which restore the chiral symmetry that is broken in the intrinsic frame. Dimitrov *et al.* [166] demonstrated that the three-dimensional Tilted Axis Cranking (TAC) model does have chiral solutions for odd-odd nuclei with triaxial shapes. Their predictions relate to configurations where the angular momentum of the valence proton, the valence neutron, and the core rotation are all perpendicular. This can occur when the Fermi level is located in the lower portion of a valence proton high-j subshell with its angular momentum aligned with the short axis (s) as seen in Fig. 6.10. The neutron, however, is located in a high-j, low-K orbital and its angular momentum will be aligned along the long axis (l). These orientations maximize the overlap of the valence particle wave functions with the triaxial nuclear shape and, thus, minimizes the interaction energy. The core is left with the intermediate axis (i) on which it aligns its angular momentum vector R. Such a situation is encountered in the mass $A \sim 130$ region, with $Z \sim 60$, $N \sim 75$. Here, the proton Fermi surface lies low in the $h_{11/2}$ shell, while the neutron Fermi surface lies high in the same $h_{11/2}$ shell. In addition, nuclei in this mass region are predicted to be soft with respect to γ deformation, and this triaxial deformation may be stabilized by the shape driving effects of the unpaired valence particles. Indeed, TRS calculations predicted stable

triaxial deformations for ^{134}Pr (N = 75, Z = 59) in the frequency interval 0.20 $\leq$ $\hbar\omega \leq$ 0.45 MeV. In fact, the observation of chiral properties may represent the first direct evidence for stable triaxial nuclei. In the TAC model, a stable triaxial (γ = -30°) mean field provides the three perpendicular axes of the mass distribution. The two orientations of the angular momentum of the rotating triaxial core (R), when coupled to the angular momentum of the valence nucleons, make up the left- and right-handed systems shown in the lower part of Fig 6.10.

6.6 Experimental Check for Chiral Bands in ^{130}La

The experimental fingerprint of chiral rotation is the observation of chiral-twin bands, which consist of a pair of nearly degenerate $\Delta I = 1$ rotational bands with the same parity. Most of the criteria discussed in the previous section for observing a chiral-twin band applies to ^{130}La. First, ^{130}La is an odd-odd nucleus with proton and neutron numbers $Z = 57$ and $N = 73$ which are very close to the predicted "ideal" case ^{134}Pr (N = 75, Z = 59) [166]. In addition, TRS calculations predict that the $\pi h_{11/2}\nu h_{11/2}$ configuration has a positive triaxial deformation of $\gamma \sim 12°$ for the frequency range $\sim 0.2 - 0.4$ MeV. However, this γ deformation value is smaller than the predicted value of $\gamma \sim 30°$ for ^{134}Pr and, therefore, the ^{130}La case will test the dependence on γ for observing chiral bands. The ability of the configuration to maintain a fixed triaxial deformation over an appreciable frequency range is critical to the formation of chiral bands [166]. In fact, recent experimental results by Koike *et al.* [167] propose a chiral twin band feeding the $\pi h_{11/2}\nu h_{11/2}$ band in ^{130}La at low spin. Therefore, an attempt to verify and investigate the properties of the proposed chiral-twin partner of the $\pi h_{11/2}\nu h_{11/2}$ band in ^{130}La has been made.

The proposed chiral band from Ref. [167] is shown in the top part of Fig. 6.11 feeding the $\pi h_{11/2}\nu h_{11/2}$ band via several mixed ($M1/E2$) transitions. The experimental data that support the presence of this band came from an experiment using the reaction ^{122}Sn (^{10}B,4n) at 47 MeV beam energy. Using six HPGe detectors, a total of $\sim$ 51 million prompt γ-γ events were recorded in that experiment [167]. For comparison purposes, our experiment had a total of approximately 1 billion γ^3 fold or

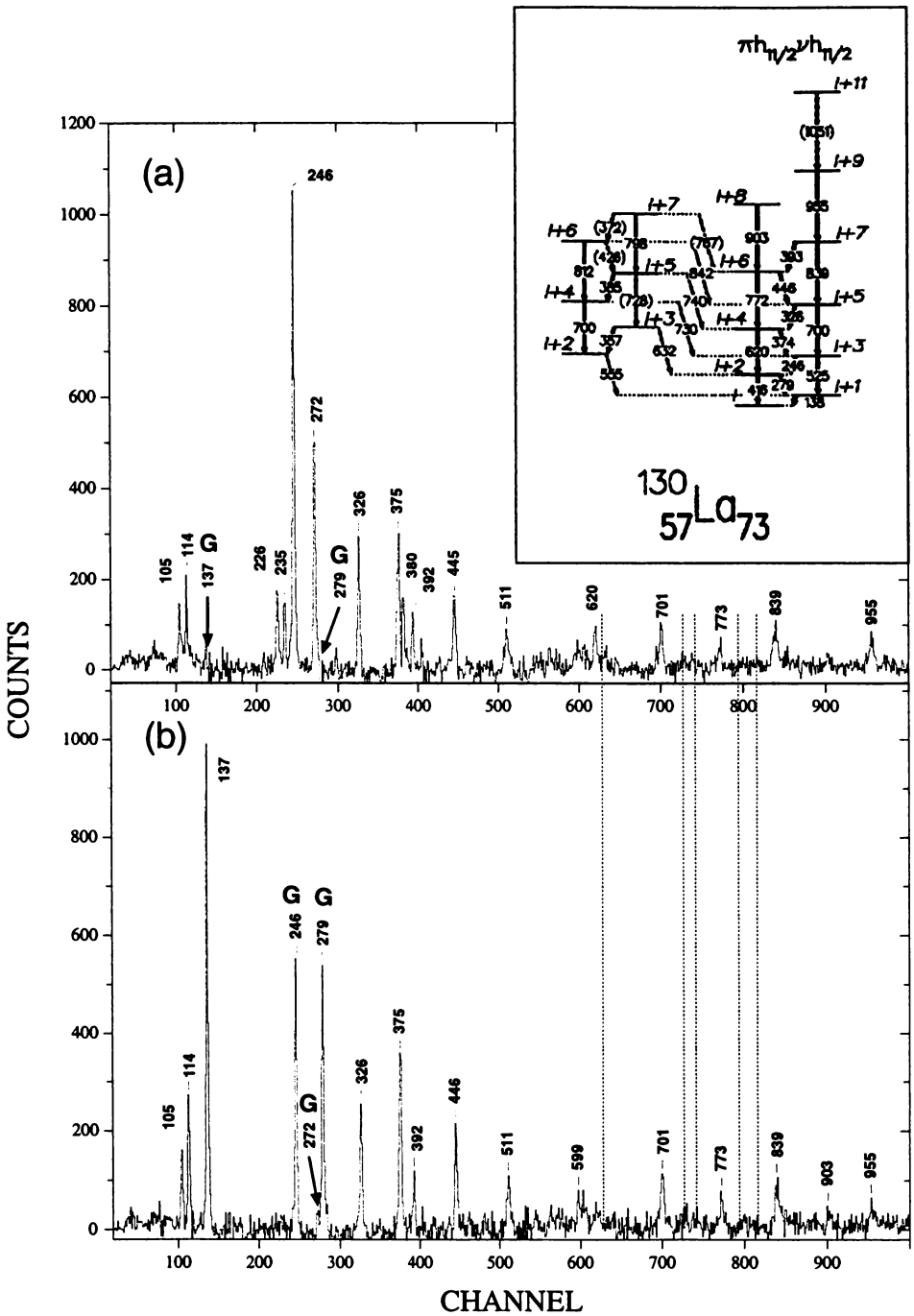


Figure 6.11: Gated spectra on bottom transitions of the $\pi h_{11/2}\nu h_{11/2}$ configuration in ^{130}La. The spectra are generated by summing double gated spectra of the transitions denoted by "G". The proposed chiral-twin band from Ref. [167] is shown in top right. The dotted lines mark the position of other coincident member transitions of the band.

higher events detected by 44 HPGe elements. Therefore, one would expect that our experimental data should easily reveal the proposed chiral band and possibly extend it to higher spins (due to the use of a heavier beam at a larger bombarding energy).

In order to confirm the presence of the γ-ray transitions for the side band shown in Fig. 6.11, we inspected our coincidence matrix. However, one should be careful when anlayzing matrix gates to take into account the presence of contaminant transitions resulting from other nuclei. In fact, several of the transitions in the proposed chiral band can be mistaken for such contaminant transitions. For example, the 357-keV transition is the $2^+ \rightarrow 0^+$ ground state of ^{130}Ba which is one of the strongest contaminants in our experiment. In addition, the 358- and 700-keV are strong in-band transitions in the $\pi h_{11/2} \nu h_{11/2}$ band, which makes it difficult to separate them even with double gating on a cube. The 842-keV transition decaying from the proposed chiral band is also close to the strong 839-keV in-band transition in the $\pi h_{11/2} \nu h_{11/2}$ configuration, which makes it difficult to separate them when gating from below. When gating on the in-band transitions of the proposed chiral-twin band, we were able to observe the lower strongest $M1$ transitions of the $\pi h_{11/2} \nu h_{11/2}$ band, but we did not observe other members of the chiral band. Moreover, we noticed that in-band gating brings the lower transitions of the ^{130}Ba ground-state band strongly in the spectra and at similar strength to the $\pi h_{11/2} \nu h_{11/2}$ band, and sometimes stronger. For example, gating on the 632- and 730-keV transitions brings back the 357-keV transition strongly, which contradicts the sequence logic shown in Fig. 6.11. Finally, it was impossible to generate a clean spectrum showing all of transitions of the proposed chiral band.

Double gating on the cube reduces the statistics, but it can be used to more accurately confirm the coincidence relations between the proposed transitions as contaminant transitions are suppressed with the extra gating condition. Fig. 6.11 shows two sample spectra generated by double gating on lower in-band transitions in the $\pi h_{11/2} \nu h_{11/2}$ configuration. Careful inspection of these two sample spectra shows that we do not observe any of the transitions in the proposed chiral band. In addition, we generated double-gates on the in-band transitions of the proposed side-band and two sample spectra are shown in Fig. 6.12. The spectra do not show other

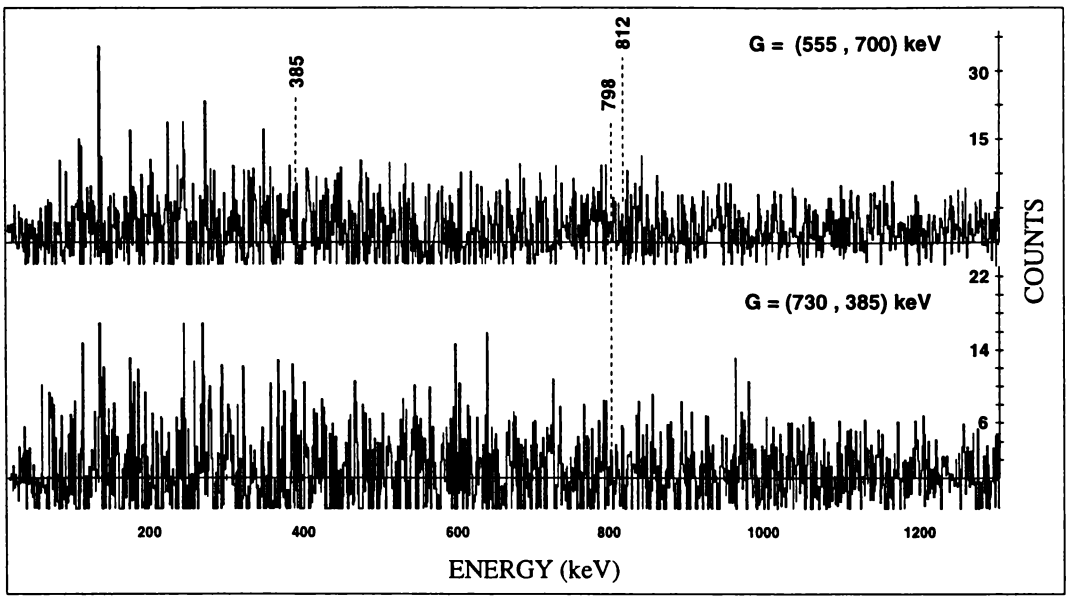


Figure 6.12: In-band gating on the proposed side-band transitions in Fig. 6.11. The spectra are produced by double gating on the 555- and 700-keV transitions above, and the 730- and 385-keV transitions below. The dashed lines mark the position of other coincident member transitions of the band.

coincident members of the band (position marked with dashed lines) indicating that there are no coincidence correlations between the proposed chiral band transitions, and only background spectra with very few counts are produced. Therefore, we arrive at the conclusion that our current data rule out the presence of a chiral-twin band in ^{130}La, and those proposed transitions for the chiral band are most likely a result of side-feedings.

In light of these results, one can now begin to establish boundaries of the chiral island in the $A \sim 130$ mass region. Fig. 6.13 shows a chart of odd-odd nuclei with known chiral bands. The experimental results on these nuclei came from the following references: ^{138}Eu [168], ^{136}Pm [152], ^{132}Pr [167], ^{134}Pr [152], ^{130}La [167], ^{132}La [152], ^{134}La [169], ^{128}Cs [167], ^{130}Cs [152]. One can see from Fig. 6.13 that most these nuclei fall in the $N = 75$ isotone chain with only three nuclei outside this chain so far. This shows that chirality is a unique phenomenon to a special class of nuclei. Further experimental work is needed to explore the extent of this island in $A \sim 130$

region and provide further understanding of the nuclear conditions that produce this novel phenomenon.

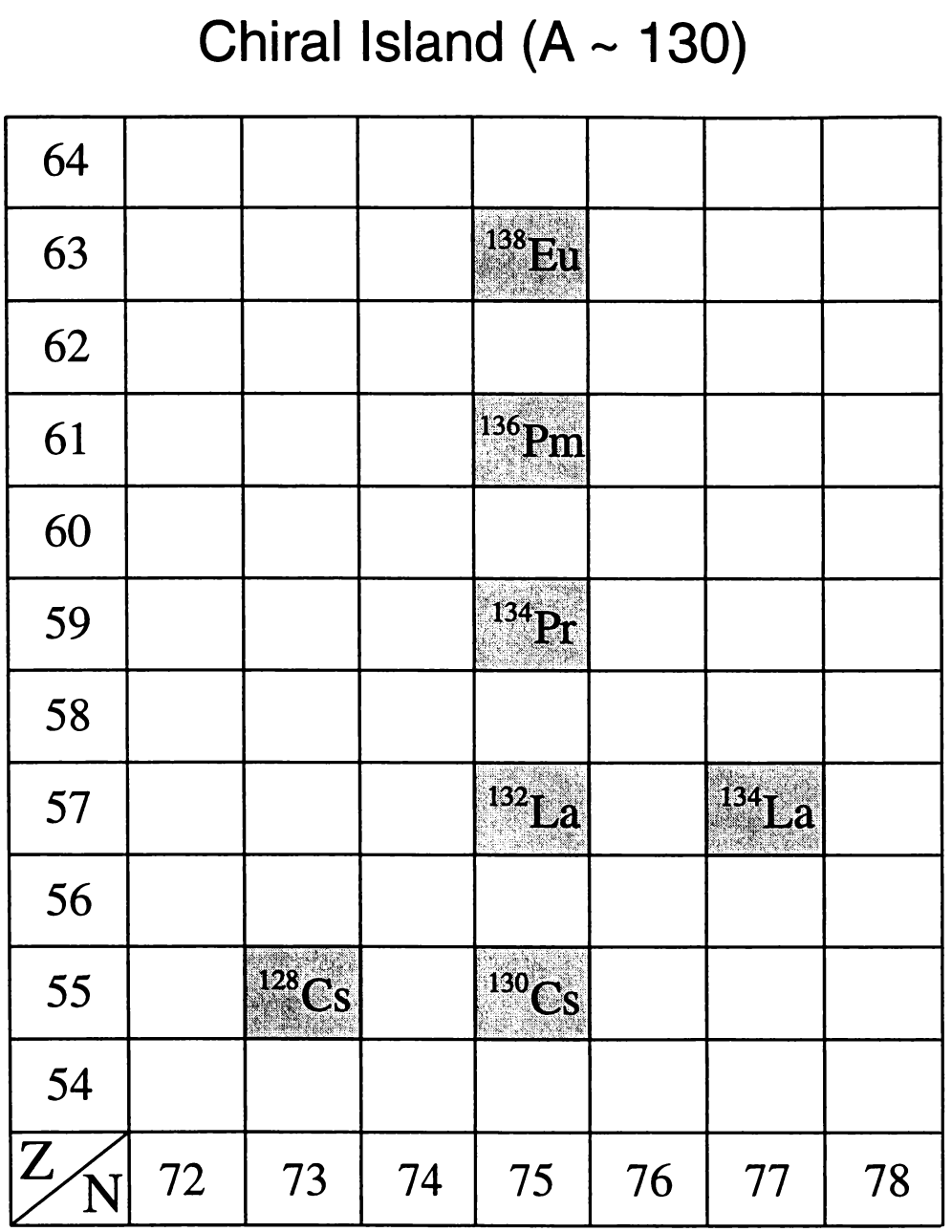


Figure 6.13: The island of chirality in the $A \sim 130$ mass region defined by the nuclei in the shaded boxes.

CHAPTER 7

Summary and Conclusions

Progress towards discrete γ-ray spectroscopy near the proton drip line has been made in the most neutron-deficient neodymium nuclei. The study of high-spin states in ^{128,129}Nd was part of an effort by our experimental group at the University of Tennessee to probe nuclear structure properties in $A \sim 130$ nuclei. Significant new spectroscopic information was added with the identification of 10 rotational sequences with more than 200 transitions in both nuclei identified for the first time. The selectivity of the Recoil Mass Spectrometer and the charged-particle array Hy-Ball in combination with the CLARION Ge array at ORNL, as well as the power of Gammasphere in conjunction with the Microball, was used to positively identify the structures. Several quasiparticle alignment processes (crossings) were observed in the bands, and were interpreted within the Cranked Shell Model (CSM).

The investigation of high-spin states in ^{128}Nd has resulted in the extension of the previously known ground-state band up to higher spins such that the $\nu h_{11/2}$ crossing was observed. This enabled us to investigate the systematic trends of this crossing over a wide range of neutron number in the most neutron-rich $A \sim 130$ nuclei. Unexpected large neutron $h_{11/2}$ crossing delays were observed in many of the nuclei surveyed (La, Ce, Pr, and Nd isotopes). In addition, a "jump" in crossing frequency was observed for most of the nuclei studied at $N = 70$. In order to understand these crossing trends, CSM calculations were performed at different values of deformations and pairing in a systematic way. The results of the calculation show that the CSM cannot reproduce the experimental crossings for any reasonable combination of its input parameters. However, the use of unrealistically large quadrupole deformation in the CSM can reproduce the large crossing values. Single-particle cranking calculations rule out the possible presence of a neutron subshell gap at $N = 70$, which

might influence pairing correlations and cause delays in the crossing frequency. We also performed Projected Shell Model (PSM) calculations and found that quadrupole pairing does not play a significant role in this neutron crossing. Having used three theoretical approaches to rule out possible factors that could affect the neutron $h_{11/2}$ crossing, further theoretical work is needed in order to understand this anomalous behavior in some of the $A \sim 130$ nuclei. The presence of octupole correlations in the most-yrast, negative-parity band in ^{128}Nd has been investigated. By comparing the strengths of the $E1$, $I \rightarrow I + 1$ transitions from this band to the ground-state band with similar transitions in other mass regions with known octupole correlations, we concluded that octupole vibrational states likely exist at low spins in this band. We found that our octupole vibrations arguments also apply to a similar band in the ^{126}Ce. Further experimental work is needed to populate side-bands in lighter even-even nuclei to see the extent of this phenomena in the mass 130 region.

Analysis of the high-spin states in ^{129}Nd has led to a significant extension of the previously known $\nu h_{11/2}$ structure which initiated a study of signature splitting systematics for $\nu h_{11/2}$ bands in the the $A \sim 130$ region. Signature splitting trends with N and Z, were established for the 17 nuclei included in the study (Sm, Ns, Ce, and Ba isotopes) and interpreted as a manifestation of the competition between γ and β_2 deformations. CSM model calculations were able to reproduce the observed signature splitting in these nuclei using appreciable negative γ deformation values that increases with N for each isotopic chain. CSM values of γ deformations were found to be smaller for the nuclei in the study than predicted γ-deformation values in TRS calculations at low spins. It was found that the signature splitting is "quenched" above the $\pi h_{11/2}$ crossing which was attributed to a shape change corresponding to $\gamma \sim 0$. A comparison was made at low and high spins with signature splitting of the $\pi h_{11/2}$ bands in $A \sim 160$ region and similar trends were observed. This systematic study appears to further strengthen the role of triaxiality in $A \sim 130$ nuclei. Signature splitting was also used to investigate the parentage of the deformation-driving [541]1/2 orbital. Evidence of an evolution from $f_{7/2}$ to $h_{9/2}$ was observed. In addition, evidence for the identification of the $\nu i_{13/2}$ band in ^{129}Nd was presented as it appears to adiabatically cross the [402]5/2 configuration at rotational frequency.

The study of high-spin states in ^{130}La has led to the confirmation of the previously published level scheme, and to a new arrangement of levels and coincidence correlations at low spins. The confirmation of the configuration structure of the $\pi h_{11/2}\nu h_{11/2}$ and $\pi h_{11/2}\nu g_{7/2}$ bands was based on alignments, $B(M1)/B(E2)$ ratios, and comparison with CSM calculations. New spin assignments for these bands were proposed based on excitation energy systematics of odd-odd La nuclei and the new measured multipolarities of transitions at low spins. A new configuration and spin assignment was made for the previously known oblate band based on the new spectroscopic information. The presence of isomeric states at low spins for all three configurations of ^{130}La has been established based on the spin assignments. Our new analysis of coincidence correlations in the $\pi h_{11/2}\nu h_{11/2}$ band questions the presence of a previously proposed chiral-twin band with the $\pi h_{11/2}\nu h_{11/2}$ configuration. As no chiral twin band is observed in ^{130}La, the shores of the island of chirality are beginning to take shape for the mass $A \sim 130$ region, indicating that this novel phenomenon requires very precise and selective nuclear conditions which apparently exist only in a limited number of nuclei. Based on the new spectroscopic information, a delayed-time experiment on this nucleus is needed in order to study isomers and link bands to the ground state and, thus, provide definite spin assignments to the rotational configurations of this nucleus. In addition, a measurement will be needed to find the time-delayed linking transitions between the oblate band and the prolate $\pi h_{11/2}\nu g_{7/2}$ band, so that the quasiparticle configuration of the oblate structure can be confirmed.

The nuclei studied in this work were produced through the fusion evaporation reaction of stable beams and targets. However, it becomes increasingly difficult to populate high-spin states in lighter $A \sim 130$ nuclei using a stable beam and target. With the use of radioactive ion beams (RIBs), new reaction choices will enable us to populate high-spin states in nuclei even further from stability. High-spin studies require large amount of statistics and RIBs are currently produced at low intensities, which means that it is essential to develop a very efficient detector array. There is an effort to build such a device called GRETA (Gamma-Ray Tracking Array) which uses High-Purity Ge detectors to cover the 4π space around the target. The use of GRETA with RIBs will push the high-spin physics in the mass 130 region further to

the proton drip line and shed light on present unexplained phenomena and reveal new ones. The author wishes that with the current efforts to develop the radioactive ^{56}Ni beam, the nuclear properties of ^{126,127}Nd can be studied through the population of high-spin states in the reaction ^{56}Ni + ^{74}Se. The results presented in this dissertation work on ^{128,129}Nd will serve as a basis for such studies.

BIBLIOGRAPHY

BIBLIOGRAPHY

[1] P. Möller, J.R. Nix, W.D. Myers, and W.J. Swiatecki, At. Data Nucl. Data Tables **59**, 185 (1995).

[2] W. Elsasser, J. Phys. Rad. **5**, 625 (1934).

[3] M.G. Mayer, Phys. Rev. **74**, 235 (1948).

[4] M.G. Mayer and J.H.D. Jensen, *Elementary Theory of Nuclear Shell Structure*, John Wiley & Sons, Inc., New York (1955).

[5] M.G. Mayer, Phys. Rev. **78**, 16 (1950).

[6] O. Haxel, J.H.D. Jensen, and H.E. Suess, Z. Physik **128**, 295 (1950).

[7] R.F. Casten, *Nuclear Structure from a Simple Perspective*, Oxford University Press, New York (1990).

[8] *Table of Isotopes*, 8th ed., R.B. Firestone (ed.), (John Wiley & Sons Inc., New York, 1996), Vol. 2.

[9] W.F. Mueller, Ph.D. thesis, Univeristy of Tennessee (1997).

[10] L.J. Rainwater, Phys. Rev. **79**, 432 (1950).

[11] A. Bohr and B.R. Mottelson, Dan. Mat.-Fys. Medd. **27** 16, (1953).

[12] A. Bohr and B.R. Mottelson, *Nuclear Structure* (World Scientific Publishing Co., 1998).

[13] S.G. Nilsson, Dan. Mat.-Fys. Medd. **29**, No. 16 (1955).

[14] C. Gustafson, I.L. Lamm, B. Nilsson, and S.G. Nilsson, Arkiv Fysik **36**, 613 (1967).

[15] Peter Ring and Peter Schuck, *The Nuclear Many-Body Problem*, Springer-Verlag, New York, 1980.

[16] R.D. Woods and D.S. Saxon, Phys. Rev. **95**, 577 (1954).

[17] D.R. Inglis, Phys. Rev. **96**, 1059 (1954); *ibid.* **97**, 701 (1955).

[18] R. Bengtsson and S. Frauendorf, Nuclear Phys. A. **327**, 139 (1979); *ibid* A **314**, 27 (1979).

[19] M.J.A de Voigt, J. Dudek, and Szymański, Rev. Mod. Phys. **55**, 949 (1983).

[20] J.D. Garrett *et al.*, Phys Scr. **T5**, 21 (1983).

[21] H. Ejiri and M.J.A. de Voigt, *Gamma-Ray and Electron Spectroscopy in Nuclear Physics*, (Clarendon Press, Oxford, 1989).

[22] J. Bardeen, L.N Cooper, and J.R. Schrieffer, Phys. Rev. **106**, 162 (1957).

[23] A. Bohr, B.R. Mottelson, and D. Pines, Phys. Rev. **110**, 936 (1958).

[24] S.M. Harris, Phys. Rev. B. **138**, 509 (1965).

[25] P. Ring and P. Schuck, *The Nuclear Many-Body Problem*, Springer-Verlag New York Inc., (1980).

[26] N.N. Bogoliubov, Sov. Phys. Usp. **2**, 236 (1959).

[27] W. Nazarewicz, G.A. Leander, and J. Dudek, Nucl. Phys. A **467**, 437 (1985).

[28] R. Wyss, J. Nyberg, A. Johnson, R. Bengtsson, and W. Nazarewicz, Nucl. Phys. B **215**, 211 (1988).

[29] W. Nazarewicz, R. Wyss, and A. Johnson, Nucl. Phys. A **503**, 285 (1989).

[30] R. Bengtsson, S. Frauendorf, and F.R. May, At. Data Nuc. Data Tables, **35**, 15 (1986).

[31] A. Johnson, H. Ryde, and J. Sztarkier, Phys. Lett. B **34**, 605 (1971).

[32] A. Johnson, H. Ryde, and S.A. Hjorth, Nucl. Phys. A **179**, 753 (1972).

[33] V.F. Weisskopf, Phys. Rev. **83**, 1073 (1951).

[34] W.D. Hamilton, *The Electromagnetic Interaction in Nuclear Spectroscopy*, North-Holland publishing company, New York, 1975.

[35] R. Ma, E.S. Paul, S. Shi, C.W. Beausang, Jr. W.F. Piel, N. Xu, D.B. Fossan, T. Chapuran, D.P. Balamuth, and J.W. Arrison, Phys. Rev. C **37**, 1926 (1988).

[36] F. Dönau, Nucl. Phys. A **471**, 469 (1987).

[37] S. Frauendorf, Phys. Lett. B **100**, 219 (1981).

[38] *Heavy ion collisions*, edited by R. Bock (North-Holland Pub. Co., Amsterdam; New York, 1982), Vol. 3.

[39] R. M. Diamond and F. S. Stephens, Annu. Rev. Nucl. Part. Sci. **30**, 85 (1980).

[40] A. Gavron, Phys. Rev. C **21**, 230 (1980).

[41] Oak Ridge National Laboratory; Oak Ridge, TN; Anonymous ftp from: ftp.ornl.phy.ornl.gov.

[42] W. Reisdorf, Z. Phys. A **300**, 227 (1981).

[43] C. J. Gross *et al.* Nucl. Instrum. Methods Phys. Res. A **450**, 12 (2000).

[44] C.J. Gross, T. N. Ginter, Y.A. Akovali, M.J. Brinkman, J.W. Johnson, J. Mas, J.W. McConnell, W.T. Milner, D. Shapira, and A.N. James, in CP392, *Application of Accelerators in Research and Industry*, edited by J. L. Duggan and I. L. Morgan (AIP Press, New York, 1997), p. 401.

[45] D.G. Sarantites, P.-F. Hua, M. Devlin, L.G. Sobotka, J. Elson, J.T. Hood, D.R. LaFosse, J.E. Sarantites, and M.R. Maier, Nucl. Instrum. Methods Phys. Res. A **381**, 418 (1996).

[46] R.V.F. Janssens and F. Stephens, Nucl. Phys. News **6**, 9 (1996).

[47] C. W. Bausang *et al.*, Nucl. Instrum. Methods Phys. Res. A **452**, 431 (2000).

[48] G.F. Knoll, *Radiation Detection and Measurement*, 2 ed. (John Wiley and Sons, Inc., New York, 1989).

[49] W.R. Leo, *Techniques for Nuclear and Particle Physics Experiments*, 2 ed. (Springer-Verlag, New York, 1994).

[50] D.G. Sarantites, private communication (1998).

[51] A.O. Macchiavellei, I. Y. Lee, B. Cederwall, R. M. Clark, M. A. Deleplanque, R. M. Diamond, P. Fallon, and F. S. Stephens, in *Conference on Physics from Large γ-ray Detector Arrays* (LBNL, Berkeley, California, 1994), p. 149, (Vol. 1).

[52] A.M. Baxter, T.L. Khoo, M.E. Bleich, M.P. Carpenter, I. Ahmad, R.V.F Janssens, E.F. Moore, I.G. Bearden, J.R. Beene, and I.Y. Lee, Nuc. Inst. and Meth. in Phys. Research. A **317**, 101 (1992).

[53] D.C. Radford, *Proceedings of the International Seminar on the Frontier of Nuclear Spectroscopy, Kyoto, October 1992*, ed. Y. Yoshizawa, H. Kusakari and T. Otsuka, World Scientific, 1993, p. 229.

[54] D.C. Radford, M. Cromaz, and C.J. Beyer, *Preceedings of Nuclear Structure 98*, p570.

[55] A. Johnson, H. Ryde and J. Sztarkier, Phys. Lett. B **34**, 605 (1971).

[56] L.L. Riedinger *et al.*, Phys. Rev. Lett. **44**, 568 (1980).

[57] H.Q. Jin, Document ru9455, Rutgers University (unpublished).

[58] <http://wunmr.wustl.edu/ dgs/mball/index.html>

[59] *Table of Isotopes*, 8th ed., edited by R.B. Firestone (John Wiley & Sons Inc., New York, NY, 1996), Vol. 2.

[60] D.C. Radford, Nucl. Inst. and Meth., A **361** 297 (1995); *ibid* A **361** 306 (1995).

[61] K.S. Krane, R. M. Steffen, and R. M. Wheeler, Nucl. Data Tab. **11**, 351 (1973).

[62] A. Krämer-Flecken, T. Morek, R. M. Lieder, W. Gast, G. Hebbinghaus, H. M. Jäger, and W. Urban, Nucl. Inst. and Meth. A **275**, 333 (1985).

[63] L. Peter Ekström and Anders Nordlund, Nucl. Inst. and Meth. A **313**, 421 (1992).

[64] D.J. Hartley *et al.*, Phys. Rev. C **63**, 024316 (2001).

[65] D.C. Radford, Nucl. Instrum. Methods Phys. Res. A **361**, 297 (1995).

[66] C.J. Lister *et al.*, Phys. Rev. Lett. **55**, 810 (1985).

[67] R. Moscrop, M. Campbell, W. Gelletly, L. Goettig, C.J. Lister, and B.J. Varley, Nucl. Phys. A **499**, 565 (1989).

[68] C.M. Petrache *et al.*, Phys. Lett. B **387**, 31 (1996).

[69] R. Wadsworth, S.M. Mullins, J.R. Hughes, P.J. Nolan, A. Kirwan, P.J. Bishop, I. Jenkins, M.J. Godfrey, and D.J. Thornley, J. Phys. G **15**, L47 (1989).

[70] R. Bengtsson and S. Frauendorf, Nucl. Phys. A **327**, 139 (1979); Nucl. Phys. **A314**, 27 (1979).

[71] D.J. Hartley *et al.* Phys. Rev. C **60**, 041301(R) (1999).

[72] B.H. Smith, L.L. Riedinger, H.Q. Jin, W. Reviol, W. Satula, A. Galindo-Uribarri, D.G. Sarantites, J.N. Wilson, D. LaFosse, and S.M. Mullins, Phys. Lett. B **443**, 89 (1998).

[73] O. Zeidan *et al.*, Phys. Rev. C (in press).

[74] P.A. Butler and W. Nazarewicz, Rev. Mod. Phys. **68**, 349 (1996).

[75] A. N. Wilson *et al.*, Phys. Rev. C **63**, 054307 (2001).

[76] W. Nazarewicz and S. L. Tabor, Phys. Rev. C. **45**, 2226 (1992).

[77] G.B. Hagemann, I. Hamamoto, and W. Satula, Phys. Rev. C **47**, 2008 (1993).

[78] M.J.A. De Voight, R. Kaczarowski, H. J. Riezebos, R. F. Noorman, J. C. Bacelar, M.A. Delephanque, R.M. Diamond, F.S. Stephens, J. Sauvage, and R. Roussiere, Nucl. Phys. A. **507**, 472 (1990).

[79] G. D. Dracoulis, C. Fahlander, and M.P. Fewell, Nucl. Phys. A **383**, 119 (1982).

[80] F.G. Kondev *et al.*, Phys. Rev. C. **61**, 044323 (2000).

[81] P.D. Cottle, Phys. Rev. C **47**, 1529 (1993).

[82] A. Granderath, P.F Mantica, R. Bengtsson, R. Wyss, P. von Brentano, A. Gelberg, and F. Seiffert, Nucl. Phys. A **597** 427 (1996).

[83] E.S. Paul *et al.*, Nucl. Phys. A **676**, 32 (2000).

[84] D.J. Hartley, L.L. Riedinger, H.Q. Jin, W. Reviol, B.H. Smith, A. Galindo-Uribarri, D.G. Sarantites, D.R. LaFosse, J.N. Wilson, and S.M. Mullins, Phys. Rev. C **60**, 014308 (1999).

[85] D.J. Hartley *et al.*, Phys. Rev. C **61**, 044328 (2000).

[86] R. Wadsworth, J.M. O'Donnel, D.L. Watson, P.J. Nolan, A. Kirwan, P.J. Bishop, M.J. Godfrey, D.J. Thornley, and D.J.G. Love, J. Phys. G **14**, 239 (1988).

[87] D. Bazzacco *et al.*, Phys. Rev. C. **58**, 2002 (1998).

[88] S.M. Mullins *et al.*, Phys. Rev. C **58**, R2626 (1998).

[89] D. J. Hartley *et al.*, unpublished.

[90] A. Galindo-Uribarri *et al.*, unpublished.

[91] B.H. Smith, Ph.D. thesis, University of Tennessee (1998).

[92] A. Galindo-Uribarri *et al.*, Phys. Rev. C **50**, R2655 (1994).

[93] C.M. Petrache, S. Brant, D. Bazzacco, G. Falconi, E. Farnea, S. Lunardi, V. Paar. Zs. Podolyák, R. Venturelli, D. Vretenar, Nucl. Phys. **A635**, 361 (1998).

[94] E.S. Paul *et al.*, Nucl. Phys. A **690**, 341 (2001).

[95] R. Aryaeinejad, D.J.G. Love, A. H. Nelson, P.J. Nolan, P.J. Smith, D.M. Todd, and P.J. Twin, J. Phys. G **10**, 955 (1984).

[96] A.T. Semple *et al.*, J. Phys. G **24**, 1125 (1998).

[97] M. Palacz, Z. Sujkowski, J. Nyberg, J. Bacelar, J. Jongman, W. Urban, W. Hesselink, J. Nasser, A. Plompen, and R. Wyss, Z. Phys. A **338**, 467 (1991).

[98] E.S. Paul *et al.*, Nucl. Phys. A **619**, 177 (1997).

[99] J. Timár *et al.*, Eur. Phys. J. A **7**, 7 (2000).

[100] K. Starosta *et al.*, Phys. Rev. C **53**, 137 (1996).

[101] M.J. Godfrey *et al.*, J. Phys. G. **15**, 487 (1989).

[102] Y. He *et al.*, J. Phys. G **18**, 99 (1992).

[103] O. Zeidan *et al.*, unpublished.

[104] E.S. Paul, C. W. Bausang, D.B. Fossan, R. Ma, W.F. Piel, Jr., N. Xu, L. Hildingsson, and G.A. Leander, Phys. Rev. lett. **58**, 984 (1987).

[105] K. Hara and Y. Sun, Int. J. Mod. Phys. E **4**, 637 (1995).

[106] Y. Sun, S.X. Wen and D.H. Feng, Phys. Rev. Lett. **72**, 3483 (1994).

[107] C.J. Gross, Z. Phys. A **358**, 249 (1997).

[108] D.B. Fossan, J.R. Hughes, Y. Lian, R. Ma, E.S. Paul, and N.Xu, Nucl. Phys. A **520**, 241c (1990).

[109] R.M. Clark *et al.*, Phys. Rev. Lett. **76**, 3510 (1996).

[110] F.G. Kondev *et al.*, Phys. Rev. C **60**, 011303(R) (1999).

[111] A. Galindo-Uribarri, D. Ward, H.R. Andrews, G.C. Ball, D.C. Radford, V.P. Janzen, S.M. Mullins, J.C. Waddington, A.V. Afanasjev, and I. Ragnarsson, Phys. Rev. C **54**, 1057 (1996).

[112] N.J. O'Brien *et al*, Phys. Rev. C **58**, 3212 (1998).

[113] R. Wyss, J. Nyberg, A. Johnson, R. Bengtsson, and W. Nazarewicz, Phys. Lett. B **215**, 211 (1988).

[114] A.V. Afanasjev and I. Ragnarsson, Nucl. Phys. A **608**, 176 (1996).

[115] D. Bazzacco *et al.*, Phys. Rev. C **58**, 2002 (1998).

[116] D.C.B. Watson, A.N. James, M.A. Skelton, and J. Simpson, Liverpool Univ., Ann. Rept., 1987-1988, p. 31 (1989).

[117] P.A. Wilmarth *et al.*, Z. Phys. A **321**, 179 (1985).

[118] A. Gizon *et al.*, Z. Phys. A **358**, 369 (1997).

[119] B.M. Nyakó, J. Gizon, V. Barci, A. Gizon, S. André, D. Barnéoud, J. Genevey, and J.C. Merdinger, Z. Phys. A **334**, 513 (1998).

[120] J.Genevey *et al.* Z. Phys. A **356**, 7 (1996).

[121] J.P. Martin, V. Barci, H. El-Samman, A. Gizon, W. Klamra, B. M. Nyakó, F.A. Beck, Th. Byrski, and J.C. Merdinger, Nuc. Phys. A **489**, 169 (1988).

[122] J. Katakura, Nucl. Data. Sheets **86**, 955 (1999).

[123] S. Ćwiok, J. Dudek, W. Nazarewicz, J. Skalski, and T. Werner, Comput. Phys. Commun. **46**, 379 (1987).

[124] J. Dudek, A. Majhofer, J. Skalski, T. Werner, S. Ćwiok, and W. Nazarewicz, J. Phys. G **5**, 1359 (1979).

[125] W. Nazarewicz, M.A. Riley, and J.D. Garrett, Nucl. Phys. A **512**, 61 (1990).

[126] R. Bengtsson, S. Frauendorf, and F.-R. May, At. Data Nucl. Data Tables **35**, 15 (1986).

[127] S.M. Mullins *et al.*, J. Phys. G **13**, L201 (1987).

[128] V.P. Janzen *et al*, Phys. Rev. C **45**, 613 (1992).

[129] F. Dönau, Nucl. Phys. A **471**, 469 (1987).

[130] L.L. Riedinger, H.Q. Jin, W. Reviol, J.Y. Zhang, R.A. Bark, G.B. Hagemann, and P.B. Semmes, Prog. Part. Nucl. Phys. **38**, 251 (1997).

[131] G. A. Leander, S. Frauendorf, and R.F. May, in *High Angular Momentum Properties of Nuclei*, ed. by N.R. Johnson, (Howard Academic, New York) p281, 1982.

[132] Y.S. Chen and G.A. Leander, University of Tennessee progress report, p. 90, 1986.

[133] M.P. Carpenter, Ph.D. thesis, University of Tennessee (1988).

[134] D.J. Hartley, T.B. Brown, F.G. Kondev, J. Pfohl, M.A. Riley, S.M. Fischer, R.V.F. Janssens, D.T. Nisius, P. Fallon, W.C. Ma, and J. Simpson, Phys. Rev. C **58**, 2720 (1998).

[135] I. Hamamoto, Nucl. Phys. A **520**, 297c (1990).

[136] R. Wyss, F. Lidén, J. Nyberg, A. Johnson, D.J.G. Love, A.H. Nelson, D.W. Banes, J. Simpson, A. Kirwan, and R. Bengtsson, Z. Phys. A **330**, 123 (1988).

[137] A. Dewald *et al.*, Eur. Phys. J **A3**, 103 (1998).

[138] K. Schiffer, A.P. Byrne, A.M. Baxter, G.D. Dracoulis, and A.E Stuchbery, Z. Phys. A **336**, 239 (1990).

[139] R. Ma, Y. Liang, E.S. Paul, N. Xu, D.B. Fossan, L. Hildingsson, and R.A. Wyss, Phys. Rev. C **41**, 717 (1990).

[140] E.S. Paul *et al.*, Phys. Rev. C **58**, 801 (1998).

[141] K. Hauschild *et al.*, Phys. Rev. C **54**, 613 (1996).

[142] F. Brandolini *et al.*, Phys. Rev. C **60**, 024310 (1999).

[143] W.F. Piel, Jr., C. W. Beausang, D.B. Fossan, L. Hildingsson, and E.S. Paul, Phys. Rev. C **35**, 959 (1987).

[144] P.H. Regan *et al.*, Nucl. Phys. A **533**, 476 (1991).

[145] E.S. Paul, R. Ma, C.W. Beausang, D.B. Fossan, W.F. Piel, Jr., S. Shi, N. Xu, and J.-y. Zhang, Phys. Rev. Lett. **61**, 42 (1988).

[146] D.J. Hartley *et al.*, Phys. Rev. C **63**, 041301(R) (2001).

[147] Y.S. Chen, S. Frauendorf, and L.L. Riedinger, Phys. Lett. B **171**, 7 (1986).

[148] N. Tajima, Nucl. Phys. A **572**, 365 (1994).

[149] S. Jónsson, J. Lyttkens, L. Carlén, N. Roy, H. Ryde, W. Waluś, J. Kownacki, G.B. Hagemann, B. Herskind, J.D. Garrett, and P.O. Tjøm, Nucl. Phys. A **422**, 397 (1984).

[150] C.-H. Yu, G.B. Hagemann, J.M. Espino, K. Furuno, J.D. Garrett, R. Chapman, D. Clarke, F. Khazaie, J.C. Lisle, J.N. Mo, M. Bergström, L. Carlén, P. Ekström, J. Lyttkens, and H. Ryde, Nucl. Phys. A **511**, 157 (1990).

[151] S. Ogaza, J. Kownacki, M.P. Carpenter, J. Gascon, G.B. Hagemann, Y. Iwata, H.J. Jensen, T. Komatsubara, J. Nyberg, G. Sletten, P.O. Tjøm, W. Waluś, and I. Hamamoto, Nucl. Phys. A **559**, 100 (1993).

[152] K. Starosta *et al.*, Phys. Rev. Lett. **86**, 971 (2001).

[153] E.S. Paul, C. W. Beausang, D.B. Fossan, R. Ma, W.F. Piel, N. Xu, and L. Hildingsson, Phys. Rev. C **36**, 1853 (1987).

[154] M.J. Godfrey, Y. He, I. Jenkins, A. Kirwan, P.J. Nolan, D.J. Thornley, S.M. Mullins, R. Wadsworth, J. Phys. G **15**, 487 (1989).

[155] M.J. Godfrey, Y. He, I. Jenkins, A. Kirwan, P.J. Nolan, D.J. Thornley, S.M. Mullins, R. Wadsworth, and R.A. Wyss, J. Phys. G **15**, 671 (1989).

[156] Xu Shuwei *et al.*, Z. Phys. A **356**, 35 (1996).

[157] Y. He, M.J. Godfrey, I. Jekins, A.J. Kirwan, S.M. Mullins, P.J. Nolan, E.S. paul, and R. Wadsworth, J. Phys. G **18**, 99 (1992).

[158] R. Kumar, D. Mehta, N. Singh, H. Kaur, A. Görgen, S. Chmel, R.P. Singh, and S. Murlithar, Eur. Phys. J. A **11**, 5 (2001).

[159] C.J. Gallagher and S.A. Moszkowski, Phys. Rev. **111**, 1282 (1958).

[160] S. Frauendorf, L.L. Riedinger, J.D. Garrett, J.J. Gaardhøje, G.B. Hagemann, and B. Herskind, Nucl. Phys. A **431**, 511 (1984).

[161] E.S. Paul, D. B. Fossan, Y. Liang, R. Ma, and N. Xu, Phys. Rev. C **40**, 619 (1989).

[162] Yunzuo Liu, Jingbin Lu, Yingjun Ma, Shangui Zhou, and Hua Zheng, Phys. Rev. C **54**, 719 (1996).

[163] N. Tajima, Nucl. Phys. A **572**, 365 (1994).

[164] D.B. Fossan, J.R. Hughes, Y. Liang, R. Ma, E.S. Paul, and N. Xu, Nucl. Phys. A **520**, 241 (1990).

[165] S. Frauendorf and Jie Meng, Nucl. Phys. A **617**, 131 (1997).

[166] V.I. Dimitrov, S. Frauendorf, and F. Dönau, Phys. Rev. Lett. **84**, 5732 (2000).

[167] T. Koike, K. Starosta, C.J. Chiara, and D.B. Fossan, and D.R. LaFosse, Phys. Rev. C **63**, 061304(R) (2001).

[168] A. A. Hecht *et al.*, Phys. Rev. C **63**, 051302(R) (2001).

[169] R.A. Bark, A.M. Baxter, A.P. Byne, G.D. Dracoulis, T.R. McGoram, and S.M. Mullins, Nucl. Phys. A **691**, 577 (2001).

[170] GAMMASPHERE booklet, M.A. Riley (ed.), http://www-gam.lbl.gov.

VITA

Omar A. Zeidan was born in Ramallah, Palestine, on May 3, 1974. He graduated from St. George High School in Jerusalem in the spring of 1991. He attended Yarmouk University, Jordan and graduated with a B.Sc. degree in physics in the spring of 1995. Pursuing an interest in nuclear physics, he joined Michigan State University and graduated with a M.Sc. in physics in May 1998. While there, he worked as a research assistant at the National Superconducting Cyclotron Lab on the development of charged particle detectors for nuclear fragmentation studies.

Starting the summer of 1998, he accepted a research assistantship to study experimental high-spin physics under the supervision of Dr. Lee Riedinger, University of Tennessee. On March 20, 2000, he married Lara A. Thalji. At the completion of this work, he has accepted a postdoctoral position at the University of Florida, College of Medicine, to conduct research in the field of Radiation Oncology.

3238 2553 5
07-24-02 MRB